

EXPERIMENTAL QUANTUM COMPUTATION WITH NUCLEAR SPINS IN LIQUID SOLUTION

A DISSERTATION
SUBMITTED TO THE DEPARTMENT OF ELECTRICAL ENGINEERING
AND THE COMMITTEE ON GRADUATE STUDIES
OF STANFORD UNIVERSITY
IN PARTIAL FULFILLMENT OF THE REQUIREMENTS
FOR THE DEGREE OF
DOCTOR OF PHILOSOPHY

Lieven M. K. Vandersypen

July 2001

© Copyright by Lieven M. K. Vandersypen 2001
All Rights Reserved

I certify that I have read this dissertation and that in my opinion it is fully adequate, in scope and quality, as a dissertation for the degree of Doctor of Philosophy.

Prof. James S. Harris (Principal adviser)

Dr. Isaac L. Chuang (Co-adviser)

Prof. Yoshihisa Yamamoto

Approved by the University Committee on Graduate Studies

Abstract

Quantum computation offers the extraordinary promise of solving mathematical and physical problems which are simply beyond the reach of classical computers. However, the experimental realization of quantum computers is extremely challenging, because of the need to initialize, manipulate and measure the state of a set of coupled quantum systems while maintaining fragile quantum coherence.

In this thesis work, we have taken significant steps towards the realization of a practical quantum computer: using nuclear spins and magnetic resonance techniques at room temperature, we provided proof of principle of quantum computing in a series of experiments which culminated in the implementation of the simplest instance of Shor's quantum algorithm for prime factorization ($15 = 3 \times 5$), using a seven-spin molecule. This algorithm achieves an exponential advantage over the best known classical factoring algorithms and its implementation represents a milestone in the experimental exploration of quantum computation.

These remarkable successes have been made possible by the synthesis of suitable molecules and the development of many novel techniques for initialization, coherent control and readout of the state of multiple coupled nuclear spins. Furthermore, we devised and implemented a model to simulate both unitary and decoherence processes in these systems, in order to study and quantify the impact of various technological as well as fundamental sources of errors.

In summary, this work has given us a much needed practical appreciation of what it takes to build a quantum computer. Furthermore, while liquid NMR quantum computing has well-understood scaling limitations, many of the techniques that originated from this research may find use in other, perhaps more scalable quantum computer implementations.

Preface

A long, long time ago, in a land far away, a man was sentenced to death. The man requested to speak to the King, and the King agreed to hear him. “If you let me live for one more year,” offered the man, “I promise to make your horse fly high above the land.” The King realized that a flying horse would be quite unique, and took immense pleasure in the prospect of possessing the only flying horse in the land. He agreed to set the man free and let him live one more year.

When the man came home and told his wife what he had promised the King, she exclaimed in anguish: “But you’ll never be able to make the King’s horse fly!” “Well,” said the man, “I know that, and you know that, but in the meantime many things can happen. The country may go to war, the King may die, or the King’s horse may die, but I will still be alive for another year.”¹



Now, can we build a quantum computer ? And should we promise to build one ? These are the broad and ambitious questions underlying this thesis work. The final verdict is not in yet, and fortunately we are given more than one year. However, it is for certain that only by studying quantum computation experimentally, can we begin to understand and appreciate at a practical level what it would take to turn the dream of quantum computation into reality. This is the purpose of my work.

¹Free after James Harris. Thanks to Nico for the drawing of the flying horse.

Acknowledgements

As a mechanical engineering sophomore at the Katholieke Universiteit Leuven, I took a great and inspiring class in quantum mechanics with Guido Langouche. It was the beginning of a profound interest in quantum mechanics, and a fascination which continues to this day. Later, a second interest developed: to build mechanical systems on a very small scale. Two other great courses, with Hendrik Van Brussel and Willy Sansen, gave me the opportunity to further explore this area.

When I came to Stanford University for graduate school, I was looking for a project to combine these two interests, for example by studying if and how quantum mechanical effects could be observed in micromachined structures. For one quarter, I worked on microcantilevers in the most stimulating group of Yoshihisa Yamamoto.

Then I talked to Jim Harris, who suggested I try to microfabricate components for an NMR quantum computer. Soon after I talked to Ike Chuang, the initiator of this project (then at Los Alamos, later at IBM Almaden), and started reading about quantum computing, I became increasingly fascinated by quantum computing itself. I knew this is what I wanted to work on!

It was the beginning of an extraordinary four years, four years I am very thankful for. The fact that this has been such a wonderful time is due to many great people.

Jim Harris, my advisor and “coach”, has generously introduced me to the right people to make my work a success, and strongly supported me in many ways, in and outside research. His view on life and on what is really important is a true inspiration to me. Ike Chuang, my co-advisor, gave me both guidance and independence, at the right times. He taught me how to present my work and put it in perspective, and also to think positive and creatively (to say “what would it take to *make* this work” instead of “this won’t work”). Also, Coach’s and Ike’s strong support and belief in my abilities, as well as their encouragement for my non-research activities, have been invaluable to me.

Matthias Steffen worked very closely with me for about two years and a half, first as an apprentice, but increasingly as a great co-worker. He brought in many useful ideas and did a lot of the work in the later experiments. Xinlan Zhou kindly helped me out with many theoretical questions throughout the past years.

Nino Yannoni discovered most of the molecules we have used, and also provided me with many wise words. Mark Sherwood has greatly contributed for concepts and techniques in NMR

and for molecule selection. Greg Breyta gave us a lot of the time he didn't have, to synthesize the five and seven spin molecules.

I am very grateful to my other co-authors, in particular Richard Cleve, with whom I worked so pleasantly. I am also indebted to the many colleagues from whom I've learnt and with whom I had such nice interactions (especially Dorit Aharonov, Michael Nielsen, David DiVincenzo and Ray Freeman).

My close colleagues Anne Verhulst and Oskar Liivak have contributed to a great working environment and provided many useful discussions. So have the many summer students in the group.

Lois Durham made her NMR lab available for my early experiments, and we have had a fruitful collaboration with the people at Varian NMR.

At Stanford, I have particularly enjoyed Tom Cover's lectures on information theory. He gave me a deep appreciation for this beautiful field, which is now being revisited in the context of quantum information. Similarly, Rajeev Motwani's course on classical complexity theory and automata helped me put quantum computation in perspective.

Patricia Ryan, coach of the Stanford Improvisors, has affected my life in a very positive way. I say "yes" more often now, I have more adventures, and I learnt it's ok if things don't always work out. Philip Zimbardo's course on psychology has been an inspiration for teaching and a lesson for life.

The financial support of a Francqui Fellowship of the Belgian-American Educational Foundation, a Yansouni Family Stanford Graduate Fellowship, DARPA, and IBM Research, have given me the opportunity to freely pursue my interests.

The warm support of my parents, family, friends (especially PS, EV and PC) and roommates has done me much good, especially in the days when things didn't go so well. I cherish the many good moments I shared with all of them.

Contents

Abstract	v
Preface	vii
Acknowledgements	ix
1 Introduction	1
1.1 Historical background	1
1.2 Purpose of my work	4
1.3 Organization of the dissertation	5
1.4 Literature	5
2 Theory of quantum computation	9
2.1 Fundamental concepts	9
2.1.1 Quantum bits	9
2.1.2 Computation using quantum systems	13
2.1.3 Quantum parallism	16
2.1.4 Quantum algorithms	20
2.1.5 Correcting quantum errors	22
2.2 Quantum gates and circuits	24
2.2.1 Directly implementable quantum gates	25
2.2.2 Universality	29
2.2.3 Remarks on unitary operators	29
2.2.4 Multi-qubit gates	31
2.3 Quantum algorithms	32
2.3.1 The Deutsch-Jozsa algorithm	32
2.3.2 Grover's algorithm	35
2.3.3 Order-finding and Shor's algorithm	38
2.3.4 Quantum simulations	45
2.3.5 Other quantum algorithms and perspectives	46
2.4 Quantum error correction	46

2.4.1	The two-qubit phase error detection code	47
2.4.2	Error correction codes and fault-tolerancy	50
2.5	Summary	51
3	Implementation of quantum computers	53
3.1	Requirements	53
3.1.1	Qubits	53
3.1.2	Quantum gates	54
3.1.3	Initialization	59
3.1.4	Read-out	62
3.1.5	Coherence	64
3.2	State of the art	69
3.2.1	Trapped ions	69
3.2.2	Neutral atoms	71
3.2.3	Quantum dots	73
3.2.4	Superconducting qubits	76
3.2.5	Solid-state NMR	78
3.2.6	Dopants in semiconductors	81
3.2.7	Other proposals	83
3.3	Summary	83
4	Liquid-state NMR quantum computing	85
4.1	Qubits	85
4.1.1	Single-spin Hamiltonian	86
4.1.2	Spin-spin interaction Hamiltonian	88
4.2	Single-qubit operations	89
4.2.1	Rotations about an axis in the $\hat{x}\hat{y}$ plane (RF pulses)	89
4.2.2	Rotations about the \hat{z} axis	92
4.2.3	Selective excitation using pulse shaping	93
4.2.4	Single pulses - artefacts and solutions	96
4.2.5	Simultaneous pulses - artefacts and solutions	99
4.3	Two-qubit operations	102
4.3.1	The controlled-NOT in a two-spin system	102
4.3.2	Refocusing select J couplings	104
4.4	Qubit initialization	106
4.4.1	The initial state of nuclear spins	107
4.4.2	Effective pure states	109
4.4.3	Logical labeling	110
4.4.4	Temporal averaging	112
4.4.5	Spatial averaging	116

4.4.6	Efficient cooling	117
4.5	Read-out	118
4.5.1	NMR spectra	118
4.5.2	Quantum state tomography	122
4.6	Decoherence	123
4.6.1	Principal mechanisms	123
4.6.2	Characterization	126
4.7	Molecule design	127
4.8	Pulse sequence design	128
4.8.1	Simplification at three levels	129
4.8.2	Design for robustness	131
4.9	Summary	132
5	Experimental realization of NMR quantum computers	133
5.1	Experimental apparatus	133
5.1.1	Sample	133
5.1.2	Magnet	135
5.1.3	Probe	137
5.1.4	Transmitter	140
5.1.5	Receiver	142
5.1.6	Workstation	143
5.2	Overview of NMR quantum computing experiments	144
5.3	A first quantum algorithm (2 spins)	147
5.3.1	Problem description	148
5.3.2	Experimental procedure	148
5.3.3	Experimental results	149
5.3.4	Discussion	151
5.4	Quantum error detection (2 spins)	152
5.4.1	Problem description	152
5.4.2	Experimental procedure	153
5.4.3	Experimental results	154
5.4.4	Discussion	155
5.5	Logical labeling (3 spins)	157
5.5.1	Problem description	157
5.5.2	Experimental procedure	157
5.5.3	Experimental results	159
5.5.4	Discussion	161
5.6	Liquid crystal solutions (2 spins)	162
5.6.1	Problem description	162

5.6.2	Experimental approach and results	163
5.6.3	Discussion	164
5.7	Cancellation and prevention of systematic errors (3 spins)	166
5.7.1	Problem description	166
5.7.2	Experimental approach	167
5.7.3	Experimental Results	167
5.7.4	Discussion	168
5.8	Efficient cooling (3 spins)	170
5.8.1	Problem description	170
5.8.2	Experimental procedure	170
5.8.3	Experimental results	172
5.8.4	Discussion	173
5.9	Order-finding (5 spins)	174
5.9.1	Problem description	174
5.9.2	Experimental approach	176
5.9.3	Experimental results	178
5.9.4	Discussion	178
5.10	Shor's factoring algorithm (7 spins)	179
5.10.1	Problem description	179
5.10.2	Experimental approach	182
5.10.3	Experimental results	187
5.10.4	Decoherence model	190
5.10.5	Discussion	193
5.11	Summary	193
6	Conclusions	195
A	Numerical model	199
A.1	Set up the Hamiltonian and Pauli matrices	199
A.2	Action unitary operator on density matrix	200
A.3	Time evolution under the Hamiltonian	201
A.4	Single-spin rotations	201
A.5	Generalized amplitude damping	202
A.6	Phase damping	203
A.7	Helper programs	204
A.8	Pulse sequence code in MATLAB	205
B	Pulse sequence three-spin Grover search	207
	Bibliography	211

Chapter 1

Introduction

1.1 Historical background

“There is plenty of room at the bottom.” This was the title of a now classic 1959 talk given by Richard Feynman at the annual meeting of the American Physical Society [Fey60]. In this talk, Feynman gave physicists and engineers a wonderful challenge: to manipulate and control things on a *small* scale. In particular, he challenged his audience to think about building very small computers, with wires just 10 or 100 atoms in diameter, and circuits just a few thousand angstroms across. Forty years later, semiconductor technology is rapidly approaching these dimensions, driven by Moore’s law. But Feynman didn’t mean just small, he meant *really* small:

“When we get to the very, very small world — say circuits of seven atoms — we have a lot of new things that would happen that represent completely new opportunities for design. Atoms on a small scale behave like nothing on a large scale, for they satisfy the laws of quantum mechanics. So, as we go down and fiddle around with the atoms down there, we are working with different laws, and we can expect to do different things. We can manufacture in different ways. We can use, not just circuits, but some system involving the quantized energy levels, or the interactions of quantized spins, etc.”

This is the earliest reference I am aware of that hints at the subject matter of my thesis work. With reference to his daring ideas, Feynman also made the following crucially important point:

“It is not an attempt to violate any laws; it is something, in principle, that can be done; but in practice, it has not been done because we are too big.”

So what *are* the laws which limit computation ? How much energy does it take to compute, and how much time and space does a computation require ?

The relationship between energy consumption and computation has been studied in detail by Rolf Landauer. In a 1961 paper [Lan61], he showed that the amount of energy dissipated into the environment when a single bit of information is *erased*, is at least $k_B T \ln 2$, where k_B is Boltzman's constant and T is the temperature of the environment. As a result, *irreversible* logic gates, such as the NAND gates in today's computers, must dissipate a finite amount of energy, as information is lost when executing the gate (it is not possible to run the gate backwards and reconstruct the input from the output). Remarkably, Lecerf [Lec63] and Bennett [Ben73] later showed that it is possible to perform *universal* computation *reversibly*, without ever erasing information, and furthermore that universal computation is possible without net dissipation of energy.

The time and space resources needed for computation, and in particular how the resources scale with the problem size, are the subject of complexity theory. Arguably the most significant result of this field, which started with Alan Turing's introduction of the Turing machine [Tur36], is the strong Church-Turing thesis [Chu36, Dav65]. It states that "Any model of computation can be simulated on a probabilistic Turing machine with at most a polynomial increase in the number of elementary operations required." As a consequence, a mechanical machine¹ such as Babbage's difference engine of the 1800's is polynomially equivalent to the fastest supercomputer.

Polynomial differences in speed can of course still be significant, and over the past decades, enormous increases in speed have been realized by making devices that are smaller, consume less power and are more highly integrated. However, no matter how impressive the progress, the laws of physics underlying the operation of today's computers are still the same as in computers fifty years ago, namely the classical laws of physics.

In the early eighties, the quest for really small computers took on a completely new face. First, Paul Benioff showed that a *quantum mechanical* Hamiltonian can represent a universal (classical) Turing machine [Ben80]. Then Richard Feynman conjectured that a *quantum computer* might be able to do *more* than classical Turing machines; it might for example efficiently simulate the dynamics of another quantum system [Fey82, Fey85], a feat which is impossible on classical computers. David Deutsch then fully developed the concept of a quantum Turing machine and highlighted the potential of quantum computers to speed up computations via *quantum parallelism* [Deu85].

Ten years later, the field of quantum computation really took off when Peter Shor announced his quantum factoring algorithm [Sho94]. This was the first *quantum algorithm* which exploited quantum parallelism to offer an exponential speed-up over classical machines for solving an important mathematical problem (prime factorization). Another two years later, Lov Grover invented a quantum algorithm for unstructured search problems [Gro97] and Seth Lloyd [Llo96]

¹Provided it has a large enough memory, similar to the tape of a Turing machine.

proved Feynman's conjecture on quantum simulations.

Despite these spectacular results, the field of quantum computation was regarded with much scepticism because of the difficulty of maintaining coherent superposition states. However, much of the scepticism was silenced when Peter Shor [Sho95] and Andrew Steane [Ste96] discovered *quantum error correction* and showed that random errors due to decoherence can in fact be corrected. Furthermore, provided the probability of error per computational step is low enough, the coding and decoding operations associated with quantum error correction introduce fewer errors than can be corrected, even with imperfect operations [ABO97, Kit97, KLZ98].

At this point, the *physical realization* of quantum computers became another grand challenge, much like Feynman's challenge of building a very, very small classical computer: to build a computer capable of solving problems beyond the reach of classical computers, by virtue of using quantum mechanical superpositions and entanglement.

Many physical systems have been proposed as potential quantum computers, including trapped ions [CZ95], cavity quantum electrodynamics [THL⁺95], electron spins in quantum dots [LD98], superconducting loops [MOL⁺99] and nuclear spins [DiV95a]. However, due to the limited state of the art in any of these experimental techniques, a demonstration of even the most modest quantum algorithm appeared to be out of reach for a number of years.

This situation changed completely when Neil Gershenfeld and Isaac Chuang [GC97] and independently David Cory, Timothy Havel and Amr Fahmy [CFH97] developed an explicit proposal to build a simple quantum computer using nuclear spins in liquid solution, requiring only standard nuclear magnetic resonance technology. Fifty five years after nuclear spin states and spin echoes were proposed for (classical) data storage [AGH⁺55], nuclear magnetic resonance thus became the workhorse for the early exploration of experimental quantum computation.

Related fields

In parallel with quantum computation, the related field of quantum information theory developed, which forms the quantum analogue of classical information theory [CT91]. Quantum information theory describes the notions of a quantum source and a quantum channel, and studies techniques for quantum source and channel coding. In particular, quantum information theory sets out to understand how entanglement, which has no classical equivalent, can be used as a resource in communication.

This field has produced spectacular results such as quantum teleportation [BBC⁺93], superdense coding [BW92] and quantum cryptography [BB84, Ben92]. Several groups have already teleported photon states [BPM⁺97, BBM⁺98], and secure key distribution using quantum cryptography has been demonstrated experimentally through optical fibers over tens of kilometers [MZG96] and through space by daylight over a distance of 1.6 km [BHL⁺00] (see [GRTZ01]

for a review). Certainly, quantum cryptography is at a more mature stage than quantum computing.

1.2 Purpose of my work

The main purpose of my work is to study quantum computation experimentally, and to increase our understanding of what it would take to build a practical quantum computer. To this purpose, I have used nuclear spins in liquid solution as quantum bits, and initialized, manipulated and read out the spin states using adaptations of standard nuclear magnetic resonance techniques [GC97, CFH97]. Specifically, my objectives have been

(1) To experimentally provide proof of principle of quantum computation.

Until 1997, quantum computers existed only on paper, and in people's imagination. I wanted to test quantum computation in the lab, and see various quantum algorithms at work for the first time.

(2) To stimulate theoretical questions by doing quantum computing experiments.

Interplay between theory and experiment is crucial for the healthy development of any research field. I hoped to stimulate theoretical thinking about the fundamentals of quantum computing by doing actual experiments. Furthermore, I hoped to interest theorists in helping with quantum control and in explaining unexpected experimental observations.

(3) To develop techniques for state initialization, coherent quantum control and read out of quantum states, useful in many implementations of quantum computers.

It is clear that many of the challenges in building quantum computers are similar across different proposed implementations. Therefore, techniques and solutions invented in the context of NMR (nuclear magnetic resonance) quantum computing have the potential to advance other, perhaps more scalable, approaches to the realization of quantum computers.

The general direction of my work has been to push the state of the art towards more qubits, more gates and more complex algorithms. At each stage, I have consciously paid attention to all three objectives. The goal was not just to demonstrate "the next algorithm", but rather to learn scientifically from the experiment, and in particular to increase our understanding of how we can meet this wonderful challenge of building a quantum computer, a computer capable of solving problems beyond the reach of any classical machine.

1.3 Organization of the dissertation

Chapter 2 lays out the principles of quantum computation, introduces quantum circuits and quantum gates, and explains the operation of quantum algorithms and quantum error correction. From this theoretical discussion, five requirements for the implementation of quantum computers naturally emerge. Those are discussed in chapter 3, along with a brief overview of the state of the art. In chapter 4, we study in detail how those five requirements can at least in principle be met in liquid solution NMR experiments. Finally, we explore NMR quantum computing in practice in a series of experiments, presented in chapter 5. This structure is illustrated in Fig. 1.1.

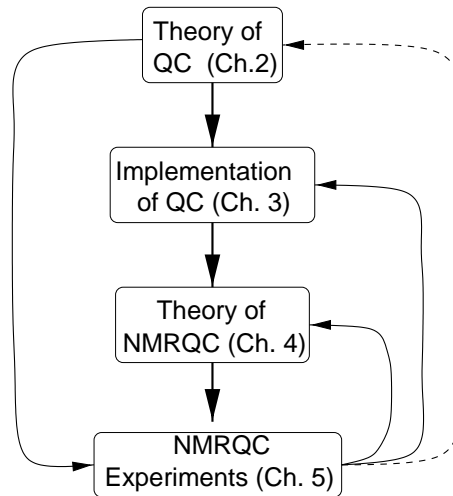


Figure 1.1: Connections between the four main chapters of this thesis work.

Additional connections between the chapters are as follows. The selection of topics and the choice of examples in chapter 2 are in function of the experiments of chapter 5. Furthermore, several of the techniques and concepts for initialization, control and readout of the spin states presented in chapters 3 and 4 were inspired by or invented in the context of the experiments of chapter 5. Finally, the NMR quantum computing experiments have raised theoretical questions about where the power of quantum computation comes from, and what the role of entanglement is [BCJ⁺99, SC99, KL98]². The bulk of my own contributions are in parts of chapter 4 and in chapter 5, as indicated there.

1.4 Literature

Many references to original papers are included throughout. In addition, the following review articles and books are particularly relevant.

²We have not gone into these questions in this thesis work, hence the dashed line.

Michael Nielsen and Isaac Chuang’s monumental text “Quantum Computation and Quantum Information” [NC00] has been an invaluable resource as I was writing chapters 2 and 3. In addition to this book, the interested reader will find the following review articles helpful. Bennett and DiVincenzo wrote a recent authoritative review of quantum computation and information [BD00]. An excellent extended pedagogic review geared towards non-specialist physicists is given by Steane [Ste98] (although the section on implementations is outdated). A great introduction to quantum computing and specifically Shor’s algorithm, also for physicists, is by Ekert and Jozsa [EJ96], and Lloyd wrote a good introduction for a general audience [Llo95b]. Introductions to a wide array of quantum computer implementations are compiled in a recent special issue of *Fortschritte der Physik* [BL00].

Of the many excellent textbooks on quantum mechanics, very few cover the topics most applicable to quantum computing. Perhaps the most helpful text for understanding the relevant concepts of quantum mechanics is the great book by Peres [Per93]. Reference works which cover some of the relevant ideas and notation of quantum mechanics include Cohen-Tannoudji, Diu and Laloë [CTDL77], Feynman, Leighton and Sands [FLS65] and Sakurai [Sak95].

Ray Freeman’s “Spin Choreography” gives a marvelous and intuitive overview of high-resolution solution NMR techniques and spin dynamics [Fre97]. I found it the most helpful textbook for the NMR techniques underlying chapter 4. A classic and comprehensive treatise of NMR is Ernst, Bodenhausen and Wokaun [EBW87]. Two other classic texts on NMR are Slichter [Sli96] and Abragam [Abr61]; both focus on spin physics more than on spin dynamics.

No textbooks exist specifically on NMR quantum computing, but there are several good introductory review papers. A good introduction for a general audience is [GC98]. Jonathan Jones wrote an introductory review for an NMR audience [Jon01], and so did we. We also wrote an accessible introduction for electrical engineers:

- L.M.K. Vandersypen, C.S. Yannoni, and I.L. Chuang, *to appear in The encyclopedia of NMR (supplement)*, 2001 [VYC01].
- M. Steffen, L.M.K. Vandersypen, and I.L. Chuang, *IEEE Micro*, 2001 [SVC01].

Each of the experiments presented in sections 5.3 through 5.9 has been published in refereed journals. These papers also include many of the techniques presented in chapter 4; only the technique of section 4.2.5 was published separately.

- 5.3: I. L. Chuang, L. M. K. Vandersypen, X. L. Zhou, D. W. Leung, and S. Lloyd, *Nature*, 1998. Reprinted by permission from [CVZ⁺98] © (1998) by Macmillan Magazines, Ltd.
- 5.4: D. Leung, L. Vandersypen, X. Zhou, M. Sherwood, C. Yannoni, and I. Chuang, *Phys. Rev. A*, 1999. Reprinted by permission from [LVZ⁺99] © (1999) by The American Physical Society.

- 5.5: L. M. K. Vandersypen, C. S. Yannoni, M. H. Sherwood, and I. L. Chuang, *Phys. Rev. Lett.*, 1999. Reprinted by permission from [VYSC99] © (1999) by The American Physical Society.
- 5.6: C.S. Yannoni, M.H. Sherwood, L.M.K. Vandersypen, M.G. Kubinec, D.C. Miller, and I.L. Chuang, *Appl. Phys. Lett.*, 1999. Reprinted by permission from [YSV⁺99] © (1999) by The American Institute of Physics.
- 5.7: L.M.K. Vandersypen, M. Steffen, M. H. Sherwood, C.S. Yannoni, G. Breyta, and I. L. Chuang, *Appl. Phys. Lett.*, 2000. Reprinted by permission from [VSS⁺00] © (2000) by The American Institute of Physics.
- 5.8: D.E. Chang, L.M.K. Vandersypen, and M. Steffen, *Chem. Phys. Lett.*, 2001. Reprinted by permission from [CVS01] © (2001) by Elsevier Science.
- 5.9: L.M.K. Vandersypen, M. Steffen, G. Breyta, C.S. Yannoni, R. Cleve, and I. L. Chuang, *Phys. Rev. Lett.*, 2000. Reprinted by permission from [VSB⁺00] ©(2000) by The American Physical Society.
- 4.2.5: M. Steffen, L.M.K. Vandersypen, and I.L. Chuang. *J. Magn. Reson.*, 2000. Reprinted by permission from [SVC00] © (2000) by Academic Press.
- 5.10: L.M.K. Vandersypen, M. Steffen, G. Breyta, C.S. Yannoni, M. Sherwood, and I. L. Chuang, *in preparation*, 2001 [VSB⁺01].

Chapter 2

Theory of quantum computation

In this chapter, we review the principles of the theory of quantum computation. From the outset, the presentation is directed towards a practical appreciation and understanding of the subject. Our starting point is the notion of quantum bits. We next present the language of quantum gates and circuits, and use this language to outline the operation of quantum algorithms and quantum error correction.

2.1 Fundamental concepts

2.1.1 Quantum bits

One quantum bit

In today's digital computers, information is stored and processed in the form of bits, entities which can take on only two values: logical zero, 0, or logical one, 1. These are typically represented by the voltage at a node, or the alignment of a piece of magnetic material, but any physical system with at least two distinct states can serve to represent a bit, including two-level quantum systems such as spins-1/2 and polarized photons. The quantum state $|0\rangle$ corresponds to 0 and the state $|1\rangle$ corresponds to 1. For a spin-1/2 particle, the two computational basis states are represented by the spin up and spin down state ($|\uparrow\rangle$ or $|\downarrow\rangle$), and for photons by the vertical or horizontal polarization state ($|\updownarrow\rangle$ or $|\leftrightarrow\rangle$).

In contrast to classical bits which can only exist as 0 or 1, two-level quantum systems, called quantum bits or *qubits*, can also exist in a superposition state of $|0\rangle$ and $|1\rangle$, mathematically written as

$$|\psi\rangle = a|0\rangle + b|1\rangle, \quad (2.1)$$

where a and b are complex numbers satisfying the normalization condition $|a|^2 + |b|^2 = 1$. The *overall* phase of $|\psi\rangle$ is physically irrelevant as it cannot be revealed by any measurement.

Therefore, we can also write $|\psi\rangle$ as

$$|\psi\rangle = \cos \frac{\theta}{2} |0\rangle + e^{i\phi} \sin \frac{\theta}{2} |1\rangle, \quad (2.2)$$

and visualize the state of a qubit as a point on a sphere, called the Bloch sphere, as in Fig. 2.1. This representation may convey the impression that a qubit is very much like an analog classical variable, with two degrees of freedom θ and ϕ . However, as we will see, qubits are in many ways very different from such analog classical variables. Rather than pointing along a certain direction, a qubit in a superposition state $a|0\rangle + b|1\rangle$ is in some sense in both $|0\rangle$ and $|1\rangle$ *at the same time*. Furthermore, as we shall see next, the number of degrees of freedom in an n -qubit state increases exponentially with n .

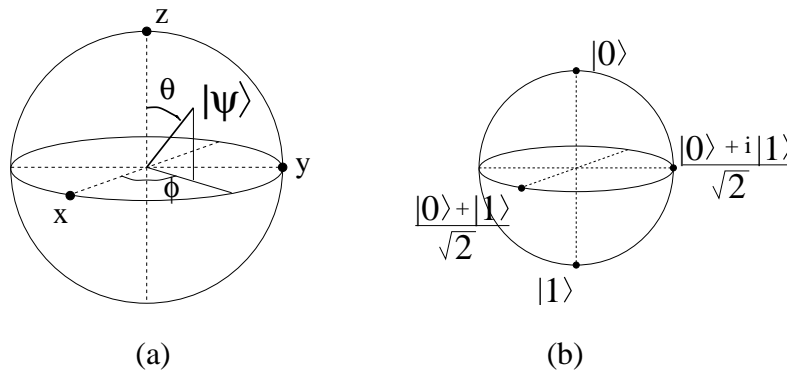


Figure 2.1: (a) Bloch sphere representation of the state $|\psi\rangle$ of a single qubit. (b) The position in the Bloch sphere of four important states. By convention, we will always let $|0\rangle$ be along $+\hat{z}$.

Multiple qubits

The state of two qubits, each in an arbitrary superposition state $|\psi\rangle_1 = a_1|0\rangle + b_1|1\rangle$ and $|\psi\rangle_2 = a_2|0\rangle + b_2|1\rangle$, is written as

$$|\psi\rangle = |\psi\rangle_1 \otimes |\psi\rangle_2 = (a_1|0\rangle + b_1|1\rangle) \otimes (a_2|0\rangle + b_2|1\rangle), \quad (2.3)$$

where \otimes is the *tensor product* or *Kronecker product* symbol. We can rearrange this expression as

$$|\psi\rangle = a_1a_2|0\rangle \otimes |0\rangle + a_1b_2|0\rangle \otimes |1\rangle + b_1a_2|1\rangle \otimes |0\rangle + b_1b_2|1\rangle \otimes |1\rangle. \quad (2.4)$$

From now on, we will leave the \otimes symbol implicit, and furthermore abbreviate $|0\rangle|0\rangle$ as $|00\rangle$, $|0\rangle|1\rangle$ as $|01\rangle$ and so forth. Thus,

$$|\psi\rangle = a_1a_2|00\rangle + a_1b_2|01\rangle + b_1a_2|10\rangle + b_1b_2|11\rangle. \quad (2.5)$$

Remarkably and surprisingly, the coefficients of the terms in the joint superposition state of the two qubits can in fact be chosen *independently*. That is, they don't need to be the product of the coefficients of two single-qubit states. We can express this by writing the joint state of two qubits in the more general form

$$|\psi\rangle = c_{00}|00\rangle + c_{01}|01\rangle + c_{10}|10\rangle + c_{11}|11\rangle. \quad (2.6)$$

or equivalently, if we represent the states in decimal instead of binary representation,

$$|\psi\rangle = c_0|0\rangle + c_1|1\rangle + c_2|2\rangle + c_3|3\rangle. \quad (2.7)$$

Similarly, a register of n qubits can be in an arbitrary superposition of 2^n states,

$$|\psi\rangle = \sum_{k=0}^{2^n-1} c_k |k\rangle, \quad (2.8)$$

where the only constraint on the complex amplitudes c_k is that they must satisfy the normalization condition

$$\sum_k |c_k|^2 = 1. \quad (2.9)$$

As for single-qubit states, the overall phase is irrelevant. Therefore,

*the description of a pure state of n qubits requires $2^n - 1$ complex numbers.*¹

This is manifestly different from classical systems. For example, the position of n points on the sphere of Fig. 2.1 is described by only n rather than 2^n complex numbers. In fact, the position of any n classical particles can always be described by a number of real or complex numbers that is linear in n .

Since we cannot visualize the state of n qubits via n Bloch spheres, or n points on a single Bloch sphere, how *can* we visualize their state? This is difficult — our intuition fails at the quantum level, because we didn't grow up with an intuition for quantum mechanics, and because our observations of the every-day world around us are observations of a classical world. Mathematically, the extension of the Bloch sphere is called *Hilbert space*, a 2^n dimensional complex vector space with an inner product. The state of a quantum system thus corresponds to a point in Hilbert space.

¹A mixed state of n qubits has $4^n - 1$ degrees of freedom. The distinction between pure and mixed states will be discussed shortly.

Entanglement

Since the number of degrees of freedom of n quantum systems grows exponentially more quickly than that of n classical systems, surely there must exist quantum states which have no classical equivalent. The state of Eq. 2.3 is a classical state: this joint state of two qubits can be fully described via a description of the individual qubits (which requires one complex number, or two real numbers, for each qubit). We say that the state of Eq. 2.3 is *separable*.

In contrast, it is impossible to find two one-qubit states $|\psi\rangle_1 = a_1|0\rangle + b_1|1\rangle$ and $|\psi\rangle_2 = a_2|0\rangle + b_2|1\rangle$, such that their tensor product gives the state

$$\frac{|00\rangle + |11\rangle}{\sqrt{2}}. \quad (2.10)$$

In other words, this state cannot be written as a product of two one-qubit states. We call such a state *non-separable* or *entangled*. Let us give two more examples: the state $\frac{1}{2}(|00\rangle - |01\rangle + |10\rangle - |11\rangle)$ can be written as $\frac{1}{2}(|0\rangle + |1\rangle)(|0\rangle - |1\rangle)$ and is thus separable; the state $\frac{1}{2}(|00\rangle + |01\rangle + |10\rangle - |11\rangle)$ cannot be factored into two one-qubit states and is thus entangled.

Mixed states versus pure states

A quantum system in a well-defined and well-known state $|\psi\rangle$ is said to be in a *pure* state. If all we know about a quantum system is that it is in one of several pure states $|\psi_i\rangle$, each with certain probabilities p_i , we say the quantum system is in a *statistical mixture* of these pure states, or for short that it is in a *mixed* state. The state of a quantum system in a statistical mixture is conveniently described by its *density operator*

$$\rho = \sum_i p_i |\psi_i\rangle \langle \psi_i|, \quad (2.11)$$

where $\langle \psi|$ represents the Hermitian conjugate of $|\psi\rangle$, and $|\psi\rangle \langle \phi|$ denotes the *outer product* (a linear operator). Obviously, the probabilities p_i must satisfy $p_i \geq 0$ and $\sum_i p_i = 1$. For a pure state $|\psi\rangle$, the density operator is simply $\rho = |\psi\rangle \langle \psi|$.

Every density operator satisfies

$$\text{Tr}(\rho) = 1, \quad (2.12)$$

since $\text{Tr}(\rho) = \sum_i p_i \text{Tr}(|\psi_i\rangle \langle \psi_i|) = \sum_i p_i$. Furthermore, the eigenvalues λ_j of ρ satisfy

$$\lambda_j \geq 0, \quad (2.13)$$

so ρ is a *positive* operator, and one can decompose it as

$$\rho = \sum_j \lambda_j |j\rangle\langle j|, \quad (2.14)$$

where the $|j\rangle$ are orthogonal eigenvectors of ρ (the $|\psi_i\rangle$ of Eq. 2.11 need not be orthogonal). We can thus also interpret a quantum system in ρ to be in the state $|j\rangle$ with probability λ_j , and make the important observation that an arbitrary density matrix does thus *not* have a *unique* decomposition into any specific mixture of states.

The mathematical distinction between pure and mixed states is that a pure state density operator has only one non-zero eigenvalue (necessarily equal to 1), whereas a mixed state density operator has more than one non-zero eigenvalue. It follows that a convenient criterion to distinguish pure and mixed states is

$$\text{Tr}(\rho^2) = 1 \Leftrightarrow \rho \text{ is pure} \quad (2.15)$$

$$\text{Tr}(\rho^2) < 1 \Leftrightarrow \rho \text{ is mixed.} \quad (2.16)$$

Of course, any quantum system is really in just one state. We emphasize therefore, that to say that a quantum system is in a mixed state is merely a statement about our *knowledge* of the state of the quantum system. As we shall see, the distinction between pure and mixed states has important implications — pure states are in many respects more “useful” than mixed states.

Promise of qubits

It may appear at first sight that a bit which is simultaneously 0 and 1 is not very useful for computation, and is, in fact, rather confusing. However, the exponential complexity of quantum systems also suggests that perhaps quantum bits could be immensely useful for computation. This observation led Richard Feynman to speculate that “quantum computers” might be able to solve certain problems exponentially faster than any classical machine [Fey85, Fey96]. In the next section, we first verify that quantum systems can indeed be used for computation. In the following section we explore the potential of quantum superpositions and entanglement for performing massively parallel computations.

2.1.2 Computation using quantum systems

So far, we have merely given a *static* description of quantum bits as two-level quantum systems which can hold information in binary form. We will now look at the *dynamics* of quantum bits, and examine whether we can perform computations by evolving the state of a set of quantum systems in a controlled way.

Unitary evolution

One of the postulates of quantum mechanics dictates that the time evolution of the state $|\psi(t)\rangle$ of a *closed* quantum system (i.e. a system which does not interact with the environment, the rest of the universe) is governed by Schrödinger's equation:

$$i\hbar \frac{d|\psi(t)\rangle}{dt} = \mathcal{H}|\psi(t)\rangle, \quad (2.17)$$

where \hbar is Plank's constant and \mathcal{H} is the *Hamiltonian*, an operator for the total energy of the system. For time-*independent* Hamiltonians, the Schrödinger equation has a straightforward solution:

$$|\psi(t)\rangle = \exp\left(\frac{-i\mathcal{H}t}{\hbar}\right) |\psi(t=0)\rangle. \quad (2.18)$$

If the Hamiltonian is time-dependent, the Schrödinger equation has no easy solution, although the evolution can be approximated as a sequence of evolutions under time-independent Hamiltonians. We usually denote the time-evolution operator as U , where

$$U = \exp\left(\frac{-i\mathcal{H}t}{\hbar}\right), \quad (2.19)$$

so

$$|\psi(t)\rangle = U|\psi(0)\rangle. \quad (2.20)$$

Similarly, the time evolution of the density operator ρ of a quantum system is

$$\rho(t) = \sum_i p_i |\psi_i(t)\rangle \langle \psi_i(t)| = \sum_i p_i U |\psi_i(0)\rangle \langle \psi_i(0)| U^\dagger = U \rho(0) U^\dagger, \quad (2.21)$$

where the † symbol indicates the Hermitian conjugate.

From Eq. 2.18, we can appreciate the important role of the Hamiltonian of a quantum system: it controls the time evolution of the quantum system. Since \mathcal{H} is a *Hermitian* operator, i.e. it is its own Hermitian conjugate $\mathcal{H} = \mathcal{H}^\dagger$, the time evolution operator $U = \exp(-i\mathcal{H}t/\hbar)$ is *unitary*, that is $UU^\dagger = e^{-i\mathcal{H}t/\hbar} e^{i\mathcal{H}^\dagger t/\hbar} = I = e^{i\mathcal{H}^\dagger t/\hbar} e^{-i\mathcal{H}t/\hbar} = U^\dagger U$. This implies that the evolution of a closed quantum system is completely *reversible*. Indeed, we can *unwind* any time evolution U by a subsequent time evolution U^\dagger .

Geometrically, we can visualize the unitary evolution of a single qubit as a rotation in the Bloch sphere (Fig. 2.1), a picture we will often use in chapter 4. By extension, the unitary evolution of multiple qubits corresponds to a rotation in Hilbert space.

Irreversible and reversible computation

Today's classical computers do not at all operate in a reversible manner. Note for example that your computer generates heat. Also note that it is not possible to reconstruct the input of a traditional AND gate from its output (Fig. 2.2 a). This is obvious since the AND gate has two input bits and only one output bit; it is never possible to reconstruct the value of two bits starting from only one bit. But even if we introduce a second output bit (Fig. 2.2 b), it is not possible to make the AND gate reversible. This is because the AND gate is not single-valued. If the output is 00 in the example of Fig. 2.2 b, we cannot know whether the input was 00 or 01.

It is thus natural to ask whether universal computation can be done reversibly. Rolf Landauer and Charles Bennett showed that indeed any computation can be performed in a completely reversible manner, that is without (or with infinitesimal) energy dissipation [Lan61][Ben73]. The only time heat must be dissipated is in the process of resetting a bit, which irreversibly erases the information contained in the bit and thus necessarily increases the entropy.

In	Out	In	Out	In	Out
0 0	0	0 0	0 0	0 0 0	0 0 0
0 1	0	0 1	0 0	0 1 0	0 1 0
1 0	0	1 0	1 0	1 0 0	1 0 0
1 1	1	1 1	1 1	1 1 0	1 1 1
0 0 1	0 0 1	0 1 1	0 1 1	0 0 1	0 0 1
0 1 1	0 1 1	1 0 1	1 0 1	1 0 1	1 0 1
1 1 1	1 1 1	1 1 1	1 1 1	1 1 1	1 1 0
(a)	(a)	(b)	(b)	(c)	(c)

Figure 2.2: Truth table for (a) The traditional AND gate; the output is 1 when both inputs are 1, and the output is 0 otherwise. (b) The extended AND gate, with two output bits. (c) A reversible AND gate, also known as the TOFFOLI gate.

Any multi-valued function f ,

$$x \mapsto f(x) \tag{2.22}$$

can be made reversible by introducing a second input bit string y of the same length as $f(x)$ and extending Eq. 2.22 to

$$(x, y) \mapsto (x, y \oplus f(x)), \tag{2.23}$$

where \oplus is the bitwise addition modulo two (equivalent to the bitwise XOR). If we set y to 0, we simply obtain $f(x)$ in the second register:

$$(x, 0) \mapsto (x, f(x)). \tag{2.24}$$

We can thus construct a reversible version of the AND gate for example, by using an additional

input bit (Fig. 2.2 c). The third bit is always initialized to 0, so in practice only the top half of the truth table is ever used. The input can now always be reconstructed from the output. Similarly, if we initialize the third bit to 1, and thus use only the bottom half of the truth table of Fig. 2.2 c, we obtain a NAND gate. Since the NAND gate is universal for classical logic, the TOFFOLI is universal for reversible classical computation [Tof80].

We will return to the implementation of quantum computers in chapter 3. For now, we will just state that it may be possible to control the Hamiltonian in such a way that the time evolution results in a transformation of the qubit states which corresponds to the transformation of bit values in a classical truth table [Ben80]. That is, the computational basis states of the qubits ($|0\rangle$ or $|1\rangle$ for each qubit) can be transformed as

$$|x\rangle \mapsto |f(x)\rangle \quad (2.25)$$

for reversible f , or, by extension, as

$$|x\rangle|y\rangle \mapsto |x\rangle|y \oplus f(x)\rangle, \quad (2.26)$$

for irreversible f , corresponding to Eqs. 2.22 and 2.23 respectively. Therefore, we can say that

quantum computation subsumes classical computation.

Now, what would happen if the quantum bits were initially in a superposition state of the computational basis states, $\sum_{k=0}^{2^n-1} c_k |k\rangle$? This is the subject of the next section.

2.1.3 Quantum parallelism

Quantum parallelism

Every computation can be seen as the concatenation of many logic gates. Each logic gate produces an output which is a function of its input. Now consider a classical and reversible² logic gate which implements a function f with one input bit x and one output bit $y = f(x)$. If $x = 0$, the gate will output $f(0)$, and if $x = 1$, the gate will output $f(1)$. Now imagine we can implement an analogous quantum logic gate, which transforms a qubit as $|x\rangle \mapsto |f(x)\rangle$. By virtue of the linearity of quantum mechanics, the same quantum gate transforms a qubit in a superposition state as

$$a|0\rangle + b|1\rangle \xrightarrow{f} a|f(0)\rangle + b|f(1)\rangle. \quad (2.27)$$

In some sense, the function f has been evaluated for both its input values (0 and 1) in one step! Next consider a different logic gate which implements a function f with two input and two

²If f is not reversible, we know how to make it reversible from section 2.1.2.

output bits. If we prepare the two qubit system in the state

$$|\psi\rangle = a|00\rangle + b|01\rangle + c|10\rangle + d|11\rangle, \quad (2.28)$$

evaluation of the function f transforms the state to

$$a|f(00)\rangle + b|f(01)\rangle + c|f(10)\rangle + d|f(11)\rangle, \quad (2.29)$$

so f has been evaluated for four input values in parallel. For every additional input bit, the potential number of parallel function evaluations doubles! In general, a function of n bits implemented on a quantum computer can be evaluated for all 2^n possible input values at the same time:

$$\sum_{x=0}^{2^n-1} c_x |x\rangle \xrightarrow{f} \sum_{x=0}^{2^n-1} c_x |f(x)\rangle, \quad (2.30)$$

where x is an integer encoded by a string of n bits. Thus, whereas for classical computers the number of parallel function evaluations increases at best linearly with their size,

the number of parallel function evaluations grows exponentially with the size of the quantum computer (the number of qubits).

This truly spectacular notion was first introduced by David Deutsch in 1985, and termed *quantum parallism* [Deu85].

Machines based on quantum bits thus appear to be exponentially more powerful than any machine using just classical bits. Of course, a computation is only meaningful if the output result can be read out, but how do we measure the state of quantum bits, and just what does the measurement give when the qubit is in a superposition state?

Measurement of quantum states

The postulates of quantum mechanics dictate that any measurement of a quantum system can be described in terms of a set of *measurement operators* P_m . Measurement of a quantum system in the state $|\psi\rangle$ immediately before the measurement gives outcome m with probability

$$p(m) = \langle\psi|P_m|\psi\rangle. \quad (2.31)$$

The state of the quantum system after the measurement is

$$\frac{P_m|\psi\rangle}{\langle\psi|P_m|\psi\rangle}. \quad (2.32)$$

The measurement operators must satisfy the completeness relation

$$\sum_m P_m = I, \quad (2.33)$$

such that the probabilities p_m sum to 1. Furthermore, for a projective measurement, we also require that the operators P_m be Hermitian and that

$$P_m P_{m'} = \delta_{mm'} P_m. \quad (2.34)$$

We can therefore associate an orthonormal basis of states $|m\rangle$ with any set of projective measurement operators P_m , such that $P_m = |m\rangle\langle m|$. Then, the probability of obtaining m in a measurement of a quantum system in $|\psi\rangle$ is $p(m) = |\langle m|\psi\rangle|^2$ (note that $0 \leq p_m \leq 1$, with equality only if $|\psi\rangle = |m\rangle$), and the post-measurement state is $|m\rangle$.

For example, if we measure a single qubit in the state $|0\rangle$ in the $\{|0\rangle, |1\rangle\}$ basis (the computational basis), the measurement always gives 0. If we measure a qubit in $a|0\rangle + b|1\rangle$ in the same basis, we obtain 0 with probability $|a|^2$ and 1 with probability $|b|^2$.

What happens if we measure a qubit in $|\psi\rangle = a|0\rangle + b|1\rangle$ twice in a row, in the same basis? From Eqs. 2.32 and 2.34, we see that the result of the second measurement will always be identical to the result of the first measurement. The first measurement will give m and in the process *collapses*³ $|\psi\rangle$ onto the corresponding measurement basis state $|m\rangle$. Since the $|m\rangle$ are orthogonal, the second measurement will with certainty return m as well.

Collapse of the quantum state implies that the information contained in the coefficients a and b is instantaneously and irreversibly destroyed. As a result, an unknown quantum state cannot be fully characterized even by repeated measurements, whether they take place in the same basis or in different bases. A second measurement of a qubit in a different basis than the first measurement will *project* the state (which now is $|m\rangle$, that is $|0\rangle$ or $|1\rangle$ in our example) onto the new measurement basis (for example the $\{\frac{|0\rangle+|1\rangle}{\sqrt{2}}, \frac{|0\rangle-|1\rangle}{\sqrt{2}}\}$ basis). This measurement does not yield any extra information about $|\psi\rangle$, however, because a and b have already been irretrievably lost; the second measurement is a measurement on the state $|m\rangle$, not on $|\psi\rangle$.

It would be possible to determine a and b with good accuracy by performing a properly designed series of measurements on a large number of copies of the qubit in the same unknown state. However, the *no-cloning theorem* [Die82, WZ82] forbids the creation of copies of a qubit in an unknown state (it is of course possible to create many copies of a qubit in a known state). In summary,

no measurement can fully reveal the state of a qubit in an unknown state.

³Collapse is only one of several interpretations of the measurement process. Since they all make the same predictions for the measurement statistics and outcomes, we will not concern ourselves with interpretation issues.

Furthermore, Eq. 2.31 implies that it is not possible to reliably distinguish two non-orthogonal quantum states $|\psi_1\rangle$ and $|\psi_2\rangle$: regardless of the basis we choose, there must be a $|m\rangle$ for which $\langle\psi_1|m\rangle^2 \neq 0$ and $\langle\psi_2|m\rangle^2 \neq 0$. Orthogonal states in contrast, can be perfectly distinguished by a measurement in the appropriate basis.

We note that while the evolution of a closed quantum system is unitary (see section 2.1.2), the measurement process inherently invokes an interaction with an external measuring device during which the quantum system cannot remain closed. As a result, the measurement process is non-unitary; it constitutes a projection onto a finite set of basis states in Hilbert space, rather than a rotation in Hilbert space.

Finally, we point out that we have restricted ourselves to projective measurements, also known as *hard* measurements. We postpone a discussion of *weak* measurements until section 3.1.4 and apply it to the case of NMR in section 4.5.

Hidden variables and measurements on entangled particles

In light of the measurement process, it is natural to ask what the meaning of superpositions is. Indeed, if upon measurement we obtain only one of the terms in a superposition, wasn't the qubit perhaps already in the corresponding state all along, instead of in several states "at the same time"? Isn't there some *hidden variable* which predetermines what the measurement outcome will be? This question has been the subject of much debate throughout the 20th century (for a good introduction, see [Mer85]).

In a 1935 paper, Einstein, Podolsky and Rosen (EPR) considered what would happen if a measurement is performed on one of two entangled particles [EPR35]. Suppose we prepare two qubits in the entangled state $\frac{1}{\sqrt{2}}|01\rangle - \frac{1}{\sqrt{2}}|10\rangle$ (the singlet state, one of the four so-called EPR states). If we measure qubit 1 in the computational basis, the outcome will be $|0\rangle$ or $|1\rangle$. Now, what would be the result of a subsequent measurement of qubit 2? Because of the entanglement, the wavefunction of *both* particles collapses to either $|01\rangle$ or $|10\rangle$ upon measuring the first qubit, and therefore the outcome for the second qubit will always be opposite to the outcome of the first qubit. In fact, for the singlet state, the outcomes for the two particles will be opposite for a measurement in *any* basis. Furthermore, this is true even if the two entangled qubits are lightyears away from each other! Actions in one location would thus appear to have instantaneous consequences for observations in a different location. Einstein rejected this "spooky action at a distance" calling it absurd. He believed that quantum theory was incomplete and had to be supplemented with a theory of local hidden variables.

In 1964, John Bell proposed an actual experiment which would either confirm or disprove

local hidden variable theories [Bel64]⁴. This experiment was carried out in 1980 by Alain Aspect [AGR81], and has been repeated many times since then, in attempts to close more and more possible loopholes in the experiment. The experimental observations have consistently refuted the existence of local hidden variables, thereby confirming the validity of quantum theory.

Implications of quantum measurements for quantum parallelism

Returning to quantum parallelism, we see that measurement of two qubits in a superposition state such as in Eq. 2.29, collapses the state of the qubits and probabilistically returns $f(00)$, $f(01)$, $f(10)$ or $f(11)$. In general, after performing a phenomenal number of parallel function evaluations (2^n for n qubits), as in Eq. 2.30, a measurement of the final state will probabilistically give one of the 2^n terms in the output superposition state. It thus appears that the exponential computational power of quantum computers is not accessible!

Remarkably, special quantum algorithms exist which allow one to take advantage of the exponential complexity of quantum systems and circumvent the limitations of quantum measurements and readout, in order to significantly speed up certain computational tasks.

2.1.4 Quantum algorithms

Quantum algorithms allow one to take advantage of quantum parallelism and thereby solve certain problems in *far fewer steps* than is possible classically.

Notions from complexity theory

The basis for comparison of the power of quantum and classical computers is provided by complexity theory, which analyzes how the minimal physical resources (time, space, energy) required for an algorithm to solve a given problem vary with the problem size n [HU79]. The key distinction is whether the resources required are *polynomial* or *exponential* in n .

Adding two n digit numbers, for example, can be done in $\mathcal{O}(n)$ (a linear function of n) elementary operations such as NAND gates. In contrast, factoring an n digit integer number into prime numbers is a task for which the best known classical algorithms require exponentially many operations, about $\mathcal{O}(e^{n^{1/3}})$ [Knu98].

Computer scientists call an algorithm *efficient* if the required resources grow only polynomially with the problem size, and call it *inefficient* if the resources increase exponentially. Problems for which there exist efficient algorithms are called *tractable*. Problems for which no efficient algorithm exists are called *intractable* or *hard*.

In order to drive home the significance of intractability, consider the travelling salesman problem, which is provably intractable classically. Suppose that on a fast computer it takes one

⁴Or to be precise, that hidden variables can only exist if information can travel faster than light, which we strongly believe is not the case.

second to find the shortest path connecting 100 cities. For 101 cities, it would then take two seconds, for 102 cities four seconds and so forth. It would then take over an hour to find the shortest path through 112 cities, and over a year for only 125 cities. The same fast computer would need over 35 billion years to solve the travelling salesman problem for only 160 cities, longer than the estimated age of the universe . . .

Quantum algorithms

The extraordinary promise of quantum computing is that

certain problems which appear intractable on any classical computer are tractable on a quantum computer.

Factorization of integers into products of prime numbers is an example of such a problem. This problem is believed to be intractable on any classical machine (although this remains to be proven): a 400-digit integer cannot be factored with high probability of success in a reasonable time, not with a handheld calculator, not with a personal computer, not with a supercomputer, and not using all the fastest supercomputers combined.

However, in 1994, almost 10 years after Deutsch introduced quantum parallelism, Peter Shor stunned the world with an efficient quantum algorithm for prime factorization and computation of discrete logarithms [Sho94, Sho97]. The practical importance of this algorithm is that it could be used to break widely used cryptographic codes, such as the RSA public key cryptographic system [RSA78]. These codes are based precisely on the fact that no efficient (classical) algorithm is known for factoring. At a more fundamental level, Shor's algorithm is the most powerful example of how quantum mechanics offers a new way of thinking about information and computation. As a result, the announcement of Shor's algorithm gave a tremendous boost to the interest in quantum computing of both funding agencies and scientists.

Historically, the first quantum algorithm was invented by David Deutsch and Richard Jozsa (1992) [DJ92]. This algorithm allows a quantum computer to solve with certainty an artificial mathematical problem known as Deutsch's problem. It provided the first steps towards Simon's algorithm [Sim94, Sim97], and later to Shor's algorithm. Furthermore, it is important as a simple quantum algorithm that can be experimentally tested.

Another class of quantum algorithms was discovered in 1996 by Lov Grover [Gro96, Gro97]. These algorithms allow a quadratic speed-up of unstructured search problems, for which there is no better approach classically than to try all L candidate solutions one at a time. A quantum computer using Grover's algorithm needs to make only \sqrt{L} such trials. Even though this speed-up is only quadratic rather than exponential, it is still significant.

The last currently known algorithmic application of quantum computers lies in the simulation of other quantum systems [Llo96], as Feynman conjectured. Even a computer consisting

of no more than a few dozen quantum bits could outperform the fastest classical computers in solving relevant physics problems, such as calculating the energy levels of an atom.

Scope of quantum computing

We close with two final remarks on quantum algorithms.

1. Quantum computing cannot offer any speed-up at all for many common tasks, such as adding up two numbers or word processing, which can already be done efficiently on a classical computer.
2. There are many problems which are classically intractable, but for which no efficient quantum algorithm is possible either [BBBV97].

An efficient quantum algorithm for the travelling salesman problem or a similar problem would have an enormous impact in the computer science community and the computer industry. Whether or not such a breakthrough will be made, it would be somewhat disappointing from a practical viewpoint if no other applications of quantum computers were found than the ones currently known. Either way, it is for certain that the developments in quantum computation have dramatically changed our understanding of the connection between physics, information and computation.

We gave here only a brief summary of the known quantum algorithms. Section 2.3 explains the operation and steps of the Deutsch-Jozsa algorithm, Grover's algorithm and Shor's algorithm in detail. We will present experimental implementations of simple instances of each of these algorithms in chapter 5.

2.1.5 Correcting quantum errors

Quantum errors or decoherence

Quantum parallelism and quantum algorithms inherently rely on quantum mechanical superpositions. However, in real quantum systems, superposition states are preserved only for a limited time: quantum bits gradually lose coherence due to unavoidable interactions with the environment, so the information stored in the coefficients of the terms in a superposition is lost. The environment in a sense acts as a measuring device which alters the state of the quantum system. This non-unitary process is called *decoherence* [Zur82, Zur91]. The time for which superposition states are preserved is called the *coherence time*.

From a fundamental point of view, decoherence is extremely interesting, although little understood. It is our explanation for the fact that we never see macroscopic objects in two states at the same time. Based on quantum theory, we would in fact expect such macroscopic

superpositions, as Schrödinger pointed out in his famous gedanken experiment [Sch35]. He imagined a cat in a perfectly closed box, and in the same box an atom in a superposition of its ground state and first excited state. If the atom decays, it emits a photon which sets off a trigger which in turn releases a poisonous gas in the box, that would kill the cat. If the atom is in a superposition of having decayed and not decayed, the cat should be in a superposition of its dead and alive states!

This prediction of quantum mechanics is contrary to our intuition based on observations of the world around us — if we see a cat, we expect it to be either alive or dead, but not dead and alive at the same time. The explanation is that a cat interacts so strongly with the environment that it decoheres almost instantaneously into either the dead or alive state, much too fast for superpositions of dead and alive cats to be observed.

From a practical point of view, decoherence can be detrimental for quantum computers, because it causes random errors in the state of the qubits [Unr95]. Therefore, quantum computations must either be completed within the coherence time or the errors resulting from decoherence must be corrected before their effect is too severe.

Quantum error correction

The correction of quantum errors arising from decoherence is much more complicated than the correction of classical errors. First, in contrast to the classical case, quantum errors occur not only as bit flips but can be arbitrary rotations in the Bloch sphere, which will influence the outcome of a subsequent measurement. Furthermore, a measurement which obtains information about a quantum state inevitably disturbs it. Finally, the no-cloning theorem (page 18) forbids making copies of unknown quantum states.

For several years, the correction of truly random errors due to decoherence looked hopeless. Therefore, the implementation of practical quantum computers appeared virtually impossible since some degree of decoherence is unavoidable.

The invention of quantum error correction in 1995, independently by Peter Shor [Sho95] and by Andrew Steane [Ste96], represented a crucial breakthrough which gave hope that practical quantum computers may be feasible. The main steps in quantum error correction are the same as in classical error correction: encoding, a noisy process, decoding, correction (Fig. 2.3). Despite this similar general outline, the difficulties in correcting quantum errors require fundamentally different solutions. These principles will be made explicit in section 2.4, where we explore quantum error correction in more detail.

Compared to the classical case, quantum error correction involves an even greater overhead: encoding, decoding and correction require many additional qubits and operations. An important question then is whether quantum error correction actually corrects for more errors than it introduces, when the operations are carried out with faulty components. The answer [ABO97, Kit97, KLZ98], a second key result for quantum computation, was that

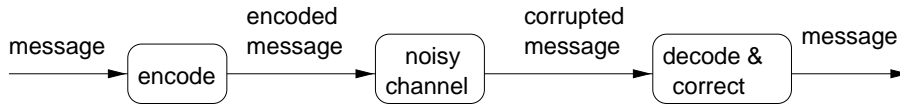


Figure 2.3: A message (one or more bits or qubits) is first redundantly encoded, the encoded message then goes through the process of interest (transmission over a noisy channel, a computation subject to errors, etcetera), and finally the corrupted encoded message is decoded and corrections are made if needed, based on the error syndrome (information about which errors occurred, contained in the redundancy bits).

provided the error rate (probability of error per elementary operation) is below a certain threshold, and given a fresh supply of qubits in $|0\rangle$, it is possible to perform arbitrarily long quantum computations.

The critical threshold is called the *accuracy threshold*. It is currently estimated to be between 10^{-4} and 10^{-6} , depending on the assumptions made about the nature of the errors and the process of interest.

2.2 Quantum gates and circuits

Any algorithm consists of a sequence of steps; in quantum algorithms, each step is a unitary transformation, U_k . In theory, we could implement the unitary transformation for each step, U_k , by letting the qubits evolve under the Hamiltonian $i \ln U_k / \Delta t$ for a duration Δt (we recall Eq. 2.19). In actual experiments, it is often not practical to turn on arbitrary Hamiltonians. Fortunately, as we will see, a small set of Hamiltonians is sufficient to generate arbitrary unitary transformations.

A convenient description of the steps in quantum algorithms at an intermediate level of abstraction is based on quantum gates, analogous to classical logic gates such as the NOT, AND and XOR gates. In this section, we will

1. describe quantum gates which can be directly implemented on realistic quantum computers,
2. provide a universal set of implementable quantum gates,
3. present methods to decompose complex quantum gates into sequences of directly-implementable gates, and
4. introduce the *quantum circuit* notation for the relevant quantum gates (quantum circuits are diagrams which represent a sequence of quantum gates applied to one or more qubits) [Deu89, Yao93].

The first three points are the subject of the following three subsections. The fourth point will be covered throughout this section.

2.2.1 Directly implementable quantum gates

The Hamiltonians present in simple quantum systems contain single-particle terms and interaction terms between two particles; three-particle terms are normally not observed. Therefore, the only quantum gates which we can easily implement directly are gates which act on one or two particles. If each particle represents a qubit, as we shall assume for now, we can thus realize one- and two-qubit gates directly.

One-qubit gates

Let us first introduce a convenient matrix representation in which to describe quantum states and unitary transformations. The quantum state $|\psi\rangle = a|0\rangle + b|1\rangle$ is written in matrix notation as

$$|\psi\rangle = \begin{bmatrix} a \\ b \end{bmatrix}, \quad (2.35)$$

a column vector containing the complex amplitudes of the $|0\rangle$ and $|1\rangle$ terms. The matrix representation of $\langle\psi|$ is the complex conjugate of the transpose of the vector $|\psi\rangle$. The inner product $\langle\psi_1|\psi_2\rangle$ and the outer product $|\psi_1\rangle\langle\psi_2|$ can be computed as the respective products of the corresponding column and row matrices.

Now let us consider the simplest building block of quantum computation, a one-qubit quantum gate, called the NOT gate. It maps $|0\rangle$ onto $|1\rangle$ and vice versa, similar to classical inversion. The unitary matrix which effects this transformation for arbitrary input states is

$$U_{\text{NOT}} = \begin{bmatrix} 0 & 1 \\ 1 & 0 \end{bmatrix}. \quad (2.36)$$

The action of a unitary operator U on a quantum state $|\psi\rangle$,

$$|\psi\rangle_{\text{final}} = U |\psi\rangle_{\text{initial}}, \quad (2.37)$$

can be calculated by standard matrix multiplication. For example, the output state obtained after applying U_{NOT} to $|\psi\rangle$ of Eq. 2.35 is

$$U_{\text{NOT}} |\psi\rangle = \begin{bmatrix} 0 & 1 \\ 1 & 0 \end{bmatrix} \begin{bmatrix} a \\ b \end{bmatrix} = \begin{bmatrix} b \\ a \end{bmatrix}, \quad (2.38)$$

which is the state vector corresponding to the state $a|1\rangle + b|0\rangle$, as expected given Eq. 2.27.

The rest of the discussion of one-qubit gates expands on the following notion: any one-qubit unitary operator can be written in the form

$$U = e^{i\alpha} R_{\hat{n}}(\theta), \quad (2.39)$$

where $R_{\hat{n}}(\theta)$ corresponds to a rotation in the Bloch sphere (Fig. 2.1) about the $\hat{n} = (n_x, n_y, n_z)$ axis and over an angle θ . If there is ambiguity about which qubit R acts on, we use a superscript to indicate the label of the qubit, $R_{\hat{n}}^i(\theta)$. In order to give an explicit definition of $R_{\hat{n}}(\theta)$, let us define the usual Pauli matrices

$$\sigma_x \equiv \begin{bmatrix} 0 & 1 \\ 1 & 0 \end{bmatrix}, \quad \sigma_y \equiv \begin{bmatrix} 0 & -i \\ i & 0 \end{bmatrix}, \quad \sigma_z \equiv \begin{bmatrix} 1 & 0 \\ 0 & -1 \end{bmatrix}, \quad (2.40)$$

which obey the relations

$$\sigma_x \sigma_y = i\sigma_z, \quad \sigma_x \sigma_z = -i\sigma_y, \quad \sigma_y \sigma_z = i\sigma_x, \quad (2.41)$$

$$\sigma_x^2 = \sigma_y^2 = \sigma_z^2 = \sigma_I, \quad (2.42)$$

where

$$\sigma_I \equiv \begin{bmatrix} 1 & 0 \\ 0 & 1 \end{bmatrix}. \quad (2.43)$$

With $\vec{\sigma} = (\sigma_x, \sigma_y, \sigma_z)$, we can construct $R_{\hat{n}}(\theta)$ by exponentiating the Pauli operators as follows:

$$R_{\hat{n}}(\theta) \equiv \exp\left(-i\frac{\theta\hat{n}\vec{\sigma}}{2}\right) = \cos(\theta/2)\sigma_I - i\sin(\theta/2)[n_x\sigma_x + n_y\sigma_y + n_z\sigma_z]. \quad (2.44)$$

Rotations about the \hat{x} , \hat{y} and \hat{z} axis respectively, are thus given by

$$R_x(\theta) = \exp\left(\frac{-i\theta\sigma_x}{2}\right) = \cos(\theta/2)\sigma_I - i\sin(\theta/2)\sigma_x = \begin{bmatrix} \cos\frac{\theta}{2} & -i\sin\frac{\theta}{2} \\ -i\sin\frac{\theta}{2} & \cos\frac{\theta}{2} \end{bmatrix}, \quad (2.45)$$

$$R_y(\theta) = \exp\left(\frac{-i\theta\sigma_y}{2}\right) = \cos(\theta/2)\sigma_I - i\sin(\theta/2)\sigma_y = \begin{bmatrix} \cos\frac{\theta}{2} & -\sin\frac{\theta}{2} \\ \sin\frac{\theta}{2} & \cos\frac{\theta}{2} \end{bmatrix}, \quad (2.46)$$

$$R_z(\theta) = \exp\left(\frac{-i\theta\sigma_z}{2}\right) = \cos(\theta/2)\sigma_I - i\sin(\theta/2)\sigma_z = \begin{bmatrix} e^{-i\theta/2} & 0 \\ 0 & e^{i\theta/2} \end{bmatrix}. \quad (2.47)$$

A one-qubit gate which deserves special mention is the HADAMARD gate, defined as

$$H = \frac{1}{\sqrt{2}} \begin{bmatrix} 1 & 1 \\ 1 & -1 \end{bmatrix}. \quad (2.48)$$

This gate transforms the computational basis states into the equal superposition states, and back:

$$|0\rangle \xleftrightarrow{H} \frac{|0\rangle + |1\rangle}{\sqrt{2}} \quad \text{and} \quad |1\rangle \xleftrightarrow{H} \frac{|0\rangle - |1\rangle}{\sqrt{2}}. \quad (2.49)$$

The HADAMARD gate corresponds to a rotation over 180° about an axis halfway between the \hat{x} and the \hat{z} axes. The NOT gate corresponds to a 180° rotation about the \hat{x} axis, up to an overall phase factor, which is irrelevant.

The quantum circuit element for a qubit is a horizontal wire. An arbitrary single-qubit gate U is represented as shown in Fig. 2.4 (a). The NOT gate is often represented by the \oplus symbol, as in Fig. 2.4 (b).



Figure 2.4: The quantum circuit representation of (a) an arbitrary one-qubit gate U and of (b) the NOT gate.

Two-qubit gates

The prototypical two-qubit gate, for historical reasons, is the controlled-NOT or CNOT gate; CNOT_{ij} flips (performs a NOT operation on) qubit j , called the target, if and only if qubit i , called the control qubit, is in the state $|1\rangle$. The truth table is shown in Fig. 2.5.

In	Out	In	Out
0 0	0 0	0 0	0 0
0 1	0 1	0 1	1 1
1 0	1 1	1 0	1 0
1 1	1 0	1 1	0 1
CNOT_{12}		CNOT_{21}	

Figure 2.5: Truth table of the CNOT gate with (Left) the first qubit in the role of the control qubit and (Right) the second qubit in the role of the control qubit.

The matrix representation for an arbitrary two-qubit state $|\psi\rangle = c_0|00\rangle + c_1|01\rangle + c_2|10\rangle +$

$c_3|11\rangle$ is

$$|\psi\rangle = \begin{bmatrix} c_0 \\ c_1 \\ c_2 \\ c_3 \end{bmatrix}, \quad (2.50)$$

and accordingly, unitary matrices representing two-qubit gates are of dimension 4×4 . For example, the unitary matrices corresponding to CNOT_{12} and CNOT_{21} are

$$U_{\text{CNOT}_{12}} = \begin{bmatrix} 1 & 0 & 0 & 0 \\ 0 & 1 & 0 & 0 \\ 0 & 0 & 0 & 1 \\ 0 & 0 & 1 & 0 \end{bmatrix} \quad \text{and} \quad U_{\text{CNOT}_{21}} = \begin{bmatrix} 1 & 0 & 0 & 0 \\ 0 & 0 & 0 & 1 \\ 0 & 0 & 1 & 0 \\ 0 & 1 & 0 & 0 \end{bmatrix}. \quad (2.51)$$

An obvious extension of the CNOT gate is the controlled- U gate, where a single-qubit operation U is performed on the target qubit if and only if the control qubit is in $|1\rangle$. Analogous to the controlled- U gate, we also define the zero-controlled- U gate, in which U is executed if and only if the control is $|0\rangle$. The last two-qubit gate we wish to introduce here is the SWAP gate,

$$U_{\text{SWAP}} = \begin{bmatrix} 1 & 0 & 0 & 0 \\ 0 & 0 & 1 & 0 \\ 0 & 1 & 0 & 0 \\ 0 & 0 & 0 & 1 \end{bmatrix}, \quad (2.52)$$

which, as the name suggests, swaps the state of the two qubits. The quantum circuit representations of all these two qubit operations are collected in Fig. 2.6.

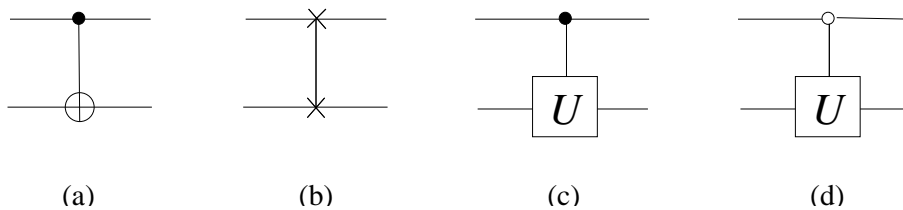


Figure 2.6: Quantum circuits for (a) the CNOT_{12} gate, (b) the SWAP gate, (c) a controlled- U gate and (d) a zero-controlled- U gate. The \bullet symbol indicates the control qubit; it controls the operation it is connected to via a vertical line. The \circ symbol indicates a zero-control qubit. A vertical line connecting two \times symbols denotes a SWAP operation of the two qubits.

Now that we have introduced a set of widely used and useful one- and two-qubit gates, we will examine if and how we can construct a universal set of quantum logic gates using only one- and two-qubit operations.

2.2.2 Universality

A *universal set of classical logic gates* has the property that any implementable Boolean function can be implemented by an arrangement of gates belonging to this set. For example, the NAND gate is in itself universal, and so is the NOR gate. Obviously, the AND gate and the NOT gate together thus also constitute a universal set of logic gates. By extension, the TOFFOLI gate is in itself universal for reversible classical logic.

A *universal set of quantum logic gates* has the property that any unitary transformation can be implemented (or approximated to arbitrary accuracy) by an arrangement of gates belonging to this set. Clearly, the TOFFOLI is not universal for quantum logic, as it is for example not possible to create a superposition state starting from the ground state using just TOFFOLI gates. Deutsch presented a three-qubit gate (a rotation of one qubit conditioned upon two other qubits being $|1\rangle$) which is universal [Deu89]; DiVincenzo presented a universal set of four two-qubit gates [DiV95b]. Lloyd [Llo95a] and independently Deutsch, Barenco and Ekert [DBE95], extended this result to show that almost any two-qubit gate is universal.

Of course, certain sets of universal quantum gates are more practical than others to work with, and we will come back to this in section 3.1.2. The most widely used result in the theory of quantum gates is that

the combination of the CNOT gate with arbitrary single-qubit rotations constitutes a set of universal quantum gates.

In fact, the CNOT along with arbitrary rotations about \hat{x} and \hat{y} is sufficient as well, as it can be shown that for any single-qubit rotation U there exist real numbers α, β, γ and δ such that

$$U = e^{i\alpha} R_x(\beta) R_y(\gamma) R_x(\delta). \quad (2.53)$$

We will give examples of decompositions of multi-qubit gates into just single-qubit gates and CNOT's in section 2.2.4.

We close by remarking that universality does not say anything about *efficiency*. In fact, it has been proven that the required number of elementary operations, such as CNOTs and single-qubit rotations, increases exponentially with n for almost all n -qubit unitary operations. Therefore, a crucial part in the design of quantum algorithms is to prove that each of the steps can be implemented efficiently, i.e. in only polynomially many elementary operations.

2.2.3 Remarks on unitary operators

This section with technical remarks answers two questions: (1) how do we compute the unitary operator corresponding to several consecutive gates, and (2) given an operation which acts on a subset of n qubits, how do we write the $2^n \times 2^n$ unitary matrix which describes the evolution of the n qubits ?

Multiplication and commutation of unitary operators

The concatenation of several quantum logic gates is described by the *product* of the corresponding unitary matrices, ordered such that the operator of the *first gate is placed on the right*. Thus, the unitary operator of k consecutive operations U_1, U_2, \dots, U_k is written as

$$U = U_k U_{k-1} \dots U_2 U_1. \quad (2.54)$$

This may seem awkward but makes sense if we recall Eq. 2.37, because this way U_1 is applied to $|\psi\rangle$ first, then U_2 and so forth. The order is important since in general

$$U_2 U_1 \neq U_1 U_2, \quad (2.55)$$

that is, in general, two *unitary operators may not commute under multiplication*. Hermitian matrices also may or may not commute with each other. Furthermore, for two non-commuting Hermitian operators H_1 and H_2 ,

$$e^{-iH_1} e^{-iH_2} \neq e^{-iH_2} e^{-iH_1}, \quad (2.56)$$

$$e^{-iH_1} e^{-iH_2} \neq e^{-i(H_1+H_2)}, \quad (2.57)$$

$$e^{-iH_2} e^{-iH_1} \neq e^{-i(H_1+H_2)}. \quad (2.58)$$

These inequalities demonstrate the importance of commutation properties for quantum computing. Turning on two terms in the Hamiltonian at the same time does not have the same effect as turning them on one after the other; and turning on one first and then the other is not the same as the other first and then the one. In closing, let us introduce a few simple practical commutation rules:

1. Any unitary operator commutes with itself.
2. Unitary operators acting on different qubits commute.
3. All diagonal operators commute with each other.

Tensor products and (non)-local operations

If a one-qubit gate U_1 is applied to one qubit l of an n qubit system, we can write the $2^n \times 2^n$ unitary matrix U acting on the n qubits as

$$U = \underbrace{\sigma_I \otimes \dots \otimes \sigma_I}_{l-1 \text{ factors}} \otimes U_1 \otimes \underbrace{\sigma_I \otimes \dots \otimes \sigma_I}_{n-l \text{ factors}}, \quad (2.59)$$

Similar extensions apply for any gate applied to any subsystem of a larger system. As an example of the effect of tensor products on matrices, the 4×4 unitary matrices representing a NOT operation on the first respectively the second of two qubits are

$$U_{\text{NOT}_1} = \begin{bmatrix} 0 & 0 & 1 & 0 \\ 0 & 0 & 0 & 1 \\ 1 & 0 & 0 & 0 \\ 0 & 1 & 0 & 0 \end{bmatrix} \quad \text{and} \quad U_{\text{NOT}_2} = \begin{bmatrix} 0 & 1 & 0 & 0 \\ 1 & 0 & 0 & 0 \\ 0 & 0 & 0 & 1 \\ 0 & 0 & 1 & 0 \end{bmatrix}. \quad (2.60)$$

Finally, we point out that any concatenation of one-qubit gates U_k on different qubits k can be written in the form

$$U = U_1 \otimes U_2 \otimes \dots \otimes U_n. \quad (2.61)$$

In contrast, a two-qubit or multi-qubit gate cannot in general be factored into such a product of single-qubit operators. This distinction is directly related to the distinction between separable and non-separable states, mentioned in section 2.1.1. *Local operations* (single-qubit operations) cannot create or undo entanglement, whereas *non-local* (multi-qubit) operations can. The CNOT_{12} gate (Eq. 2.51) for example transforms the non-entangled state $\frac{1}{\sqrt{2}}(|0\rangle + |1\rangle)|0\rangle = \frac{1}{\sqrt{2}}(|00\rangle + |10\rangle)$ to the entangled state of Eq. 2.10, $\frac{1}{\sqrt{2}}(|00\rangle + |11\rangle)$.

2.2.4 Multi-qubit gates

We will refer to all gates which act on more than two-qubits as multi-qubit gates. We already saw one example of such a gate in section 2.1.2, namely the TOFFOLI gate. From its truth table (Fig. 2.2), we can see that this gate flips the state of the target qubit (the third qubit in this case) if and only if two control qubits are in $|1\rangle$. It is therefore also called the doubly-controlled NOT or CCNOT gate, as conveyed in Fig. 2.7.

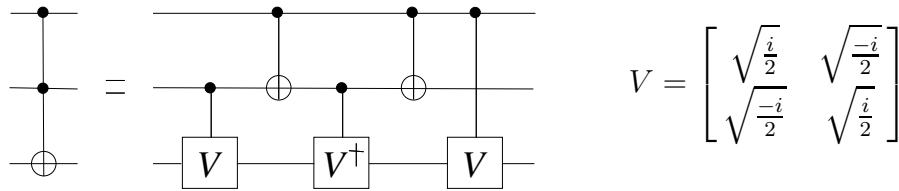


Figure 2.7: Quantum circuit representation of the TOFFOLI or CCNOT gate, and its decomposition into two-qubit gates. We note that $V^2 = U_{\text{NOT}}$.

The doubly-controlled NOT gate has obvious extensions to multiply-controlled NOT's. The number of elementary (one- and two-qubit) operations needed to implement a gate with $n - 1$ control qubits is $\mathcal{O}(n^2)$. If we allow a scratch pad qubit (an ancilla), the number of elementary operations is only $\mathcal{O}(n)$ [BBC⁺95].

Another useful and historically important gate is the FREDKIN gate [FT82], or controlled-SWAP gate, which swaps the state of two qubits if and only if a third qubit is in $|1\rangle$. The two-qubit SWAP gate (see page 28) between qubits 2 and 3 can be implemented as $\text{CNOT}_{23} \text{CNOT}_{32} \text{CNOT}_{23}$, or by symmetry also as $\text{CNOT}_{32} \text{CNOT}_{23} \text{CNOT}_{32}$. Therefore, a possible implementation of a SWAP of qubits 2 and 3 controlled by qubit 1 is as given in Fig. 2.8.

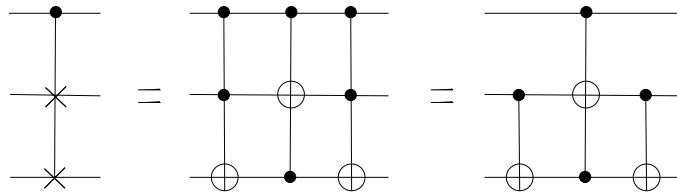


Figure 2.8: Quantum circuit representation of the FREDKIN or CSWAP gate, and two quantum circuits equivalent to the FREDKIN gate.

Efficient constructions for gates controlled by more than two qubits are extensively described in the literature [BBC⁺95, DiV98]. In sections 5.9 and 5.10 respectively, we will present quantum circuits for specific multi-qubit gates that were implemented in our experiments.

2.3 Quantum algorithms

2.3.1 The Deutsch-Jozsa algorithm

In 1992, David Deutsch and Richard Jozsa invented the first ever quantum algorithm [DJ92]. The Deutsch-Jozsa algorithm achieves an exponential advantage over classical algorithms in solving Deutsch's problem [DBE95] with certainty. Deutsch's problem may be described as follows. You are given a black box or *oracle* f which takes n input bits and returns one output bit. Furthermore you are told that the black box either outputs the same value (0 or 1) for all possible input strings x , or outputs 0 for exactly half the possible input values and 1 for the other input values. Deutsch's problem is thus a *promise* problem, and the promise is that f is either *constant* or *balanced*.

How many oracle queries do you need classically to solve Deutsch's problem *with certainty*? As soon as you find that the oracle returns 0 for some inputs and 1 for other inputs, you know for certain that f is balanced. However, if the output is still the same after trying $2^n/2$ different input values, the function f might still be balanced, even though most likely it is constant. Only when $2^n/2 + 1$ input values produce the same output, you can be sure the function is really constant. Thus, in the worst case, you need $2^n/2 + 1$ queries.

Using a quantum computer, the input of the oracle can be put in a superposition of all possible input values, and a single oracle query suffices to determine with certainty whether f is constant or balanced. We note that rather than to compute individual $f(x)$, which we know a

quantum computer cannot do in fewer steps than a classical computer, the task is to determine a *global property* of the function, namely whether f is constant or balanced. This is a type of problem for which quantum computers may offer an advantage.

Procedure

The steps of the Deutsch-Jozsa algorithm, as improved by Cleve *et al.* [CEMM98] and Tapp [Tap98], are outlined in Fig. 2.9. The initial state is

$$|\psi_0\rangle = |0\rangle^{\otimes n}|1\rangle, \quad (2.62)$$

where \otimes^n indicates that the first register, the input register, is of size n (we will often leave this implicit). The second register, the output register, contains only one qubit. First we apply a HADAMARD gate on each of the $n + 1$ qubits, resulting in the state

$$|\psi_1\rangle = \sum_{x=0}^{2^n-1} \frac{|x\rangle}{\sqrt{2^n}} \left[\frac{|0\rangle - |1\rangle}{\sqrt{2}} \right]. \quad (2.63)$$

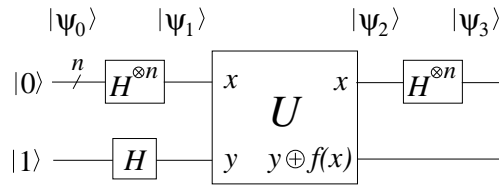


Figure 2.9: Quantum circuit for the Deutsch-Jozsa algorithm.

The input register is now in an equal superposition of all possible x . The reason why the output register is placed in $\frac{|0\rangle - |1\rangle}{\sqrt{2}}$ will become clear shortly. Next we query the oracle f (we come back to what it means in practice to query an oracle on page 36), which effects the unitary transformation

$$U_f = |x\rangle|y\rangle \mapsto |x\rangle|y \oplus f(x)\rangle, \quad (2.64)$$

where \oplus stands for addition modulo 2. The oracle thus transforms $|\psi_1\rangle$ to

$$|\psi_2\rangle = \sum_x \frac{|x\rangle}{\sqrt{2^n}} \left[\frac{|0 \oplus f(x)\rangle - |1 \oplus f(x)\rangle}{\sqrt{2}} \right]. \quad (2.65)$$

This is an instance of quantum parallelism. Now, we see that whenever $f(x) = 0$, the output register does not change, and whenever $f(x) = 1$, the output register is changed to $\frac{|1\rangle - |0\rangle}{\sqrt{2}} = -\frac{|0\rangle - |1\rangle}{\sqrt{2}}$. Thus the oracle query has no net effect other than a sign flip whenever $f(x) = 1$ and

we can rewrite $|\psi_2\rangle$ as

$$|\psi_2\rangle = \sum_x \frac{(-1)^{f(x)}|x\rangle}{\sqrt{2^n}} \left[\frac{|0\rangle - |1\rangle}{\sqrt{2}} \right]. \quad (2.66)$$

The value of $f(x)$ is thus encoded in the coefficient of $|x\rangle$, by virtue of initializing the output qubit to $\frac{|0\rangle - |1\rangle}{\sqrt{2}}$. Since the state of the output qubit never changes, we could in fact leave this qubit out altogether and implement f via the unitary transformation $|\psi\rangle \xrightarrow{f} (-1)^{f(x)}|x\rangle$ [CEMM98].

We already see that if f is constant, the phase factor $(-1)^{f(x)}$ is constant as well, so it becomes a physically irrelevant overall phase. In this case, the subsequent $H^{\otimes n}$ operation restores the first register to the state $|0\rangle$. For the case of balanced f , let us first calculate $H|x_i\rangle$ and then $H^{\otimes n}|x\rangle$. From Eq. 2.49, we see that

$$H|x_i\rangle = \frac{|0\rangle + (-1)^{x_i}|1\rangle}{\sqrt{2}} = \sum_{z=0,1} \frac{(-1)^{x_i z}|z\rangle}{\sqrt{2}}. \quad (2.67)$$

Therefore,

$$H^{\otimes n}|x_1, \dots, x_n\rangle = \frac{\sum_{z_1, \dots, z_n} (-1)^{x_1 z_1 + \dots + x_n z_n} |z_1 \dots z_n\rangle}{\sqrt{2^n}} = \frac{\sum_z (-1)^{x \cdot z} |z\rangle}{\sqrt{2^n}}, \quad (2.68)$$

where $x \cdot z$ is the bitwise inner product of x and z , modulo 2. Using this result, we find that

$$|\psi_3\rangle = H^{\otimes n}|\psi_2\rangle = \sum_z \sum_x \frac{(-1)^{x \cdot z + f(x)}|z\rangle}{\sqrt{2^n}} \left[\frac{|0\rangle - |1\rangle}{\sqrt{2}} \right]. \quad (2.69)$$

We now measure the first register. For constant f , the amplitude of the $|0\rangle^{\otimes n}$ term, $\sum_x (-1)^{f(x)}$, is either $+1$ or -1 , depending on the constant value f takes. Given the normalization condition of Eq. 2.9, the amplitude of the remaining terms must thus be zero, like we anticipated. For balanced f , we always have that $\sum_x (-1)^{f(x)} = 0$ as there are as many positive as negative $f(x)$. The amplitude of the $|0\rangle^{\otimes n}$ term is thus zero in this case. In summary, if the measurement of the first register gives all 0's we know f is constant, and otherwise f is balanced.

Significance

We have thus shown that the Deutsch-Jozsa algorithm solves Deutsch's problem exponentially faster than any classical machine. While this is truly remarkable in itself, the practical importance of this algorithm is limited. First, Deutsch's problem is an artificial mathematical problem which has no known applications. Second, classical computers can solve this problem quickly and with high probability of success by asking the oracle what $f(x)$ is for a few random x : the probability for obtaining k times the same answer (either 0 or 1) if f is balanced decreases

as $(1/2)^{k-1}$. Only if absolute certainty is required, exponentially many oracle queries may be required classically.

The significance of this algorithm therefore lies mostly in that it inspired later, more useful algorithms, is relatively easily understood, and can be used as a simple test for implementations of quantum computers. In section 5.3, we will present such an experiment on a two-qubit NMR quantum computer.

2.3.2 Grover's algorithm

In 1996, Lov Grover invented a quantum algorithm for *unstructured searches* [Gro96, Gro97]. An example of a structured search is finding the phone number matching with a certain name using a phone book with N alphabetically listed names. An example of an unstructured search is to find the name matching with a certain phone number using the same phone book. The time this takes goes up linearly with N : on average you will have to try $[N(N+1)/2 - 1]/N \approx N/2$ different names before you find the one with the desired number. In contrast, using Grover's algorithm, such a search can be accomplished in \sqrt{N} attempts.

Mathematically, we can describe this as the following promise problem. Given an oracle which returns $f(x) = 0$ for all values of x except for a unique entry $x = x_0$ for which $f(x) = 1$ (there is a unique name x_0 in the phone book which has the desired phone number), find the special element x_0 in the least number of oracle queries.

As in the Deutsch-Jozsa algorithm, the oracle query takes the form of the transformation

$$U_f = |x\rangle|y\rangle \xrightarrow{f} |x\rangle|x \oplus y\rangle, \quad (2.70)$$

where we will initialize the state of the output qubit $|y\rangle$ to $\frac{|0\rangle - |1\rangle}{\sqrt{2}}$. As we have seen in section 2.3.1, the content of the output register in fact doesn't change, and $f(x)$ is encoded in the sign of $|x\rangle$. We will therefore leave out the second register and from now on only consider the effect of the oracle call on $|x\rangle$.

Procedure and performance

The steps in Grover's algorithm for a search space of size $N = 2^n$ are:

(a) Initialize to $|0\rangle^{\otimes n}$.

(b) Apply $H^{\otimes n}$ to obtain $\frac{1}{\sqrt{N}} \sum_{x=0}^{N-1} |x\rangle$.

(c) Repeat the following subroutine, known as the *Grover iteration*, $\lceil \pi\sqrt{N}/4 \rceil$ times:

1. Query the oracle $U_f : |x\rangle \xrightarrow{f} (-1)^{f(x)}|x\rangle$. This flips the phase of the $|x_0\rangle$ term.

2. Apply $H^{\otimes n}$.
3. Flip the phase of all terms except the $|0\rangle$ term. Thus, $\forall x \neq 0 : |x\rangle \mapsto -|x\rangle; |0\rangle \mapsto |0\rangle$.
4. Apply $H^{\otimes n}$.

Steps 2, 3 and 4 together are often referred to as *inversion about the average*, because their combined effect is to invert the amplitude of each term $|x\rangle$ about the average amplitude of all 2^n terms.

Figure 2.10 graphically illustrates the operation of Grover's algorithm. The amplitude of all terms $|x\rangle$ are equal after step (b) in the algorithm. The amplitude of $|x_0\rangle$ builds up after each Grover iteration, at the expense of the amplitude of the remaining terms, until it reaches a maximum and decreases again. For increasing numbers of Grover iterations, the amplitude of the special element $|x_0\rangle$ oscillates sinusoidally. The first maximum occurs after $\lceil \pi\sqrt{N}/4 \rceil$ iterations. If we measure the n qubits at this point, the measurement result will be x_0 with high probability and the search has succeeded.

How does the number of elementary operations required for a Grover search scale with the size N of the search space? Steps 2 and 4 take $n = \log_2 N$ HADAMARD gates each. Step 3, the conditional phase flip, can be done in $\mathcal{O}(n) = \mathcal{O}(\log_2 N)$ operations, as noted in section 2.2.4. The cost of the oracle depends on f and we will come back to it shortly, but in any case the oracle is called only once per iteration. The Grover iteration must be repeated $\mathcal{O}(\sqrt{N})$ times, so the entire algorithm requires $\mathcal{O}(\sqrt{N} \log_2 N)$ operations and $\mathcal{O}(\sqrt{N})$ oracle calls, as opposed to $\mathcal{O}(N)$ calls classically. We therefore say that Grover's algorithm achieves a quadratic speed-up over classical search algorithms.

Application and implementation

What does it mean to call an oracle? In real life, we don't have actual oracles available (much less oracles which interface with quantum computers), so we need to implement U_f ourselves. In the phone book example, U_f would have to reflect a phone book of N entries and would therefore take at least $\mathcal{O}(N)$ operations to implement. This is not a useful application of Grover's algorithm: we may have to make only $\mathcal{O}(\sqrt{N})$ oracle calls, but each oracle call takes $\mathcal{O}(N)$ operations in itself.

Then, what are useful applications of Grover's algorithm? The general answer is: problems where we want to find $x_0 = f^{-1}(y_0)$ where f is easily computable (unlike the case of phone-books) but f^{-1} is hard to compute, such that there is no better approach than to evaluate $f(x)$ for random values of x until we hit $x = x_0$ such that $f(x_0) = y_0$.

As an example, consider the following instance of the satisfiability problem: find the values of x_1 , x_2 and x_3 which satisfy the boolean expression $(x_1\bar{x}_2 + x_3)\bar{x}_3$. In this case, it is easy to see that there is one unique solution, $x_1x_2x_3 = 100$. However, the effort needed to find a

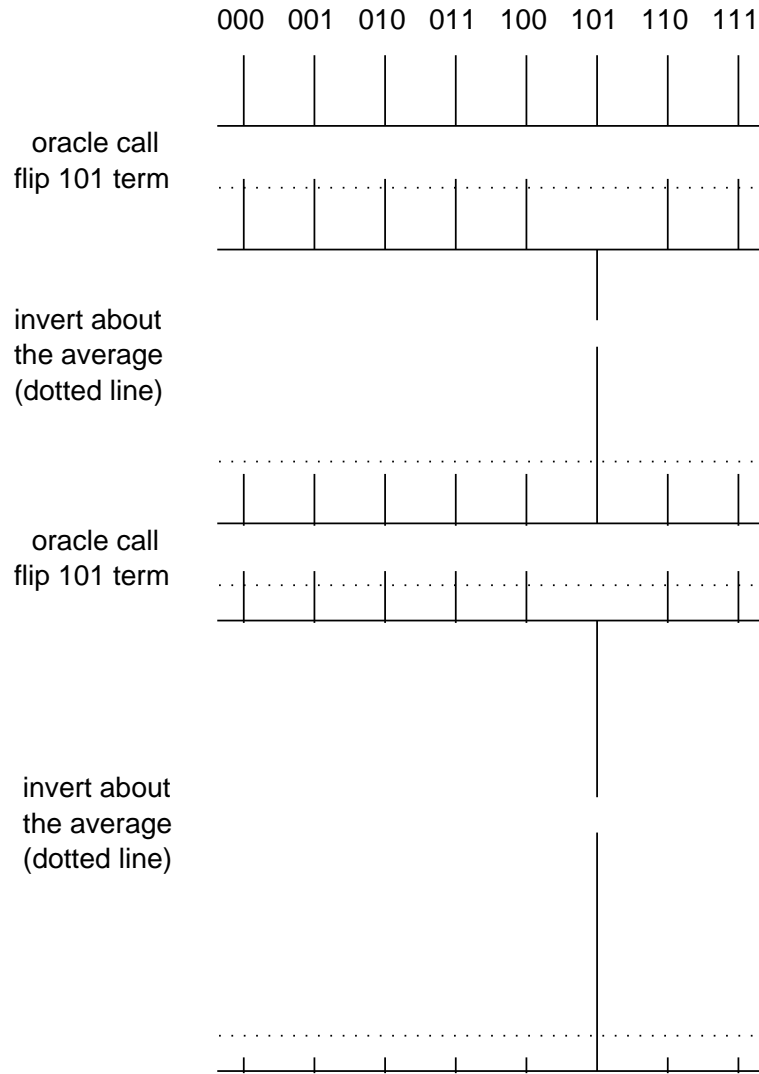


Figure 2.10: Illustration of amplitude amplification in Grover's algorithm for $N = 8$ ($n = 3$) and $|x_0\rangle = |101\rangle$. The diagrams shows the (real) amplitude of the eight terms $|000\rangle$ through $|111\rangle$. The starting point is an equal superposition of all terms. After each Grover iteration (an oracle call followed by inversion about the average), the amplitude of the special element is amplified. For the case $N = 8$, the amplitude of the $|x_0\rangle$ reaches almost 1 after two Grover iterations.

solution for an arbitrary Boolean expression, or even to ascertain whether there is a solution, increases exponentially with the problem size for any known classical algorithm. The general satisfiability problem is thus hard [Pap94]⁵. A quantum computer running Grover's algorithm could solve this problem in quadratically fewer operations than is possible classically.

For many realistic applications, such as the satisfiability problem, there may be more than one solution. However, if there are M solutions, the amplitude of the solutions is highest after $\mathcal{O}(\sqrt{N/M})$ Grover iterations [BBHT98]. We thus need to know M in order to know the optimal number of iterations. Fortunately, M can be found in $\mathcal{O}(\sqrt{N})$ oracle calls as well, via a procedure called quantum counting [BHT98]. In summary, by combining quantum counting and quantum search, unstructured searches with an unknown number of solutions can be sped up quadratically compared to any classical algorithm.

In section 5.7, we will present an experimental realization of Grover's algorithm on a search space of eight elements. This experiment also nicely illustrates the oscillatory behavior of the amplitude of $|x_0\rangle$ as a function of the number of Grover iterations.

2.3.3 Order-finding and Shor's algorithm

In 1994, Peter Shor discovered an efficient quantum algorithm for prime factorization and for computing discrete logarithms [Sho94, Sho97]. This algorithm represented a tremendous breakthrough, because it offered an exponential speed-up over both deterministic and probabilistic classical algorithms for an important mathematical problem.

Shor's algorithm was later generalized to an algorithm for order-finding and the Abelian hidden-subgroup problem [Kit95]. The key step common to all algorithms in this class is the quantum Fourier transform. We will first introduce the quantum Fourier transform (QFT), then describe an algorithm which uses the QFT for order-finding, and finally present the factoring algorithm as a specific instance of order-finding. For a good introductory article on Shor's algorithm, see [EJ96].

The quantum Fourier transform

The quantum Fourier transform (QFT) performs the same transformation as the (classical) fast Fourier transform (FFT), but it can be computed efficiently, which is classically not possible. Or more precisely, the QFT allows us to efficiently *sample* the FFT. Even this is impossible classically and, as we will see, being able to sample the FFT is sufficient for order-finding.

The FFT_N takes as input a string of N complex numbers x_j and produces as output another

⁵A restricted case of the satisfiability problem, 2-SAT, is not hard.

string of N complex numbers y_k , such that

$$y_k = \frac{1}{\sqrt{N}} \sum_{j=0}^{N-1} x_j e^{2\pi i j k / N}. \quad (2.71)$$

For an input string with numbers which repeat themselves with period r , the FFT_N *inverts the periodicity*, i.e. it produces an output string with period N/r , as illustrated in the following four examples for $N = 8$ (the output strings have been rescaled for clarity)

$$\begin{array}{rcccl} r & \text{input string} & & \text{output string} & N/r \\ 8 & 1\ 0\ 0\ 0\ 0\ 0\ 0\ 0 & \mapsto & 1\ 1\ 1\ 1\ 1\ 1\ 1\ 1 & 1 \end{array} \quad (2.72)$$

$$4 \quad 1\ 0\ 0\ 0\ 1\ 0\ 0\ 0 \mapsto 1\ 0\ 1\ 0\ 1\ 0\ 1\ 0 \quad 2 \quad (2.73)$$

$$2 \quad 1\ 0\ 1\ 0\ 1\ 0\ 1\ 0 \mapsto 1\ 0\ 0\ 0\ 1\ 0\ 0\ 0 \quad 4 \quad (2.74)$$

$$1 \quad 1\ 1\ 1\ 1\ 1\ 1\ 1\ 1 \mapsto 1\ 0\ 0\ 0\ 0\ 0\ 0\ 0 \quad 8 \quad (2.75)$$

If r does not divide N , the inversion of the period is approximate. In addition to inverting the period, the FFT *converts off-sets* in the locations of the numbers in the input string *into phase factors* in front of the numbers in the output string:

$$1\ 0\ 0\ 0\ 1\ 0\ 0\ 0 \mapsto 1\ 0\ 1\ 0\ 1\ 0\ 1\ 0 \quad (2.76)$$

$$0\ 1\ 0\ 0\ 0\ 1\ 0\ 0 \mapsto 1\ 0\ -i\ 0\ -1\ 0\ i\ 0 \quad (2.77)$$

$$0\ 0\ 1\ 0\ 0\ 0\ 1\ 0 \mapsto 1\ 0\ -1\ 0\ 1\ 0\ -1\ 0 \quad (2.78)$$

$$0\ 0\ 0\ 1\ 0\ 0\ 0\ 1 \mapsto 1\ 0\ i\ 0\ -1\ 0\ -i\ 0 \quad (2.79)$$

The QFT performs exactly the same transformation, but differs from the FFT in that the complex numbers are stored in the amplitude and phase of the terms in a superposition state of $n = \log_2 N$ qubits. For $N = 8$, the qubit string is of length $\log_2 8 = 3$, and the amplitude of the $|000\rangle$ term represents the first complex number, the amplitude of the $|001\rangle$ term represents the second number and so forth. As before, we will label the states $|000\rangle, |001\rangle, \dots, |111\rangle$ as $|0\rangle, |1\rangle, \dots, |7\rangle$. As an example, we see from Eq. 2.77 that the QFT thus transforms the state $(|1\rangle + |5\rangle)\sqrt{2}$ to the state $(|0\rangle - i|2\rangle - |4\rangle + i|6\rangle)/2$.

The action of the QFT on a computational basis state of length n is

$$|j\rangle \mapsto \frac{1}{\sqrt{N}} \sum_{k=0}^{N-1} e^{2\pi i j k / N} |k\rangle, \quad (2.80)$$

which we can rewrite (after some algebra) as

$$|j_1, \dots, j_n\rangle \mapsto \frac{(|0\rangle + e^{2\pi i 0 \cdot j_n} |1\rangle)(|0\rangle + e^{2\pi i 0 \cdot j_{n-1} j_n} |1\rangle) \dots (|0\rangle + e^{2\pi i 0 \cdot j_1 j_2 \dots j_n} |1\rangle)}{\sqrt{2^n}}, \quad (2.81)$$

where $0 \cdot j_1 j_2 \dots j_n$ stands for $2^{-j_1} + 2^{-2j_2} + \dots + 2^{-nj_n}$. Suppose we now reverse the order of the qubits in the output of the QFT, so output qubit j_n becomes output qubit 1, qubit j_{n-1} becomes qubit j_2 and so forth. The transformation of Eq. 2.81 then changes into

$$|j_1, \dots, j_n\rangle \mapsto \frac{(|0\rangle + e^{2\pi i 0 \cdot j_1} |1\rangle)(|0\rangle + e^{2\pi i 0 \cdot j_2 j_1} |1\rangle) \dots (|0\rangle + e^{2\pi i 0 \cdot j_n j_{n-1} \dots j_1} |1\rangle)}{\sqrt{2^n}}. \quad (2.82)$$

which we can easily implement as follows. The first factor of this expression represents a 180° phase shift of qubit 1 controlled by qubit 1 itself; this is accomplished by a HADAMARD gate on qubit 1. The next factor shifts the phase of qubit 2 over 180° controlled by qubit 2 (a HADAMARD gate on qubit 2), and over another 90° controlled by qubit 1, which corresponds to a controlled- Z rotation. The next factor requires a HADAMARD gate on qubit 3, a Z rotation of qubit 3 controlled by qubit 2 and a $Z^{1/2}$ (45°) rotation of 3 controlled by 1. The quantum circuit for the QFT acting on three qubits is shown in Fig. 2.11, and it can be easily extended for $n > 3$, using a total of n HADAMARD gates and $n(n-1)/2$ controlled rotations. We next see how the QFT is incorporated in a quantum algorithm for order-finding.

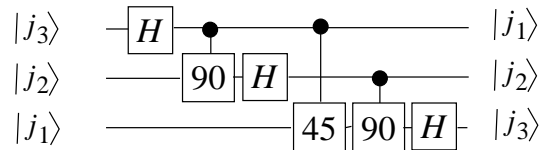


Figure 2.11: Quantum circuit for the quantum Fourier transform (QFT) acting on three qubits. In this implementation of the QFT, due to Coppersmith [Cop94], the order of the qubits is reversed at the output with respect to the input.

Order-finding

The order of a permutation π on M elements can be understood via the following analogy: imagine M rooms and M one-way passages connecting the rooms, with *exactly* one entrance and one exit in each room (for some rooms, the passage going out may loop back to the room itself). The rooms are thus connected in subcycles, as shown in Fig. 2.12. This configuration ensures that if you start in some room y and keep going from one room to the next using the one-way passages, you must eventually come back to the room you started from. We then define the order r of the permutation π as the *minimum number of transitions needed to return to the starting room y* , where r may depend on y but is never greater than M .

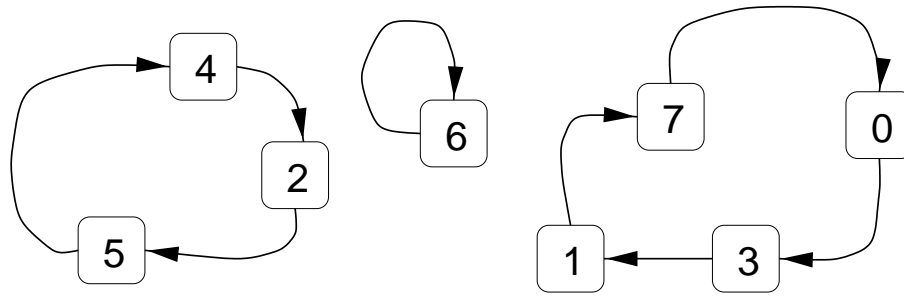


Figure 2.12: Pictorial representation of a permutation π on eight elements. The order r is 3 if $y \in \{2, 4, 5\}$, $r = 1$ if $y = 6$, and $r = 4$ if $y \in \{0, 1, 3, 7\}$.

Suppose you are in a room y and must determine the order r solely by making trials of the type “make x transitions starting from room y and check which room you are in”. Mathematically, we will describe such trials as queries of an oracle or black box which outputs $\pi^x(y)$, that is the element obtained after permuting x times starting from y using π (so for the permutation of Fig. 2.12, we have $\pi^1(5) = 4$, $\pi^2(5) = 2$ and so forth). How many such queries are needed in order to find r with a given probability of success ?

Richard Cleve [Cle00] showed that the minimum number of classical oracle queries needed for a given probability of success increases exponentially with the problem size $m = \lceil \log_2 M \rceil$ (the number of bits needed to represent M numbers). In contrast, on a quantum computer using a generalization of Shor’s quantum algorithm, the number of oracle queries needed in order to achieve a given probability of success does not increase with m . Thus, there is an exponential gap in the number of oracle queries required between the quantum and classical cases.

We now will explain the steps in the order-finding quantum algorithm via an example where the permutation π acts on $M = 4$ elements (Fig. 2.13).

First, initialize a register of $n = \log_2 N = 3$ qubits in the ground state, and a second register of two qubits in the state $|y_1 y_0\rangle$ or for short $|y\rangle$, where $y_1 y_0$ is the binary representation of y . Apply a HADAMARD transformation to all qubits in the first register. The state of the quantum computer is now

$$|\psi_1\rangle = (|0\rangle + |1\rangle + |2\rangle + |3\rangle + |4\rangle + |5\rangle + |6\rangle + |7\rangle) |y\rangle, \quad (2.83)$$

where we have left out the normalization factor.

Then query the oracle, i.e. evaluate the function $\pi^x(y)$, and store the result in the second register, via the transformation

$$|x\rangle|y\rangle \mapsto |x\rangle|\pi^x(y)\rangle, \quad (2.84)$$

which is conveniently implemented in $n = 3$ exponentiated permutations (Fig. 2.13), using $x = 4x_2 + 2x_1 + x_0$ and thus $\pi^x = \pi^{4x_2} \pi^{2x_1} \pi^{x_0}$. Since the first register is in an equal superposition of

all values of x between 0 and 2^n , the function is evaluated for all those values of x in parallel. In the analogy of the rooms and one-way passages, the quantum computer thus makes transitions to many rooms at once. For the sake of the argument, let us say for example that $y = 3$, and that $\pi^1(3) = 1$ and $\pi^2(3) = 3$.⁶ For this example, evaluation of $\pi^x(y)$ transforms the state of Eq. 2.83 into

$$|\psi_2\rangle = |0\rangle|3\rangle + |1\rangle|1\rangle + |2\rangle|3\rangle + |3\rangle|1\rangle + |4\rangle|3\rangle + |5\rangle|1\rangle + |6\rangle|3\rangle + |7\rangle|1\rangle \quad (2.85)$$

$$= (|0\rangle + |2\rangle + |4\rangle + |6\rangle)|3\rangle + (|1\rangle + |3\rangle + |5\rangle + |7\rangle)|1\rangle. \quad (2.86)$$

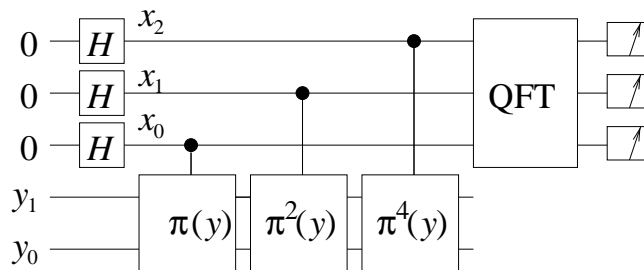


Figure 2.13: Outline of the order-finding quantum algorithm.

Next, apply the QFT to the first register. In order to appreciate the need for and role of the QFT, suppose we now measured $|\psi_2\rangle$ directly. In $|\psi_2\rangle$, the first register is still in a superposition of eight states, regardless of π so this measurement will not tell us much useful. Suppose we instead measure the second register. The result will be either 1 or 3 but that in itself isn't of much help either — it is merely a sample of $\pi^x(y)$ for a random x , which we could do equally well classically. Now suppose we measure both registers. In the measurement process of the second register, the state of the first register will collapse to either

$$|0\rangle + |2\rangle + |4\rangle + |6\rangle \quad \text{OR} \quad |1\rangle + |3\rangle + |5\rangle + |7\rangle. \quad (2.87)$$

depending on whether the measurement of register 2 gave 3 or 1. However at this point, a measurement of the first register still does not yield any information at all, because all eight possible outcomes are still equally likely, as we don't know from which subset of values of x the measured x will come. But if we apply the QFT, the first register will be transformed to⁷

$$|0\rangle + |4\rangle \quad \text{OR} \quad |0\rangle - |4\rangle. \quad (2.88)$$

⁶This already tells us that the order is 2 (because after permuting twice we get back to the starting element y), and we can also deduce that $\pi^3(3) = 1$, $\pi^4(3) = 3$ and so forth. Of course, in a realistic application we don't know the order in advance; we only have a description of the permutation to help us determine r .

⁷Note that while introducing the measurement of the second register makes it easier to explain things, this measurement can actually be left out. The QFT will still transform the first register as shown.

Now a measurement of the first register does give useful information, because only multiples of N/r are possible outcomes, in this example 0 and 4. In general, we can derive r from the measurement outcome with high probability of success, using the continued fraction expansion [HW60, Kob94], provided $n \geq 2m$, that is $N \geq M^2$ (this was in fact not the case in the simple example we presented).

The order-finding algorithm for arbitrary m is summarized as follows. Let the first register be of size $n = 2m$, and the second register of size m . Let furthermore $y = 0$, without loss of generality.

1. Initialize

$$|0\rangle|0\rangle$$

2. Create a superposition using $H^{\otimes n}$

$$\mapsto \frac{1}{\sqrt{2^n}} \sum_{j=0}^{2^n-1} |j\rangle|0\rangle$$

3. Apply $f(j)$ (where $f(j) = \pi^j(0)$)

$$\mapsto \frac{1}{\sqrt{2^n}} \sum_{j=0}^{2^n-1} |j\rangle|f(j)\rangle$$

4. Apply the QFT $_N$ to the first register (Eq. 2.80)

$$\begin{aligned} \mapsto & \frac{1}{2^n} \sum_{j=0}^{2^n-1} \sum_{k=0}^{2^n-1} e^{2\pi i j k / N} |k\rangle|f(j)\rangle \\ = & \frac{1}{2^n} \sum_{k=0}^{2^n-1} \sum_{j=0}^{2^n-1} e^{2\pi i j k / N} |k\rangle|f(j)\rangle \end{aligned}$$

5. Measure the first register

The probability for obtaining $|k\rangle$ upon measurement is the square of the amplitude of $|k\rangle$ in the output state of the QFT,

$$\left(\sum_{j=0}^{2^n-1} e^{2\pi i j k / N} \right)^2. \quad (2.89)$$

Due to interference of the terms in this summation, the probability is high for values of k which are an integer multiple of N/r and very small or zero for other values of k . In fact, if r divides

N exactly, the probability for obtaining a multiple of N/r upon measuring the output state is equal to 1 (this was the case in the examples for the FFT of Eqs. 2.72-2.75).

In section 5.9, we will present the first implementation of the order-finding algorithm. We will now describe a specific instance of the order-finding algorithm, namely Shor's famous algorithm for prime factorization.

Factoring

The most famous application of the order-finding algorithm, and historically the first one to be discovered, is to decompose large integer numbers into their prime factors. Quantum factoring consists of finding the order of the permutation

$$\pi(y) = ay \bmod L, \quad (2.90)$$

for $y = 1$. L is the integer we want to factor and a can be any integer $< L$ that is coprime with L (i.e. a and L should have no common factors other than 1). In words, the permutation consists of multiplying y by a , and taking the remainder of the division of ay by L .

Given the order r of the permutation $ay \bmod L$ for $y = 1$, at least one prime factor of L is given by

$$\gcd(a^{r/2} - 1, L) \quad \text{or} \quad \gcd(a^{r/2} + 1, L) \quad (2.91)$$

with high probability. Computing the greatest common denominator of two integers can be done efficiently on a classical computer, using Euclid's algorithm. These are results from number theory [HW60, Kob94].

An important difference between our description of the order-finding problem and the factoring problem is that for order-finding we assumed that an oracle was available which we can ask queries of the type $\pi^x(y)$. As was pointed out in section 2.3.2, we must in practice implement oracle calls ourselves, and we must therefore consider whether this can be done efficiently. For factoring, calling the oracle means implementing the permutation $\pi^x(y) = a^x y \bmod L$ with $y = 1$, which is equivalent to evaluation of the function

$$a^x \bmod L, \quad (2.92)$$

known as the *modular exponentiation* function.

Since $a^x \bmod L$ is by definition a number between 0 and $L - 1$, the second register must be of size $m = \lceil \log_2 L \rceil$. The first register must be at least twice as large, so $n = 2m$. Since $x = x_{n-1}2^{n-1} + \dots + x_12^1 + x_02^0$, we have

$$\begin{aligned} a^x y \bmod L &= a^{2^{n-1}x_{n-1}} \dots a^{2x_1} a^{x_0} y \bmod L \\ &= [a^{2^{n-1}x_{n-1}} \dots [a^{2x_2} [a^{x_0} y \bmod L] \bmod L] \dots \bmod L] \end{aligned} \quad (2.93)$$

In words, this means that we first multiply y by a modulo L , if and only if $x_0 = 1$; then we multiply the result by a^2 modulo L , if and only if $x_1 = 1$ and so forth, until we finally multiply by $a^{2^{n-1}}$ modulo L if and only if $x_{n-1} = 1$.

Thus, modular exponentiation is reduced to $n = 2m \approx 2 \log_2 L$ multiplications modulo L , each controlled by just a single qubit x_i . The numbers $a^2, \dots, a^{2^{n-1}} \bmod L$ by which we need to multiply can be found efficiently on a classical computer by *repeated squaring*, and multiplication of m -bit numbers take $\mathcal{O}(m^2)$ elementary operations.

The modular exponentiation step can thus be done efficiently, in $\mathcal{O}((\log_2 L)^3)$ one- and two-qubit gates, and we showed earlier that the other key step in Shor's factoring algorithm, the quantum Fourier transform, can also be realized efficiently. The factoring problem, widely believed to be intractable on classical computers,⁸ is thus tractable on quantum computers.

In section 5.10, we present the first experimental realization of Shor's algorithm. It is an implementation of the simplest possible instance for which the algorithm can be non-trivially demonstrated, namely factorization of the number fifteen⁹.

2.3.4 Quantum simulations

The possibility of using quantum computers to solve problems in quantum physics was conjectured by Feynman [Fey82] long before quantum algorithms for solving mathematical problems such as factoring were discovered. Seth Lloyd proved this conjecture in 1996 [Llo96].

The general procedure is to map the possible states of the simulated system onto the states of a set of qubits, and then to apply a sequence of quantum gates which produce qubit dynamics analogous to the dynamics of the simulated system. The final state of the qubits is then mapped back onto the state of the simulated system.

Explicit protocols have been worked out for several realistic physical problems. These include

- Estimation of the eigenvalues and eigenvectors of a Hamiltonian (this algorithm invokes the QFT), which can be used to find the energy levels of an atom for example [AL99].
- Simulation of the dynamics of many-body Fermi systems, using either first or second quantized descriptions [AL97].
- Simulation of quantum chaos and localization [GS01].

⁸We note that classically, there are many approaches known to factoring integers besides finding the order of $ay \bmod N$, but all of them are inefficient. It is possible, although unlikely, that one day an efficient classical factoring algorithm will be found. Or perhaps a proof will be constructed that such an algorithm is not possible.

⁹The algorithm fails for even L and for L which are powers of prime numbers (e.g. the number nine), and factoring is obviously not applicable to prime L . This includes all numbers smaller than 15. The next simplest instance of factoring is 21.

2.3.5 Other quantum algorithms and perspectives

The three main classes of quantum algorithms are (1) those based on the quantum Fourier transform, (2) search algorithms, and (3) quantum simulations. All of these were invented in the mid-nineties. Since then, the range of applications of these algorithms has been extended and refined. However, virtually no fundamentally new algorithms for quantum computers have been discovered, despite intense effort all over the world.

It would be disappointing if no other applications were found than those currently known. Nevertheless, existing algorithms are already of significant practical interest. In particular, quantum simulations may address a broad range of physics problems which are otherwise intractable. For example, as transistors and other devices continue to shrink, simulation of their operation at the quantum level may be crucially important but impossible to do on classical computers.

The impact of quantum computing on the fundamentals of computer science may be just as profound and long-lasting, as it appears that the strong Church-Turing thesis must be revised. This thesis states that any two universal Turing machines (a general computational device [Tur36]) are polynomially equivalent; in other words, the Church-Turing thesis says that problems which can be efficiently computed on one Turing machine can always be efficiently computed on another Turing machine. However, quantum Turing machines, proposed by David Deutsch [Deu85], appear to be capable of efficiently solving problems which are intractable on classical Turing machines.

2.4 Quantum error correction

Quantum computers, like any machine, may have faulty or unreliable components. In order to nevertheless perform reliable computations, errors in the state of the qubits must be corrected.

Quantum error correction is similar to its classical analogue in many respects. Input states are encoded in a larger system which is more robust against noise or other error processes than unencoded states, in the sense that the original information can be retrieved with greater likelihood if the input states are encoded than if they are not.

For example, a simple classical code encodes 0 as 000 and encodes 1 as 111. If we send an uncoded bit of information through a noisy channel which flips a bit with probability p , then the probability of error per use of the channel is also p . However, if we send the same bit of information in encoded form (three physical bits), and take a majority vote between the three bits after the noise process, we can correctly guess the bit of information unless two of the physical bits are flipped, which happens with probability $3(1-p)p^2$, or all three physical bits are flipped, which occurs with probability p^3 . The resulting probability of error per bit of information is thus only $3p^2 - 2p^3$, which is smaller than p if $0 < p < 1/2$. Classically, encoding

can thus decrease the error probability at the expense of using extra bits and encoding/decoding operations.

We would like to use similar schemes to encode quantum information, in order to protect quantum computers and quantum communication channels against errors caused by decoherence. However, quantum error correction is much more tricky than classical error correction, because

1. it is not possible to build up redundancy by simply making copies of the quantum state, due to the no-cloning theorem [Die82, WZ82].
2. measurement of a quantum system destroys its state, so it is not possible to check the state of a qubit,
3. quantum errors can be arbitrary rotations in the Bloch sphere, while in classical computers only bit flips ($0 \leftrightarrow 1$) can occur.

The remarkable and surprising achievement of Shor [Sho95] and Steane [Ste96] was to show that it is nevertheless possible to reverse the truly random errors due to decoherence. The underlying principles are

1. to use entanglement in order to realize a quantum analogue of redundancy,
2. to measure errors without measuring the quantum state itself,
3. to digitize the errors (force an arbitrary error to collapse into either no error or a full bit flip, a phase flip or a bit-and-phase flip).

There are many excellent references on the theory of quantum error correction [EM96, KL96]. We here describe in detail a two-qubit error detection code, which nicely illustrates how the three guiding principles of quantum error correction are put into practice. Next, we give a brief overview of larger codes, capable of detecting and correcting more errors, and introduce the notion of fault-tolerancy.

2.4.1 The two-qubit phase error detection code

The two-qubit phase error detection code [CL95] encodes one qubit information in the joint state of two qubits. After decoding, it is possible to tell whether or not a phase error occurred on one of the qubits. If an error is detected, the state is rejected; otherwise it is kept.

The two-qubit phase error detection code encodes logical 0 and 1 as

$$|0_L\rangle = \frac{1}{\sqrt{2}}(|00\rangle + |11\rangle) \quad (2.94)$$

$$|1_L\rangle = \frac{1}{\sqrt{2}}(|01\rangle + |10\rangle), \quad (2.95)$$

where the subscript L denotes logical states. An arbitrary qubit state $a|0\rangle + b|1\rangle$ is encoded as

$$|\psi_3\rangle = a|0_L\rangle + b|1_L\rangle \quad (2.96)$$

$$= \frac{1}{\sqrt{2}} \left[a(|00\rangle + |11\rangle) + b(|01\rangle + |10\rangle) \right], \quad (2.97)$$

via the quantum circuit of Fig. 2.14. We thus build up *redundancy* by encoding the logical qubit in the state of two qubits using entanglement (principle 1).

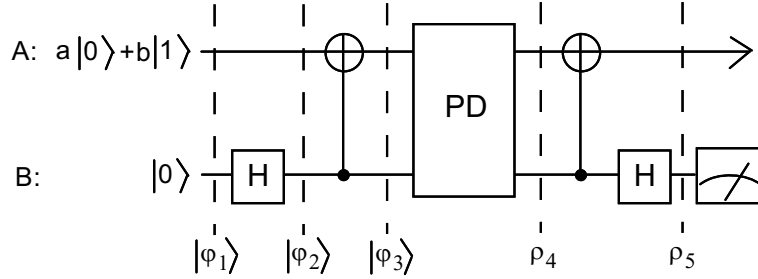


Figure 2.14: Encoding and decoding quantum circuit for the two-qubit code. In between encoding and decoding, phase damping may disturb the qubit states.

Now let us first consider an error process which causes a complete phase flip of one or more qubits, where we define a phase flip of qubit i as $\sigma_z^i \rho \sigma_z^i$. For a code to detect errors, it suffices that all errors to be detected map the codeword space \mathcal{C} (the space spanned by $|0_L\rangle$ and $|1_L\rangle$) onto its orthogonal complement. In this way, *detection of errors* can be done unambiguously by a projection onto \mathcal{C} *without distinguishing individual codewords*, hence without disturbing the encoded information (principle 2). This is precisely what the code of Eq. 2.95 achieves.

The four possible outcomes of the error process are

$$|\psi_{II}\rangle = I \otimes I |\psi\rangle = a \frac{|00\rangle + |11\rangle}{\sqrt{2}} + b \frac{|01\rangle + |10\rangle}{\sqrt{2}} \quad (2.98)$$

$$|\psi_{ZI}\rangle = \sigma_z \otimes I |\psi\rangle = a \frac{|00\rangle - |11\rangle}{\sqrt{2}} + b \frac{|01\rangle - |10\rangle}{\sqrt{2}} \quad (2.99)$$

$$|\psi_{IZ}\rangle = I \otimes \sigma_z |\psi\rangle = a \frac{|00\rangle - |11\rangle}{\sqrt{2}} + b \frac{-|01\rangle + |10\rangle}{\sqrt{2}} \quad (2.100)$$

$$|\psi_{ZZ}\rangle = \sigma_z \otimes \sigma_z |\psi\rangle = a \frac{|00\rangle + |11\rangle}{\sqrt{2}} + b \frac{-|01\rangle - |10\rangle}{\sqrt{2}}, \quad (2.101)$$

with the erroneous states $|\psi_{ZI}\rangle$ and $|\psi_{IZ}\rangle$ orthogonal to the correct state $|\psi_{II}\rangle$. After decoding, which is the inverse of the encoding operation (see Fig. 2.14):

$$|\psi_{II}\rangle \xrightarrow{dec} (a|0\rangle + b|1\rangle)|0\rangle \quad (2.102)$$

$$|\psi_{ZI}\rangle \Rightarrow (a|0\rangle - b|1\rangle)|1\rangle \quad (2.103)$$

$$|\psi_{IZ}\rangle \Rightarrow (a|0\rangle + b|1\rangle)|1\rangle \quad (2.104)$$

$$|\psi_{ZZ}\rangle \Rightarrow (a|0\rangle - b|1\rangle)|0\rangle. \quad (2.105)$$

We note that the ancilla (the auxiliary qubit) becomes $|1\rangle$ upon decoding if and only if a *single* phase error has occurred. Furthermore, the two qubits are in a product state after decoding, so it is possible to read out the syndrome (which indicates whether or not a phase error occurred) by a projective measurement on the ancilla without measuring the encoded state, which is held in the first qubit. If the final state of the ancilla is $|0\rangle$, we trust the state of the first qubit is properly preserved, and accept it. If the ancilla is in $|1\rangle$, we distrust the state of the first qubit and reject it.

Clearly, the error $\sigma_z \otimes \sigma_z$ cannot be detected, but this occurs only with probability p^2 , where we let p be the probability that the phase of a qubit is flipped in the error process. Furthermore, the code can detect phase errors but cannot reveal which qubit has the error, so it cannot correct errors. Moreover, $|\psi_{IZ}\rangle$ decodes to a correct state in the first qubit which is rejected. This affects the absolute fidelity (the overall probability of successful recovery) but not the conditional fidelity (the probability of successful recovery if the state is accepted). All of these properties are intrinsic limitations of using an error detection code as opposed to an error correction code. With only two physical qubits per qubit of information, an error detection code is the best we can do.

So far we have considered only complete phase flip errors, but in reality phase shifts over arbitrary angles may occur. Fortunately, we can *discretize* such *errors* (principle 3) as follows. Suppose the error is an arbitrary phase shift on the first qubit: $|0\rangle \rightarrow |0\rangle$, $|1\rangle \rightarrow e^{i\theta}|1\rangle$. Then, the encoded state becomes

$$\frac{1}{\sqrt{2}} \left[a(|00\rangle + e^{i\theta}|11\rangle) + b(e^{i\theta}|10\rangle + |01\rangle) \right] \quad (2.106)$$

$$= \frac{1}{\sqrt{2}} \frac{1+e^{i\theta}}{2} \left[a(|00\rangle + |11\rangle) + b(|10\rangle + |01\rangle) \right] \\ + \frac{1}{\sqrt{2}} \frac{1-e^{i\theta}}{2} \left[a(|00\rangle - |11\rangle) + b(-|10\rangle + |01\rangle) \right]. \quad (2.107)$$

The decoded state is now a superposition of the states given by Eqs.(2.102) and (2.103):

$$\frac{1}{\sqrt{2}} \frac{1+e^{i\theta}}{2} (a|0\rangle + b|1\rangle)|0\rangle + \frac{1}{\sqrt{2}} \frac{1-e^{i\theta}}{2} (a|0\rangle - b|1\rangle)|1\rangle. \quad (2.108)$$

Measurement of the second qubit projects it to either $|0\rangle$ or $|1\rangle$. *Because of entanglement*, the first qubit is projected accordingly to having no phase error, or a complete phase flip! An arbitrary phase shift of the second qubit is discretized in the same manner.

In section 5.4, we will present an NMR demonstration of the operation of the two-qubit

phase error detection code.

2.4.2 Error correction codes and fault-tolerancy

Codes with more than two physical qubits per logical qubit are capable not only of detecting errors but also of correcting errors. Historically, the first two quantum codes capable of correcting arbitrary single-qubit errors were a nine-qubit code [Ste96] and a seven-qubit code [Sho95]. A five-qubit code followed later [LMPZ96].

Using counting arguments based on the (quantum) Hamming bound, we can see that five is the minimum number of qubits that can be used to correct arbitrary errors. A code which encodes one logical qubit in k physical qubits has $k - 1$ ancillae which can represent up to 2^{k-1} orthogonal error syndromes. There are three types of errors which can occur on each of the physical qubits: a phase flip, a bit flip and a combined phase and bit flip (those can be expressed mathematically as σ_x , σ_z and σ_y errors respectively). It is also possible that no error occurs on any of the k qubits. Thus, assuming that the errors acting on different qubits are uncorrelated, we need $3k + 1$ orthogonal error syndromes, to be represented by the $2^k - 1$ ancillae. This way, we can simply measure the ancilla qubits upon decoding, infer precisely what error occurred and on which qubit it acted, and then correct the error. The requirement for the length k of the codewords is therefore that

$$2^{k-1} \geq 3k + 1. \quad (2.109)$$

If only one type of error is expected to occur, say phase errors, Eq. 2.109 can be relaxed to $2^{k-1} \geq k + 1$, and a three-qubit code is sufficient. Also, analogous to the case of classical codes, more efficient codes can be constructed by encoding several logical qubits per codeword.

Implicit in our discussion of quantum error correction so far is the assumption that the encoding and decoding operations are perfect, and that the qubits are simply sent through a noisy channel. In the context of quantum computation, such a channel would correspond to a quantum memory device. However, in realistic quantum computers, information must also be protected in the course of a computation, and furthermore encoding and decoding operations are themselves subject to errors. Would it still be helpful to apply quantum error correction under these circumstances?

The surprising answer is yes, provided the decoherence rate is below a certain level, the *accuracy threshold*, expressed as the probability of error per elementary logic operation on one or two qubits [ABO97, Kit97, KLZ98].

This notion is developed in the theory of *fault-tolerant* quantum computation [Got98]. Using concatenated quantum codes and quantum circuits which minimize error propagation between qubits, the net error rate can be made *arbitrarily small*, provided the “raw” error rate is below the accuracy threshold. Thus, a reliable quantum computer can be constructed from unreliable

components.

2.5 Summary

The combination of fundamental concepts in quantum physics, computer science and information theory have led to the rich field of quantum computation. Three main theoretical results of this field are that

1. the complexity of quantum systems grows exponentially with the number of elementary quantum systems involved,
2. certain problems which appear intractable on any classical computer are tractable on a quantum computer,
3. reliable quantum computers can be constructed from unreliable components, provided the error rate is below the accuracy threshold.

These results highlight the theoretical potential of quantum computation for fundamentally new systems and devices, capable of reliably solving problems beyond the reach of classical machines. From the presentation in this chapter, requirements for the implementation of quantum computers naturally emerge. This is the subject of the next chapter.

Chapter 3

Implementation of quantum computers

In the first half of this chapter, we ask ourselves what the fundamental requirements are for building a quantum computer. In the second half, we briefly review the state of the art in various proposed embodiments of quantum computers.

3.1 Requirements

Our understanding of the minimal requirements for quantum computation has grown considerably over the years. They are often formulated as the five criteria of David DiVincenzo [DiV00]. These are

1. a scalable physical system with well characterized qubits,
2. a universal set of quantum gates,
3. the ability to initialize the state of the qubits to a simple fiducial state, such as $|00 \dots 0\rangle$,
4. a qubit-specific measurement capability,
5. long relevant decoherence times, much longer than the gate operation time.

We shall now explore each of these criteria in detail, in order to develop a good understanding of their significance as well as their stringency.

3.1.1 Qubits

The heart of a quantum computer is a set of physical systems which represent the state of the quantum bits. Since a qubit is by definition a *two-level* quantum system, spin-1/2 particles and polarized photons are natural realizations of qubits. In practice, a qubit may also be represented by two levels of a large manifold of levels, for example two energy levels of an atom. Proposed

qubit embodiments range from trapped atoms and ions to nuclear and electron spins, electric charge, magnetic flux and photons (see section 3.2).

Size of the qubit register

The complexity of just a 40-qubit quantum computer far exceeds the complexity of most classical computers. That is, a classical computer would need vastly more time to simulate the dynamics of a 40 qubit computer than it would take the quantum computer itself to run, even if the clock speed of the classical computer is much greater than the clock speed of the quantum computer, because the quantum computer can explore 2^{40} computational paths in parallel.

However, in order to factor a 400 digit number (a task well beyond the capability of classical computers for the foreseeable future), a few thousand logical qubits are required.¹ With error correction, 10 to 100 times more qubits would be needed.

Fortunately, some other interesting applications require much more moderate numbers of qubits. For example, a quantum computer with 50 to 100 qubits (not counting a possible overhead for error correction) could compute the electronic orbitals of a small atom such as boron with greater accuracy than any classical simulation performed to date [AL99].

Alternatives to qubits

In principle, a three-level (or higher) quantum system could also serve as the basic unit of quantum information. However, this offers no computational advantage and all current proposals for the physical implementation of quantum computers are based on qubits.

Could we use one 2^n -level system instead of n two-level systems? Both have a 2^n dimensional Hilbert space and are mathematically perfectly equivalent. However, in a 2^n -level system, the levels must either extend over an exponentially large range of energies or must lie exponentially close together. Clearly, this is not a scalable approach to quantum computing.

Finally, could we use continuous variables, such as the position or momentum of a particle, to represent quantum information? Properties such as entanglement of continuous variables have been explored both theoretically and experimentally [BK98]. However, the precision of any physical device is limited by noise, and it thus appears always necessary for a realistic computer to discretize the continuous variables in order to perform computations [LB99].

3.1.2 Quantum gates

The time evolution of a closed quantum system is determined by its Hamiltonian (section 2.1.2). In order to realize quantum logic gates, we must therefore be able to control the Hamiltonian

¹The second register in the order-finding algorithm must be large enough to represent the integer to be factored, which would be $\log_2 10^{400} = 400 \log_2 10 \approx 1329$ bits, and the first register must be at least twice as large as the second register. In practice, additional scratchpad qubits may be desired.

over time such that the resulting time evolutions correspond to the computational steps of an algorithm [Ben80]. A tremendously helpful theoretical result is that there exist small sets of unitary transformations which are universal for quantum computation (section 2.2.2). We shall here single out one particular universal set of gates, the combination of arbitrary single-qubit rotations with the CNOT gate, which has also been the set of choice in the literature. The starting point for our discussion of quantum gates is that we require

the ability to manipulate the Hamiltonian accurately, quickly and selectively such that we can perform a universal set of one- and two-qubit gates on individual qubits or pairs of qubits.

Coupling network

We must be able to perform two-qubit gates between any two qubits in a quantum computer. However, a computer with pairwise couplings between all the qubits (Fig. 3.1 a) is nearly impossible to build, as interactions between physical particles tend to rapidly decrease with the separation between the particles. For example, nuclear spins in a molecule are well coupled if they are united in a chemical bond, but the couplings are weaker or sometimes zero for two- and three-bond couplings.

A common architecture in proposed quantum computer realizations uses *exclusively* nearest-neighbour couplings between qubits placed in a linear or two-dimensional array (Fig. 3.1 b). This is the case for many solid-state proposals, such as inductively coupled SQUID loops, quantum dots connected by tunneling barriers and nuclear spins of donor atoms, coupled via the overlap between the respective electron clouds.

Fortunately, we can effect two-qubit gates between any pair of qubits even if they aren't all directly coupled to each other, as long as there exists a path of couplings that indirectly connects any two qubits. For example, in order to perform a CNOT_{13} gate with the coupling network of Fig. 3.1 (b), we can first swap the state of qubits 1 and 2 (this can be done via the sequence $\text{CNOT}_{12} \text{CNOT}_{21} \text{CNOT}_{12}$), then perform a CNOT_{23} , and finally swap qubits 1 and 2 again. The net effect is a CNOT_{13} .

Even if none of the qubits are directly coupled to each other, it is still possible to perform universal computation provided an external (but still quantum mechanical) degree of freedom can be selectively coupled to any one qubit in a controlled manner (Fig. 3.1 c). The external degree of freedom serves as a *bus* and can facilitate two-qubit gates between any pair of qubits in much the same way intermediary qubits can facilitate two-qubit gates between any two qubits in Fig. 3.1.

Examples of such bus degrees of freedom are the collective motional state of an array of trapped ions, a photon inside an optical cavity which holds several trapped atoms or a photon which couples to several quantum dots embedded in a semiconductor structure. Typically, the

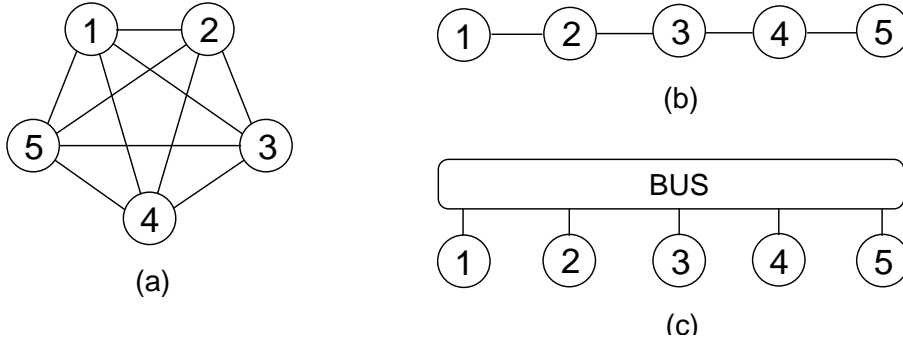


Figure 3.1: Three extreme coupling networks between five qubits. (a) A full coupling network. (b) A nearest-neighbour coupling network. (c) Coupling via a bus.

spatial range over which collective degrees of freedom can extend while maintaining the ability to significantly couple to the qubits, is also limited. Therefore, such architectures may have to be supplemented by additional means for interactions between different groups of qubits.

Time-dependent control over the Hamiltonian

It is not always necessary that we can turn on and off all the terms in the Hamiltonian at will, as long as we can reverse undesired time evolutions at a later stage. This is commonly done for example in NMR, by so-called refocusing techniques (similar to spin-echoes), where the $\omega\sigma_z$ term in the Hamiltonian cannot be switched off but it is possible to perform a $R_x(180)$ or NOT gate. By applying the NOT gate halfway a time interval t and again at the end, the $\omega\sigma_z$ evolution which took place in the first time interval is unwound in the second interval, so there is no net evolution (up to an overall and thus irrelevant phase shift). We can verify this mathematically using Eqs. 2.41, 2.42, 2.45 and 2.47:

$$R_x(180)e^{-i\omega\sigma_z t/2}R_x(180)e^{-i\omega\sigma_z t/2} = (-i\sigma_x) [\cos(\omega t/4)\sigma_I - i \sin(\omega t/4)\sigma_z] (-i\sigma_x) [\cos(\omega t/4)\sigma_I - i \sin(\omega t/4)\sigma_z] = -\sigma_I \quad (3.1)$$

for any t . The same refocusing technique can be used to time-reverse evolution under the Hamiltonian $\sigma_z^i\sigma_z^j$, as also

$$\sigma_x^i \exp(-it\sigma_z^i\sigma_z^j/2) \sigma_x^i \exp(-it\sigma_z^i\sigma_z^j/2) = -\sigma_I^i\sigma_I^j, \quad (3.2)$$

for any t . This is pictorially illustrated for the case of NMR in Fig. 4.11. Of course, it isn't always so easy to reverse undesired evolutions, as we will see for example in section 4.2, but nevertheless the use of unitary operations to time-reverse specific undesired evolutions can tremendously reduce the fabrication requirements for quantum computers.

Selective addressability

We have started from the assumption that we must be able to *selectively* perform one- and two-qubit logic gates on arbitrary qubits. However, we can circumvent the need for selective control of single- and two-particle Hamiltonians by storing each logical qubit in the state of three physical qubits.

Seth Lloyd showed that universal quantum computation is possible using a *cellular automata*² architecture of the form

$$D - ABC - ABC - \dots - ABC$$

where the different physical qubits A cannot be distinguished from each other nor selectively addressed, and likewise for the B 's and C 's [Llo93]. Each unit cell ABC is used to represent one qubit. In the default situation, the qubits of information are stored in the physical qubits B , and the A 's and C 's are set to 0, except in one unit cell i , where A is set to 1.

A single-qubit operation U on qubit i and qubit i only is obtained via a controlled- U operation of A on B when A_i is set to 1 while the A_j ($j \neq i$) are set to 0. By applying CNOT gates on the whole array, we can move up or down the index of the unique A which is marked as 1. A controlled- U operation of qubit i onto qubit $i - 1$ can be realized using CNOTs and a doubly-controlled U gate for which A_i (set to 1) acts as one of the control qubits. The special site D is needed to load the initial state. The same site D can be used to read out the answer to the computation one bit at a time.

This model is reasonably well approximated by nuclear spins in long polymers. It may also ease the fabrication requirements for many solid-state proposals, including electron spins in quantum dots, nuclear spins in donor atoms, or nuclear spins in a crystal.

Universality without single-qubit terms in the Hamiltonian

Single-qubit operations are not strictly necessary for universal quantum computation; in fact, it has been shown that “almost any” two-qubit gate is universal [DBE95, Llo95a]. Unfortunately, virtually none of these universal two-qubit gates can be generated by naturally occurring two-particle Hamiltonians. The underlying reason is that most interaction Hamiltonians provided by nature exhibit too much symmetry in the two qubits. The exchange Hamiltonian,

$$\mathcal{H} = \vec{\sigma}^1 \cdot \vec{\sigma}^2 = \sigma_x^1 \sigma_x^2 + \sigma_y^1 \sigma_y^2 + \sigma_z^1 \sigma_z^2, \quad (3.3)$$

²Computer scientists actually use this term to describe an even more stringent computational model, where *the same operation* is applied over and over on all the bits in the computer. Surprisingly, even such a stringent model can be used to perform meaningful (classical) computations.

which describes the interaction between electron spins in quantum dots coupled through a tunneling barrier (and related proposals), is an example of such a symmetrical two-qubit Hamiltonian.

However, by encoding each logical qubit in the state of three physical qubits, universal quantum computation is nevertheless possible [DBLW00]. The physical qubits must be placed in a linear array and it must be possible to selectively switch on and off the interactions between neighbouring physical qubits (by tweaking the tunneling barrier in the example). State initialization to an encoded basis state is accomplished by cooling the system down to its ground state in the presence of select couplings.

Encoding each logical qubit in the state of two physical qubits is also possible but only if the two physical qubits have a different effective magnetic moment [Lev01]. The two encoded basis states are $|01\rangle$ and $|10\rangle$; they are clearly susceptible to the exchange interaction. An additional advantage is that fewer operations are needed.

Universality without two-qubit terms in the Hamiltonian

Quantum computation appears to inherently require non-linear interactions, i.e. two-qubit terms in the Hamiltonian, in order to realize two-qubit gates. However, universal quantum computation is possible with only linear (i.e. single-qubit) quantum gate elements, supplemented by measurements and classical feedback, which provide the needed non-linearity [KLM01] and allow one to create entangled qubits via a probabilistic scenario. Using the entanglement thus created, two-qubit gates are accomplished by a clever combination of teleportation and single-qubit gates [GC99].

This proposal has been developed in the context of optical realizations of quantum computers, where it is difficult to obtain appreciable non-linear interactions between quantum bits (photons) without too much absorption. Potentially, the scheme may be translated into other physical systems.

Accuracy and speed

An obvious requirement is that the quantum gates be executed with high fidelity, i.e. that the resulting unitary transformation be as close as possible to the desired unitary evolution. If that is not possible, we must have sufficient information over the actual evolution and sufficient control over the Hamiltonian such that we can undo erroneous evolutions at a later point in time.

Erroneous unitary evolutions that cannot be unwound, have the same detrimental effect on the computation as random errors due to decoherence and thus effectively increase the decoherence rate. While they can still be corrected using quantum error correction, this is associated with a large overhead. Furthermore, quantum error correction is only effective if the total error rate (due to decoherence and erroneous unitary evolutions combined) is below the accuracy

threshold, introduced in section 2.4.2.

In order to achieve the accuracy threshold, the duration of a typical logic operation τ_{op} must be short compared to the coherence time τ_c . Obviously, the speed and accuracy of logic gates do usually not go hand in hand, so it is key to make an optimal trade-off.

Finally, whereas the clock speed is irrelevant from a complexity theory point of view — only the scaling of the number of operations with the problem size is relevant —, a quantum computer with a clock speed of 20 Hz (a realistic number for solution NMR for example) may appear to be of little practical use. However, let us say that factoring a 400 digit number would take two hundred thousand quantum operations, which is a reasonable estimate, and further that quantum error correction would increase this number by a factor of one hundred. The resulting twenty million operations would take a “lousy” 20 Hz quantum processor one million seconds, which is not even 12 days, still quite fast given that the same problem would classically take even the fastest supercomputer longer than the age of the universe to solve.

3.1.3 Initialization

A fundamental condition for computation which is often taken for granted is the ability to reliably prepare a known input state. If the input state of a computation is random, the output is of little use³. Thus, we demand

the ability to reliably prepare a pure input state.

We recall from section 2.1.1, page 12 that the term “pure” implies that the state is known. If all we know about a qubit is that it is in one of several states $|\psi_i\rangle$, with certain probabilities, then the qubit is said to be in a *statistical mixture* of states, as opposed to a pure state.

Unlike for the case of classical computers where it is usually easy to reset or initialize bits, state initialization can be very difficult in quantum computers, depending on the physical realization of the qubits. In qubit implementations where the $|0\rangle$ and $|1\rangle$ states have distinct energies, we can prepare the qubits in their ground state by letting them equilibrate at a low enough temperature T such that the energy difference ΔE between the ground and excited states satisfies the condition

$$\Delta E \gg k_B T, \quad (3.4)$$

where k_B is Boltzmann’s constant. Otherwise, the thermally equilibrated qubits are in a statistical mixture of states, described by the density matrix $\rho_{eq} = \exp(-\mathcal{H}/k_B T)/\mathcal{Z}$, where \mathcal{Z} is a normalization factor. At room temperature, $k_B T \approx 26$ meV, which is much larger than realistic

³Classically, the output for a random input value may sometimes be of interest, for example if the task is to determine whether a certain output value occurs at all. However, since quantum computations are reversible, the output is always a permutation of the input, and therefore the output for a random input holds no information at all.

values of ΔE for many quantum systems. Therefore, many proposed realizations of quantum computers require cryogenic temperatures, often in the 10 or 100 mK range.

We note that the ability to perform a hard measurement (introduced on page 19 and further discussed in section 3.1.4), automatically leads to the ability to prepare a pure input state: it suffices to measure the qubit's state, and change it if needed.

Unfortunately, in many proposed realizations of quantum computers, it is impossible or very difficult to set up the qubits in a pure initial state. However, might it not be possible to access the computational power of quantum systems as long as the state of the qubits is not completely random ($\rho \neq I/2^n$) ?

Effective pure states

Remarkably, it is indeed possible to perform arbitrary quantum computations on a mixed state, provided the mixed state is *effective pure*, or *pseudo-pure* and the observables are traceless [GC97, CPH98] (see section 3.1.4). Effective pure states are mixed states described by a density matrix of the form

$$\rho_{\text{eff}} = \frac{1 - \alpha}{2^n} I + \alpha |\psi\rangle\langle\psi|. \quad (3.5)$$

For traceless observables, the identity component I does not produce any signal at all. Furthermore, I doesn't evolve under unitary transformations, as $UIU^\dagger = I$ for all unitary operations U . A system in an effective pure state ρ_{eff} thus has the same dynamical behavior and produces the same signal (up to a proportionality factor α) as a system in the corresponding pure state $|\psi\rangle$.

It is crucial that α not decrease exponentially with the number of qubits n , as α is directly proportional to the signal strength. If it did, the precision of the measurement would have to increase exponentially with n or the signal would have to be averaged over exponentially many experiments. Such an exponential cost would obviously offset the exponential benefit of quantum computers.

Several methods are known for the preparation of effective pure states starting from a state in thermal equilibrium at high temperatures, all of which have been developed in the context of liquid state NMR quantum computation. Unfortunately, all these methods have in common that $\alpha \propto n/2^n$. Then, is such an exponential overhead inevitably associated with the use of high temperature qubits?

Cooling down a subset of hot qubits

The truly surprising answer is no: there exists a *scalable* algorithm for obtaining k pure qubits starting from n partly mixed qubits. This algorithm, invented by Schulman and Vazirani [SV99],

has only a linear overhead in the number of qubits ($k \propto n$) and a quasi-linear, $\mathcal{O}(k \log k)$, overhead in the number of operations. A related algorithm was devised earlier by Cleve and DiVincenzo in the context of Schumacher compression; this algorithm requires $\mathcal{O}(k^3)$ operations and $\mathcal{O}(\sqrt{k})$ zero entropy auxiliary qubits (which are recovered at the end of the procedure). The Schulman-Vazirani algorithm, in contrast, is capable of bootstrapping in the sense that it can create bits with (near) zero entropy starting from only high entropy bits.

The idea behind the Schulman-Vazirani scheme is to redistribute the entropy over the qubits, such that the entropy of a subset of the qubits approaches zero while the entropy of the remaining qubits increases (the total entropy is preserved). In order to calculate the maximum possible k as a function of n , let us define the *polarization* ϵ of a qubit as the difference in probabilities between the ground and excited state, tracing out any other qubits. Mathematically, the polarization of qubit i is defined as

$$\epsilon = \text{Tr}(\rho\sigma_z^i). \quad (3.6)$$

A qubit is thus in $|0\rangle$ with probability $\frac{1+\epsilon}{2}$ and in $|1\rangle$ with probability $\frac{1-\epsilon}{2}$. The theoretical maximum k_{max} of zero temperature ($\epsilon = 1$) bits that can be extracted from n bits with initial polarization ϵ_0 is given by entropy conservation,

$$nH\left(\frac{1+\epsilon_0}{2}\right) = kH(1) + (n-k)H(1/2), \quad (3.7)$$

where the entropy H is given by

$$H(p) = -p \log_2 p - (1-p) \log_2(1-p), \quad (3.8)$$

so $H(1) = H(0) = 0$ and $H(1/2) = 1$. From Eq. 3.7, we find

$$k_{max} = \left[1 - H\left(\frac{1+\epsilon_0}{2}\right) \right] n, \quad (3.9)$$

which for small ϵ_0 is well approximated by

$$k_{max} \approx \epsilon_0^2 n. \quad (3.10)$$

Schulman and Vazirani showed that their scheme is not only efficient (the overhead is only polynomial in n) but is also optimal, in that it achieves the entropic bound in the limit of large n .

We will present an NMR implementation of the elementary building block of the Schulman-Vazirani scheme in section 5.8, and describe the operation of this building block when we discuss state initialization in NMR quantum computation (section 4.4.6).

3.1.4 Read-out

A computation can only be useful if we can access the final result. In a quantum computer, the final result is represented by the final state of one or more qubits. We recall (section 2.1.3, page 17) that it is not possible to obtain full information about unknown qubit states, but also (section 2.3) that projective measurements in the $\{|0\rangle, |1\rangle\}$ basis are sufficient if we use quantum algorithms. Furthermore, a different measurement basis is fine too, since we can always change basis via a unitary transformation just before the measurement. In summary, we need

the ability to perform accurate projective measurements of the qubit states.

Strong and weak measurements

Read-out of the state of a quantum system requires some form of coupling of the quantum system to a classical measuring device, such that at the end of the measurement process, the meter indicates the state of the quantum system, projected onto the measurement basis. For example, measurement of the state of a qubit represented by two energy levels ($|0\rangle$ and $|1\rangle$) in an atom can be done by pumping the $|1\rangle$ state and looking for fluorescence. If the qubit was in $|1\rangle$, the atom will fluoresce, a stream of electrons will flow in a nearby photomultiplier tube, and a signal will appear on the display of an electrometer. If the atom was in $|0\rangle$, the electrometer will show no signal. If the qubit state was $a|0\rangle + b|1\rangle$, the measurement process will collapse the state into $|0\rangle$ or $|1\rangle$ and the observer will either see a signal or see no signal, with probabilities $|a|^2$ and $|b|^2$.

Clearly, if the coupling with the measuring apparatus is so strong that the qubit states instantaneously collapse — a scenario known as a *hard* or *strong* measurement — we must be able to switch off the measuring device during the computation. However, it is also possible to never switch off the measurement provided the quantum system is only weakly coupled to the meter. In this scenario, called a *weak* measurement, information only very slowly leaks out of the quantum system. On the one hand, the qubits therefore decohere only very gradually, as opposed to instantaneously⁴, but on the other hand, a weak measurement implies that we cannot learn much about the state of the qubit.

Weak measurements therefore require the use of signal averaging, either over a large ensemble of identical computers or over time-sequential experiments performed on a single computer. Signal averaging may also be needed to boost the reliability of the measurement if the detector efficiency and/or accuracy is limited.

⁴Weak and strong measurements are understood as taking place on a timescale much slower or faster than the duration of the computation.

Averaged measurements

Averaging the result of quantum computations poses a specific difficulty. For example, we recall that in the order-finding algorithm (section 2.3.3), the measurement will with high probability return an integer multiple of N/r , but we don't know *which* multiple. From any multiple lN/r , we can determine r with high probability of success via a classical computation called the continued fraction expansion. A time averaged measurement, however, gives $\approx \sum_{l=0}^r lN/r = \langle l \rangle N/r$, and an ensemble averaged measurement gives $\langle l_n \rangle \dots \langle l_1 \rangle N/r$ (where the $\langle l_i \rangle$ are the bitwise averages of l). Either way, it is not possible to compute r from the averaged measurement outcome except in a few special cases.

This problem can be circumvented by calculating the continued fraction expansion on the quantum computer without first measuring the output state of the order-finding quantum algorithm [GC97]. Since the output of the continued fraction expansion is deterministic (it is r), a time or ensemble averaged measurement of the qubits after the continued fraction expansion will always give r as well. For all the known quantum algorithms with probabilistic outputs, we can use similar *derandomization* procedures which permit the use of averaged measurements.

Other remarks

- Do we have to be able to read out each individual physical qubits (the implicit assumption so far)? The answer is no. It is sufficient to be able to measure the state of just one physical qubit: at the end of the computation, we can swap one after the other logical qubit into that physical qubit and measure it. Note that it would not be good to measure one qubit, then repeat the computation and measure the next qubit, and so forth (unless the output is derandomized [GC97]). Again taking order-finding as an example, we see that at the end of each experiment, the one bit may come from to a different multiple of N/r every time.
- Do we need to be able to measure qubits during the computation? Again, the answer is no. If no subsequent operations depend on the measurement outcome, such measurements can be left out altogether. If subsequent operations on the remaining qubits do depend on the measurement outcome, we can use controlled quantum gates instead.
- Does it matter if a measurement destroys the physical qubit that was measured? Here also, the answer is no. In fact, after we measure a qubit, we can do almost anything we want to it, including throw it away, because this will not affect the state of the remaining qubits. However, interactions between the measured qubits and the remaining qubits must be avoided or neutralized, because such interactions would alter the state of the remaining qubits.

3.1.5 Coherence

The final requirement is that the qubits have a sufficiently long coherence time τ_c such that quantum mechanical superposition states can be preserved throughout the execution of a quantum algorithm (section 2.1.5). Or alternatively, and more realistically given the large number of qubits and operations involved in realistic computations,

*the decoherence rate must lie below the threshold error rate for fault-tolerant quantum computation*⁵:

$$\tau_{op}/\tau_c < 10^{-4}, \quad (3.11)$$

where τ_{op} is the typical duration of a quantum gate. Obviously, this is only a crude measure, as τ_{op} covers a wide range of logic gates and τ_c lumps together a broad range of errors due to a variety of decoherence processes and systematic errors which somehow cannot be reversed.

Mathematically, the effect of decoherence can be conveniently described in the *operator sum representation*

$$\rho \mapsto \sum_k E_k \rho E_k^\dagger. \quad (3.12)$$

where the E_k are operators acting on the Hilbert space of the system. The interpretation of this expression is that ρ is transformed to

$$\frac{E_k \rho E_k^\dagger}{\text{Tr}(E_k \rho E_k^\dagger)} \quad (3.13)$$

with probability

$$p(k) = \text{Tr}(E_k \rho E_k^\dagger). \quad (3.14)$$

For trace-preserving processes, the operators E_k must satisfy the completeness relation

$$\sum_k E_k^\dagger E_k = I. \quad (3.15)$$

The operator sum representation encompasses all physical processes which can act on a quantum system, including non-unitary processes. We point out that any given physical process has many possible operator sum representations, and can thus also be interpreted in different ways. We also note that for unitary processes, there is only one term in Eq. 3.12, $E_0 = U$.

The general rule for obtaining long coherence times is that the qubits be highly isolated from the environment, because interactions with the environment and information leakage to

⁵The estimated values for the accuracy threshold depend on the error model and on the architecture of the quantum computer (e.g. whether or not there are only nearest-neighbour interactions between the qubits and whether or not parallel operations are allowed). Most estimates lie in the range of 10^{-6} to 10^{-4} .

the environment are the cause of decoherence [Zur82, Zur91]. We will now review several ways in which decoherence can manifest itself.

Energy dissipation

Energy dissipation is a decoherence process caused by the exchange of energy between a quantum system and the environment (the bath). Physical examples of this process are spontaneous emission in atoms or semiconductor structures, nuclear or electron spins which return to the thermal equilibrium with the environment, heating of the motional state of trapped ions, and so forth.

Energy dissipation to a bath at *zero temperature* is described by

$$\rho \mapsto E_0 \rho E_0^\dagger + E_1 \rho E_1^\dagger, \quad (3.16)$$

where

$$E_0 = \begin{bmatrix} 1 & 0 \\ 0 & \sqrt{1-\gamma} \end{bmatrix}, \quad E_1 = \begin{bmatrix} 0 & \sqrt{\gamma} \\ 0 & 0 \end{bmatrix}. \quad (3.17)$$

The E_0 operation preserves a qubit in the ground state $|0\rangle$ but attenuates the excited state $|1\rangle$; the E_1 operation changes the $|1\rangle$ state into the $|0\rangle$ state with probability γ . The overall result of this process, known as *amplitude damping*, is that a qubit in the excited state decays into the ground state with probability γ , thereby losing a quantum of energy to the environment. As a result, an arbitrary one-qubit density matrix is transformed as

$$\begin{bmatrix} a & b^* \\ b & c \end{bmatrix} \mapsto \begin{bmatrix} 1 - (1-\gamma)(1-a) & b^* \sqrt{1-\gamma} \\ b \sqrt{1-\gamma} & c(1-\gamma) \end{bmatrix}. \quad (3.18)$$

If the environment is at *finite temperature*, the process of Eq. 3.16 must be generalized to

$$\rho \mapsto \sum_{k=0}^3 E_k \rho E_k^\dagger, \quad (3.19)$$

where

$$\begin{aligned} E_0 &= \sqrt{p} \begin{bmatrix} 1 & 0 \\ 0 & \sqrt{1-\gamma} \end{bmatrix}, & E_1 &= \sqrt{p} \begin{bmatrix} 0 & \sqrt{\gamma} \\ 0 & 0 \end{bmatrix}, \\ E_2 &= \sqrt{1-p} \begin{bmatrix} \sqrt{1-\gamma} & 0 \\ 0 & 1 \end{bmatrix}, & E_3 &= \sqrt{1-p} \begin{bmatrix} 0 & 0 \\ \sqrt{\gamma} & 0 \end{bmatrix}. \end{aligned} \quad (3.20)$$

Thus, a qubit in the excited state decays to the ground state with probability γp , and a qubit in the ground state is lifted to the excited state with probability $\gamma(1-p)$. The parameter p depends on the temperature of the environment and the energy difference between $|0\rangle$ and $|1\rangle$.

The stationary state of this process, called *generalized amplitude damping*, is the mixed state

$$\rho_\infty = \begin{bmatrix} p & 0 \\ 0 & 1-p \end{bmatrix}. \quad (3.21)$$

We can geometrically visualize the effect of generalized amplitude damping via the transformation of an arbitrary vector on the surface of the Bloch sphere

$$(r_x, r_y, r_z) \mapsto (r_x\sqrt{1-\gamma}, r_y\sqrt{1-\gamma}, r_z(1-\gamma) + \gamma(2p-1)). \quad (3.22)$$

In many physical systems, γ is a time-varying function of the form $\gamma = 1 - e^{-t/T_1}$, where T_1 is a characteristic time constant, which was first introduced in NMR [Blo46]. It corresponds to the *lifetime* of excited states. In real physical systems, non-unitary exchange of energy can also take place between different qubits in the system. This random process also represents a form of decoherence, just like energy exchange between qubits and the bath.

Finally, we point out that in most proposed quantum bit implementations, energy dissipation on the one hand adversely affects quantum computations, but on the other hand also represents a natural mechanism for state initialization. After waiting for a sufficiently long time (several times the T_1), the qubits approach thermal equilibrium with the environment. The thermal equilibrium state thus constitutes a reproducible and fiducial initial state. If the environment is close enough to zero Kelvin such that $\Delta E \gg k_B T$, the thermal equilibrium state is very close to being pure. For qubits in equilibrium with a high temperature bath, additional state preparation operations must be performed in order to distill pure qubits (section 3.1.3).

Phase randomization

Phase randomization results in the loss of coherence (the phase relationship) between different basis states, and can be caused by interactions with the environment. For example, local fluctuations in the magnetic field randomize the phase of nuclear or electron spins; and scattering with defects randomly disturbs the phase of free electrons in solids. In many systems, phase randomization is the dominant decoherence process and the coherence time τ_c is therefore often loosely taken to be the characteristic phase randomization time.

A phase shift over some random angle θ changes an arbitrary pure one-qubit state $|\psi\rangle = a|0\rangle + b|1\rangle$ into $R_z(\theta)|\psi\rangle = ae^{-i\theta/2}|0\rangle + be^{i\theta/2}|1\rangle$ (see Eq. 2.47). The density matrix changes accordingly:

$$\rho = |\psi\rangle\langle\psi| = \begin{bmatrix} |a|^2 & ab^* \\ a^*b & |b|^2 \end{bmatrix} \mapsto R_z(\theta)\rho R_z(\theta)^\dagger = \begin{bmatrix} |a|^2 & ab^*e^{-i\theta} \\ a^*be^{i\theta} & |b|^2 \end{bmatrix}. \quad (3.23)$$

If we model phase randomization as a stochastic process with θ drawn from a normal distribution with variance 2λ , the density matrix resulting from averaging over θ is

$$\langle \rho' \rangle_\theta = \int \frac{1}{\sqrt{4\pi\lambda}} e^{-\theta^2/4\lambda} R_z(\theta) \rho R_z(\theta)^\dagger d\theta = \begin{bmatrix} |a|^2 & ab^* e^{-\lambda} \\ a^* b e^{-\lambda} & |b|^2 \end{bmatrix}. \quad (3.24)$$

A mixed initial density matrix is transformed similarly:

$$\begin{bmatrix} a & b^* \\ b & c \end{bmatrix} \mapsto \begin{bmatrix} a & e^{-\lambda} b^* \\ e^{-\lambda} b & c \end{bmatrix}, \quad (3.25)$$

since it is a weighted average of the constituent pure states.

The off-diagonal elements of the density matrix thus decay exponentially over time, and phase randomization is therefore also called *phase damping*. Since the diagonal elements, which represent the populations of the basis states, remain unaffected, phase randomization signifies the *loss of coherence without net change of energy*.

The operator sum representation of the phase damping process is given by the operators

$$E_0 = \sqrt{\gamma} \begin{bmatrix} 1 & 0 \\ 0 & 1 \end{bmatrix}, \quad E_1 = \sqrt{1-\gamma} \begin{bmatrix} 1 & 0 \\ 0 & -1 \end{bmatrix}, \quad (3.26)$$

so phase randomization is equivalent to a phase flip which occurs with probability $1 - \gamma$, where $\gamma = (1 + e^{-\lambda})/2$.

We can geometrically visualize the effect of phase randomization via the transformation of an arbitrary vector on the surface of the Bloch sphere. Using Eq. 3.25, we find that

$$(r_x, r_y, r_z) \mapsto (r_x e^{-\lambda}, r_y e^{-\lambda}, r_z). \quad (3.27)$$

In many physical systems, λ increases linearly over time, $\lambda = t/T_2$. Like T_1 , the characteristic time constant T_2 originated in NMR [Blo46]. Intrinsic phase randomization T_2 must be distinguished from systematic dephasing T_2^{sys} where the information about the erroneous evolution is known, as opposed to lost in the environment. Systematic dephasing can in principle be reversed without quantum error correction, e.g. spin-echo techniques can reverse dephasing of spins in an inhomogeneous magnetic field. The decay rate of the off-diagonal elements due to the combined effects of systematic and random loss of phase coherence is often described via the time constant T_2^* , given by

$$\frac{1}{T_2^*} = \frac{1}{T_2} + \frac{1}{T_2^{sys}}. \quad (3.28)$$

A clean measurement of the phase damping time constant is complicated by the fact that amplitude damping also results in loss of coherence and the decay of off-diagonal entries in

the density matrix. The measured “ T_2 ” therefore usually includes contributions from amplitude damping (those contributions are negligible only if $T_1 \gg T_2$), in addition to phase damping. On the other hand, phase damping does not affect the diagonal entries of the density matrix; those entries relax solely due to amplitude damping. Therefore, a clean measurement of T_1 can be done by measuring the decay rate of the diagonal entries of the density matrix.

For multiple qubits, the effect of phase randomization is often more pronounced the more qubits are entangled with each other, and the stronger the degree of entanglement. For example, random phase kicks acting on qubit i will change the maximally entangled state of n qubits $|\psi_n\rangle = (|00\dots 0\rangle + |11\dots 1\rangle)/\sqrt{2}$ into $(e^{-\theta/2}|00\dots 0\rangle + e^{\theta/2}|11\dots 1\rangle)/\sqrt{2}$. If random phase kicks occur on all qubits, $|\psi_n\rangle$ becomes $(e^{-n\theta/2}|00\dots 0\rangle + e^{n\theta/2}|11\dots 1\rangle)/\sqrt{2}$. Therefore the decoherence rate of an n -qubit maximally entangled state is n times higher than for a 1-qubit system.⁶

Qubit disappearance

In some realizations of qubits, the physical qubit itself is very fragile (not just the qubit state). For example, an atom may easily escape from an optical trap, a photon may leak out of an optical cavity, or may be absorbed when it is sent through a non-linear medium, and so forth. The qubit itself may thus disappear or be annihilated altogether. The resulting error is called an erasure error.

Quantum error correction can deal with erasure errors if it is possible to detect the absence or presence of a qubit and to replace a missing qubit with a qubit in some standard state. This state is generally different than the state of the original qubit, but it can be corrected using standard quantum error correction. In fact, the overhead can be smaller than usual because the error occurred in a known location.

We note that it is not a problem if qubits are destroyed in the measurement process, provided a fresh supply of qubits is readily available. Traditional single photon detectors are an example of such destructive meters. Non-demolition photon detection is in principle also possible and has been demonstrated in the lab, but remains very hard.

Leakage outside the qubit manifold

A related problem arises if a qubit is embodied by two levels which are part of a larger manifold of levels. If the quantum system transitions outside the qubit manifold, the computation will obviously go awry.

This can occur in trapped ions and atoms, electronic states in quantum dots, magnetic flux states in SQUIDS, and so forth. In contrast, the Hilbert space of spin-1/2 particles and polarized

⁶This is obviously a crucially important consideration for quantum error correction, which relies precisely on entanglement to combat decoherence.

photons is naturally confined to two dimensions, so here it is impossible for the qubit to leak into extraneous levels.

The extra degrees of freedom can also represent an advantage. For example, it is common to temporarily take the state of an atom or ion out of the qubit subspace, in order to facilitate quantum logic operations. This may be needed because of selection rules, or it may simply be technologically easier to perform the desired logic operations in this way. Extra levels also lie at the basis of selective measurement schemes, such as fluorescence measurements in trapped ions.

3.2 State of the art

This section gives only a quick survey of some of the possibilities and challenges that characterize various proposed quantum computer implementations. A recent collection of articles [BL00] reviews the operation, feasibility and state of the art of these schemes in much more detail. Many important original papers are collected in [MPZ00].

3.2.1 Trapped ions

Concept

Cirac and Zoller [CZ95] showed in a seminal paper that a set of cold ions interacting with laser light and moving in a linear trap provides a realistic physical system in which to implement a quantum computer. Two internal states of the ion serve as the $|0\rangle$ and $|1\rangle$ levels; they may be electronic levels, hyperfine levels or Zeeman levels, depending on the ion (e.g. $^9\text{Be}^+$, $^{25}\text{Mg}^+$, $^{40}\text{Ca}^+$ or $^{138}\text{Ba}^+$), and all of these internal states can have coherence times of several seconds.

A register of n quantum bits is obtained by loading n ions into an RF trap. Usually the trapping potential is such that the ions are held in a linear array (Fig. 3.2), spaced apart by several micrometers due to the ion-ion Coulomb repulsion. The ions are cooled down to their motional ground state, usually in two stages, first by Doppler cooling and then by sideband cooling. For weak traps, cooling via electromagnetically induced transparency techniques can be used instead of sideband cooling.

Single qubit operations are accomplished using laser pulses focused tightly on the desired ion. Either the pulses are resonant with the $|0\rangle \leftrightarrow |1\rangle$ transition, or alternatively Raman transitions are used, depending on the selection rules, energy differences and available lasers.

Two qubit operations are accomplished by using the collective quantized motion of the ions as a bus. First a laser is turned on, acting on the k th ion, and detuned by an amount equal to the energy of one center-of-mass phonon. The interaction Hamiltonian is then a Jaynes-Cummings

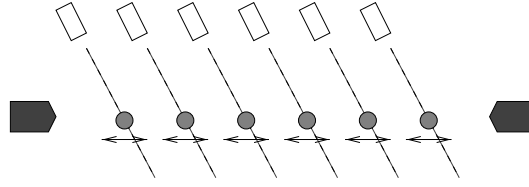


Figure 3.2: Schematic diagram (after [CZ95]) of an ion trap containing six ions (the electrodes needed to keep the ions on one line are not shown). Each ion can be individually addressed with laser pulses, and the collective vibrational motion of the ions serves as a bus qubit.

type Hamiltonian of the form

$$\mathcal{H}_{k,q} \propto \Omega [|1_q\rangle_k \langle 0| a e^{-i\phi} + |0\rangle_k \langle 1_q| a^\dagger e^{i\phi}] , \quad (3.29)$$

where a^\dagger and a are the creation and annihilation operator of the center-of-mass phonons, Ω is the Rabi frequency and ϕ is the laser phase. The subscript $q = 0, 1$ refers to the transition excited by the laser light; $q = 0$ excites the $|0\rangle \leftrightarrow |1\rangle$ transition whereas $q = 1$ excites the $|0\rangle \leftrightarrow |1'\rangle$ transition, where $|1'\rangle$ is an auxiliary energy level (Fig. 3.3). A three-step process then results in a conditional phase shift between two ions k and l [CZ95]. First apply a π pulse on ion k , with $q = 0$ and $\phi = 0$ (U_1). Then apply a 2π pulse on ion l , with $q = 1$ and $\phi = 0$ (U_2). Finally apply the first pulse again (U_1). The resulting operation $U_1 U_2 U_1$ can be converted into a CNOT gate via additional single qubit rotations.

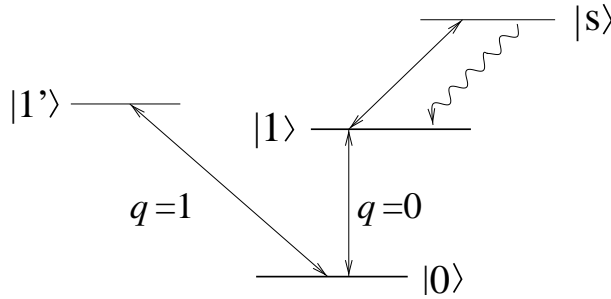


Figure 3.3: Model energy level diagram of the relevant internal states in a trapped ion. The qubit is embodied by $|0\rangle$ and $|1\rangle$. Level $|1'\rangle$ assists in two qubit operations and level $|s\rangle$ is used during read-out.

Measurement is done by exciting the transition between $|1\rangle$ and an auxiliary “shelving” level $|s\rangle$, which exhibits strong spontaneous decay. Thus, if fluorescence is observed during excitation of the $|1\rangle \leftrightarrow |s\rangle$ transition, the ion was in $|1\rangle$; if no fluorescence is observed, we conclude that it was in $|0\rangle$.⁷

⁷The assumption is that the ion remains in the $\{|0\rangle, |1\rangle\}$ manifold except temporarily during the two-qubit gates.

Inspired by the original Cirac-Zoller scheme, many variations of ion trap quantum computation have been proposed. Most notably, Mølmer and Sørensen [MS99] proposed a technique for entangling n ions using a wide laser beam which covers all ions (instead of a set of tightly focused beams). Furthermore, this scheme relaxes the requirement for cooling of the motion.

Experiments

Ion traps have been used as frequency standards for a number of years. Several groups across the world have trapped a single ion and cooled it down to its motional ground state [DBIW89, RLM⁺00]. The state of single ions can be well controlled using laser pulses, and measurement can be done with near 100% efficiency [NSD86, BHIW86]. David Wineland's group at NIST in Boulder, CO, and Rainer Blatt's group in Innsbruck, Austria, have cooled more than one trapped ion to the ground state of the collective motion [KWM⁺98, RGR⁺01]. Only the NIST group has reported the realization of two-qubit gates with trapped ions. In an impressive series of experiments, they first demonstrated a controlled phase shift between an ion and the motion [MMK⁺95], then entangled two ions [TWK⁺98], and later used the Mølmer-Sørensen scheme to entangle four ions [SKK⁺00].

One of the major challenges in the experiments is heating of the motional state, and this issue is only partly understood and resolved [WMI⁺98]. Also, additional know-how must be built up such that universal quantum logic gates can be implemented, which would allow the realization of simple quantum algorithms. Finally, even though several proposals for “scalable” arrayed approaches to ion traps exist (e.g. [CZ00]), it remains unclear how many ions could be held in a single trap, or how ions in different traps could be made to communicate in a practical and coherent way.

3.2.2 Neutral atoms

Concept

We will distinguish two very different strategies for trapping atoms: cavity quantum electrodynamics (QED) and optical lattices. Both have been proposed as the basis for quantum computers.

In *cavity QED* [PRS00], an atom interacts with a single-photon mode in an optical or microwave cavity (Fig. 3.4). The atom-cavity interaction Hamiltonian is a Jaynes-Cummins Hamiltonian

$$\mathcal{H} \propto g (a^\dagger |g\rangle\langle e| + a |e\rangle\langle g|) , \quad (3.30)$$

where a^\dagger and a are the raising and lowering operator of the cavity, $|g\rangle$ and $|e\rangle$ are the ground and excited states of the atom and g is the vacuum Rabi frequency. The coherent interaction of the atom and the cavity competes with spontaneous decay of the atom at a rate γ and with

cavity decay at a rate κ . In order to obtain “strong” coupling between the atom and the cavity, we need $g \gg (\gamma, \kappa)$, and the dwell time of the atom in the cavity must be long compared to the inverse of these rates. A high value of γ requires a small cavity (only about $10 \mu\text{m}$ long) so the electric field of the single photon is very intense; κ is determined by the reflectivity of the mirrors and γ depends on the atom and also on the cavity.

Such cavities, in particular microwave cavities, could in principle be used for quantum computation, with two internal levels of the atom ($|g\rangle$ and $|e\rangle$) as a qubit. A register of several qubits could be realized by trapping several atoms in a cavity. Tightly focused laser beams coming in from the sides of the cavity could address individual atoms for one-qubit gates, and the cavity mode could serve as a bus qubit for two-qubit gates, as it interacts with all the atoms. However, such schemes appear very difficult to realize.

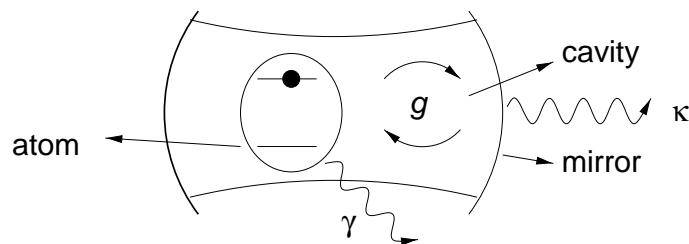


Figure 3.4: A single two-level atom is trapped by the cavity mode of a single photon. The cavity consists of two curved mirrors. (after Mabuchi in [MPZ00])

A more suitable application of cavity-QED, especially for optical cavities, may lie in the area of quantum communication. A trapped atom could mediate an interaction between “flying” (photon) qubits. Furthermore, appropriate excitation of an atom trapped in a cavity could emit single photons in a controlled way, and thus serve as a source for quantum cryptography. In microwave cavities, an atom travelling through the cavity could transfer its quantum information to the cavity, which in turn could transfer the information to a second atom travelling through the cavity at a later time. All these schemes illustrate that atom-cavity interactions provide a rich system for the exchange of quantum information between “flying” qubits and “standing” qubits.

Atoms trapped in far off-resonance *optical lattices* have also been proposed as qubits [DB00, BCJD99]. An optical lattice is created by three sets of optical standing waves at right angles, created by laser beams. A large number of neutral atoms can be loaded into the optical lattice for example from a magneto-optical atom trap or from a Bose-Einstein condensate; the atoms are trapped by the lattice at regular spacings in the “wells” of the standing waves. On-resonance laser beams can produce single-qubit rotations. By varying the polarization of the trapping lasers, two sets of atoms in adjacent wells can be made to pairwise occupy the same well so electric dipole-dipole interactions between the two atoms in each pair are induced. Two-qubit gates are thus performed on many pairs of atoms in parallel, which can be advantageous in

some cases but also constitutes a limitation. Good ways to measure the internal state of atoms trapped in an optical lattice are currently being investigated.

Experiments

Strong atom-cavity coupling has been achieved in both optical cavities, most notably with Cs atoms in Kimble's group at Caltech, [MTCK96] and with Rydberg atoms in microwave cavities, in Haroche's lab at the ENS in Paris [BSKM⁺96]. An atom trapped in an optical cavity has been used to cause a conditional phase shift between two photons flying through the cavity and interacting with the atom [THL⁺95]. This experiment represented the first explicit realization of a two-qubit gate. An optical cavity has been used as a single-photon source [LK97] and quantum memory operation of a single photon mode has been accomplished in a microwave cavity [MHN⁺97]. Also via a microwave cavity, three Rydberg atoms have been entangled with each other [RNO⁺00].

Compared to trapped ions, coherent control and readout are more complicated in trapped atoms, since the trapping potentials are much weaker for neutral atoms than for charged ions. For this and other reasons, it appears that the potential of cavity QED for quantum computing is limited, but optical cavities may find good use in quantum communication. Both optical and microwave cavities also provide a beautiful testbed for the study of decoherence and quantum (non-demolition) measurements, as in [NRO⁺99].

The state of the art in optical lattices is still extremely limited. On the order of 10^6 neutral Cs atoms have been trapped in a two-dimensional lattice [HHK⁺98], but it is not currently possible to reliably create a completely full lattice, much less to selectively control or read out the state of atoms trapped in an optical lattice.

3.2.3 Quantum dots

Loss and DiVincenzo [LD98] worked out a proposal for quantum computing based on "artificial atoms", created via semiconductor structures. In such quantum dots, the qubit is given by the spin of the excess electron on a single-electron quantum dot, placed in a static magnetic field. The confinement of the electron in the dot must be strong enough such that excited excitonic and electronic states have much higher energies than the spin Zeeman energy, and thus have negligible occupancy. The lay out of a possible device is shown schematically in Fig. 3.5.

One-qubit rotations could be realized in several ways. Via advanced scanning probe techniques, it may be possible to locally and selectively manipulate the electron spin in just one quantum dot. Alternatively, the Larmor frequency of the electron could be shifted selectively by changing the bias on the side gates of a specific dot, or by opening a tunneling barrier to an auxiliary dot which is ferro-magnetic. A narrowband microwave transverse magnetic field can then selectively rotate the spin of the electron on a specific dot.

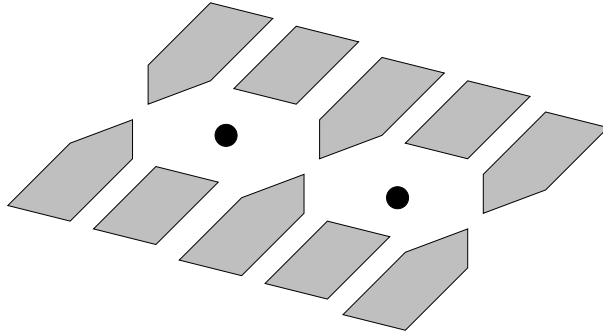


Figure 3.5: Conceptual schematic (after [DL99]) of one variant of a quantum dot quantum computer. Lateral side gates on top of a two-dimensional electron gas (created for example via a AlGaAs/GaAs/AlGaAs quantum well) confine the motion of an electron to a very small area (the quantum dot). The tunneling barrier between neighbouring quantum dots can be controlled via the voltages on the gates.

Two-qubit gates rely on the exchange interaction between the electrons in adjacent dots, which arises from tunneling through the barrier between the dots:

$$\mathcal{H} = J \vec{I}^1 \cdot \vec{I}^2. \quad (3.31)$$

By gating the tunneling barrier via the side gates, this interaction can be turned on and off in a controlled way.

Qubit measurement could be done using a spin-valve tunneling barrier between the quantum dot and an auxiliary dot. Such spin-dependent barriers let spin-up electrons pass but block spin-down electrons (or vice-versa). The presence of an electron in the auxiliary dot can be detected with a single-electron transistor. Depending on whether or not we detect an electron on the measuring dot after opening the spin-dependent barrier, we can conclude that the electron spin was up or down before measurement.

Highly polarized spins can be obtained by going to very low temperatures (say 100 mK), by injection from a nearby ferromagnetic or paramagnetic material or by irradiation with circularly polarized laser light. The spin states could also be initialized if a good measuring device is available.

This concept of a quantum computer has been further studied and worked out [DL99]; it has also inspired several detailed related proposals for quantum computing, for example based on ferro-electrically coupled Si/Ge quantum dots [Lev01].

A very different approach [IAB⁺99] to using electron spins in quantum dots consists of creating quantum dots in a high finesse microdisk cavity, so a single optical mode in the cavity can act as a “bus” qubit. Near-field laser techniques would enable qubit-selective one-qubit rotations as well as selective coupling of the electron spin of a specific quantum dot to the

optical cavity mode.

Finally, other degrees of freedom than spin could serve as quantum bit levels in quantum dots, such as the spatial coordinate (e.g. an e^- on dot 1 represents $|0\rangle$ and an e^- on dot 2 represents $|1\rangle$), or excitonic or electronic energy levels. However, the expectation is that for these degrees of freedom, it may not be possible to obtain coherence times sufficiently long for meaningful quantum computation.

Experiments

Tarucha's group at the University of Tokyo has fabricated quantum dots with a small and controlled number (0-20) of free electrons using vertical structures made of multiple III-V heterostructure quantum wells [TAH⁺96]. Coupled quantum dots have also been created using lateral side gates on top of a GaAs/AlGaAs two-dimensional electron gas, and molecule-like behavior of such coupled dots has been exhibited [LCW⁺96]. The advantage of this type of quantum dots over the vertically stacked dots is that it is easier to gate the dot potentials and the inter-dot coupling. However, smaller structures ($< 0.01\mu\text{m}^2$) than those currently available with sidegates must be constructed in order to obtain sufficiently strong confinement. Also, charge fluctuations in the electrodes may cause substantial decoherence, so the vertical dots appear to be intrinsically more suitable for quantum computing.

The Awschalom group at UC Santa Barbara measured coherence times (specifically T_2^*) of electron spins in GaAs/AlGaAs quantum wells which approach $1\mu\text{s}$ [KA98]. Furthermore, they observed the preservation of spin coherence as electrons were dragged across a GaAs/ZnSe interface [MKA⁺00]. Coherence time measurements of the spin of a single excess electron in a quantum dot still need to be done, and are much needed in order to assess the viability of the quantum dot electron spin approach to quantum computation.

Spin injection from a paramagnetic semiconductor into GaAs has been observed to produce nearly 90% spin polarized electrons in a magnetic field of 3 T [FKR⁺99]. Spin polarized holes have been injected from a ferromagnetic semiconductor into a quantum well, without a magnetic field [OYB⁺99]. Finally, circularly polarized laser light has been used to create spin polarization in the coherence time measurements [KA98].

Spin-filters (or spin-valves) have been first demonstrated for a variety of materials in the 70's [TM73]. Modern spin-dependent tunneling barriers, with polarizations of up to 85%, are made of metal-EuS-metal junctions [HMM90].

Self-assembled InAs quantum dots have been embedded in microdisk structures ($2\mu\text{m}$ in diameter and $0.1\mu\text{m}$ thick) with a cavity quality factor $Q \approx 12000$ [GG99], but the short photon lifetime in state-of-the-art cavities forms an important technological limitation. Furthermore, the need to address each quantum dot selectively via the tip of an optical fiber and near-field techniques constrains the density of the quantum dots in the microdisk to a separation of about

1000 Å. This in turn limits the number of quantum dots that can be coupled to a single cavity-mode to a few dozen.

It is clear that the realization of any of the quantum dot based proposals requires significant advances in semiconductor nanofabrication, magnetic semiconductor synthesis and high frequency measurement techniques. Still, the inherent scalability of the gated quantum dot proposals combined with the robustness of the spin degree of freedom make them good long-term candidates for practical quantum computers.

3.2.4 Superconducting qubits

Concept

The superconducting qubit proposals differ from all the other proposals discussed here in that the qubit is represented by two quantized states which are collective states of a “macroscopic” number of particles: flux states resulting from the motion of millions to billions of Cooper pairs through a SQUID or charge states produced by millions of Cooper pairs in a “box”.

Josephson junctions play a central role in both approaches [Ave00]: if the charging energy $E_C = e^2/2C_J$ (with C_J the capacitance of the Josephson junction) is much larger than the Josephson coupling energy E_J , the device is charge-dominated. In contrast, if $E_C \ll E_J$, the device is dominated by the phase across the junction, which is the conjugate variable of the charge (or equivalently the number) of the excess electrons on one side of the junction.

Flux qubits [MOL⁺99] are given by two energy levels of the quantized flux through a superconducting ring with one or more Josephson junctions in the phase regime (Fig. 3.6). In a micrometer sized loop, each flux state arises from the collective motion of up to 10^9 Cooper pairs producing a μA current through the loop.

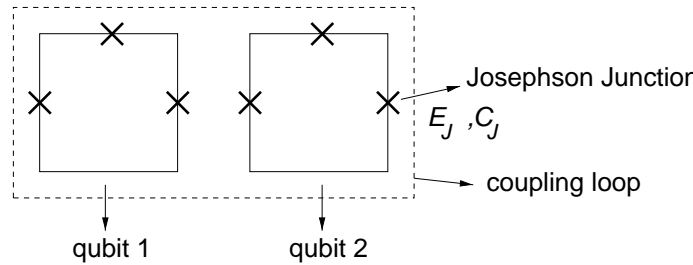


Figure 3.6: Schematic of two superconducting flux qubits, each embodied by a small superconducting loop interrupted by Josephson junctions (small barriers made of a resistive material). The devices shown contain three Josephson junctions, as in [vtW⁺00].

Several schemes have been proposed for logic gates. One-qubit rotations involve the application of local magnetic fields which change the environment of a specific qubit. In addition, by changing the parameters of the Josephson junctions, one-qubit operations can be performed

in different basis. The interaction mechanism for two-qubit gates is inductive coupling between neighbouring loops. This coupling can be enhanced via a separate superconducting coupling loop with encloses the two qubits (Fig. 3.6), or alternatively the two loops can be part of the same superconducting circuit.

Measurement of the flux state of a qubit can be done using a DC measuring SQUID (not shown in the figure), either enclosing the qubit or placed next to the qubit. Unfortunately, it is not possible with current technology to switch the measuring SQUID off by opening the measuring loop, so the coupling between the measuring SQUID and the qubit must be very weak in order to prevent excessive decoherence. Of course, the flip side of very weak coupling is that extensive signal averaging is required in the measurement.

Charge qubits [MSS99] rely on the quantized number of excess electrons on a small superconducting island when it is coupled to the ground by a number-state dominated Josephson junction (Fig. 3.7). As for flux qubits, one-qubit operations can be realized via local magnetic fields. Two qubit operations can be done by embedding multiple charge qubits in parallel in a larger circuit, so the different qubits are coupled. The number of excess Cooper pairs on the box can be measured via a probe Josephson junction through which Cooper pairs can tunnel out of the box, depending on the charge state of the box and on the probe voltage V_p (Fig. 3.7).

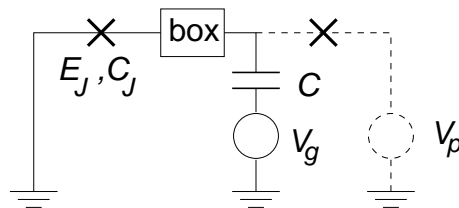


Figure 3.7: Schematic of a superconducting charge qubit, realized by a small superconducting island or “box”, coupled to the ground via a Josephson junction. The electrostatic potential of the island is controlled by the gate voltage V_g . The dashed part of the circuit serves for readout; it is not part of the actual qubit. In practice, improved variations of this design are used, which use more Josephson junctions in order to be able to have more control over the qubit parameters.

Both the charge qubit and the flux qubit devices must be operated at low temperature (say 20 mK, which is well below the critical temperature of Al or other superconducting materials of choice), such that the ground state is occupied with probability near 1.

Experiments

Nakamura and coworkers at NEC in Tsukuba have observed evidence for coherent superpositions of two charge states in a single-Cooper-pair box [NCT97]. The energy levels were shifted via a gate-induced charge e (Fig. 3.7) such that the energies of the two lowest levels (and excess charge of 0 and $2e$) would become equal (while the next lowest level is at a much higher energy);

however, the Josephson energy splits these two levels and the resulting eigenstates are coherent superpositions of two collective states of a macroscopic number of Cooper pairs, which differ in charge by $2e$. Energy level splitting was experimentally observed, which suggests that the box was in a coherent superposition of two charge states [NCT97]. Later, the same group demonstrated coherent control of the quantum states in the single-Cooper-pair box, via pulsed experiments and time domain measurements of multiple Rabi oscillations [NPT99].

The groups of Mooij at Delft and Lukens at SUNY Stony Brook both observed similar evidence for macroscopic superpositions of flux states in small SQUID loops [FPC⁺00, vtW⁺00]. Here the classical energy of two flux states was made equal via an externally applied static magnetic field. When quantum tunneling between these two states of equal energy is possible, the loop's eigenstates become the symmetric and antisymmetric superposition of the original flux states. The creation of such superposition states was deduced from the observation of energy level splitting. No time domain measurements demonstrating coherent control have been performed to date in these systems.

Even though the state of the art is currently more advanced in charge qubits than in flux qubits, the expectation is that flux qubits have longer coherence times than charge qubits, so flux states may be better qubits than charge states. Measurements of coherence times in either system would represent significant progress in evaluating superconducting qubit proposals.

3.2.5 Solid-state NMR

Concept

In a very different solid-state approach, Yamaguchi and Yamamoto [YY99] propose the use of nuclear spins in a crystal lattice as quantum bits (Fig. 3.8). In this proposal, which was further developed by the same group [LGD⁺00], a quantum computer consists of a one-dimensional array of spin-1/2 nuclei spaced by a few Å along the \hat{z} axis; the presence of a magnetic field with a strong gradient along \hat{z} (on the order of 1 T/ μm) separates the Larmor frequency of the qubits so they can be individually distinguished and addressed.

In the transverse direction, the magnetic field must be homogeneous so the crystal contains many identical copies of this one-dimensional chain of nuclei. All the copies operate as independent quantum computers provided the interactions between them are switched off. An important advantage of such a scheme is that the measurement of a qubit can take place over a large ensemble of nuclear spins instead of just a single nuclear spin as is required in the Kane proposal (section 3.2.6).

Two qubit gates rely on the magnetic dipole-dipole coupling between spins in the same computer. With both the magnetic field and the strong field gradient along the direction of the chain of spins \hat{z} , the coupling Hamiltonian between two spins i and j within the same chain is

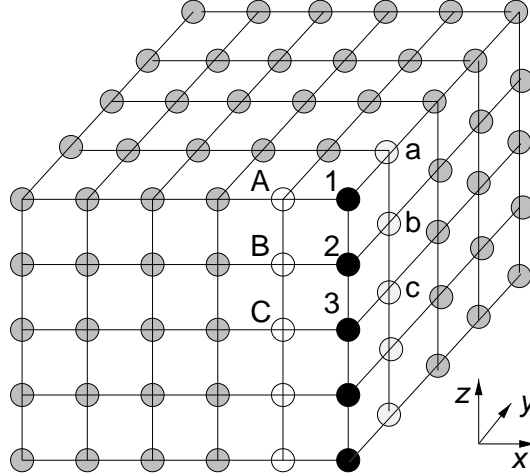


Figure 3.8: Model of a crystal lattice quantum computer. The crystal shown here has a simple cubic lattice; in practice other lattices have been proposed, but the idea is the same. The nuclei $1, 2, 3, \dots$ form one quantum computer, the nuclei a, b, c, \dots form an independent computer, and so forth. Nuclei $1, a$ and A represent the analogous qubit in the respective computers.

of the form

$$\mathcal{H}_{i,j} \propto \frac{I_z^i I_z^j}{(|j-i|a)^3}, \quad (3.32)$$

where a is the distance between neighbouring nuclei. This Hamiltonian is easy to work with and can be selectively suppressed simply by applying a suitable periodic train of narrowband 180° pulses [LCYY00].

The coupling between spins in different copies has a different form. For two spins with the same Larmor frequency but located in different chains m and n (i.e. analogous qubits in different computers), the coupling Hamiltonian is of the form

$$\mathcal{H}_{mn} \propto \frac{1 - 3 \cos^2 \theta_{mn}}{(a\lambda_{mn})^3} \left(3I_z^m I_z^n - \vec{I}^m \cdot \vec{I}^n \right), \quad (3.33)$$

where λ_{mn} is the distance between the two nuclei in units of a and θ_{mn} is the angle between the vector which connects them and the direction of the applied field \hat{z} . This coupling can be largely switched off as well, using well-known solid-state NMR broadband decoupling pulse sequences, such as the WAHUA sequence [Meh83].

The WAHUA pulse sequence also affects the qubit-qubit coupling of Eq. 3.32 but this coupling can still be sufficiently controlled for two-qubit gates using additional narrowband pulses. However, the coupling between qubits with different resonance frequencies ($i \neq j$) and in different chains ($m \neq n$) is partially reintroduced during such two-qubit gates, and causes decoherence. Fortunately, this effect can be kept quite small by choosing a very one-dimensional crystal, for example fluorapatite, $\text{Ca}_5\text{F}(\text{PO})_4)_3$, where the ^{19}F nuclei serve as qubits

[LGD⁺00].

Unlike for liquid NMR, state initialization can in principle be done by cooling down the sample to the milli-Kelvin regime. In practice, such low temperature may be difficult to maintain given the many RF pulses involved in broadband decoupling. Optical pumping or polarization transfer from electron spins may then be needed.

Readout is much helped by the ensemble nature of the experiment; even for a relatively small crystal, there are on the order of 10^7 members in the ensemble. Given the presence of a strong magnetic field gradient, magnetic resonance force microscopy using microcantilevers [RYS92] has been proposed as a natural way to measure the spin states.

The main source of decoherence in this system is residual dipolar couplings. Furthermore, magnetic impurities and cantilever drift (as the sample would be mounted on the cantilever) also contribute to decoherence.

An independent but less detailed proposal for solid-state NMR quantum computing was presented by Cory *et al.* [CLK⁺00]. The main difference with the crystal lattice proposal is that in the Cory scheme the quantum computer would be an ensemble of specially designed molecules, held and aligned in a solid state lattice.

Experiments

Solid-state NMR has a tradition of over 50 years, and coherence times and decoherence mechanisms have been studied since the early days [Blo49]. The T_1 of nuclear spins in reasonably pure crystals is limited by thermal fluctuations of paramagnetic impurities but can easily be several hours. While T_2 is typically only on the order of milliseconds due to dipolar broadening, it can be lengthened by several orders of magnitude using well-established broadband decoupling techniques which have proven their effectiveness.

Growth of high purity crystals of fluorapatite is relatively well understood. Furthermore, force microscopy with sufficient sensitivity to detect 10^7 nuclear spins has been demonstrated [SMY⁺01].

No actual quantum logic gates have been implemented yet, but the crystal lattice quantum computer has the potential for scaling up to several hundred qubits, and experiments are underway. The main challenge lies in the integration and alignment of the different components, and the design of a micromagnet which produces a strong magnetic field which is uniform along two axes but has a steep gradient along the third axis.

The approach based on molecules in solid solutions aims at intermediate sized quantum computers containing several tens of qubits. Here also, experiments are underway.

3.2.6 Dopants in semiconductors

Bruce Kane, of the University of Maryland, proposed an approach which integrates solid-state NMR on donor atoms with semiconductor electronics [Kan98]; this scheme has some conceptual similarities with the quantum dot scheme of section 3.2.3. The quantum bits are embodied by the spin-1/2 nucleus of ^{31}P dopants arranged in a regular array below the surface of a silicon substrate (Fig. 3.9), placed in a static magnetic field perpendicular to the surface.

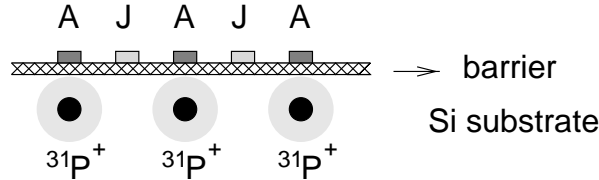


Figure 3.9: Model of a Kane-type quantum computer (cross-section), after [Kan98].

Phosphorus in silicon is an electron donor at room temperature, but at low temperatures (100 mK), the electron is weakly bound to the phosphorus ion. A voltage applied to the A gate located about 200 \AA above a specific ^{31}P ion, shifts the electron away from that nucleus and thereby reduces the hyperfine interaction. As a result, the energy difference between the spin-up and spin-down state of the nuclear spin changes and a radio-frequency pulse can then selectively rotate the state of the one ^{31}P nuclear spin for which the A gate is biased.

Two-qubit gates between adjacent phosphorus nuclei rely on an indirect coupling mechanism mediated by their respective electrons. The coupling Hamiltonian of two donor-electron spin systems is

$$\mathcal{H} = A_1 \vec{I}^{1n} \cdot \vec{I}^{1e} + A_2 \vec{I}^{2n} \cdot \vec{I}^{2e} + J \vec{I}^{1e} \cdot \vec{I}^{2e} \quad (3.34)$$

where A_1 and A_2 are the hyperfine interaction energies and J is the exchange energy. In order to obtain reasonable values of J ($> 10 \text{ GHz}$), the donor separation must be no more than 100-200 \AA . A negative voltage applied to the J gate in between two ^{31}P nuclei repels the electrons and diminishes their overlap. Because J is proportional to the electron wavefunction overlap, the e^- - e^- interaction can thus be turned off at will via the J gates.

Measurement of the ^{31}P nuclear spin states is done in an innovative two-step process. First, the A gate of the nuclear spin we want to measure, say spin i , is biased, while the A gate of a neighbouring nuclear spin, j , is not ($A_i > A_j$). Under these conditions, the J gate between the two dopant atoms i and j is ramped up such that $J > \mu_B B/2$ and therefore the singlet state $(|\uparrow\downarrow\rangle - |\downarrow\uparrow\rangle)/\sqrt{2}$ becomes the lowest energy state of the two electron spins (during the computation, $J < \mu_B B/2$ so the ground state of the two electron spins is $|\downarrow\downarrow\rangle$). The electron spins will then adiabatically evolve into the singlet state if spin i is in $|0\rangle$, whereas they remain in the metastable state $|\downarrow\downarrow\rangle$ if spin i is in $|1\rangle$; the state of spin j is inconsequential. In the second step, the electron spin state is measured electronically. Both electrons can be bound to the same

donor by biasing the A gates appropriately provided the electron spins are in $(|\uparrow\downarrow\rangle - |\downarrow\uparrow\rangle)/\sqrt{2}$; if the electron spins are in $|\downarrow\downarrow\rangle$, the electrons cannot be bound to the same donor. Thus, by alternating the voltage applied to the two respective A gates, charge motion can be induced between the two donors if and only the electrons are in the singlet state, which in turns depends on the state of nuclear spin i . The charge motion can be detected via a single-electron transistor.

The electron spins are initialized to the ground state by working at 2 T and 100 mK. The nuclear spin can be initialized via the measurement process: measure the nuclear spin and flip it if necessary.

Voltage fluctuations in the control gates, especially the A gates, are expected to contribute to decoherence, as the Larmor precession frequency of the nuclear spins is affected by the voltage on the A electrodes. More significantly, the presence of a single-electron transistor also induces relaxation, at an estimated rate of 1 kHz.

The Kane proposal inspired a related proposal by Yablonovitch and coworkers [VYW⁺99]. There are two main differences with the Kane scheme: (1) the donor electron spin represents the qubit, instead of the dopant nuclear spin; (2) there are no J gates; both one-qubit and two-qubit gates could be realized using A gates, which is made possible by using silicon-germanium heterostructures, bandgap engineering and g -factor engineering.

Experiments

The fabrication technology required for a Kane-type computer is still beyond the state of the art: it is not currently possible to deposit individual phosphorus atoms over large areas and with atomic precision below a silicon surface, nor can we pattern many electrodes of only 50 Å wide and spaced by 200 Å. Alignment of the gates with respect to the buried dopant atoms represents an additional challenge. Finally, further advances in materials technology would be needed to obtain highly pure ^{28}Si (the natural abundance of ^{29}Si is about 5%), and nearly defect-free oxide barriers.

Nevertheless, Kane's proposal is very appealing for its scalability and elegance, and provides a strong motivation for developing the necessary technology. In a first step towards the fabrication of a Kane-type quantum computer, atomic hydrogen has been adsorbed on a silicon surface, hydrogen desorbed with an STM tip over an area of 1 nm across, and single phosphine molecules have been adsorbed onto the silicon substrate through the 1 nm holes in the hydrogen layers [OSS⁺01].

Measurements of T_1 have been done long ago [FG59]. The electron spin T_1 at low ^{31}P concentrations in pure ^{28}Si and at 1.5 K has been measured to be thousands of seconds; the phosphorus spin T_1 was over 10 hours. At 100 mK, even longer T_1 's are expected. Finally, Rabi oscillations have been observed between two low-lying hydrogen-atom like states of an electron weakly bound to a donor impurity in GaAs [CWK⁺01].

The Yablonovitch variant puts less demands on lithography, as only one gate must be fabricated per qubit, and in addition the spacing between the qubits can be much larger than in the original proposal (up to 200 nm). On the other hand, there are additional demands on epitaxial growth techniques due to the need for bandgap and g -factor engineering.

3.2.7 Other proposals

Several other proposals exist for the implementation of quantum computers, in addition to those we have discussed in the preceding sections. We will just mention two of them.

Platzman and Dykman suggested the use of a quasi-two dimensional set of electrons floating in vacuum above liquid helium [PD99]. Individual electrons are laterally confined by μm sized electrodes below the helium, and strongly interact with neighbouring electrons. The qubit states are given by the lowest hydrogenic levels, at 10 mK. Locally applied electric fields would produce one-qubit gates and read-out would be done by selectively releasing excited electrons from the surface, and absorbing them in an electrometer placed above the surface.

There also exist proposals for all-optical quantum computers [Mil89]. The main obstacle to such devices, the high losses associated with sufficiently non-linear optical elements, was recently circumvented by a proposed scheme for efficient quantum computation with just linear optics [KLM01] (see page 58).

3.3 Summary

Today's technology enables physicists to separately meet any one of the five requirements for building a quantum computer exceedingly well. For example, it is possible already to

1. integrate tens of thousands of quantum dots on a single chip using semiconductor technology,
2. realize extremely precise two-qubit gates using the natural coupling between neighbouring spins,
3. reliably initialize an atom to its internal ground state by atomic cooling techniques,
4. perform near-ideal measurements of the internal state of trapped ions using fluorescence techniques,
5. obtain lifetimes of several days for nuclear spins in solids.

Furthermore, we have seen that many of the traditional requirements for the physical requirements of quantum computers can be relaxed or circumvented.

Nevertheless, satisfying all five criteria within one device still remains an extraordinary challenge which hasn't been met in any of these systems. In fact, it has not been possible so far to realize even the simplest quantum algorithms with any of the proposed implementations we have discussed.

The crucial difficulty can be summarized as follows: on the one hand, long coherence times require that the qubits be highly isolated from the environment; on the other hand, we must have external access to the qubits in order to initialize, control and read out their state. The system which best reconciles these opposing requirements will eventually come out as the "winning" quantum computer realization.

In the next chapter, we describe in detail an experimental system which we haven't yet discussed, but which, as we shall see, truly stands out in its accessibility: nuclear spins in molecules dissolved in liquid solution, and manipulated by magnetic resonance techniques.

Chapter 4

Liquid-state NMR quantum computing

In this chapter, we will examine whether nuclear spins in molecules in liquid solution satisfy the five requirements for the implementation of quantum computers. One section will be devoted to each requirement, except that single-qubit gates and two-qubit gates are treated in separate sections. Based on this discussion, we will close with guidelines for molecule design and NMR pulse sequence design.

4.1 Qubits

The qubits in NMR quantum computing are given by the spins of suitable atomic nuclei, placed in a static magnetic field \vec{B}_0 .

We shall here be exclusively interested in spin-1/2 nuclei, such as ^1H , ^{13}C , ^{15}N , ^{19}F and ^{31}P , as they have two discrete eigenstates.

Spin-0 nuclei, for example ^{12}C and ^{16}O , are not magnetic and therefore not detectable with NMR. Nuclei with spin quantum number greater than 1/2, such as ^2H , ^{14}N , ^{35}Cl , ^{37}Cl , ^{79}Br and ^{81}Br , don't make for good qubits either; mapping the larger number of states (e.g. the spin quantum number of a spin-3/2 particle can be $-3/2$, $-1/2$, $1/2$ or $3/2$) onto qubit states, and performing quantum logic gates on them, introduces additional complications. More significantly, nuclear spins with spin $> 1/2$ tend to have very short coherence times.

4.1.1 Single-spin Hamiltonian

The Hamiltonian of a spin-1/2 particle in a magnetic field of strength B_0 along the \hat{z} axis is [Fre97, EBW87]¹

$$\mathcal{H}_0 = -\hbar\gamma B_0 I_z = -\hbar\omega_0 I_z = \begin{bmatrix} -\hbar\omega_0/2 & 0 \\ 0 & \hbar\omega_0/2 \end{bmatrix}, \quad (4.1)$$

where γ is the gyromagnetic ratio of the nucleus and $\omega_0/2\pi$ is the Larmor frequency of the spin (we will sometimes leave the factor of 2π implicit and call ω_0 the Larmor frequency). I_z is the angular momentum operator in the \hat{z} direction, which relates to the well-known Pauli matrix as $2I_z = \sigma_z$; similarly, we will later use $2I_x = \sigma_x$ and $2I_y = \sigma_y$.

The interpretation of Eq. 4.1 is that the energy of the $|0\rangle$ or $|\uparrow\rangle$ state (given by $\langle 0|\mathcal{H}|0\rangle$, the upper left element of \mathcal{H}) is lower than the energy of $|1\rangle$ or $|\downarrow\rangle$ ($\langle 1|\mathcal{H}|1\rangle$) by an amount $\hbar\omega_0$, as illustrated in the energy diagram of Fig. 4.1. The energy splitting is known as the *Zeeman splitting*.

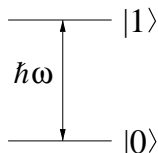


Figure 4.1: Energy diagram for a single spin-1/2.

The time evolution $e^{-i\mathcal{H}t/\hbar}$ of the spin state under the Hamiltonian of Eq. 4.1 corresponds to a precession motion in the Bloch sphere (Fig. 2.1) about the axis of the static magnetic field, similar to the precession of a spinning top about the axis of gravitation, as shown in Fig. 4.2. The B_0 field is typically on the order of 10 Tesla, resulting in precession frequencies ω_0 of a few hundred MHz, which is in the radio-frequency range .

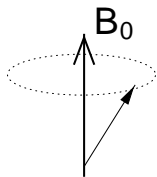


Figure 4.2: Precession of a spin-1/2 about the axis of a static magnetic field.

¹Some authors use a different convention, leaving out the minus sign in Eq. 4.1.

Distinguishing the nuclear spins in a molecule

A molecule with n distinguishable spin-1/2 nuclei constitutes an n -qubit quantum computer. Spins of different nuclear species (*heteronuclear* spins) can be easily distinguished spectrally, as they generally have very distinct values of γ and thus also very different Larmor frequencies (Table 4.1). Furthermore, spins of the same nuclear species (*homonuclear* spins) which are part of the same molecule can also have distinct frequencies, due to chemical shifts σ^i : the electron clouds slightly shield the nuclei from the externally applied magnetic field so a different electronic environment leads to a different degree of shielding and hence different Larmor frequencies (Fig. 4.3).

nucleus	^1H	^2H	^{13}C	^{15}N	^{19}F	^{31}P
ω_0	500	77	126	-51	470	202

Table 4.1: Larmor frequencies [Mhz] of some relevant nuclei, at 11.74 Tesla.

The nuclear spin Hamiltonian for a molecule with n nuclei with different chemical shifts is thus

$$\mathcal{H}_0 = - \sum_{i=1}^n \hbar (1 - \sigma_i) \gamma B_0 I_z^i = - \sum_{i=1}^n \hbar \omega_0^i I_z^i. \quad (4.2)$$

The range of typical chemical shifts σ_i varies from nucleus to nucleus: it is ≈ 10 parts per million (ppm) for ^1H , ≈ 200 ppm for ^{19}F and ≈ 200 ppm for ^{13}C . For a B_0 field of about 10 Tesla (ω_0 's of several hundred MHz), this corresponds to a few kHz to tens of kHz. Pronounced asymmetries in the molecular structure and strong differences in the electronegativity of the atoms in the molecule promote strong chemical shifts.

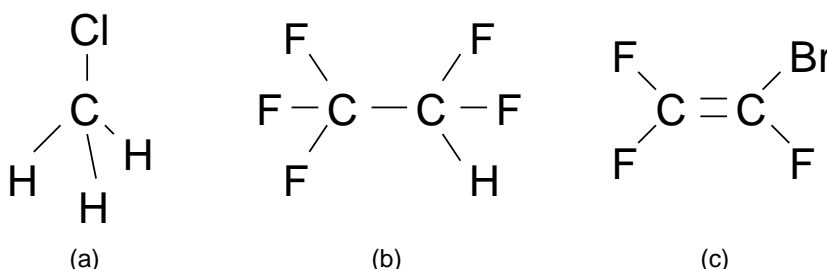


Figure 4.3: (a) The three H atoms in this tetrahedral molecule are in equivalent locations with respect to the C and Cl atoms; their Larmor frequencies are thus identical. (b) The two F nuclei on the right have a different chemical shift from the three F nuclei on the left, because the H atom makes both sides inequivalent. However, the three F nuclei on the left hand side of the molecule are chemically equivalent to each other, because both ends of the molecule rapidly rotate with respect to each other around the single C-C bond. (c) The double C=C bond is rigid, so the left and right side cannot rotate with respect to each other. All three F nuclei have different chemical shifts.

We shall first describe the nature of the interactions between nuclear spins, and then discuss the operation of two-qubit gates in NMR.

4.1.2 Spin-spin interaction Hamiltonian

For nuclear spins in molecules, nature provides two distinct interaction mechanisms [Abr61, Sli96]. The first is a *magnetic dipole-dipole* interaction, similar to the interaction between two bar magnets in each other's vicinity. It takes place purely *through space* — no medium is required for this interaction and it is inversely proportional in strength to the distance between the two nuclei and depends on the relative position of the nuclei with respect to the magnetic field. Both intramolecular dipolar couplings (between spins in the same molecule) and intermolecular dipolar couplings (between spins in different molecules) are present. However, when the molecules are dissolved in an isotropic liquid, all dipolar couplings are averaged away due to rapid tumbling.

The second mechanism is known as the *J-coupling* or *scalar coupling*. This interaction is mediated by the electrons shared in the chemical bonds between atoms in a molecule. The *through-bond* coupling strength J depends on the element and isotope of the respective nuclei and decreases with the number of chemical bonds separating the nuclei. The Hamiltonian is

$$\mathcal{H}_J = \hbar \sum_{i<j} 2\pi J_{ij} I^i \cdot I^j = \hbar \sum_{i<j} 2\pi J_{ij} (I_x^i I_x^j + I_y^i I_y^j + I_z^i I_z^j), \quad (4.3)$$

where J_{ij} is the coupling between spins i and j . If the spectra are first-order, i.e. $|\omega_i - \omega_j| \gg 2\pi|J|$, Eq. 4.3 simplifies to [Fre97, EBW87]

$$\mathcal{H}_J = \hbar \sum_{i<j}^n 2\pi J_{ij} I_z^i I_z^j, \quad (4.4)$$

which was the case for all the molecules we selected for our experiments. The complete Hamiltonian of a closed system of n nuclear spins in isotropic solution and with first order spectra is then (from Eqs. 4.2 and 4.4)

$$\mathcal{H} = - \sum_{i=1}^n \hbar \omega_0^i I_z^i + \hbar \sum_{i<j} 2\pi J_{ij} I_z^i I_z^j, \quad (4.5)$$

The interpretation of the scalar coupling term is that a spin “feels” a static magnetic field along $\pm \hat{z}$ produced by neighbouring spins, in addition to the externally applied \vec{B}_0 field. This additional field shifts the energy levels as in Fig. 4.4 and the Larmor frequency of spin i shifts by $-J_{ij}/2$ if spin j is in $|0\rangle$ and by $+J_{ij}/2$ if spin j is in $|1\rangle$.

In a system of two coupled spins, the spectrum (section 4.5) of each spin therefore actually

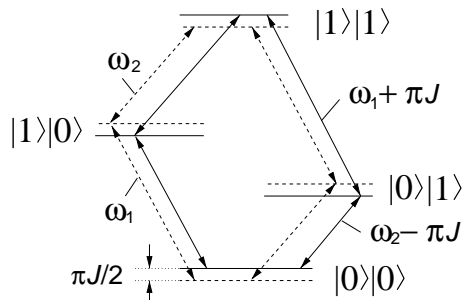


Figure 4.4: Energy level diagram for two J -coupled spins in isotropic solution (in units of \hbar).

consists of two lines, each of which can be associated with the state of the other spin, $|0\rangle$ or $|1\rangle$. For three pairwise coupled spins, the spectrum of each spin contains four lines. For every spin we add, the number of lines per multiplet doubles, provided all the couplings are resolved and different lines do not lie on top of each other. This is illustrated for a five spin system in Fig. 4.15.

The magnitude of all the pairwise couplings can be found by looking for common splittings in the multiplets of different spins. Typical values for J are up to a few hundred Hertz for one-bond couplings and down to only a few Hertz for three- or four-bond couplings. The signs of the J couplings can be determined via two-dimensional correlation experiments with spin-selective pulses (soft-COSY) [BMG⁺87] or related selective decoupling experiments; they cannot be derived just from a single spectrum.

Finally, we note that J couplings with spins $> 1/2$ average to zero, because such nuclei have a quadrupole moment which interacts with electric field fluctuations and causes the nucleus to rapidly oscillate between the spin-up and spin-down states. We also point out that the coupling between magnetically equivalent nuclei is not observable for symmetry reasons.

4.2 Single-qubit operations

4.2.1 Rotations about an axis in the $\hat{x}\hat{y}$ plane (RF pulses)

We can manipulate the state of a spin-1/2 particle by applying an electromagnetic field of strength B_1 which rotates in the transverse plane at ω_{rf} , at or near the spin precession frequency ω_0 . The Hamiltonian of the RF field is [Fre97, EBW87]

$$\mathcal{H}_{rf} = -\hbar\omega_1 [\cos(\omega_{rf}t + \phi)I_x + \sin(\omega_{rf}t + \phi)I_y] , \quad (4.6)$$

where $\omega_1 = \gamma B_1$.

In practice, we apply a transverse RF magnetic field which *oscillates* at ω_{rf} along a fixed axis in the lab frame, rather than *rotates*. The oscillating field can be decomposed into two

counter-rotating fields, one of which rotates at ω_{rf} in the same direction as the spin. We call this component the B_1 field. The other component goes in the opposite direction and has a negligible effect on the spin dynamics.²

Nutation under an RF field

The motion of a nuclear spin subject to both a static and a rotating magnetic field is rather complex when described in the usual laboratory coordinate system (the *lab frame*). It is much simplified, however, by describing the motion in a coordinate system rotating about \hat{z} at or near the spin precession frequency ω_0 (the *rotating frame*).

Suppose we apply the B_1 field exactly on resonance with ω_0 . In a frame rotating at $\omega_{rf} = \omega_0$, the B_1 field then appears to lie along a fixed axis in the transverse plane, so the RF field Hamiltonian in the rotating frame becomes

$$\mathcal{H}_{rf}^{rot} = -\hbar\omega_1 [\cos(\phi)I_x + \sin(\phi)I_y] \quad (4.7)$$

An observer in this rotating frame will thus see the spin simply precess about the axis of the B_1 field (Fig. 4.5 a); this motion is called the *nutation*. The rotation axis is controlled by the phase of the RF field ϕ . An observer in the lab frame sees the spin spiral down over the surface of the Bloch sphere, the combined result of precession and nutation (Fig. 4.5 b). In typical NMR experiments, the static field is much stronger than the RF field, so the precession about \hat{z} is much faster than the nutation (hundreds of MHz versus tens of kHz).

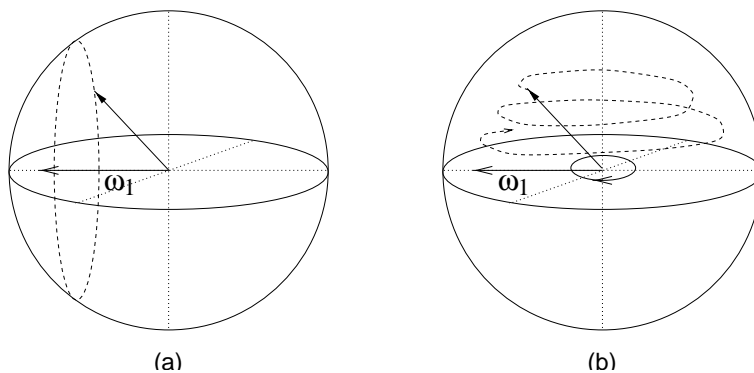


Figure 4.5: Nutation of a spin subject to a transverse RF field (a) observed in the rotating frame and (b) observed in the lab frame.

If the RF field is *off-resonance* with respect to the spin frequency by $\Delta\omega = \omega_0 - \omega_{rf}$, the

²The presence of this second component produces a tiny shift in the Larmor frequency, called the Bloch-Siegert shift [BS40].

RF Hamiltonian in the frame rotating at $\omega_{rf} (\neq \omega_0)$ becomes

$$\mathcal{H}_{rf}^{rot} = -\hbar\Delta\omega I_z - \hbar\omega_1 [\cos(\phi)I_x + \sin(\phi)I_y] \quad (4.8)$$

In words, the spin now precesses with frequency

$$\omega'_1 = \sqrt{\Delta\omega^2 + \omega_1^2} \quad (4.9)$$

about an axis tilted away from the \hat{z} axis by an angle

$$\alpha = \arctan(\omega_1/\Delta\omega), \quad (4.10)$$

as illustrated in Fig. 4.6. An off-resonant pulse thus results in a rotation about a different axis and over a different angle than the same pulse applied on resonance. Off-resonance pulses can thus be used to effect a rotation about an axis outside the $\hat{x}\hat{y}$ plane.

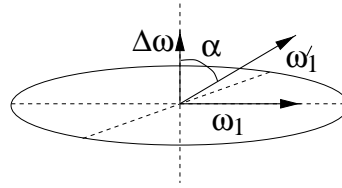


Figure 4.6: Axis of rotation (in the rotating frame) during an off-resonant radio-frequency pulse.

RF pulses

A resonant RF field gated on for a duration pw , nutates a spin in the rotating frame over an angle

$$\theta = \gamma B_1 pw. \quad (4.11)$$

The parameter pw is called the *pulse width* or *pulse length*.

Thus, a properly timed and calibrated RF pulse with the right phase can perform a rotation about \hat{x} of 90° , which we will denote $R_x(90)$ (see Eq. 2.45) or for short X . A similar pulse but twice as long realizes a $R_x(180)$ rotation, written for short as X^2 . By changing the phase of the RF by 90° , we can similarly implement Y and Y^2 pulses. Changing the phase another 90° gives a negative rotation about \hat{x} , denoted $R_x(-90)$ or \bar{X} , and so forth.

We point out that only the relative phase between pulses applied to the same spin matters. As soon as we send one pulse on any given spin, the phase of that pulse sets the phase reference of the corresponding rotating frame for the remainder of the pulse sequence.

Quantum picture

The description of single-spin rotations has been purely classical so far, and in fact it does not need quantum mechanics at all. For example, a bar magnet with angular momentum responds in exactly the same way to magnetic fields as does a nuclear spin. However, the quantum nature of spins, and qubits in general, unmistakably emerges as soon as two or more spins are involved (section 2.1.1).

Underlying the classical Bloch sphere picture is the evolution of a two-level quantum mechanical system. An RF field induces transitions between the ground and excited state of the qubit (Fig. 4.1). After applying an RF pulse, a spin initially in the ground state will upon measurement be found in the excited state with probability $\sin^2(\omega_1 pw/2)$. The projection on the \hat{z} axis of the Bloch sphere oscillates with pw as $\cos(\omega_1 pw)$. These oscillations are known as *Rabi oscillations*, and $\omega_1/2\pi$ is the *Rabi frequency*, with typical values of a few hundred Hz to a few hundred kHz.

4.2.2 Rotations about the \hat{z} axis

We recall from Eq. 2.53 that the ability to implement arbitrary rotations about \hat{x} and \hat{y} is sufficient for performing arbitrary single-qubit rotations. For example, two ways to implement a Z rotation using *composite* X and Y pulses are

$$Z = XY\bar{X} = Y\bar{X}\bar{Y}, \quad (4.12)$$

where *time goes from right to left*, as always for concatenated unitary operations (see section 2.2.3). We have used this technique in our first few experiments (sections 5.3-5.5). However, there are two alternative and more convenient ways to implement Z rotations.

The first approach takes place at the pulse sequence design level. The goal is to move down all the Z rotations to the very end or the beginning of the pulse sequence. For example, using Eq. 4.12, we can move a Z rotation past a X or Y rotation,

$$Z\bar{Y} = XY\bar{X}\bar{Y} = XZ. \quad (4.13)$$

Since Z rotations commute with the Hamiltonian of nuclear spins in liquid solution, they can be moved across time evolution intervals as well. Once all Z rotations are gathered at the end of the pulse sequence, we only need to execute the net remaining Z rotation for each spin. Z rotations moved to the start of the sequence have no effect as the initial state is diagonal (see section 4.4), so they don't need to be implemented altogether. This approach was used in the experiment of section 5.7.

The second approach has the same effect, but the experimental procedure is different. It

makes use of an artificial software rotating frame, on top of the hardware rotating frame provided by a reference oscillator. A Z rotation is implemented simply by shifting the software reference frame by 90° . Subsequent X and Y pulses are then executed with respect to the new reference frame (e.g. X in the new frame corresponds to Y in the old frame, and so forth), and the receiver phase is also set with respect to the new software frame. We have used this procedure in our latest experiments (sections 5.8- 5.10), as it is by far the easiest to use once the software for the artificial reference frame is written. Since the Z rotations are now done entirely in the software and do not require any physical pulses anymore, they are in a sense “for free” and perfectly executed. It is in this case advantageous to convert as many X and Y rotations as possible into Z rotations, using identities similar to Eq. 4.12, for example

$$XY = XY\bar{X}X = ZX. \quad (4.14)$$

We will come back to pulse sequence simplification in section 4.8.

4.2.3 Selective excitation using pulse shaping

We can selectively address one spin without exciting any other spins in the molecule by sending a sufficiently long RF pulse at the resonance frequency of the desired spin. The frequency selectivity of RF pulses can be much improved by using so-called *soft pulses* or *shaped pulses*, which are designed to excite or invert spins over a limited frequency region, while minimizing \hat{x} and \hat{y} rotations for spins outside this region [Fre98, Fre97]. Soft pulses start off at low amplitude B_1 (and thus also ω_1), gradually build up to a maximum amplitude, and taper off again towards the end. Pulse shaping is usually done by dividing the pulse in a few tens to many hundreds of discrete time slices, and by changing the amplitude and/or phase³ slice by slice to create a tailored amplitude and phase profile.

Fourier theory can give us a rough idea of the frequency response of a spin to an RF pulse. For example, it tells us that the power of a pulse of length pw will be confined to a frequency window of roughly $1/pw$. However, the Fourier transform is a linear transformation whereas the spin response to an RF field is not linear (it is sinusoidal); it must thus be calculated with different methods.

For a rectangular (constant amplitude) pulse, the spin response as a function of $\Delta\omega = \omega_{rf} - \omega_0$ is easy to calculate analytically from Eqs. 4.9 and 4.10, or numerically by computing the unitary operator $e^{-i\mathcal{H}t/\hbar}$ generated by the Hamiltonian of Eq. 4.8 (see section 2.1.2). The response to a shaped pulse is most easily computed by concatenating the unitary operators of each time slice of the shaped pulse, as the Hamiltonian is time-independent within each time slice. Fig. 4.7 shows the time profile and the excitation profile for four standard pulse shapes.

³In common pulse shapes, the phase is usually just 0° or 180° . During phase ramping, the phase is incremented linearly throughout the pulse profile, as discussed on page 94.

Pulse shape design

The properties relevant for choosing a pulse shape are:

- selectivity: product of excitation bandwidth and pulse length (lower is more selective),
- transition range: the width of the transition region between the selected and unselected frequency region,
- power: the peak power required for a given pulse length (low is less demanding),
- self-refocusing behavior (see section 4.2.4): degree to which the J couplings between the selected spin and other spins are refocused (the signature for self-refocusing behavior is a flat top in the excitation profile),
- robustness: whether the spin response is very sensitive to experimental imperfections such as RF field inhomogeneities and calibration errors,
- universality: whether the pulse performs the correct rotation for arbitrary input states or only for specific input states.

Figure 4.7 strikingly illustrates the difference in performance between different pulse shapes. Table 4.2 summarizes these properties for a selection of important pulse shapes. All the pulses in the table are universal pulses; quantum computations must work for any input state so we cannot compromise on universality.⁴ Obviously, no single pulse shape optimizes for all properties simultaneously, so pulse shape design consists of finding the optimal trade-off for the desired application. For our experiments, we have selected molecules with large chemical shifts, so sharp transition regions are not so important. Furthermore, the probe and spectrometer can deal with relatively high powers. The crucial parameters are the effect of coupling during the pulses, the selectivity (short, selective pulses minimize relaxation) and to some extent the robustness.

Phase ramping

Excitation at a frequency which differs from the RF carrier frequency ω_{rf} by $\Delta\omega$, is made possible by linearly incrementing the phase of the pulse during the application of the pulse, at a rate $\delta\phi/\delta t = \Delta\omega$. The result of this procedure, known as *phase-ramping* [Pat91], is that the frequency of the output signal of the phase shifter is $\delta\phi/\delta t$ higher than ω_{rf} , the frequency at the input of the phase shifter. This is expressed by replacing Eq. 4.6 by

$$\mathcal{H}_{rf} = \hbar\omega_1 \left\{ \cos \left[\omega_{rf}t + \left(\phi_0 + \frac{\delta\phi}{\delta t}t \right) \right] I_x + \sin \left[\omega_{rf}t + \left(\phi_0 + \frac{\delta\phi}{\delta t}t \right) \right] I_y \right\}$$

⁴Strictly speaking, one could use non-universal pulses in the early stages of certain algorithms, or during the state preparation sequences, but we have never done this.

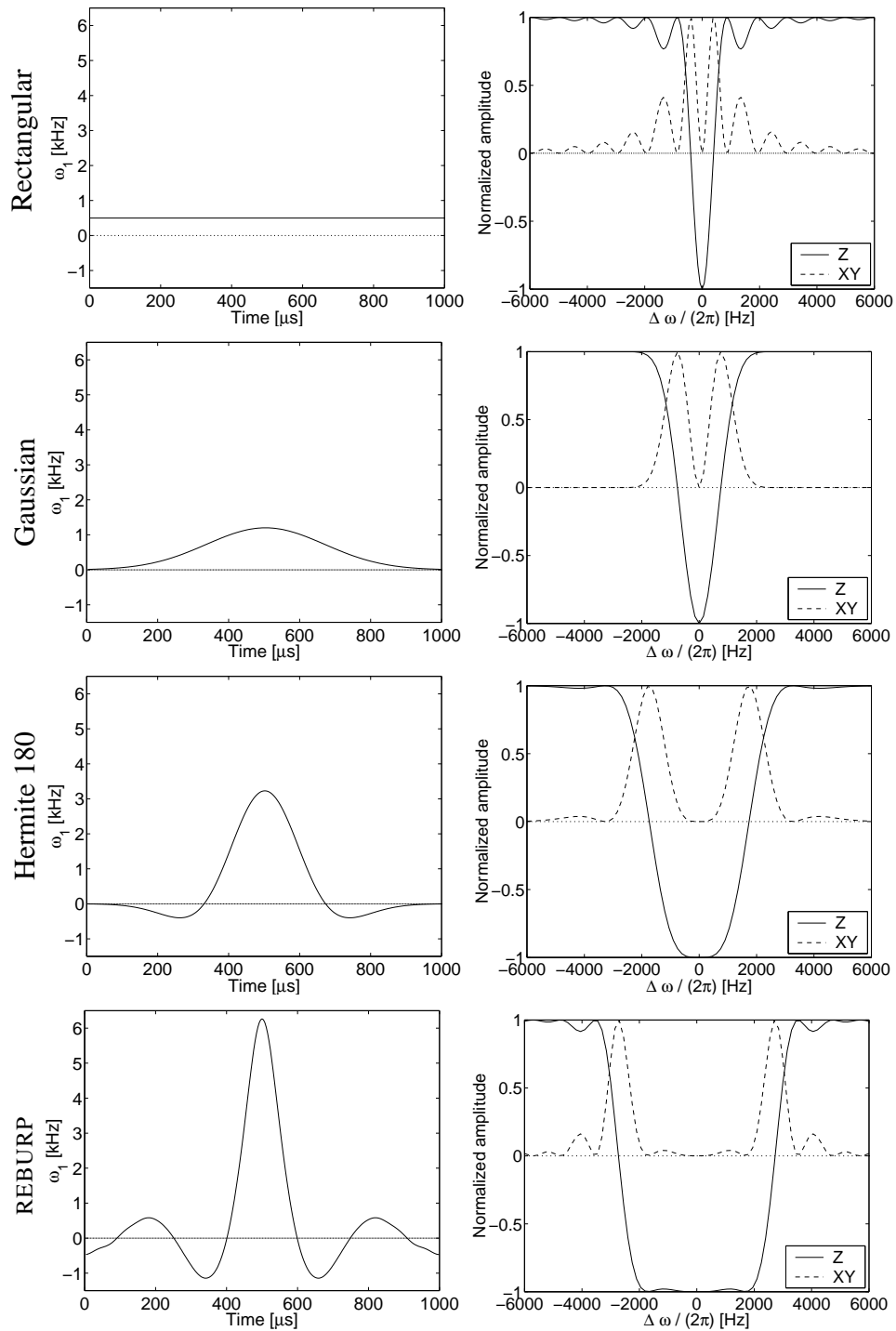


Figure 4.7: (Left) Time profile and (Right) frequency excitation profiles (displaying the z and xy component of the Bloch vector after a pulse when the Bloch vector is along $+\hat{z}$ before the pulse) for four relevant pulse shapes.

$$= \hbar\omega_1 \left\{ \cos \left[\left(\omega_{rf} + \frac{\delta\phi}{\delta t} \right) t + \phi_0 \right] I_x + \sin \left[\left(\omega_{rf} + \frac{\delta\phi}{\delta t} \right) t + \phi_0 \right] I_y \right\}. \quad (4.15)$$

In practice, the continuous phase ramp is approximated by discrete steps $\Delta\phi$ from one time slice of duration Δt to the next, such that $\Delta\phi/\Delta t = \delta\phi/\delta t$. If Δt is short enough such that $\Delta\phi$ is only a few degrees to about 10 degrees, this is a good approximation of a continuous phase ramp.

Excitation at multiple frequencies simultaneously via a single pulse can be accomplished by an extension of phase ramping. Within each time slice, the amplitude and phase of each pulse describe a vector. In order to merge several pulses into a single pulse, it suffices to take the vector sum of all the original pulses within each slice and use this sum to describe the corresponding time slice of the combined pulse.

	selectivity	transition range	power	self-refocusing	robustness
Rectangular	poor	very wide	minimal	no	good
Gauss 90 [BFF ⁺ 84]	excellent	wide	low	fair	good
Gauss 180 [BFF ⁺ 84]	excellent	wide	low	fair	good
Hrm 90 [War84]	moderate	moderate	average	good	fair
Hrm 180 [War84]	good	moderate	average	very good	fair
UBURP 90 [GF91]	poor	narrow	high	excellent	poor
REBURP 180 [GF91]	poor	narrow	high	excellent	poor
AV 90 [AV93]	fair	moderate	average	good	fair

Table 4.2: Properties of relevant pulse shapes

4.2.4 Single pulses - artefacts and solutions

Bloch-Siegert shifts

The presence of RF irradiation during pulses causes a shift $\Delta\omega_{BS}$ in the precession frequency of spins at frequencies well outside the excitation frequency window [EB90]. This effect has become known as a transient (generalized) Bloch-Siegert shift⁵; at a deeper level, the acquired phase can be understood as an instance of Berry's phase [Ber84]. The magnitude of $\Delta\omega_{BS}$ is approximately $\omega_1^2/2(\omega_{rf} - \omega_0)$ (for $\omega_1 \ll \omega_{rf} - \omega_0$), where $\omega_0/2\pi$ is the Larmor frequency in the absence of an RF field. The frequency shifts can easily reach several hundred Hz and the direction of the shift is always away from the frequency of the RF field.

⁵The original paper by Bloch and Siegert [BS40] refers to the frequency shift produced by the counter-rotating RF field (see page 90), but the term Bloch-Siegert shift has been used in a generalized sense in the NMR community.

Each spin thus accumulates a spurious phase shift during RF pulses applied to spins at nearby frequencies. Since ω_1 varies over time for shaped pulses, the Bloch-Siegert shift generally varies throughout the pulse, but the cumulative phase shifts can be easily computed in advance for each possible spin-pulse combination, if all the frequency separations, pulse shapes and pulse lengths are known. The unintended phase shifts $R_z(\theta)$ can then be compensated for during the execution of a pulse sequence by inserting appropriate $R_z(-\theta)$. This is easy to do, especially if software reference frames are used (section 4.2.2).

Coupled evolution during pulses

Spins within the same molecule interact with each other via the J coupling (Eq. 4.4). This interaction forms the basis for two-qubit gates (section 4.3), but the spin-spin interactions cannot be turned off and are thus also active during the RF pulses, which are intended to be just single-qubit transformations. For short pulses at high power, J is very small compared to ω_1 so the coupled evolution which takes place during the pulses is negligible. However, for soft pulses, ω_1 is often of the same order of magnitude as J , and in this case the coupling terms strongly affect the intended nutation, in a way similar to off-resonance effects (Fig. 4.6): coupling to another spin shifts the spin frequency to $\omega_0/2\pi \pm J/2$, so a pulse sent at $\omega_0/2\pi$ hits the spin off-resonance by $\pm J/2$.

Fortunately, specialized pulse shapes exist which minimize the effect of coupling during the pulses (see Table 4.2). Such *self-refocusing* pulses [GF91] take a spin over a complicated trajectory in the Bloch sphere, in such a way that the net effect of couplings between the selected and non-selected spins is reduced. It is as if those couplings are only in part or even not at all active during the pulse (couplings between pairs of non-selected spins will still be fully active). Although the self-refocusing behavior of certain shaped pulses can be intuitively explained to some degree, many actual pulse shapes have been the result of numerical optimizations. Table 4.2 summarizes how effective several common pulse shapes are at refocusing the J couplings. A general observation is that it is relatively easy to make 180° pulses self-refocusing, but much harder for 90° pulses.

Complementary to the use of self-refocusing pulses, undesired coupled evolution that still takes place during a pulse can be (in part) *unwound at a different time* in the pulse sequence via a “negative” time evolution (section 4.3.1). A complication in unwinding the coupled evolution is that \mathcal{H}_{rf} and \mathcal{H}_J *do not commute*; this implies that a real pulse cannot be perfectly decomposed into an idealized pulse (no coupling present) followed and/or preceded by a time interval of coupled evolution.

Nevertheless, we found that the coupled evolution is reversed quite well by a negative time interval *both before and after the pulse*,

$$e^{+i\mathcal{H}_J pw \tau / \hbar} e^{-i(\mathcal{H}_{rf} + \mathcal{H}_J) pw / \hbar} e^{+i\mathcal{H}_J pw \tau / \hbar} \approx e^{-i\mathcal{H}_{rf} pw / \hbar}, \quad (4.16)$$

where τ is chosen in each equation such that the approximations are as good as possible according to some matrix distance (we have used the 2-norm distance measure). A negative time interval only before *or* after the pulse,

$$e^{+i\mathcal{H}_J pw \tau/\hbar} e^{-i(\mathcal{H}_{rf} + \mathcal{H}_J) pw/\hbar} \approx e^{-i\mathcal{H}_{rf} pw/\hbar} \approx e^{-i(\mathcal{H}_{rf} + \mathcal{H}_J) pw/\hbar} e^{+i\mathcal{H}_J pw \tau/\hbar}, \quad (4.17)$$

is much less effective. This is can be seen from Table 4.3, which we will now discuss.

For Gaussian 90° pulses, the J_{1i} evolution, which doesn't commute with X_1 , is unwound much better by two symmetrically placed negative time evolution intervals of duration $pw \tau$ than by a single τ (we will from now on leave pw implicit; τ will be in units of pw throughout) before or after the pulse. Furthermore, while evolution under J_{ij} ($i, j \neq 1$) commutes with a pulse on spin 1 and can thus be perfectly reversed, the optimal values of τ to unwind J_{1i} and J_{jk} evolution lie much closer together if the τ 's are placed symmetrically.

Hermite shaped 180° pulses are self-refocusing, so J_{1i} is not active during the pulse and need not be reversed. In the asymmetric scheme with only a single τ either before or after the pulse, τ must thus be 0 such that no J_{1i} evolution is introduced. However, in order to unwind J_{ij} , we need τ to be 1. We can thus not take care of both J_{1i} and J_{ij} in the asymmetric scheme. In contrast, a symmetric pair of intervals τ separated by a 180° pulse on spin 1 gives net zero J_{1i} evolution for any value of τ . We can thus set τ to the optimal value for unwinding J_{jk} and obtain an excellent net single-qubit 180° rotation.

gauss90	$X_1\tau$	$\tau X_1\tau$
J_{1i}	fair, $\tau \approx 0.6$	excellent, $\tau \approx 0.57$
J_{ij}	perfect, $\tau = 1$	perfect, $\tau = 0.5$
J_{1i}, J_{ij}	fair, $(0.6 <) \tau < 1$	very good, $0.5 < \tau < 0.57$

hrm180	$X_1\tau$	$\tau X_1\tau$
J_{1i}	excellent, $\tau = 0$	excellent, $\forall \tau$
J_{ij}	perfect, $\tau = 1$	perfect, $\tau = 0.5$
J_{1i}, J_{ij}	poor, $0 < \tau < 1$	excellent, $\tau = 0.5$

Table 4.3: Comparison of the degree to which J -coupled evolution during a single pulse on spin 1 is unwound via asymmetric versus symmetric negative time intervals τ (expressed as a fraction of the duration of pw), for various coupling scenarios. The optimal τ is indicated in each case.

In practice, we have used the symmetrized decomposition of Eq. 4.16 in order to obtain a first order improvement in the unitary evolution. Further fine-tuning can be done if different negative evolution times are allowed to unwind different coupling terms. Higher-order corrections are in principle possible because the undesired evolution is known and can be fully characterized, although such a scheme would be substantially more complicated to implement.

Also, with the degree of control in current implementations, it is unclear if such higher order corrections would be effective. Finally, if the input state is diagonal, as is the case in many input state preparation pulse sequences, couplings that do not involve the selected spin (e.g. J_{23} during X_1 pulses) have no effect, and need not be unwound. In this case, τ should be optimized to refocus just the J_{1i} couplings.

It is clear that properly controlling non-commuting terms in the Hamiltonian will be a recurring challenge for virtually any proposed quantum computer implementation. We believe that the development of a *general* (as opposed to an ad-hoc) and *practical* method for removing the effect of select terms in the Hamiltonian constitutes an important and interesting open problem.

4.2.5 Simultaneous pulses - artefacts and solutions

Simultaneous pulses, as opposed to consecutive pulses, are desirable for quantum computation because they help keep the pulse sequence within the coherence time. However, the effects of Bloch-Siegert shifts, discussed in the previous section for single pulses, are aggravated during simultaneous pulses. The effect of J couplings during simultaneous pulses also deserves a separate discussion.

Bloch-Siegert shifts

The Bloch-Siegert shifts introduced in the previous section result in additional problems during *simultaneous pulses* applied to two or more spins *at nearby frequencies*. If we apply spin-selective pulses simultaneously to two spins 1 and 2 with resonance frequencies ω_0^1 and ω_0^2 (say $\omega_0^1 < \omega_0^2$), the pulse at ω_0^1 temporarily shifts the frequency of spin 2 to $\omega_0^2 + \Delta\omega_{BS}$. As a result, the pulse on spin 2, which is still applied at ω_0^2 , will be off-resonance by an amount $-\Delta\omega_{BS}$. Analogously, the pulse at ω_0^1 is now off the resonance of spin 1 by $\Delta\omega_{BS}$. The resulting rotations of the spins deviate significantly from the intended rotations.

Fig. 4.8 shows the simulated inversion profiles for a spin subject to two simultaneous Hermitian 180° pulses separated by 3273 Hz. The centers of the inversion profiles have shifted away from the intended frequencies and the inversion is incomplete, which can be seen most clearly from the substantial residual xy -magnetization ($> 30\%$) over the whole region intended to be inverted. Note that since the frequencies of the applied pulses are off the spin resonance frequencies, perfect rotations cannot be achieved no matter what tip angle is chosen. In practice, simultaneous soft pulses at nearby frequencies have been avoided in NMR [LKF99] or the poor quality of the spin rotations was accepted.

We have developed an effective, intuitive, albeit simple procedure [SVC00]⁶ to address this problem, as an alternative to the existing brute force optimizations [PRN91]: the rotations of

⁶The idea for this technique is due to Matthias Steffen, inspired by discussions between Matthias and myself. We worked out and refined this method together.

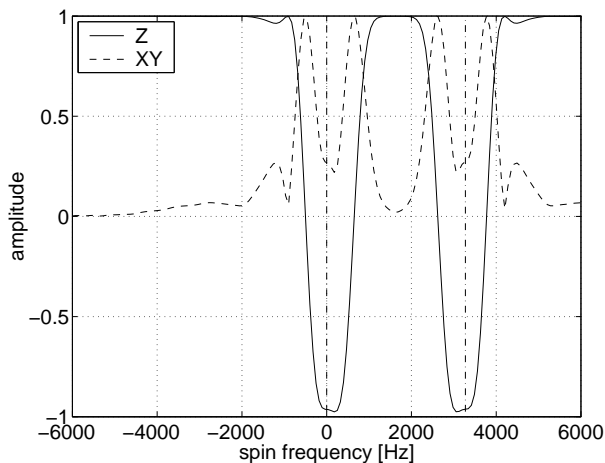


Figure 4.8: Simulation of the amplitude of the z and xy component of the magnetization of a spin as a function of its frequency. The spin starts out along $+\hat{z}$ and is subject to two simultaneous Hermitian shaped pulses with carrier frequencies at 0 Hz and 3273 Hz (vertical dashed lines), with a calibrated pulse length of $2650\mu\text{s}$ (ideally 180°).

the spins can be significantly improved simply by shifting the carrier frequencies (in practice most easily done via the phase-ramping techniques described in section 4.2.3) such that they track the shifts of the corresponding spin frequencies. This way, the pulses are always applied on-resonance with the corresponding spins. The calculation of the frequency shift throughout a shaped pulse is straightforward and needs to be done only once, at the start of a series of experiments.

Fig. 4.9 shows the simulated inversion profiles for the same conditions as in Fig. 4.8, but this time using the frequency shift corrected scheme. The inversion profiles are much improved and there is very little left-over xy magnetization.

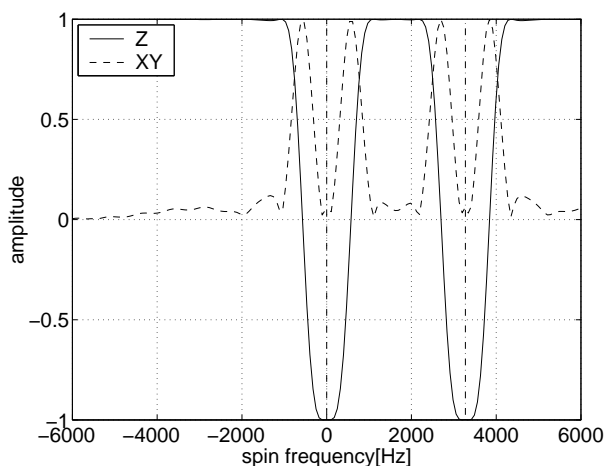


Figure 4.9: Similar to Fig. 4.8 but *with* the frequency shift correction.

We simulated the inversion profiles for a variety of pulse widths and frequency separations, for hermite shaped, gaussian shaped and REBURP pulses, and verified that the same technique can be used to correct the frequency offsets caused by three or more simultaneous soft pulses at nearby frequencies. The improvement is particularly pronounced when the frequency window of the shaped pulse is two to eight times the frequency separation between the pulses, with improvements in the accuracy of the unitary operator up to a factor of fifteen. In all cases the improvements are impressive, illustrating the robustness and versatility of this method [SVC00].

We have experimentally confirmed the improvements predicted by the simulations, and used this technique in the experiments of sections 5.9 and 5.10.

Coupled evolution during pulses

The evolution of two coupled spins which are pulsed simultaneously leads to multiple-quantum coherences, even if the pulses are self-refocusing, because the interaction between the two pulses disturbs the self-refocusing behavior [KF95]. Can we compensate for this coupled evolution using negative time evolution before and after? Or is it better to send the pulses back to back? Table 4.4 reviews these questions for the case of gaussian 90° and Hermite 180° pulses.

The back to back Gaussian 90° pulses very poorly unwind any J 's involving one or both selected spins. Using simultaneous pulses and symmetrically placed τ 's, J_{12} is still not very well reversed, but all the J_{1i} and J_{2i} ($i \neq 1, 2$) are unwound very well. J_{ij} ($i, j \neq 1, 2$) always commutes with pulses on spins 1 and 2, and can thus be perfectly unwound, with an optimal value of τ close to the optimal value for reversing the evolution under other J 's. In the end, the achieved unitary evolution is quite good when using simultaneous pulses with negative evolution before and after, as long as J_{12} is not too strong.

Because Hermite shaped 180° pulses are self-refocusing, J_{12} is not active during the back to back pulses and need not be reversed; however, all the other couplings are very poorly unwound when using back to back pulses. During two simultaneous pulses, J_{12} is almost fully active, but can be unwound quite well; the J_{1i} and J_{2i} can be reversed very well too. As always, J_{ij} commutes with pulses on spins 1 and 2, and can thus be perfectly unwound. If the negative evolution is arranged symmetrically (and only then), the optimal values of τ for unwinding the evolution under the respective couplings are all approximately the same, resulting in a very good unitary transformation for simultaneous pulses with symmetric unwinding.

The general conclusion is that it is much better to send the two pulses simultaneously than back to back. Furthermore, as was the case for single pulses, it is by far better to have negative evolution both before and after the pulses.

Even with symmetrically placed negative time intervals and using simultaneous pulses, the coupled evolution which takes place during the pulses is often (depending on the value of the respective J_{ij}) not unwound to the same degree as in the case of single pulses, and $\tau X_1 2\tau X_2 \tau$ may in some cases give better results than simultaneous pulses. However, implementing the

gauss90	$\tau X_1 X_2 \tau$	$\tau X_{1,2} \tau$	$X_{1,2} \tau$
J_{12}	poor, $\tau \approx 0.57$	fair, $\tau \approx 0.5$	poor, $\tau \approx 0.9$
J_{1i}, J_{2i}	poor, $\tau \approx 1.06$	excellent, $\tau \approx 0.57$	fair, $\tau \approx 0.57$
J_{12}, J_{1i}, J_{2i}	poor, $0.57 < \tau < 1.15$	good, $(0.5 <) \tau < 0.57$	poor, $0.45 < \tau < 0.65$
J_{ij}	perfect, $\tau = 1$	perfect, $\tau = 0.5$	perfect, $\tau = 1$

hrm180	$\tau X_1 X_2 \tau$	$\tau X_{1,2} \tau$	$X_{1,2} \tau$
J_{12}	excellent, $\tau = 0$	good, $\tau \approx 0.45$	good, $\tau \approx 0.9$
J_{1i}, J_{2i}	poor, $\tau > 0$	excellent, $\forall \tau$	excellent, $\tau = 0$
J_{12}, J_{1j}, J_{2i}	poor, $\tau = 0$	very good, $\tau \approx 0.45$	poor, $0 < \tau < 0.9$
J_{ij}	perfect, $\tau = 1$	perfect, $\tau = 0.5$	perfect, $\tau = 1$

Table 4.4: Comparison of the degree to which J -coupled evolution during two pulses is unwound for three scenario's: (1) two pulses back to back preceded and followed by negative evolution, (2) two simultaneous pulses preceded and followed by negative evolution, and for comparison (3) two simultaneous pulses only followed by negative evolution. The optimal τ is indicated in each case.

negative time evolution in between the two pulses makes the pulse sequence much longer.

In the experiments, we have also used three simultaneous pulses. Similar arguments for the compensation of J -coupled evolution as those we made for two simultaneous pulses, hold for three or more simultaneous pulses.

4.3 Two-qubit operations

4.3.1 The controlled-NOT in a two-spin system

The basis for two-qubit gates in NMR is the pairwise interaction between spins in the same molecule, described in section 4.1.2. The most natural two-qubit gate between nuclear spins in a molecule is therefore an evolution under the coupling Hamiltonian of Eq. 4.4 for a duration t ,

$$U_J(t) = \exp[-i2\pi J I_z^1 I_z^2 t] = \begin{bmatrix} e^{-i\pi J t/2} & 0 & 0 & 0 \\ 0 & e^{+i\pi J t/2} & 0 & 0 \\ 0 & 0 & e^{+i\pi J t/2} & 0 \\ 0 & 0 & 0 & e^{-i\pi J t/2} \end{bmatrix}. \quad (4.18)$$

Because of the central importance of the controlled-NOT gate in the theory of quantum computation (section 2.2), we shall now discuss the implementation of the CNOT gate using the J coupling.

A first possible implementation of the CNOT gate consists of applying a line-selective 180° pulse at $\omega_0^2 + J_{12}/2$. This pulse inverts spin 2 (the target qubit) if and only if spin 1 (the control)

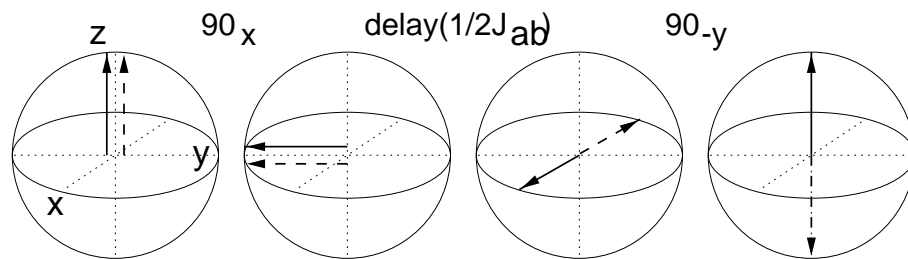


Figure 4.10: Bloch-sphere representation of the operation of the CNOT_{12} gate between two nuclear spins 1 and 2 in a molecule. Spin 2 is shown in a reference frame rotating about \hat{z} at $\omega_0^2/2\pi$, in case spin 1 is $|0\rangle$ (solid line) and $|1\rangle$ (dashed line).

is $|1\rangle$ [CPH98]. In general, if a spin is coupled to more than one other spin, half the lines in the multiplet must be selectively inverted. This is usually very impractical and it may in fact be impossible when some of the lines in the multiplet fall on top of each other.

An alternative and more widely used implementation of the CNOT gate is illustrated in Fig. 4.10 [GC97]. First, a spin-selective pulse on spin 2 about \hat{x} (an rf pulse centered at $\omega_0^2/2\pi$ and of a spectral bandwidth such that it covers the frequency range $\omega_0^2/2\pi \pm J_{12}/2$ but not $\omega_0^1/2\pi$), rotates spin 2 from $+\hat{z}$ to $-\hat{y}$. Then the spin system is allowed to freely evolve for a duration of $1/2J_{12}$ seconds. Because the precession frequency of spin 2 is shifted by $\pm J_{12}/2$ depending on whether spin 1 is in $|1\rangle$ or $|0\rangle$, after $1/2J$ seconds spin 2 will have rotated to either $+\hat{x}$ or to $-\hat{x}$ (in the reference frame rotating at $\omega_0^2/2\pi$), depending on the state of spin 1. Finally, a 90° pulse on spin 2 about the $-\hat{y}$ axis (still in the rotating frame) rotates spin 2 back to $+\hat{z}$ if spin 1 is $|0\rangle$, or to $-\hat{z}$ if spin 1 is in $|1\rangle$. The net result is that spin 2 is flipped if and only if spin 1 is in $|1\rangle$, which corresponds exactly to the classical truth table for the CNOT presented in Fig. 2.5.

However, a sequence as in Fig. 4.10 actually implements the unitary transformation

$$X_2 U_J(1/2J) Y_2 = \tilde{U}_{\text{CNOT}_{12}} = \begin{bmatrix} 1 & 0 & 0 & 0 \\ 0 & i & 0 & 0 \\ 0 & 0 & 0 & -i \\ 0 & 0 & 1 & 0 \end{bmatrix}, \quad (4.19)$$

which is similar to but different from U_{CNOT} of Eq. 2.51. An additional phase shift on both spins is needed in order to obtain U_{CNOT} exactly:

$$Z_1 \bar{Z}_2 X_2 U_J(1/2J) Y_2 = U_{\text{CNOT}_{12}} = \begin{bmatrix} 1 & 0 & 0 & 0 \\ 0 & 1 & 0 & 0 \\ 0 & 0 & 0 & 1 \\ 0 & 0 & 1 & 0 \end{bmatrix}. \quad (4.20)$$

4.3.2 Refocusing select J couplings

The coupling terms in the Hamiltonian of nuclear spins in a molecule are given by nature and cannot be turned off. Therefore, in order to implement a CNOT_{ij} in a molecule with n coupled spins, we need a means to effectively deactivate all couplings except J_{ij} . This is done in NMR by *refocusing* the undesired coupled evolutions via a sequence of 180° pulses, in a similar way as is done in spin-echo experiments.

Fig. 4.11 pictorially shows how refocusing pulses can neutralize the J coupling between two spins. In (a), the evolution of spin 1 which takes place in the first time interval is reversed in the second time interval, due to the 180° pulse on spin 2. In (b), spin 1 continues to evolve in the same direction the whole time, but still comes back to its initial position thanks to the 180° pulse on spin 1. The second 180° pulse is needed to ensure that both spins return to their initial state regardless of the initial state. We note that if refocusing pulses are sent on both spins simultaneously, the coupling is active again.

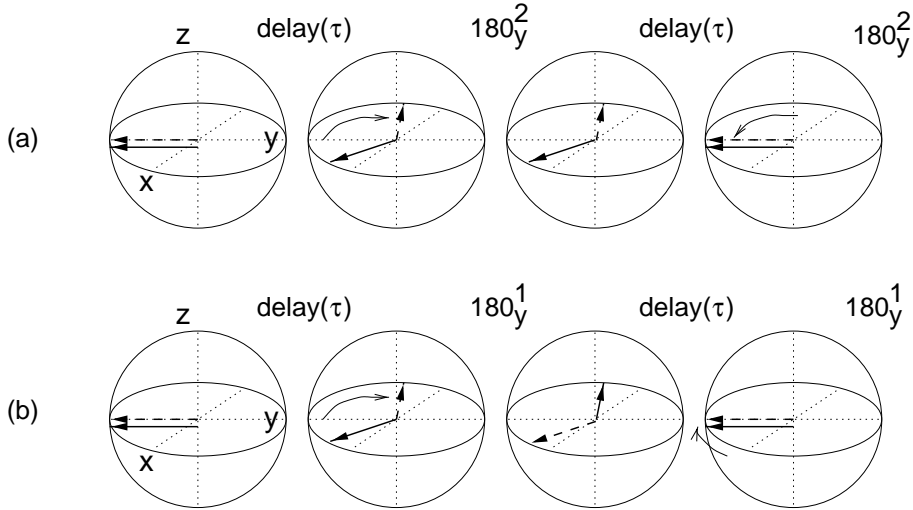


Figure 4.11: Bloch-sphere representation of the operation of a simple scheme to refocus the coupling between two coupled spins. The diagram shows the evolution of spin 1 (in the rotating frame) initially along $-\hat{y}$, when spin 1 is in $|0\rangle$ (solid) or in $|1\rangle$ (dashed).

Mathematically, we can see how refocusing of J couplings works via

$$X_1^2 U_J(\tau) X_1^2 = U_J(-\tau) = X_2^2 U_J(\tau) X_2^2, \quad (4.21)$$

which leads to

$$X_1^2 U_J(\tau) X_1^2 U_J(\tau) = I = X_2^2 U_J(\tau) X_2^2 U_J(\tau) \quad (4.22)$$

for all values of τ (all X_i^2 may also be Y_i^2).

Fig. 4.12 shows a refocusing scheme which preserves the effect of the J_{12} coupling in a four spin system, while effectively inactivating all the other couplings. The underlying idea is that a

coupling between spins i and j acts “forward” during intervals where both spins have the same sign in the diagram, and acts “in reverse” whenever the spins have opposite signs. Whenever a coupling acts forward and in reverse for the same duration over the course of a refocusing scheme, it has no net effect. If the forward and reverse evolutions are not balanced in duration, a net coupled evolution takes place corresponding to the excess forward or reverse evolution.

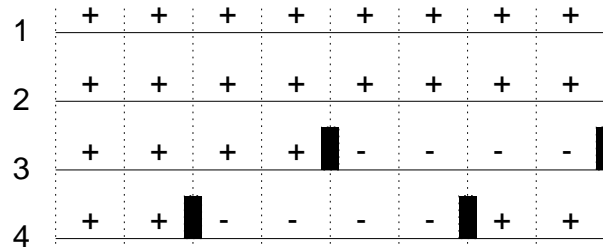


Figure 4.12: Refocusing scheme for a four spin system. J_{12} is active the whole time but the effect of the other J_{ij} is neutralized. The interval is divided into slices of equal duration, and the “+” and “-” signs indicate whether a spin is still in its original position, or upside down. At the interface of certain time slices, 180° pulses (assumed to be instantaneous, and shown as black rectangles) are sent on one or more spins; the pulsed spins transition from + to – or back.

Systematic methods for designing refocusing schemes for multi-spin systems have been developed specifically for the purpose of quantum computing. The most compact scheme is based on Hadamard matrices [LCYY00, JK99], but this is also the experimentally most demanding, as it requires that many spins be pulsed simultaneously. On the other extreme are schemes without any simultaneous pulses [LBCF99], but which take significantly longer.

Finally, we point out that refocusing schemes can be considerably simplified if we know that certain spins are along the \hat{z} axis, because the J coupling does not affect spins along the \hat{z} axis. This is a common situation in the early stages of a quantum computation. Fig. 4.13 gives such a simplified refocusing scheme for five coupled spins.

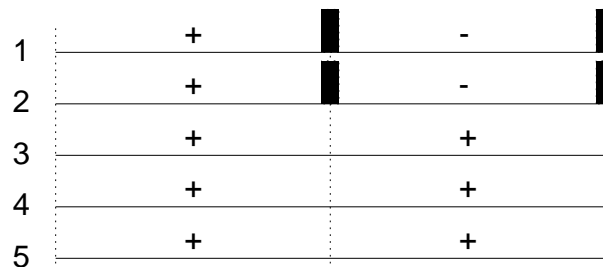


Figure 4.13: Simplified refocusing scheme for five spins, which can be used if we know in advance that spins 3, 4 and 5 are along $\pm\hat{z}$. J_{12} is active, but J_{13} , J_{14} , J_{15} , J_{23} , J_{24} , J_{25} are inactive. The remaining couplings are active but have no effect given the initial state.

Negative time evolution

It is sometimes necessary to implement a unitary transformation which corresponds to a free evolution under certain couplings for a negative time. From the preceding paragraphs, we see that this can be achieved using a refocusing sequence where the desired couplings evolve in reverse for a longer time than they act forward.

Starting from an existing refocusing scheme, negative evolutions can thus be obtained simply by *reducing the appropriate delay times*. Of course, the effective negative time evolution obtained in this way cannot be longer than the original delay times. If longer negative delay times are needed, we can *increase the remaining delay times* in order to increase the imbalance between forward and reverse evolutions for the desired couplings.

If there is no refocusing sequence already in place which can be changed, realizing negative time evolution under certain couplings requires an additional refocusing sequence. This is obviously to be avoided if possible.

Coupling network considerations

For systems with more than two spins, two complications arise when performing two-qubit gates. They are illustrated by the two extreme coupling networks in Fig. 3.1 (a) and (b). First, if two spins are not directly coupled to each other, a CNOT between these two spins must be done using intermediary spins (see section 3.1.2, p. 55) [CKH⁺00]. Second, if every spin is coupled to every other spin (this is possible only in relatively small molecules), the pulse sequence of Fig. 4.10 must be supplemented by a complex refocusing scheme which selects only the desired coupling.

Clearly, both scenarios are associated with a considerable overhead. It is important to note that this overhead is only polynomial (at most quadratic) in the number of qubits. A CNOT between any two qubits along a chain of n spins with just nearest-neighbour couplings takes at most $2(n - 2)$ swap operations, and a Hadamard based refocusing scheme between n fully coupled spins takes at most n time segments and no more than n 180° pulses per segment.

From a computer science point of view, the overhead during two-qubit gates is thus almost irrelevant, as it does not affect the efficiency (polynomial versus exponential cost) of an algorithm. From an experimentalist's point of view, the overhead is of course significant given the limited state-of-the-art in experimental quantum computing. Any possibility for minimizing the number of refocusing or swap operations, for example by mapping the coupling network onto the particular algorithm at hand, should therefore be exploited. Furthermore, this overhead does potentially negate the benefits of quadratic speed-ups obtained in algorithms such as Grover's.

4.4 Qubit initialization

4.4.1 The initial state of nuclear spins

Nuclear spins in thermal equilibrium

The experimentally most accessible state is the state where the spin is in *thermal equilibrium with the environment*, described by

$$\rho_{eq} = \frac{\exp -\mathcal{H}_0/k_B T}{\mathcal{Z}} = \frac{1}{\mathcal{Z}} \begin{bmatrix} e^{-\hbar\omega_0/2k_B T} & 0 \\ 0 & e^{+\hbar\omega_0/2k_B T} \end{bmatrix} \quad (4.23)$$

so the spin statistics are given by the Boltzman distribution,

$$\Pr[|0\rangle] = \frac{e^{-\hbar\omega_0/2k_B T}}{\mathcal{Z}} = \frac{e^{-\hbar\omega_0/2k_B T}}{e^{-\hbar\omega_0/2k_B T} + e^{+\hbar\omega_0/2k_B T}} \quad (4.24)$$

$$\Pr[|1\rangle] = \frac{e^{+\hbar\omega_0/2k_B T}}{\mathcal{Z}} = 1 - \Pr[|0\rangle]. \quad (4.25)$$

For typical magnetic field strengths (about 10 Tesla), $\hbar\omega_0/k_B T \approx 10^{-5} \ll 1$, so we can very well approximate the exponentials in Eqs. 4.23-4.25 via the first order Taylor expansion,

$$\rho_{eq} \approx \frac{1}{2} \begin{bmatrix} 1 + \hbar\omega_0/2k_B T & 0 \\ 0 & 1 - \hbar\omega_0/2k_B T \end{bmatrix}, \quad (4.26)$$

and the spin polarization (Eq. 3.6) in thermal equilibrium, ϵ_0 , is

$$\epsilon_0 = \hbar\omega_0/2k_B T \ll 1. \quad (4.27)$$

Since $\hbar\omega_0/k_B T \approx 10^{-5} \ll 1$, we have that $\Pr[|0\rangle] \approx \Pr[|1\rangle]$.

Similarly, the state of n spins in thermal equilibrium is described by

$$\rho_{eq} \approx \frac{1}{2^n} \begin{bmatrix} 1 + \sum_k^n \frac{\hbar\omega_0^k}{2k_B T} & & & \\ & 1 - \frac{\hbar\omega_0^n}{2k_B T} + \sum_k^{n-1} \frac{\hbar\omega_0^k}{2k_B T} & & \\ & & \ddots & \\ & & & 1 - \sum_k^n \frac{\hbar\omega_0^k}{2k_B T} \end{bmatrix}, \quad (4.28)$$

where we have neglected the effect of the coupling energies, a perfectly valid approximation at typical magnetic fields (10 Tesla), as $\hbar\omega_0$ is about 10^6 times larger than $\hbar 2\pi J_{ij}$.

The 2^n possible states of n spins then occur with almost equal probabilities; we cannot know in which state a thermally equilibrated n -spin system really is⁷. The situation we desire is very different: a single and known state (say the $|00 \dots 0\rangle$ state) should be occupied with probability

⁷It may appear that we do know the state very well, namely ρ_{eq} of Eq. 4.28, but it is important to note that this density matrix represents a statistical mixture of states. The mixedness expresses precisely our uncertainty about whether each spin is up or down.

1.

Hyperpolarization

Various physical cooling methods could be used to boost the polarization of the spins. Cooling the liquid NMR sample down to the milli-Kelvin regime would result in very high polarizations. However, the sample would be frozen, so the molecules wouldn't be able to tumble around as is the case in liquids, and as a result, dipolar couplings would be reintroduced. Intramolecular dipolar couplings complicate the spin dynamics and intermolecular couplings result in broad spectral lines. Several proposals [YY99, LGD⁺00, CLK⁺00] exist to address these complications (see also section 3.2.5) and it is conceivable that quantum computers will be realized using solid-state NMR in the future.

The use of optical pumping [FSH98] for polarization enhancement has already been demonstrated in a two-qubit molecule ($^{13}\text{CHCl}_3$) in liquid solution, which was then used for a quantum computation [VLV⁺01]. The pumping procedure consists of several steps. First, the spin of an unpaired electron in vaporized rubidium is hyperpolarized by shining circularly polarized laser light on the D1 electronic transition of Rb. Then the Rb vapor is mixed with xenon gas, and polarization is transferred from the Rb electron spin to the ^{129}Xe nuclear spins as Van der Waals molecules are formed or two-body collisions take place. Finally, the hyperpolarized ^{129}Xe is mixed with the quantum computer molecule and polarization is transferred (via SPINOE cross-relaxation) to the spins which serve as quantum bits. Qubit polarization enhancements by a factor of 10 to 100 have already been achieved, but the resulting polarization of 10^{-4} to 10^{-3} is still several orders of magnitude away from full polarization.

Two proton spins have recently been polarized to an estimated 10% polarization using *para* hydrogen, and subsequently used in a quantum computation [HBG00]. In thermal equilibrium at 20.4 K (the boiling point of H_2), H_2 contains more than 99% *para* hydrogen. These are dihydrogen molecules with the two ^1H spins in the singlet state. Activated charcoal or some other catalyst is needed to accelerate the *ortho/para* conversion. By reacting $n/2$ *para* hydrogen molecules with an appropriate precursor molecule, an n qubit quantum computer molecule with highly polarized spins can be formed. With this method, polarizations of about 50% should be within reach. However, while finding suitable quantum computer molecules is difficult in itself (section 4.7), the additional requirement that the molecule must be easily formed from a precursor and H_2 presents a substantial limitation.

Other hyperpolarization techniques used in NMR are dynamic nuclear polarization (DNP) [Jef63] and chemically induced dynamic nuclear polarization (CIDNP). In DNP, polarization is transferred from the electron spin in a free radical to the nuclear spins. Since the magnetic moment of an electron spin is about 1800 times stronger than that of nuclear spins, its equilibrium polarization is accordingly higher. These techniques have not yet been demonstrated in combination with a quantum computation.

Clearly, the state of the art in any of the hyperpolarization techniques is still far from producing fully polarized spins useful for quantum computing. Even though these techniques may be significantly further developed in the future, we must look for other state initialization procedures if we want to study quantum computation with room temperature spins today.

4.4.2 Effective pure states

The use of room temperature nuclear spins for quantum computing has been made possible by the invention of *effective pure* states, or *pseudo-pure* states, briefly introduced on page 60. This surprising concept makes an ensemble of nuclear spins at room temperature look as if it were at zero temperature, up to a decrease in signal strength.

The starting point is a well-known fact, namely that the NMR signal is proportional to population *differences*, irrespective of the populations themselves. Thus, a density matrix proportional to the identity matrix does not produce a signal — for every molecule in which a spin points one way, there is another molecule where the corresponding spin points the opposite way, so their signals cancel out. Mathematically, we say that the observables in NMR are traceless (see section 4.5). Furthermore, $UIU^\dagger = I$, that is the identity matrix does not transform under unitary transformations. We thus need to concern us only with the *deviation density matrix* ρ_Δ , the component of the density matrix which deviates from the identity background:

$$\rho_\Delta = \rho - I/2^n, \quad (4.29)$$

where we assume that ρ is normalized, that is $\text{Tr}(\rho) = 1$.

Gershenfeld and Chuang [GC97], and independently Cory, Havel and Fahmy [CFH97, CPH98], then observed that a density matrix of the form of Eq. 3.5,

$$\rho_{\text{eff}} = \frac{1 - \alpha}{2^n} I + \alpha |\psi\rangle\langle\psi|. \quad (4.30)$$

gives the signal and has the dynamical behavior of just the second term, $|\psi\rangle\langle\psi|$, which represents a pure state. We therefore call ρ_{eff} an effective pure state, or pseudo-pure state.

Written out in matrix form for $|\psi\rangle = |00\dots 0\rangle$, Eq. 4.30 becomes

$$\rho_{\text{eff}} = \frac{1 - \alpha}{2^n} \begin{bmatrix} 1 & & & \\ & 1 & & \\ & & \ddots & \\ & & & 1 \end{bmatrix} + \alpha \begin{bmatrix} 1 & & & \\ & 0 & & \\ & & \ddots & \\ & & & 0 \end{bmatrix}. \quad (4.31)$$

We see that the signature of an effective pure basis state of n spins is that the density matrix ρ_{eff} is diagonal and that *all the diagonal entries (populations) are equal, except one*, in this case the

first entry (the ground state population).

How do we obtain ρ_{eff} (Eq. 4.30) from ρ_{eq} (Eq. 4.28) ? The procedure for preparing effective pure states must incorporate a non-unitary step one way or another as the eigenvalues of ρ_{eq} and ρ_{eff} are not the same. Three methods are known to do this: logical labeling[GC97], spatial averaging[CPH98] and temporal averaging[KCL98]. Logical labeling consists of the selection of a subspace of the Hilbert space, in which all subsequent computations take place. In temporal averaging, the output spectra of separate, consecutive experiments are added together (each with a different state preparation sequence). Spatial averaging is similar to temporal averaging, but averaging takes place over space instead of over time.

These three methods will be explained in detail in the next three sections. To date, temporal and spatial averaging have been the most widely used techniques for preparing effective pure states. Several hybrid schemes [KCL98, KLMT00] have also been developed which trade off complexity of the preparation steps for the number of experiments.

Unfortunately, as we shall see, all these state preparation schemes have in common that creating effective pure states incurs an exponential cost either in the signal strength or in the number of consecutive experiments involved. The reason for this cost is that effective state preparation techniques simply select out the signal from the ground state population present in thermal equilibrium and the fraction of the molecules in the ground state is proportional to $n/2^n$. Such an exponential overhead obviously defeats the purpose of quantum computation, but is not problematic for experiments with small numbers of qubits.

4.4.3 Logical labeling

Logical labeling [GC97, VYSC99] consists of applying a pulse sequence which rearranges the thermal equilibrium populations such that a subset of the spins is in an effective pure state, conditioned upon the state of the remaining spins. Then the computation is carried out within this embedded subsystem. This concept of embedding was previously used to observe Berry's phase in NMR spectroscopy [SPM86].

For example, the thermal equilibrium deviation density matrix for a homonuclear three-spin system is approximately

$$000 \ 001 \ 010 \ 011 \ 100 \ 101 \ 110 \ 111$$

$$\rho_{eq} = \frac{1}{2^3} \frac{\hbar\omega_0}{2k_B T} \begin{bmatrix} 3 & & & & & & & \\ & 1 & & & & & & \\ & & 1 & & & & & \\ & & & -1 & & & & \\ & & & & 1 & & & \\ & & & & & -1 & & \\ & & & & & & -1 & \\ & & & & & & & -3 \end{bmatrix}, \quad (4.32)$$

where the labels above the density matrix help identify the populations of the respective states. We note that the populations within the *subspace* spanned by the states $|000\rangle$, $|011\rangle$, $|101\rangle$ and $|110\rangle$ naturally have the signature of an effective pure state.

In order to simplify subsequent logical operations and to separate the signals of the effective pure subspace and its complement, the populations can be rearranged by a sequence of 1 and 2-qubit unitary operations to obtain

$$\rho_{\text{eff}} = \frac{1}{2^3} \frac{\hbar\omega_0}{2k_B T} \begin{matrix} 000 & 001 & 010 & 011 & 100 & 101 & 110 & 111 \\ \begin{bmatrix} 3 & & & & & & & \\ & 1 & & & & & & \\ & & 1 & & & & & \\ & & & 1 & & & & \\ & & & & -1 & & & \\ & & & & & -1 & & \\ & & & & & & -1 & \\ & & & & & & & -3 \end{bmatrix} \end{matrix}. \quad (4.33)$$

Now the subspace $\{|000\rangle, |001\rangle, |010\rangle, |011\rangle\}$ is in an effective pure state. This subspace corresponds to just spins 2 and 3 conditioned on or *labeled* by the state of the spin 1 being $|0\rangle$ (we will call this the $|0\rangle_1$ subspace). The logical labeling procedure, combined with removal of coupling to spin 1 for the remainder of the pulse sequence, thus allows 2-qubit quantum computations on an effective pure state of spins 2 and 3.

The subspace dimension is limited by the number of equally populated states in equilibrium, which is $C_n^{n/2} = n! / [(n/2)!]^2$ (for even n) in a homonuclear system, giving $k = \log_2(1 + C_n^{n/2})$. Thus for large n , k/n tends to 1 ($n=40$ for $k=37$). For heteronuclear spin systems, the analysis is more complex and k/n is generally smaller, but the number k of cold qubits that logical labeling can extract from n hot spins still scales favorably. The number of operations required to rearrange the populations also scales polynomially with n .

What is the signal strength obtained via logical labeling? We recall that the NMR signal strength is proportional to population differences. For homonuclear systems with even n , the $C_n^{n/2}$ equal entries in ρ_{eq} (and thus ρ_{eff}) are all zero (for large odd n , they are very close to zero).

The largest entry in ρ_{eq} is $n\hbar\omega_0/2^n 2k_B T$. The maximum signal strength S obtainable from a logically labeled state thus scales as $n/2^n$. Since only one experiment is involved, the noise N is independent of n . The dependence of the signal-to-noise ratio on n is thus

$$\frac{S}{N} \propto \frac{n}{2^n} \quad (4.34)$$

In section 5.5, we will present an implementation of logical labeling on a three-spin system. Despite its elegance, the logical labeling procedure has not been used much in practice. The main reason is that one or more spins must be sacrificed as labeling spins, and extra spins are still very “expensive” due to the difficulty of finding large molecules with suitable properties for quantum computing.

4.4.4 Temporal averaging

Temporal labeling consists of adding up the spectra of multiple experiments, where each experiment starts off with a different state preparation pulse sequence which permutes the populations. The preparation sequences are designed such that the sum of the resulting input states has the effective pure state signature. By the linearity of quantum mechanics, the sum of the output states of the respective experiments corresponds to the output which would be obtained if the input state were the sum of the respective input states. This will become clear as we discuss three variations of temporal averaging.

Cyclic permutations

The original temporal averaging scheme takes a sum over $2^n - 1$ experiments for an n spin molecule. Each of the state preparation sequences implements a different cyclic permutation of all populations except the ground state population.

For example, suppose the thermal equilibrium density matrix of two spins is

$$\rho_1 = \rho_{eq} = \begin{bmatrix} a & & & \\ & b & & \\ & & c & \\ & & & d \end{bmatrix}, \quad (4.35)$$

where we use a, b, c and d in order to emphasize that this method works for arbitrary initial population distributions. If we cyclicly permute the last three diagonal entries via a unitary

transformation $U_p = U_{\text{cnot}_{12}}U_{\text{cnot}_{21}}$, we obtain

$$\rho_2 = U_p \rho_{eq} U_p^\dagger = \begin{bmatrix} a & & & \\ & d & & \\ & & b & \\ & & & c \end{bmatrix}, \quad (4.36)$$

and if we permute ρ_{eq} with $U_p^2 = U_{\text{cnot}_{21}}U_{\text{cnot}_{12}}$, we get

$$\rho_3 = U_p^2 \rho_{eq} U_p^{\dagger 2} = \begin{bmatrix} a & & & \\ & c & & \\ & & d & \\ & & & b \end{bmatrix}. \quad (4.37)$$

We see that with $\rho_{\text{eff}} = \rho_1 + \rho_2 + \rho_3$ and $e = b + c + d$,

$$\rho_{\text{eff}} = \begin{bmatrix} 3a & & & \\ & e & & \\ & & e & \\ & & & e \end{bmatrix} = e \begin{bmatrix} 1 & & & \\ & 1 & & \\ & & 1 & \\ & & & 1 \end{bmatrix} + (3a - e) \begin{bmatrix} 1 & & & \\ & 0 & & \\ & & 0 & \\ & & & 0 \end{bmatrix}. \quad (4.38)$$

How does the signal-to-noise ratio (SNR) obtained from the resulting summation scale with n ? The ground state populations from all $2^n - 1$ experiments simply add up, and the ground state population of any one experiment goes as $n/2^n$; the noise N increases as the square root of the number of experiments. Thus, with the number of experiments

$$l = 2^n - 1 \quad (4.39)$$

the signal-to-noise ratio goes as

$$\frac{S}{N} \propto \frac{n}{2^n} \frac{2^n - 1}{\sqrt{2^n - 1}} = \frac{n}{2^n} \sqrt{2^n - 1} = \frac{n}{2^n} \sqrt{l}. \quad (4.40)$$

This is the same S/N we would obtain if we signal averaged over l identical logical labeling experiments.

Since the implementation of cyclic permutations becomes rapidly very complex for $n > 2$, we have used this temporal averaging scheme only for experiments on two qubits (sections 5.3-5.4). We have developed the following more practical approach for larger n .

Linearly independent permutations

The purpose of temporal averaging is just to average out differences between $2^n - 1$ populations. This can be done in many ways besides doing cyclic permutations. In fact, for any set of $2^n - 1$ linearly independent population distributions $\text{diag}(\rho_i)$, we can solve for a set of weights v_i such that

$$\rho_{\text{eff}} = \sum_{i=1}^l v_i \rho_i. \quad (4.41)$$

The main advantage is that each of the state preparation pulse sequences can be kept much simpler than the sequences needed for cyclic permutations. Furthermore, while this approach may still require up to $2^n - 1$ experiments to get exactly ρ_{eff} , it is flexible enough that ρ_{eff} can be well approximated using far fewer experiments.

The main disadvantage is that S/N is suboptimal. For l experiments with v_i ,

$$\frac{S}{N} \propto \frac{n}{2^n} \frac{\sum_{i=1}^l v_i}{\sqrt{\sum_{i=1}^l v_i^2}} \leq \frac{n}{2^n} \frac{l}{\sqrt{l}} = \frac{n}{2^n} \sqrt{l}, \quad (4.42)$$

with equality only if all the weights, v_i , are equal to 1. Especially if some of the v_i are negative, the S/N can be quite poor. Nevertheless, we successfully used this method to prepare an effective pure state of $n = 3$ spins (section 5.7), and then used this state as the input state for Grover's algorithm.

Product operator approach

Temporal averaging can be simplified significantly further by taking advantage of the *structure* in the thermal equilibrium and effective pure state density matrices. This structure is most easily understood not in terms of the density matrices themselves but instead of their Pauli matrix expansion. In this description, the thermal equilibrium deviation density matrix for five homonuclear spins is

$$\rho_{\text{eq}} = ZIIII + IZIII + IIZII + IIIZI + IIIIZ \quad (4.43)$$

where we use $IIIIZ$ instead of the more cumbersome notation $\sigma_I \otimes \sigma_I \otimes \sigma_I \otimes \sigma_I \otimes \sigma_z$. For n spins, ρ_{eq} thus consists of n product operator terms. The five-spin effective pure ground state is⁸

$$\rho_{\text{eff}} = ZIIII + \dots + IIIIZ + ZZIII + \dots + IIIZZ + ZZZII + \dots + IIZZZ + ZZZZI + \dots + IZZZZ + ZZZZZ, \quad (4.44)$$

⁸We chose to use $Z = \sigma_z$ instead of $I_z = \sigma_z/2$ in order not to have different powers of two in front of the respective terms ($ZZ = 4I_z I_z$, $ZZZ = 8I_z I_z I_z$ and so forth).

a total of $31 = 2^n - 1$ terms. Using short sequences of CNOT operations, the $n = 5$ terms obtained in equilibrium can be transformed into different sets of five terms, according to the following simple transformation rules, which follow from the definition of the controlled-NOT:

$$II \xrightarrow{\text{CNOT}_{12}} II, \quad (4.45)$$

$$IZ \xrightarrow{\text{CNOT}_{12}} ZZ, \quad (4.46)$$

$$ZI \xrightarrow{\text{CNOT}_{12}} ZI, \quad (4.47)$$

$$ZZ \xrightarrow{\text{CNOT}_{12}} IZ. \quad (4.48)$$

For homonuclear n spin systems, the summation of as few as $\lceil (2^n - 1)/n \rceil$ different experiments thus suffices to create all $2^n - 1$ terms.

This scheme achieves a savings in the number of separate experiments l by a factor of n , compared to cyclic permutations. Furthermore, the S/N is optimal because all the terms are added up with equal and positive weights:

$$l = \frac{2^n - 1}{n}, \quad (4.49)$$

$$\frac{S}{N} = \frac{n}{2^n} \frac{2^n - 1/n}{\sqrt{2^n - 1/n}} = \frac{n}{2^n} \sqrt{l}. \quad (4.50)$$

In practice, it may be advantageous to use slightly more experiments in order to keep the preparation sequences as short as possible. In the five-qubit experiment presented in section 5.9, we used nine experiments, giving a total of $9 \times 5 = 45$ product operator terms in the summation. The fourteen extra terms were canceled out pairwise, using NOT (X_i^2) operations to flip the sign of selected terms, using

$$I \xrightarrow{\text{NOT}} I, \quad (4.51)$$

$$Z \xrightarrow{\text{NOT}} -Z. \quad (4.52)$$

Of course, terms which are canceled out do not contribute to the signal, but they do still contribute to the noise, so this diminishes S/N .

For heteronuclear systems, the situation is slightly more complex, as the terms in Eq. 4.43 must be weighted by the respective ω_i . For example, for a fully heteronuclear five-spin system,

$$\rho_{eq} = \omega_1 ZIIII + \omega_2 IZIII + \omega_3 IIZII + \omega_4 IIIZI + \omega_5 IIIIZ. \quad (4.53)$$

The density matrix obtained via temporal averaging contains the same weights, and may thus not be effective pure. Nevertheless, for partly heteronuclear, partly homonuclear molecules, significant reductions in the number of experiments can be achieved while preserving a good

S/N , as we demonstrated in a seven-spin experiment (section 5.10).

4.4.5 Spatial averaging

Spatial averaging [CPH98] uses a pulse sequence containing *magnetic field gradients* to equalize all the populations except the ground state population. The magnetic field gradient causes spins in different regions of the sample to precess at different frequencies, so their phases are apparently randomized. In fact, the dephasing is not really random and can be undone by applying a reverse field gradient, as long as molecules haven't randomly diffused too far through the sample volume to a region of different magnetic field strength. Either way, the effect on the density matrix is that all the off-diagonal entries (except zero quantum coherences) are erased.

Spatial averaging pulse sequences are most easily understood in terms of product operators too. A possible procedure for two homonuclear spins, in a similar notation as in Eqs. 4.43-4.53, goes as follows [CPH98]:

$$\begin{array}{l} \\ \xrightarrow{R_x^2(60)} \end{array} \quad \begin{array}{l} ZI + IZ \\ ZI + \frac{1}{2}IZ - \frac{\sqrt{3}}{2}IY \end{array} \quad (4.54)$$

$$\xrightarrow{\text{grad}_z} \quad \begin{array}{l} ZI + \frac{1}{2}IZ \end{array} \quad (4.55)$$

$$\xrightarrow{R_x^1(45)} \quad \begin{array}{l} \frac{\sqrt{2}}{2}ZI + \frac{1}{2}IZ - \frac{\sqrt{2}}{2}YI \end{array} \quad (4.56)$$

$$\xrightarrow{d(1/2J_{12})} \quad \begin{array}{l} \frac{\sqrt{2}}{2}ZI + \frac{1}{2}IZ + \frac{\sqrt{2}}{2}XZ \end{array} \quad (4.57)$$

$$\xrightarrow{R_y^1(-45)} \quad \begin{array}{l} \frac{1}{2}ZI - \frac{1}{2}XI + \frac{1}{2}IZ + \frac{1}{2}XZ + \frac{1}{2}ZZ \end{array} \quad (4.58)$$

$$\xrightarrow{\text{grad}_z} \quad \begin{array}{l} \frac{1}{2}ZI + \frac{1}{2}IZ + \frac{1}{2}ZZ \end{array} \quad (4.59)$$

The last term (ZZ) contains no net polarization for either spin, and the total final polarization is thus a factor of two lower than the initial polarization; half of the initial polarization has been erased by the gradient fields. For every additional spin involved in the spatial averaging procedure, the signal decreases by another factor of two, similar to the case of logical labeling. Thus,

$$\frac{S}{N} \propto \frac{n}{2^n}. \quad (4.60)$$

Only one experiment is involved, but the preparation sequence quickly becomes unwieldy for large spin systems, although methods for designing the spatial averaging sequence for arbitrary n exist [SHC00, SOF94]. Also, since the signal strength decreases rapidly, signal averaging the same experiment many times may be required anyways, so the number of experiments needed may in the end be comparable to the case of temporal averaging. This technique has

been successfully used by several groups for state preparation on two or three spins, but we have never used it.

4.4.6 Efficient cooling

We recall from section 3.1.3 that surprisingly, the exponential cost characteristic of effective pure states is not inherent to the use of “high temperature” qubits ($\hbar\omega \ll k_B T$). Schulman and Vazirani, invented an algorithm to cool a subset of the spins in a molecule down to the ground state without any exponential overhead [SV99, CVS01].

The following “boosting procedure” serves as the building block for this algorithm (Fig. 4.14). Given three qubits 1, 2, and 3 with identical $\epsilon = \epsilon_0$, the initial state $|x_1\rangle|x_2\rangle|x_3\rangle$ is one of the eight possible states $|0\rangle|0\rangle|0\rangle, |0\rangle|0\rangle|1\rangle, \dots, |1\rangle|1\rangle|1\rangle$, with respective probabilities $(\frac{1+\epsilon_0}{2})^3, (\frac{1+\epsilon_0}{2})^2(\frac{1-\epsilon_0}{2}), \dots, (\frac{1-\epsilon_0}{2})^3$.

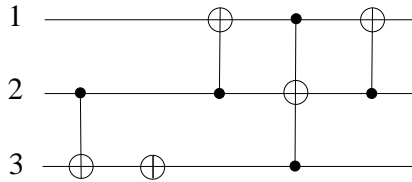


Figure 4.14: A quantum circuit that implements the Schulman-Vazirani boosting procedure. The controlled-swap (Fredkin) gate has been replaced by two CNOT’s and a TOFFOLI gate, as in Fig. 2.8.

First perform a CNOT operation on 3 conditioned on the state of 2. The new state of the three qubits is $|x'_1\rangle|x'_2\rangle|x'_3\rangle = |x_1\rangle|x_2\rangle|x_2 \oplus x_3\rangle$, where \oplus denotes addition modulo 2. Note that *conditioned* on $|x'_3\rangle = |0\rangle$, the polarization of 2 is now $\frac{2\epsilon_0}{1+\epsilon_0^2}$ (2 is almost twice as “cold” as before); *conditioned* on $|x'_3\rangle = |1\rangle$, the polarization of 2 is 0 (2 is at infinite temperature). However, *overall*, the polarization of 2 is still the same as before, ϵ_0 . The polarization of 1 is of course also still ϵ_0 . We then perform a NOT operation on 3 followed by a FREDKIN gate with 3 as the control qubit. The result is that 1 and 2 are swapped if and only if $|x'_3\rangle = |0\rangle$ (and thus if and only if 2 has been cooled): $|x''_1\rangle|x''_2\rangle|x''_3\rangle = |x'_2\rangle|x'_1\rangle|x'_3\rangle$ if $|x'_3\rangle = |0\rangle$, and $|x''_1\rangle|x''_2\rangle|x''_3\rangle = |x'_1\rangle|x'_2\rangle|x'_3\rangle$ otherwise. On average, 1 will thus be colder than before. The resulting polarization of 1 is $\epsilon = \frac{3\epsilon_0}{2} + \mathcal{O}(\epsilon_0^3)$, where the higher order terms are negligible, so the polarization of spin 1 is enhanced by a factor of 3/2.

In order to achieve increasingly higher polarizations, this boosting procedure must be applied repeatedly, whereby a fraction of the cold spins obtained from one round is made progressively colder in the next. Spins of little or no polarization are discarded in each round. Analyzing the polarization transfer using energy and temperature considerations, Schulman

and Vazirani showed [SV99] that the progression of rounds can be arranged so that k bits with nearly optimal enhancement can be extracted, approaching the entropy bound of Eq. 3.7. Furthermore, the number of elementary operations (pulses and delay times in NMR) required to accomplish the entire process is only $\mathcal{O}(n \log n)$. In summary,

the highly random initial state of room temperature nuclear spins represents no fundamental obstacle to scalable quantum computation.

However, the prefactor in the overhead in the number of spins is $n/k \approx 1/\epsilon_0^2$ (Eq. 3.10, for small ϵ_0), which is unreasonably high (about 10^9) for thermally equilibrated nuclear spins at room temperature with current magnetic field strengths. It means we would need a molecule with at least $k10^9$ spins in order to obtain a k -qubit computer. This is clearly impractical.

Until hyperpolarization techniques become much more advanced, the significance of the Schulman-Vazirani scheme for NMR quantum computing is thus purely at a fundamental level: NMR quantum computing is in principle scalable. However, for systems with much higher initial polarizations, Schulman-Vazirani cooling can be very useful if it is difficult to otherwise obtain completely pure qubits.

4.5 Read-out

4.5.1 NMR spectra

Measurement procedure

The magnetic signal of a *single* nuclear spin is too weak to be directly detected⁹. Therefore, NMR experiments are done using a large *ensemble* of identical molecules, typically on the order of 10^{18} , dissolved in a liquid solvent. The same¹⁰ operations are applied to all the molecules in the ensemble, so the final state of the spins is the same in all molecules.

The measurement is done with an RF coil mounted next to the sample (section 5.1), which records the oscillating magnetic signal produced by the transverse component of the magnetic moment of the precessing spins (the longitudinal component does not precess and is not picked up by the coil); this time-domain signal is Fourier-transformed in order to obtain a *spectrum*.

Different spins (qubits) in a molecule are spectrally distinguishable via their Larmor frequencies ω_i (section 4.1), and the amplitude and phase of the different spectral lines give information about the respective spin states. Mathematically, the time-domain signal of spin i can

⁹Under certain circumstances, the spin states can be inferred via optical techniques. This is the case for example in ion traps.

¹⁰This requires extremely homogeneous magnetic fields (both DC and RF). In practice, the operations applied to different molecules are only approximately the same (see section 5.1).

be expressed as

$$V(t) = 2V_0 \text{Tr} [e^{-i\mathcal{H}t/\hbar} \rho(0) e^{i\mathcal{H}t/\hbar} (-iI_x^i - I_y^i)] , \quad (4.61)$$

where $\rho(0)$ is the density matrix at the start of the measurement and V_0 is the maximum signal strength (discussed on page 121). The phases of the observable $(-iI_x^i - I_y^i)$ are chosen¹¹ such that a positive absorptive line corresponds to a spin along $-\hat{y}$, a negative absorptive line to a spin along $+\hat{y}$, and positive and negative dispersive lines to a spin along $+\hat{x}$ and $-\hat{x}$ respectively. Eq. 4.61 represents the signal in the lab frame, but by mixing the signal with a reference oscillator at ω_0^i , we obtain instead the *expectation value* of $-iI_x^i - I_y^i$ in the rotating frame, which is the relevant reference frame for quantum computing. If ρ is mixed, as is the case in room temperature experiments, the expectation value represents an averaged read out over the statistical mixture of states. What we observe is the excess of spins in the most populated state(s).

Since a spin along the $\pm\hat{z}$ axis of the Bloch-sphere, which corresponds to the $\{|0\rangle, |1\rangle\}$ basis, does not produce an NMR signal, we have to *change basis* via a $R_x(90)$ *read-out pulse* in order to perform a measurement in the $\{|0\rangle, |1\rangle\}$ basis. With the above phase conventions, a spin in $|0\rangle$ before the read-out pulse will give a positive absorptive line after the read-out pulse, and a spin in $|1\rangle$ will give a negative line. Inspection of the spectrum acquired after a read-out pulse thus immediately reveals the projection of the spin state onto the $\{|0\rangle, |1\rangle\}$ basis just before the read-out pulse.

Measurement process

What is really happening to the spins during the measurement process? What difference does it make whether or not an observer looks at the signal, or even whether the signal is recorded? And why can we accurately measure both the (non-commuting) \hat{x} and \hat{y} components of the state of a quantum mechanical object ?

The measurement of the spin states in NMR is a weak measurement (see section 3.1.4): the measuring apparatus, the RF coil, is present all the time, but it is only very weakly coupled to the nuclear spins and contributes very little to decoherence. Of course, the spins still decohere through interactions with other spins and with the “bath”, and in addition the spins dephase due to \vec{B}_0 inhomogeneities. The oscillation of the magnetic signal therefore decays over time (usually exponentially). The decaying time domain signal picked up by the the RF coil is called the *free induction decay* (FID).

If the envelope of the FID decays as $e^{-t/T}$ (usually $T = T_2^*$, defined in section 4.6), the Fourier transform of the FID is a Lorentzian line,

$$\propto \frac{1}{1 + (\omega - \omega_0)^2} - \frac{i\omega}{1 + (\omega - \omega_0)^2} , \quad (4.62)$$

¹¹Other authors have adopted different conventions.

which has a linewidth at half height of

$$\Delta f = \frac{\Delta\omega}{2\pi} = \frac{1}{2\pi T}. \quad (4.63)$$

Since the measurement is weak, only very little information can be obtained about the state of individual spins. However, thanks to the large number of identical molecules in an NMR sample, we can acquire much more information about the (average) spin state than we could even in principle ever obtain about the state of an individual spin. For example, the built-in averaging nature of ensemble measurements allows us to directly measure the expectation value of two non-commuting observables.

Ensemble averaged measurements can thus in some respects provide more information than projective measurements on single quantum systems. At the same time, averaging erases certain information which quantum algorithms rely on. Fortunately, all current quantum algorithms can be modified to circumvent this difficulty, as explained in section 3.1.4.

Multiplet fine structure

Extra information about the spin states is contained in the multiplet fine structure of the spectra. The spectrum of each spin in a n -spin molecule may be split in up to 2^{n-1} lines, due to J -coupling terms in the Hamiltonian which modulate the time domain signal of Eq. 4.61 by J Hertz. After we have determined the magnitude and sign of the J couplings, we can then associate each line in the multiplet with the state of the other spins, as shown in Fig. 4.15 for a five-spin molecule.

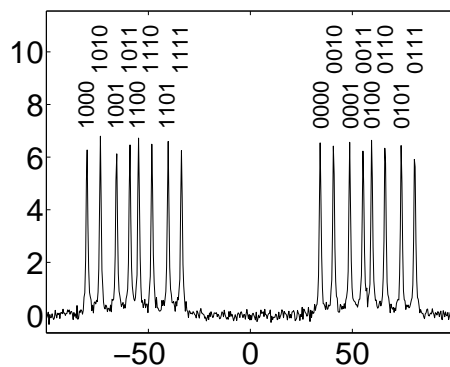


Figure 4.15: The thermal equilibrium spectrum (amplitude of the real part) of spin 1 in a molecule of five coupled spins (more details on this molecule are given in section 5.9). Frequencies are given in units of Hz, with respect to ω_0^1 . The state of the remaining spins is as indicated, based on $J_{12} < 0$ and $J_{13}, J_{14}, J_{15} > 0$; furthermore, $|J_{12}| > |J_{13}| > |J_{15}| > |J_{14}|$.

The presence or absence of specific lines in a multiplet of one spin can thus reveal information about the other spins. For example, for an effective pure ground state (section 4.4.2), the

only line we expect to see in the spectrum of Fig. 4.15 is the line labeled 0000. Similarly, in logical labeling (section 4.4.3), the multiplet structure can be used to identify the logically labeled subspace. We have used the extra information in the fine structure in many of the experiments presented in chapter 5.

Signal-to-noise ratio

The maximum NMR signal, V_0 , measured via a pick-up coil after applying a read-out pulse to a spin in thermal equilibrium, is proportional to

1. the number of molecules, which is linear in the volume, V , and the concentration, n_c ,
2. the number of equivalent sites, n_e , in the molecule for the spin (e.g. this number is three for ^1H in CH_3Cl),
3. the equilibrium polarization, ϵ_0 , which is proportional to γ , B_0 and $1/T_s$, where T_s is the absolute temperature of the sample,
4. ω_0 (because the measurement is inductive), which is proportional to γ and B_0 ,
5. the quality factor, Q , of the coil,
6. the filling factor, η , (the fraction of the coil volume occupied by the sample),
7. a factor, K , which depends on the coil geometry and reflects the coupling of the spins to the coil.

The *noise* in NMR measurements is normally dominated by the thermal noise of the coil. The rms noise amplitude is proportional to the square root of

1. the absolute temperature of the coil, T_c ,
2. the shunt resistance of the tuned circuit, $R = QL\omega_0$, (L is the inductance),
3. the width of the narrow band audio-filter, Δf .

How much the lines in an NMR spectrum rise above the noise level depends not only on the actual signal strength and noise level, but also on the degree to which the signal is spread out in frequency. Thus, the signal-to-noise ratio of an NMR spectrum is also proportional to $1/m$, where m is the multiplicity of the multiplet, and to T_2^* , as $\int_0^\infty \exp(-t/T_2^*) = T_2^*$ (a long T_2^* gives narrow and thus tall lines).

In summary, the signal-to-noise ratio can be expressed as

$$\frac{S}{N} \propto \frac{n_c V n_e \gamma^2 B_0^2 Q \eta K T_2^*}{m T_s (T_c Q L \gamma B_0 \Delta f)^{1/2}} = \frac{n_c V n_e \gamma^{3/2} B_0^{3/2} Q^{1/2} \eta K T_2^*}{m T_s (T_c L \Delta f)^{1/2}}. \quad (4.64)$$

In practice, many of these parameters are interdependent. For a more detailed discussion of the signal-to-noise ratio, see Ref [HR76].

4.5.2 Quantum state tomography

The spectra of a few select spins suffice to obtain the answer to a computation. Nevertheless, the full density matrix conveys a lot of extra information, which can be used to expose the presence of errors not visible in the single output spectra and furthermore is a useful tool for debugging pulse sequences.

The procedure for reconstructing the density matrix is called quantum state tomography [CGKL98, CGK98, CVZ⁺98]. In order to explain the idea behind this procedure, we take another look at the signal of Eq. 4.61. The operator $-iI_x^i - I_y^i$ selects specific entries in the density matrix, called *single quantum coherence* (SQC) elements. The SQC elements “connect” basis states which differ by only one quantum of energy (for example $|00\rangle \leftrightarrow |01\rangle$ but not $|00\rangle \leftrightarrow |11\rangle$). The SQC elements of a two-spin density matrix are

$$\begin{bmatrix} \cdot & \cdot & \times & \cdot \\ \cdot & \cdot & \cdot & \times \\ \times & \cdot & \cdot & \cdot \\ \cdot & \times & \cdot & \cdot \end{bmatrix} \quad \text{and} \quad \begin{bmatrix} \cdot & \times & \cdot & \cdot \\ \times & \cdot & \cdot & \cdot \\ \cdot & \cdot & \cdot & \times \\ \cdot & \cdot & \times & \cdot \end{bmatrix} \quad (4.65)$$

for spins 1 and 2 respectively. We recall that the density matrix is Hermitian, so the entries above and below the diagonal (going from upper left to lower right) are each other’s complex conjugate. In Eq. 4.65, there are thus only two independent SQC elements for each spin. Those complex numbers are directly proportional to the area underneath the two spectral lines in each of the doublets of the two-spin spectrum. For an n spin system, the 2^{n-1} lines within each multiplet can be identified with 2^{n-1} SQC elements per spin.

Quantum state tomography then consists of repeating the computation many times, each time looking at the final state of the spins “from a different angle”, by applying different sets of read-out pulses which rotate different elements of the density matrix into observable positions. In an idealized experiment (no imperfections), the density matrix uniquely follows from the area underneath the individual lines within all the multiplets. In real experiments, all the spectral information may not be compatible with each other, but we can obtain a good estimate of the actual density matrix via a least-squares fit.

Since quantum state tomography involves on the order of 4^n experiments (the number of degrees of freedom in the density matrix), it is practical only for experiments involving a few spins; we have reconstructed density matrices only for experiments with two or three spins (sections 5.3- 5.7).

4.6 Decoherence

The decoherence process of uncoupled nuclear spins is well described by a combination of two phenomena: longitudinal and transverse relaxation¹² [Abr61, Sli96]. These two processes are closely related to generalized amplitude damping and phase damping respectively, which have been described mathematically in section 3.1.5. We will first present the main decoherence mechanisms and then describe standard methods to measure the characteristic relaxation time constants.

4.6.1 Principal mechanisms

Relaxation of nuclear spins is caused by fluctuations in the magnetic field experienced by the spins. Whether the magnetic field fluctuations contribute to energy exchange with the bath or phase randomization depends on the *time scale* of the fluctuations. Roughly speaking, we have that

- fluctuations at ω_0 lead to efficient energy exchange with the spins (the bath and the spins act as RF transmitters and receivers tuned to the same frequency),
- fluctuations at zero frequency, i.e. slow fluctuations, give rise to phase randomization.

Depending on the mechanism, however, fluctuations at ω_0 and at $2\omega_0$, may also contribute to phase randomization. Similarly, fluctuations at $2\omega_0$ may also contribute to energy exchange. Finally, if two or more coupled spins are present, energy exchange is also promoted by fluctuations at the sum and difference frequencies of the spins ($\omega_0^i \pm \omega_0^j$) [Abr61].

The following mechanisms at a microscopic scale contribute to relaxation of nuclear spins in liquid solution:

1. Intermolecular dipole-dipole interactions with nuclear spins.

This interaction is modulated by molecular translation and rotation and contributes to phase randomization (T_2). It can be dominant in relatively large molecules, when all the high- γ nuclei are well separated in the molecule.

2. Intramolecular dipole-dipole interactions with nuclear spins.

This interaction fluctuates due to molecular tumbling; its contribution to T_1 scales as $T_1^{-1} \propto \gamma_i \gamma_j / r_{ij}$, where γ_i and γ_j are the gyromagnetic ratios for spins i and j , and r_{ij} is the distance between the two nuclei.

¹²For coupled spins (dipole coupled or J coupled), the decoherence process also includes cross-relaxation and the nuclear Overhauser effect (NOE), but we shall not discuss those here.

3. Intra- and intermolecular dipole-dipole interactions with electron spins.

If unpaired electrons are present, such as in paramagnetic ions and free radicals, this decoherence mechanism will usually dominate because electrons have a much larger magnetic moment than the nuclei.

4. Chemical shift anisotropy.

If the chemical shift is anisotropic, it rapidly fluctuates due to molecular tumbling. This effect increases with magnetic field strength as $T_1^{-1} \propto B_0^2$ (chemical shifts are linear in the field strength).

5. Spin-rotation interaction.

Molecular rotations create magnetic fields which are modulated due to collisions. This mechanism is important especially in small, symmetric molecules.

6. Scalar coupling.

Rapid fluctuations in the J coupling contribute to relaxation.

7. Quadrupolar coupling.

Nuclei with a spin quantum number larger than 1/2 don't have a spherically symmetric nuclear charge. As a result, such nuclei interact with electric field gradients. Fluctuations in the electric field gradient due to molecular tumbling cause quadrupolar nuclei to relax very fast.

8. Coupling to quadrupolar nuclei.

The rapidly fluctuating spin state of quadrupolar nuclei contributes to relaxation of other spins.

9. Chemical exchange.

Fast chemical exchange of part of a molecule causes the chemical shifts of nuclei in the remaining part of the molecule to rapidly jump back and forth between two or more values.

In addition, fluctuations due to noisy RF amplifiers or other external sources which emit electro-magnetic fields at ω_0 shorten T_1 . Similarly, magnetic field inhomogeneities (in B_0 or B_1) shorten the apparent T_2 . However, magnetic field inhomogeneities can in principle be easily unwound via refocusing pulses, provided diffusion rates are slow compared to the time scale of the operations. The literature therefore distinguishes between T_2 , the intrinsic transverse relaxation time constant, and T_2^* , which incorporates both intrinsic relaxation and inhomogeneous broadening.

Minimizing relaxation

To some degree, relaxation is influenced by parameters under the control of the experimenter. For quantum computation, it is crucial to maximally take advantage of the possibilities to reduce relaxation.

A first set of guidelines hinges on the idea of *motional narrowing*. Rapid molecular tumbling shortens the correlation times of many fluctuations and therefore tends to lengthen T_2 (which is usually much shorter than T_1). The tumbling rate depends on the following parameters:

1. Molecule size: small molecules tumble more easily.
2. Viscosity of the solvent: lower viscosity obviously promotes rapid tumbling (supercritical solvents are ideal from this point of view, as they combine the high density and solubility of liquids with the low viscosity of gases).
3. Temperature: higher temperatures provide more thermal energy for tumbling and also tend to reduce solvent viscosity.

Additional guidelines for sample preparation and molecule selection are:

1. Remove oxygen and other paramagnetic impurities from the solution.
2. Avoid quadrupolar nuclei in the molecule.
3. Reduce the solute concentration in order to reduce intermolecular relaxation, and choose solvents preferably with nonmagnetic nuclei or low- γ nuclei, or else with different nuclear species than those in the solute molecule, because like nuclei relax each other more efficiently than unlike nuclei.
4. Remove reagents with which the molecule may exchange chemically.

Finally, non-intrinsic relaxation can be minimized by

1. making the B_0 field as homogeneous as possible.
2. Spinning the sample about the \hat{z} axis in order to average out the remaining transverse field inhomogeneities.
3. Filter out particles in the solvent, as they create magnetic field inhomogeneities (assuming their magnetic susceptibility is different than that of the solvent).
4. Using RF coils with good homogeneity.
5. Blanking the amplifiers in between RF pulses.

6. Reduce radiation damping by reducing the sample concentration or lowering the Q of the probe (during a pulse, the spins are tipped into the transverse plane, so they induce a voltage in the coil which in turn tips the spins back).

4.6.2 Characterization

We have used the following (standard) procedures for measuring the T_1 , T_2 and T_2^* [Fre97].

Inversion recovery constitutes a clean measurement of T_1 . First, a 180° pulse inverts the spin from $+\hat{z}$ to $-\hat{z}$; then the spin is allowed to relax back to its equilibrium state $+\hat{z}$ for a variable duration t ; finally, a 90° read out pulse tips the spin into the $\hat{x}\hat{y}$ plane and the signal is recorded. The pulse sequence is thus

$$X^2 - t - X - \text{acquisition} . \quad (4.66)$$

With properly set receiver phase settings, the peak height of the measured spectrum varies with t as

$$S = S_0 [1 - \alpha e^{-t/T_1}] , \quad (4.67)$$

where α is a fitting parameter which compensates for incomplete inversion due to RF field inhomogeneities (ideally $\alpha = 2$). Typical values for T_1 are a few seconds to a few tens of seconds.

T_2^* is the time constant of the free induction decay, so $T = T_2^*$ in Eq. 4.63 (assuming the line is Lorentzian, which is not necessarily the case in an inhomogeneous magnetic field), and

$$\Delta f = \frac{\Delta\omega}{2\pi} = \frac{1}{2\pi T_2^*} . \quad (4.68)$$

We can thus easily derive T_2^* from the *linewidth* at half height. Measurement of T_2 requires that dephasing due to magnetic field inhomogeneities be refocused. The standard measurement for T_2 is the *Carr-Purcell-Meiboom-Gill* (CPMG) pulse sequence. First a Y pulse takes the spin to $+\hat{x}$. Then, the subsequence

$$\frac{\tau}{4} X^2 \frac{\tau}{2} X^2 \frac{\tau}{4} \quad (4.69)$$

is repeated k times, where k is arrayed, and the signal is recorded for each value of k . Typical values of τ are 1-10 ms, short enough such that minimal diffusion takes place during the delay times, and long enough such that the duty cycle (the ratio of the duration of the pulses over the delay times) is not too high. The measured signal will decay exponentially with the total decay time $t = k\tau$,

$$S = S_0 e^{-t/T_2} . \quad (4.70)$$

In theory for small molecules $T_2 \approx T_1$, although in practice T_2 values were a few tenths of a second to a few seconds in the molecules we have used, substantially shorter than T_1 .

We note that the measured values of T_2 (and T_2^*) do not correspond exactly to the phase

damping time constants defined in section 3.1.5. The CPMG measurement gives the decay rate of the single quantum coherence elements of the density matrix, to which both amplitude damping and phase damping contribute. However, in practice, often $T_1 \gg T_2$ in which case the CPMG measurement does give the phase damping time constant, to good approximation.

Finally, the T_2 measurement is affected by coupled evolution, in particular when τ is on the order of $1/2J$. In a multi-spin system, it becomes difficult to choose τ so it is different enough from $1/2J$ for the various J -coupling strengths. Different choices of τ give considerably different measured T_2 's, so their meaning is diminished [VV78].

4.7 Molecule design

The choice of a suitable molecule is crucial for the success of NMR quantum computing experiments. The fundamental properties which make a molecule suitable for quantum computation follow from the preceding sections.

First, the number of spin-1/2 nuclei in the molecule must be equal or larger than the required number of qubits. Reasonable choices for qubits include ^1H , ^{13}C , ^{15}N , ^{19}F and ^{31}P , as they all have a spin-1/2 nucleus, and are found relatively easily in small organic molecules (however, isotopic labeling is needed to obtain ^{13}C and ^{15}N in high concentration).

Second, in order to be able to complete a large number of two-qubit operations within the coherence time, we desire

$$|J_{ij}| \gg \frac{1}{T_2}, \frac{1}{T_1}. \quad (4.71)$$

Third, in order to have sufficiently slow coupled evolution during spin-selective shaped pulses, we need $|\omega_1| \gg |J_{ij}|$ and since spin-selectivity requires $|\omega_0^i - \omega_0^j| > |\omega_1|$, we desire

$$|\omega_0^i - \omega_0^j| \gg |J_{ij}|. \quad (4.72)$$

This condition at the same time ensures that the spectra are first order. We note that Eqs. 4.71 and 4.72 automatically guarantee that $|\omega_0^i - \omega_0^j| \gg 1/T_2, 1/T_1$, such that many one-qubit operations can be done within the coherence time as well.

Eq. 4.72 is exceedingly well satisfied in heteronuclear molecules. In homonuclear molecules, strong chemical shifts are promoted by strong asymmetries in the molecule. The normal range of chemical shifts is about 200 ppm for ^{19}F (about 100 kHz at 10 Tesla), 200 ppm for ^{13}C nuclei (about 25 kHz), 10 ppm for ^1H (about 5 kHz) and > 300 ppm for ^{15}N (about 7.5 kHz). In homonuclear molecules, ^{19}F and ^{13}C are thus preferred. ^{19}F and ^{13}C also tend to have strong J couplings, needed to satisfy Eq. 4.71 while ^1H often has smaller J couplings.

On the one hand, low- γ nuclei such as ^{15}N and ^{13}C tend to have longer coherence times than high- γ nuclei such as ^1H and ^{19}F . On the other hand, high- γ nuclei such as ^1H and ^{19}F have the

advantage that they give the strongest signals (recall Eq. 4.64). ^{13}C , ^{15}N have a low γ , and the γ of ^{31}P is intermediate (see Table 4.1).

Section 4.6.1 discusses several other elements related to molecule design which affect the coherence time.

We have already seen (section 4.3) that Eq. 4.71 is not binding. This condition can be extended to say that a sufficient network of J 's larger than $1/T_2$ must be available, such that a two-qubit gate between any pair of spins (implemented directly or indirectly) takes a short time compared to the coherence time.

Similarly, Eq. 4.72 assumes that we need to individually address all the spins, but this isn't always necessary either (section 3.1.2). A polymer with a unit cell ABC which repeats itself n times and terminates on a D (where A, B, C and D have distinct chemical shifts) can possibly serve as an n qubit computer (Fig. 3.1). The caveat is that it isn't known how to set up a proper initial state when using nuclear spins at room temperature in such an architecture.

Finally, there are several more mundane but even more important practical requirements for quantum computer molecules: they must be stable (i.e. not decompose) for a reasonably long time, dissolve in an NMR solvent (chloroform, acetone, ether, DMSO, benzene, toluene, among others), be available or possible to synthesize, be affordable (99% ^{13}C or ^{15}N enriched compounds can be very expensive) and safe. Indeed, many molecules which one could draw on the board for their beautiful presumed NMR properties turn out to be unstable, very hard to synthesize, or toxic.

4.8 Pulse sequence design

A computation with nuclear spins consists of a carefully designed sequence of RF pulses separated by delay times, corresponding to computational steps. Those elementary instructions, pulses and delay times, can be viewed as the *machine language* of an NMR quantum computer.

The goal of pulse sequence design is to translate a high-level description of a quantum algorithm into unitary transformations acting on one or several qubits, then to decompose each unitary operation into one- and two-qubit gates, and finally into pulses and delay times. This process is analogous to *compiling* code on traditional computers.

We know from previous sections on quantum gates (2.2) and their implementation in NMR (4.2-4.3) that many pulse sequences result in exactly the same unitary transformation. Good pulse sequence design therefore attempts to find the *shortest and most robust* pulse sequence that implements the desired transformations.

A key point in pulse sequence design is that the process must itself be *efficient*. For example, suppose an algorithm acts on five qubits with initial state $|00000\rangle$ and that the final state is $(|01000\rangle + |01100\rangle)/\sqrt{2}$. The overall result of the sequence of unitary transformations is thus that qubit 2 is flipped and that qubit 3 is placed in an equal superposition of $|0\rangle$ and $|1\rangle$. This

net transformation can obviously be obtained immediately by the sequence $X_2^2 Y_3$. However, the effort needed to compute this net transformation generally increases exponentially with the problem size, so such extreme simplifications are not practical.

4.8.1 Simplification at three levels

At the most abstract level of pulse sequence simplification, careful study of a quantum algorithm can give insight in how to reduce the resources needed. For example, we recall that a key step in both the Deutsch-Jozsa algorithm and the Grover algorithm can be described as the transformation $|x\rangle|y\rangle \rightarrow |x\rangle|x \oplus y\rangle$ (see Eqs. 2.64 and 2.70), where $|y\rangle$ is set to $(|0\rangle - |1\rangle)/\sqrt{2}$, so that the transformation in effect is $|x\rangle(|0\rangle - |1\rangle)/\sqrt{2} \rightarrow (-1)^{f(x)}|x\rangle(|0\rangle - |1\rangle)/\sqrt{2}$. We might thus as well leave the last qubit out as it is never changed.

At the next level, that of quantum circuits, we can use the simplification rules such as those illustrated in Fig. 4.16. In this process, we can fully take advantage of commutation rules to move building blocks around, as illustrated in Fig. 4.17 (see also page 30). Commutation rules can also tell us which gates can in principle be executed simultaneously. Furthermore, we can use the fact that U acting on a diagonal density matrix doesn't need to have the right phases (e.g. compare Eq. 4.19 and Eq. 4.20). Finally, we can take advantage of the fact the most building blocks have many equivalent implementations, as shown in Fig. 4.18.

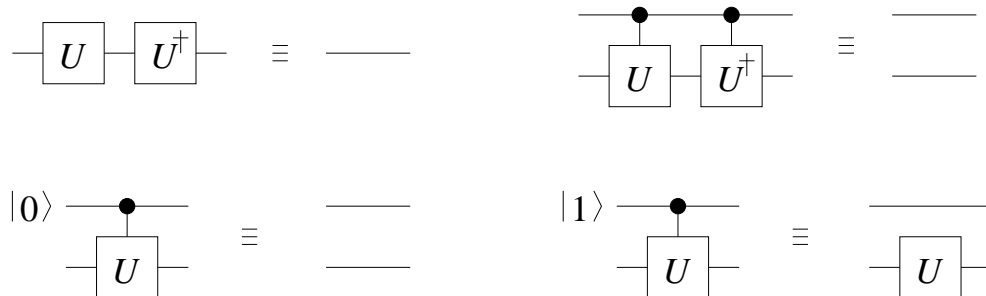


Figure 4.16: Simplification rules for quantum circuits

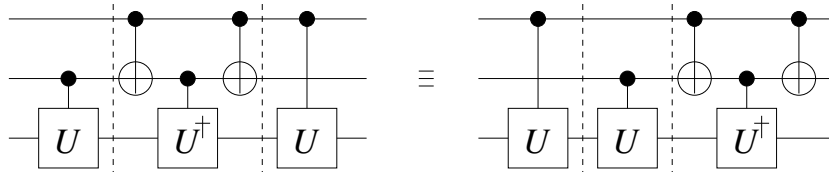


Figure 4.17: Commutation of unitary operators can help simplify quantum circuits by moving building blocks around such that cancellations of operations as in Fig. 4.16 become possible. For example, the three components (separated by dashed lines) in these two equivalent realizations of the TOFFOLI gate commute with each other and can thus be executed in any order.

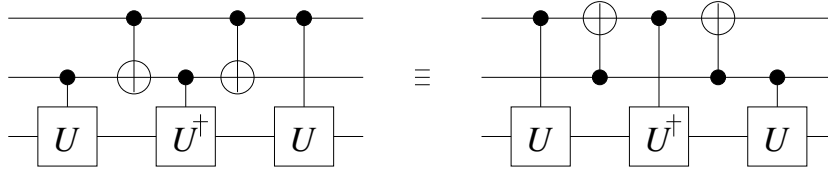


Figure 4.18: Choosing one of several equivalent implementations can help simplify quantum circuits, again by enabling cancellation of operations as in Fig. 4.16. The TOFFOLI gate has two control qubits, whose role is symmetric and can thus be swapped.

At the lowest level, that of pulses and delay times, further simplification is possible by taking out adjacent pulses which cancel out, such as X and \bar{X} . In fact, we can go one step further and choose those pulses sequence for each building block which will give the most cancellation of pulses. For this purpose, it is convenient to have a library of equivalent implementations for the most commonly used quantum gates. For example, two equivalent decompositions of a CNOT_{12} gate (with $J_{12} > 0$) are

$$Z_1 \bar{Z}_2 X_2 1/2J Y_2, \quad (4.73)$$

where time goes *from right to left*, and

$$\bar{Z}_1 \bar{Z}_2 \bar{X}_2 1/2J \bar{Y}_2, \quad (4.74)$$

and two equivalent implementations of the HADAMARD gate on qubit 2 are

$$X_2^2 Y_2 \quad (4.75)$$

and

$$\bar{Y}_2 X_2. \quad (4.76)$$

Then, if we want to perform a HADAMARD operation on qubit 2 followed by a CNOT_{12} gate, it is best to choose the decompositions of Eqs. 4.73 and 4.76, such that the resulting pulse sequence,

$$Z_1 \bar{Z}_2 X_2 1/2J Y_2 \bar{Y}_2 X_2 \quad (4.77)$$

simplifies to

$$Z_1 \bar{Z}_2 X_2 1/2J X_2. \quad (4.78)$$

Furthermore, refocusing sequences can be kept as simple as possible by examining which couplings really need to be refocused. Early on in a pulse sequence, several qubits may still be along $\pm\hat{z}$ in which case their mutual coupling has no effect and thus need not be refocused. Similarly, if a subset of the qubits can be traced out at some point in the sequence, the mutual interaction between these qubits does not matter anymore, so only their coupling with the

remaining qubits must be refocused.

There is of course some interplay between the three levels of pulse sequence simplification. For example, the value of individual J couplings doesn't come in explicitly until the lowest level, but it is possible (and important) to work around small or zero couplings already at the level of quantum circuits.

Finally, we note that pulse sequence design the way we have described it assumes that the quantum computer molecule is fully known and characterized in advance. In contrast, conventional NMR pulse sequences must work for any molecule, because the spectral properties of the molecule are usually not known in advance. Exact knowledge of the Larmor frequencies and J -coupling constants allows one not only to greatly simplify the pulse sequences, but also to achieve much more accurate unitary transformations than would otherwise be possible.

4.8.2 Design for robustness

The exact choice of pulse sequence greatly affects the robustness against erroneous unitary evolutions, in particular those due to coupled evolution during pulses and the inhomogeneity of the RF field used to pulse the spins. In addition to keeping pulse sequences short, robustness is thus an important consideration in the process of designing pulse sequences.

Undesired coupled evolution can be minimized by choosing suitable pulse shapes (section 4.2.4) but also through pulse sequence design, at the lowest level. Simultaneous pulses, especially 90° pulses, on spins with a large mutual J coupling should be avoided (section 4.2.5) and coupled evolution during pulses can be unwound by adjusting the adjacent refocusing sequences (section 4.2.5).

Erroneous evolution because of RF field inhomogeneity can be very substantial (section 5.1), but can in principle be unwound: a X^2 pulse causes some spread in the spin states and we expect a subsequent \bar{X}^2 pulse to unwind this spread quite well, definitely much better than another X^2 pulse. For longer trains of 180° pulses, it isn't always so easy to predict which choice of phase for the pulses is most robust to RF field inhomogeneities. For example, contrary to our intuition, $X^2 X^2 \bar{X}^2 \bar{X}^2$ performs much better than $X^2 \bar{X}^2 X^2 \bar{X}^2$ and similar extensions exist for longer trains of 180° pulses [LFF82].

Quantum computing pulse sequences are hardly ever so transparent, unfortunately. Actual refocusing sequences are complicated by the fact that spin-selective 180° pulses on different spins are interspersed with each other. Furthermore, 90° pulses disturb possible cancellation between preceding and subsequent 180° pulses.

A general framework for undoing systematic errors such as those due to RF field inhomogeneities is highly desirable. This is clearly an ambitious undertaking, but it is encouraging to know that very strong cancellation of such errors *has* been observed, even in complex quantum computing sequences (see sections 5.5 and 5.7).

4.9 Summary

The main message of this chapter is that nuclear spins in molecules in liquid solution largely satisfy the five requirements for the implementation of quantum computers:

1. ✓ spin-1/2 nuclei in a molecule are well-defined qubits,
2. ✓ the dynamics of coupled nuclear spins can be controlled via RF pulses and delay times, even though certain terms in the Hamiltonian cannot be switched off,
3. (✓) room temperature nuclear spins can be made to look like they are at zero temperature, although currently only at an exponential cost,
4. ✓ the state of each qubit can be read out spectroscopically, provided a large ensemble of molecules is used,
5. ✓ nuclear spins have long coherence times (easily a few seconds).

In the next chapter, we will present a series of experiments in which we explore how these methods and concepts translate into the reality of actual quantum computations.

Chapter 5

Experimental realization of NMR quantum computers

After a description of the experimental apparatus¹, we will give a brief overview of the experimental NMR quantum computing work performed to date (section 5.2). We then present in detail a series of eight experiments in which we explored quantum computing in practice. These are an early quantum computation (5.3), an early quantum error detection experiment (5.4), an explicit demonstration of cold dynamics using room temperature spins (5.5), a quantum computation performed in a liquid crystal solvent (5.6), a study of systematic errors with three spins (5.7), an implementation of efficient cooling of one out of three spins (5.8), a realization of the order-finding algorithm with five qubits (5.9) and prime factorization of the number fifteen using seven spins and Shor's algorithm (5.10).

5.1 Experimental apparatus

Figure 5.1 schematically shows the main components of an NMR spectrometer. A sample containing a large number of identical molecules dissolved in liquid solution is placed in a strong magnetic field. Radio-frequency pulses are applied to the sample via a radio-frequency coil and the same coil is used to detect the magnetic signal of the spins during read out. The whole experiment is controlled by a workstation. We now describe each component in more detail.

5.1.1 Sample

The heart of an NMR quantum computer is a molecule containing several atoms with spin- $1/2$ nuclei. In practice, the signal from a single molecule is too weak to be detected with

¹The experiments of sections 5.3 and 5.4 took place in the Chemistry Department at Stanford University. The remaining experiments took place at the IBM Almaden Research Center. Both NMR spectrometers are largely identical, but where they differ, the description is for the instrument at IBM.

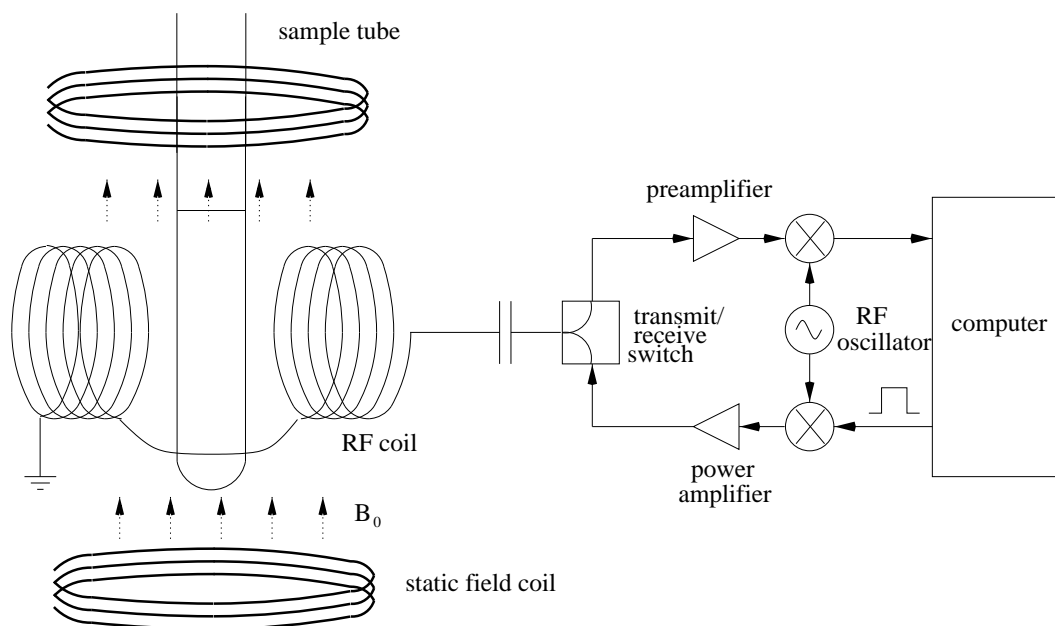


Figure 5.1: Schematic overview of an NMR apparatus.

current techniques, so on the order of 10^{18} molecules are used in order to boost the signal. Each molecule in the ensemble acts as an individual quantum computer, and all 10^{18} quantum computers go through the same operations. The fact that there are many molecules in the sample does not increase the power of the computer; it just increases the signal strength. The power of the computer depends only the number of spins per molecule (see section 4.7 for a discussion of molecule design).

The molecules are dissolved in a liquid solvent at room temperature and atmospheric pressure. Solvent selection is based on the solubility of the quantum computer molecule in the solvent and on the coherence time of the qubits obtained in the solvent, which depends on residual couplings between spins in the solvent and in the solute (see section 4.6). The solute concentration is a trade-off between signal strength and coherence times.

The liquid solution is held in a thin-walled glass NMR sample tube (5mm outer diameter, 4.2 mm inner diameter), filled to about 5 cm from the bottom of the tube (Fig. 5.2). The walls of the glass vial must be very straight and of uniform thickness, in order to minimize magnetic susceptibility variations. We have used high quality sample tubes purchased from New Era Enterprises and from Wilmad.

Sample preparation includes careful removal of oxygen (O_2 is paramagnetic and causes rapid relaxation), water (needed if the quantum computer molecules react with H_2O) and particulates (they degrade the magnetic field homogeneity). Afterwards, the open end of the glass sample tube is flame sealed so that water, oxygen and other impurities cannot leak in.

NMR solvents are usually deuterated. The deuterium NMR signal is used as part of a

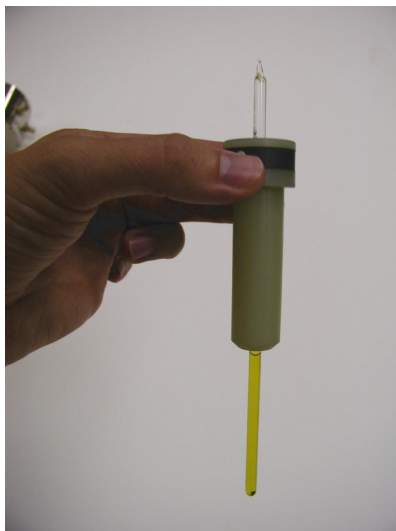


Figure 5.2: A typical NMR sample. The sample tube is held by a sample holder when it is inserted in the superconducting magnet.

feedback loop which keeps the magnetic field strength constant over the course of a series of experiments (section 5.1.2). We have purchased deuterated solvents from Cambridge Isotopes Laboratories and Aldrich.

5.1.2 Magnet

The sample tube is placed in the room temperature bore of a superconducting magnet built by Oxford Instruments (Fig. 5.3). The magnet consists of a superconducting solenoid immersed in a bath of liquid Helium (at 4.2 Kelvin). The Helium vessel is surrounded by a vacuum seal, a liquid Nitrogen vessel and another vacuum seal. The whole magnet is mounted on air-cushioned vibration isolation legs.

A persistent current of about 100 A through the windings of the solenoid produces a magnetic field in the bore of 11.7 Tesla, reasonably strong for an NMR magnet and about 200,000 times the strength of the earth's magnetic field. The resulting Larmor frequencies are in the range of 50 to 500 MHz (see Table 4.1). About three meters away from the center of the magnet, the stray magnetic field is still about five Gauss (10 times the earth's magnetic field). Clearly, it is important to keep all magnetic objects away from the magnet, as they may otherwise be pulled in and damage the magnet.

Strong fields are advantageous because the separation between the spectral lines of nuclei of the same isotope (the chemical shift) increases linearly with the field strength. Large frequency separations make it easier to address each qubit individually. However, spin coherence times may decrease as the field goes up (relaxation due to chemical shift anisotropies increases as the field increases), so it isn't clear that an even stronger field would be better for quantum



Figure 5.3: Oxford Instruments 500 MHz wide-bore NMR magnet. Fill ports for liquid nitrogen and helium stick out from the top. The cabinet near one of the magnet legs contains transmit/receive switches, preamplifiers and mixers. The probe is inserted in the bore of the magnet from below and the sample is inserted from the top. It sits in the probe in the center of the solenoid.

computing.

The bore diameter of our magnet is 89 mm, compared to 52 mm for standard magnets intended for liquid state NMR. The extra space permits the use of custom-built probes with better performance than the commercially available liquids probes, although we did use narrow-bore probes in all the experiments presented in this work.

Of crucial importance is the *homogeneity* of the magnetic field, as it directly affects the spectral linewidths and thereby both the signal-to-noise ratio and the overlap of lines within a multiplet. An inhomogeneous field also causes dephasing in the course of a pulse sequence, although this can in large part be refocused.

Two sets of *shimming coils* mounted around the bore produce magnetic fields which even out any inhomogeneities in the field of the main solenoid. One set consists of about ten superconducting coils, which are energized upon installation and never readjusted. The current of the second set of about 25 room temperature coils can be adjusted by the user. Each shimming coil creates a magnetic field with a specific spatial variation in strength: the field strength of the Z_1 coil varies linearly along the \hat{z} axis, the Z_2 coil varies quadratically along \hat{z} and so forth. A typical set of shimming coils contains Z coils up to fifth or sixth order, transverse (X and Y) coils up to fourth order, and combined coils (e.g. X_2Z) up to fourth order as well.

The optimal shim settings are sensitive to the RF coil geometry, the solvent susceptibility,

the sample height, the glass tube dimensions and susceptibility, the temperature and the presence of magnetic objects in the vicinity of the magnet. The homogeneity of the coil can be assessed via the lock signal strength (see below), the shape and decay rate of the FID and the lineshape and linewidth. With a lot of effort, variations in the strength of the static magnetic field can be made better than 1 part in 2×10^9 over the active region of the sample (4.2 mm in diameter by 1.5 to 2 cm in height), giving linewidths of only 0.2 Hz at 500 MHz ², a truly extraordinary homogeneity.

A second important consideration is that the field strength of a superconducting magnet slowly *drifts* over time, as the current through the windings does dissipate power, albeit only a tiny amount. For a good NMR magnet, the drift is below one Hertz per hour. To put this in perspective, at a drift rate of 1 Hz/hr the field decreases by only 8.76 kHz per year, which is $8.76 \text{ kHz} / 500 \text{ MHz} < 0.002\%$ per year. An NMR magnet can thus easily be used for several decades without any substantial loss in field strength.

Even though the field drift is very slow, it is still appreciable in experiments where precise control over the spin dynamics is required, as is the case of quantum computation. The spin Larmor frequencies slowly drift away from the RF source frequencies so pulses will be off-resonance. Furthermore, the rotating reference frame provided by the RF sources gets progressively out of phase with the actual rotating frame of the spins.

The drift of the magnetic field is therefore compensated for via a room temperature Z_0 coil which superimposes a magnetic field on top of the field produced by the main solenoid. The current through the compensating coil is regulated via a feed-back loop aimed at *locking* the frequency of the deuterium signal of the solvent (and thus also the field strength) to a prescribed value; the deuterium nuclei in the solvent are pulsed every few seconds, and the deuterium signal is monitored (the deuterium frequency is 77 MHz, far away from other frequencies of interest). At the start of a series of experiments, the user must set up the lock power and the gain and phase of the lock feed-back signal. From then on, the lock mechanism operates automatically in the background.

Other possible solutions for B_0 drift include making the RF source frequencies track the drifting Larmor frequencies, or the use of additional 180° pulses to refocus chemical shift evolution. The latter involves additional pulses and is not desirable.

5.1.3 Probe

The probe is in a cylindrical aluminum housing (Fig. 5.4) which contains the RF coils, a tuning and matching electrical circuit, a temperature control system, a sample spinning mechanism

²At this point, the intrinsic T_2 of most samples dominates the linewidth. In fact, with most samples it is not possible to obtain such narrow lines.

and sometimes gradient coils.

RF coils and tune/match circuits

Saddle-shaped Helmholtz RF coils mounted near the top of the probe closely surround the glass sample tube over a height of about 1.5 cm. The region of the sample which is well coupled to the coils, called the *active region*, is a little larger than the region surrounded by the RF coil, usually about 2cm. The coils typically have only one to three windings, and are made of low-resistivity metals such as copper or Pd-plated copper foil or Al filled copper wire in order to compensate for susceptibility differences.



Figure 5.4: Nalorac HFX Probe. The RF coils sit near the top of the probe. BNC connectors, a cooling air inlet, a connector for the gradient coils and knobs to adjust to tune/match capacitors are visible at the bottom of the probe.

The coils are incorporated in a resonant circuit tuned to the Larmor frequency of one or several nuclei, in order to obtain a high quality factor Q (values of 100 to 300 are typical), and thus a high signal-to-noise ratio (Eq. 4.64). The exact resonance frequency of the circuit can be adjusted via a mechanically variable capacitor. Using a second variable capacitor, the impedance of the circuit is matched to 50Ω . The tune and match capacitors are usually mounted close by the coil, and are adjustable via long mechanical rods which stick out from the bottom of the probe. Probe tuning and matching is done by minimizing the reflected power for the desired frequencies.

Because of the difficulty of building high Q resonant circuits with multiple resonances over a wide frequency range, many commercial probes contain two pairs of Helmholtz coils, mounted at right angles with little overlap such that there is little cross-talk between the two sets of coils. One coil then serves the *high-band* nuclei ^1H and ^{19}F (500 and 470 MHz at 11.7 T) and the

other coil serves the *low-band* nuclei (the highest of which is ^{31}P , at 202 MHz). The lock (^2H , at 77 MHz) is usually on the high-band coil such that the lock signal interferes as little as possible with the other low-band signals. Our probe is a “normal” probe, with the high-band coil on the inside; “inverse” probes have the high-band coil on the outside.

The sensitivity of a probe depends not only on the Q but also on the filling factor η and the geometrical coupling K between the coils and the spins (Eq. 4.64). Because of the reciprocity between transmitting and receiving RF signals, a convenient measure for the sensitivity is the minimum 90° pulse length for a given power and coil volume. The absolute minimum achievable 90° pulse length (typically $6 - 15\mu\text{s}$) depends also on how much power the probe can take before the coil windings or the capacitors arc.

The RF field homogeneity of saddle shaped Helmholtz coils is quite poor: the envelope of the Rabi oscillation decays by about 5% per 90° rotation. In other words, the error of a single one-qubit rotation just due to RF coil inhomogeneity is on the order of 5%. Fortunately, the effects of this error can, at least in principle, be largely undone by clever pulse sequence design (sections 4.8 and 5.7).

More homogeneous RF coils could be easily designed, for example, by using a solenoidal geometry. However, this would sacrifice B_0 homogeneity. The B_0 homogeneity is several orders of magnitude better than the B_1 homogeneity, and this is needed because in typical pulse sequences the number of revolutions about \vec{B}_0 is also many orders of magnitude larger than the number of Rabi oscillations about \vec{B}_1 .

Another possibility to improve the RF field homogeneity would be to limit the sample volume to the homogeneous region of the RF coils. However, the abrupt change in magnetic susceptibility at the interface of the liquid sample and the glass or gas would then distort the B_0 field in the active region. We have experimented with specially designed plugs with a susceptibility matched to that of the solvent, but such plugs give only modest improvements and are hard to use in combination with flame sealed sample tubes.

Other functions of the probe

The sample temperature is regulated and under user control via a temperature controlled nitrogen flow inside the probe, directed over the sample tube. Separate nitrogen flows suspend the sample holder on a thin layer of nitrogen gas and make the sample spin about the \hat{z} axis. The spinning rate is regulated and under user control over the range of 0 to 50 Hertz.

In addition to the RF coils, some NMR probes contain also either one (Z) or three (X, Y, Z) gradient coils. These coils produce a static magnetic field in the \hat{z} direction, but the strength of this field varies linearly along the \hat{x}, \hat{y} or \hat{z} axis.

For the first two experiments (5.3-5.4), we used a Varian made tripple resonance HCN probe (i.e. simultaneously tuned to ^1H , ^{13}C and ^{15}N). For all the other experiments, we have used a

tripple resonance HFX probe made by Nalorac (X means that the low band coil is tunable over a wide range). Both probes are equipped with gradient coils but we have not used them in any of the experiments of chapter 5.

5.1.4 Transmitter

The function of the transmitter is to send RF pulses to the probe. We used a custom-modified Varian ^{UNITY} INOVA spectrometer, equipped with four transmitter channels. Fig. 5.5 shows a photograph of the spectrometer electronics cabinet.

A *master oscillator* crystal (a temperature controlled crystal oscillator) provides four *frequency sources* (PTS 620 RKN2X-62/X-116) with a 10 MHz reference signal. From the 10 MHz input signal, each PTS source creates a continuous wave signal (up to 1 V_{rms}) in the range of 1-620 MHz via direct synthesis. The resolution of the sources is 0.01 Hz (we didn't set the last digit, though), the phase noise is -63 dBc) and the stability is as good as that of the master oscillator. The frequency sources are set 20 MHz higher than the frequency desired for the RF pulses.

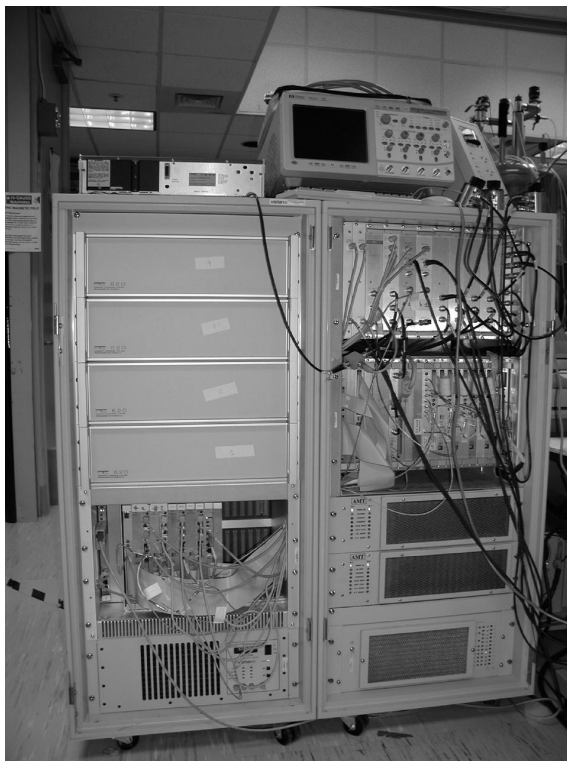


Figure 5.5: Spectrometer electronics cabinet. The magnet is visible behind the cabinet.

The four resulting CW signals are input to a set of four *transmitter boards*. These boards gate the signals in order to create pulses of the intended duration. The minimum pulse length is 100 ns and the resolution is 50 ns. The phase of the pulses can be set in steps of 0.5° .

This is implemented in two stages: a 90° step coarse phase shifter is complemented by a fine phase shifter which achieves a resolution of 0.5° by mixing two quadratures with adjustable amplitudes. Each transmitter board contains a linear attenuator, which controls the amplitude of the outgoing signal from zero amplitude to full amplitude in 4095 steps. The transmitter boards also contain a *single-sideband mixer* which mixes the gated signals with a 20 MHz signal so the outgoing signals have the frequency desired for the RF pulses sent to the probe.

The amplitude and phase control of the transmitter boards can be used to create shaped pulses. A set of four fast memory boards, called *waveform generator boards* is used to load all the information needed for several consecutive shaped pulses quickly enough onto the respective transmitter boards.

From the transmitter boards, the signals are routed to four coarse *attenuators*, which can attenuate the signals over a range of 79 dB in steps of 1 dB. The coarse attenuators thus have a far greater dynamic range than the linear attenuators in the transmitter boards, but lack the fine control needed to create shaped pulses. During a pulse, the coarse attenuator is kept at a fixed setting, but the setting can be changed from one pulse to the next.

Next, a set of *linear amplifiers* turns the signal-level pulses into high power RF pulses. Two amplifier units (AMT model 3900-15) each contain a low-band amplifier (6-200 MHz, 300 W maximum pulse power, 60 dB gain) and a high band amplifier (200-500 MHz, 100 W maximum pulse power, 50 dB gain). In CW mode, the maximum power is 30 W and 15 W respectively. These amplifiers are especially designed for NMR experiments, with rise and fall times of 200 ns and fast blanking circuits ($< 2\mu\text{s}$ on/off, TTL signal) which are crucial to avoid the amplifiers putting out excessive noise in between pulses. The blanked output noise is < 20 dB over the thermal noise.

In the standard configuration, the spectrometer automatically routes the signals from transmitter boards 1 and 2 (via the coarse attenuator) to the high- or low band amplifier within the first dual amplifier unit, depending on whether the signals are high or low band. Similarly, the signals from transmitter boards 3 and 4 go to the correct side of the second dual amplifier unit. In some experiments, we have used different configurations, using external combiners, in order to extend the routing capabilities of the spectrometer as needed. We have also inserted stepper attenuators with a range of 1 dB and a resolution of 0.1 dB in order to even out differences in output power between the four transmitter boards.

The output of the two high- and low-band power amplifiers are combined as needed with high power combiners, and then routed to the high and low band coil of the probe via active PIN diode *transmit/receive switches*. In transmit mode (during the pulse sequence), these switches connect the probe to the power amplifier output with less than 0.5 dB loss and isolate the power amplifiers from the receiver preamplifiers (see section 5.1.5). Extra protection for the preamplifiers is provided by quarter wave length cables and shunt diodes.

In order to attenuate broadband noise put out by the amplifiers, narrow band, high-pass

or low-pass *filters* are inserted between the power amplifier and the transmit/receive switch as needed.

The pulse amplitude and duration are calibrated via a series of experiments in which the amplitude and/or duration are systematically varied. The amplitude of the resulting output spectra varies sinusoidally as a function of the pulse amplitude and duration. The settings which give the first zero crossing of the output signal are the optimal 180° pulse settings. For a 90° pulse, either the amplitude or the duration must be halved.

For the seven-qubit experiment of section 5.10, we installed an additional frequency source (PTS 620 MHO 2YX-62), gating circuit and power amplifier (ENI model 500 LA, 1 V max input, 27 dB gain) in order to be able to send CW power at the ^1H frequency during the pulse sequence (but not during the read-out) without sacrificing any of the four transmitter channels which were used to pulse the ^{19}F and ^{13}C spins. A narrow-band ^1H filter at the output of the ENI amplifier ensured a low noise level going into the probe at the ^{19}F and ^{13}C frequencies.

5.1.5 Receiver

The function of the receiver is to record the voltage induced in the coil by the oscillating magnetic signals from the spins. We have tested and used a prototype four-channel receiver system designed by Varian NMR. Conventional spectrometers have only one receiver channel.

With the transmit/receive switch in receive mode, the NMR signal is routed from the high-band and low-band RF coils to a high- or low-band *preamplifier*, with a typical loss of 0.1-0.2 dB. The overall noise figure of the preamplifiers is 1.7 dB for the high band preamp and 1.2-1.6 dB for the low band preamp, low enough such that the total noise level is dominated by the coil rather than by the preamp. The preamp gain is about 35 dB.

The amplified RF signals are then *mixed* with the output of the PTS sources to an intermediate frequency (IF) around 20 MHz. The four IF signals are routed to the receiver boards in the electronics cabinet, where the signals are mixed with a 20 MHz signal down to audio-frequencies, separated into two quadratures, and sent through audio *filters* (the filter bandwidth can be adjusted from 1000 Hz to 256 kHz). Both quadratures are then amplified to the desired level and *digitized* (the maximum number of points is 524288 and the maximum sampling rate is 1 MHz). Finally, the digitized signals are uploaded to a workstation.

We note that the digitized signal is phase referenced against the same frequency sources (PTS RF sources and the 20 MHz source) as are used in the transmitter chain. For each channel, the phase of the receiver is thus coherent with the phase of the transmitter, and the phase of the output spectra will be exactly the same every time the same pulse sequence is executed.

5.1.6 Workstation

The spectrometer is operated via Vnmr (Varian software) running on a Sun Ultra 10 workstation. Once the hardware is configured properly for a certain type of experiment and for a certain number and kind of spins, the user can set up new experiments entirely by computer.

Pulse sequences are written in C, with additional commands such as “send a pulse on channel 2”, provided by Varian. Such a command must be accompanied by parameters and extra commands to specify, for example, that the pulse must last $426 \mu\text{s}$, be phase shifted by -29° with respect to the \hat{x} axis of the oscillator reference frame (the lab frame), be 14 dB below full power, have a gaussian shaped profile, and also that it causes a 12° phase shift on spin 4 and a -25° phase shift on spin 1, has a pre-pulse delay of $10 \mu\text{s}$, a post-pulse delay of $20 \mu\text{s}$, and so forth.

For each experiment, we wrote a *framework* with convenient macros which can be called in actual pulse sequence programs. For example, all of the information of the preceding paragraph can then be replaced by a simple statement of the type “send a 90° pulse about \hat{y} on spin 2” (where \hat{y} is now understood to be in the rotating frame of the spin). Based on the preceding pulses in the sequence, on correction factors computed in advance, and on calibration values, the computer will then automatically find and set the right values for all the parameters.

Each pulse sequence and framework must be compiled, and the compiled code is submitted to the spectrometer. A FIFO buffer absorbs timing differences between how long the hardware takes to execute specific instructions and how long the workstation takes to process and submit the instructions. The FIFO buffer can hold only a few simple shaped pulses, so pulse shaping instructions are loaded onto dedicated waveform generator boards instead.

The Varian software can also be used to Fourier transform the FID, and to display the output spectra. The spectra can then be further processed, for example by applying line-broadening, zeroth and first order phase corrections, and baseline corrections.

In addition, we wrote extensive MATLAB routines which interface with the standard Varian software. These routines make it easier to set up a large number of different experiments in an automated way. The data is automatically stored in the desired directory on the hard disk and processed by another set of MATLAB routines. For example, in temporal labeling experiments (section 4.4.4), these routines add up the data from multiple experiments with precomputed phase settings, and in quantum state tomography experiments (section 4.5), the density matrix is derived from a large set of output spectra. The versatility and generality of MATLAB thus easily allows us to process the data in a specialized way.

Clearly, an NMR quantum computer, or any quantum computer, is not a stand-alone unit. Its operation must be controlled by a (powerful) classical computer. Similar to pulse sequence design, it is key that the classical resources needed to control the quantum computer not increase exponentially with the problem size, or with the size of the quantum computer. This condition

is indeed met in the NMR experiments.

Later in this chapter, we shall present eight experiments in which we explore the use of the apparatus described here. First we give an overview of NMR quantum computing experiments by our and other groups. All the experiments mentioned in this overview were done using an apparatus similar to ours.

5.2 Overview of NMR quantum computing experiments

Nuclear magnetic resonance spectroscopy, invented in 1946, developed from a method to study magnetism into a powerful and versatile tool for the study of molecular structure and reaction dynamics. The first 25 years of NMR were dominated by CW slow passage experiments. In the 1970's, pulsed Fourier transform spectroscopy was developed, which led to an unprecedented expansion of the field and its applications. Many of the pulsed NMR protocols have a structure which we now recognize is similar to quantum computing pulse sequences; for example, the INEPT pulse sequence for polarization transfer is in essence the same as the sequence for a CNOT gate.

Only in the last four years have researchers begun to implement NMR pulse sequences with the explicit purpose of studying quantum computation. Several groups besides our own have pursued liquid NMR quantum computing very actively and they continue to implement a variety of quantum information processing tasks. We will now give a very brief overview of this work.

Quantum algorithms

The first quantum algorithms ever implemented experimentally were Grover's algorithm for two qubits [CGK98, JMH98] and the Deutsch-Jozsa algorithm for two qubits [CVZ⁺98, JM98] (section 5.3). These experiments were performed in the Fall of 1997 and Winter of 1998, by Ike Chuang's group at UC Berkeley and Stanford University using the ¹³C and ¹H spins of ¹³C-labeled chloroform and in Jonathan Jones's lab at Oxford University using two ¹H spins of cytosine.

Later, the quantum counting algorithm (an extension of Grover's search algorithm) was also implemented on the two spins of cytosine [JM99]. The two-qubit Grover algorithm was implemented again on a subspace of two spins out of the three ¹⁹F spins of bromotrifluoroethylene, in the first demonstration of logical labeling [VYSC99] (section 5.5). Finally, the three-qubit Grover algorithm was realized using the ¹H-¹³C-¹⁹F spin system of dibromofluoromethane, with up to 28 Grover iterations, involving a record 280 two-qubit gates [VSS⁺00] (section 5.7).

The Deutsch-Jozsa algorithm for three qubits was implemented in Ray Freeman's lab at Cambridge University using the three ¹H nuclei in 2,3-dibromopropionic acid, and exploring

the use of transition selective pulses [LBF98]. The same molecule was used again later in a similar experiment [DAK00]. A more advanced version of the algorithm was demonstrated using the three ^{13}C nuclei in fully labeled alanine, and swap gates to realize two-qubit gates between the two weakly coupled ^{13}C spins [CKH⁺00]. The same molecule was used without swap gates for another three-qubit Deutsch-Jozsa experiment [KLL00]. A partial (particularly simple) implementation of the five-qubit Deutsch-Jozsa algorithm was carried out using one ^1H , ^{15}N and ^{19}F nucleus and two ^{13}C nuclei in a molecule derived from glycine [MFM⁺00]. This experiment, done by Steffen Glaser's group in Frankfurt, was the first demonstration of coherent control over five qubits.

The implementation of quantum algorithms was taken to a new level of complexity by the first implementation of a Shor-type quantum algorithm for order-finding on a five-fluorine spin system, carried out at IBM/Stanford [VSB⁺00] (section 5.9). This algorithm combined exponentiated permutations with the three-qubit quantum Fourier transform; the latter had been implemented earlier in itself using ^{13}C labeled alanine [WPF⁺01]. The five-qubit experiment was followed by a seven-qubit demonstration, also at IBM/Stanford, of the simplest instance of Shor's quantum factoring algorithm, the prime factorization of the number 15 [VSB⁺01] (section 5.10).

Quantum error correction

The first demonstration of quantum error correction was done using alanine and trichloroethylene, in David Cory's group at MIT/Harvard and by Raymond Laflamme and Emmanuel Knill at Los Alamos [CMP⁺98]. They implemented the three-qubit phase error correction code and studied its operation for one particular input state in the presence of gradient fields to introduce artificial errors, and also when subject to just intrinsic decoherence. A more complete version of this experiment was carried out later by the same groups, using gradient fields [SCS⁺00]. Meanwhile, a complete experiment for the two-bit phase error detection code had been implemented by our group, for intrinsic decoherence [LVZ⁺99] (section 5.4). Recently, the Los Alamos group demonstrated the five-bit phase and amplitude error correction code for full bit and phase flip errors that were artificially introduced [KLMN01].

Quantum simulations

Relatively little but very interesting work has been done on quantum simulations. David Cory's group first simulated the dynamics of truncated quantum harmonic and anharmonic oscillators, using the two proton spins of 2,3-dibromothiophene [STH⁺99]. Later, the same group simulated a non-physical three-body interaction using the three carbon spins in fully labeled alanine [TSS⁺99].

Other quantum protocols

The group at Los Alamos prepared an effective pure GHZ state (a GHZ state is a maximally entangled state of three particles) [LKZ⁺98], and later performed a similar experiment on seven spins [KLMT00]. Even though the claim that entangled states or cat states had been prepared has been refuted on the basis that the spin states at room temperature are too mixed to be entangled [BCJ⁺99] (rather than entangled states, a three spin and seven spin coherence has been observed), these experiments remain the first, albeit relatively simple, experiments with three respectively seven qubits. GHZ correlations on mixed states have been studied further in an experiment by the MIT group [NCL00].

Also at Los Alamos, a teleportation protocol has been carried out using two ¹³C nuclei and one ¹H nucleus in ¹³C labeled trichloroethylene [NKL98]. Superdense coding was also demonstrated, with ¹³C labeled chloroform [FZF⁺00]. Just like the work on pseudo-entangled states, the significance of these experiments is limited by the mixedness of the states and furthermore by the fact that the nuclei are separated from each other by only a few Angstroms.

Polarization enhancement

It is clear that the tiny polarizations obtained for nuclear spins in thermal equilibrium at room temperature severely limit the usefulness of NMR quantum computers. Several experiments have been done to study the feasibility of boosting the nuclear spin polarization. In an algorithmic approach, the building block of the Schulman-Vazirani cooling scheme has been demonstrated at IBM/Stanford using the three fluorine spins of bromotrifluoroethylene [CVS01] (section 5.8). However, this scheme is impractical as long as the starting polarization remains very low. Also at IBM/Stanford, the initial polarization of the ¹H and ¹³C spins in labeled chloroform has been increased by a factor of about 10 using optical pumping techniques [VLV⁺01]. Using a different approach, namely the transfer of *para* hydrogen into a suitable molecule, a molecule with two spins with 10% polarization (compared to 10⁻⁵) has been created [HBG00]. In both the optical pumping and the *para* hydrogen experiment, a quantum algorithm was executed on the hyperpolarized qubits.

Solvent work

The use of liquid crystal solvents for NMR quantum computing was first demonstrated at IBM/Stanford [YSV⁺99] (section 5.6), and further studied at IBM/ Berkeley [MCK00]. Liquid crystal solvents have also been used as a solvent for a molecule containing ¹³³Cs atoms, which have a spin-7/2 nucleus [KSF01].

5.3.1 Problem description

In this first experiment [CVZ⁺98]³, we implemented the simplest possible version of the Deutsch-Jozsa algorithm (see section 2.3.1), which determines whether an unknown function f with one input bit and one output bit is constant or balanced. There are four possible such functions, two of which are constant, $f_1(x) = 0$, $f_2(x) = 1$ and two of which have an equal number of 0 and 1 outputs: $f_3(x) = x$, $f_4(x) = \text{NOT}x$.

To determine whether such a function is constant or balanced is analogous to determining whether a coin is fair, with heads on one side and tails on the other, or fake, with heads or tails on both sides. Classically, one must look at the coin twice, first one side then the other, to determine if it is fair or fake. The Deutsch-Jozsa algorithm exploits quantum coherence to determine if a quantum ‘coin’ is fair or fake while looking at it only once. This simplest instance of the algorithm requires one ‘input’ spin and one ‘work’ spin, and is schematically represented by the quantum circuit shown in Fig. 5.7.

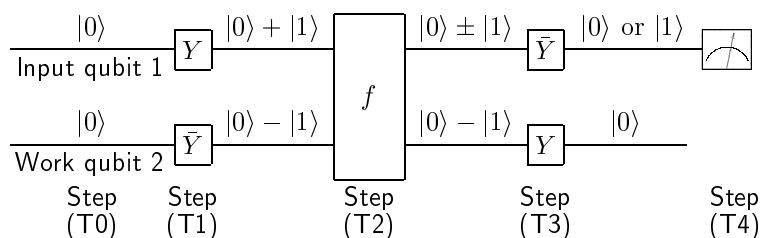


Figure 5.7: Quantum circuit for performing the simplest instance of the Deutsch-Jozsa algorithm.

5.3.2 Experimental procedure

Experimentally, this quantum algorithm was implemented using the nuclear spins of the ^1H and ^{13}C atoms in a chloroform molecule (CHCl_3) as the input and work qubits. The sample contained a 200 mM, 0.5 ml solution of 99% ^{13}C enriched chloroform (purchased from Cambridge Isotope Laboratories, Inc. [CLM-262]) dissolved in deuterated acetone, at room temperature and standard pressure.

The five theoretical steps (T0)–(T1) shown in Fig. 5.7 were experimentally implemented as follows:

(E0) We prepared an effective pure ground state using temporal averaging with cyclic permutations (section 4.4.4). For two spins, this involves the summation of three experiments in which

³ The theory for this experiment was worked out by Ike Chuang and Seth Lloyd. Ike also wrote the framework for the pulse sequences and an interface with MATLAB. The actual experiments were carried out by myself. The data analysis and discussion of errors was the joint work of myself, Xinlan Zhou, Debbie Leung and Ike Chuang.

the populations of the $|01\rangle$, $|10\rangle$, and $|11\rangle$ states are cyclically permuted before performing the computation, as in Eqs. 4.35-4.38.

Note that while this method requires $f(x)$ to be evaluated 3 times, it is actually not necessary. Although step (T0) stipulates a pure input state $|00\rangle$, the algorithm works equally well if the input qubit is initially $|1\rangle$; furthermore, when the work qubit is initially $|1\rangle$, it fails, and cannot distinguish constant from balanced functions, but this does not interfere with other computers which have worked (Fig. 5.8). Thus, a thermal state is a good input for this algorithm, and only one experiment needs to be performed. We will present data from both thermal and effective pure input states.

(E1) The Hadamard operations in the general description of the Deutsch-Jozsa algorithm (section 2.3.1) can be implemented by Y_1 and \bar{Y}_2 rotations since we know the initial state of each qubit is $|0\rangle$.

(E2) The function $y \rightarrow y \oplus f(x)$ is implemented using RF pulses and the spin-spin interaction. Recall that spin 1 represents the input qubit x , and spin 2 the work qubit y where f stores its output. f_1 is then implemented as $\tau/2 X_2^2 \tau/2 X_2^2$, to be read from left to right, where $\tau/2$ represents a time interval of $1/4J \approx 1.163$ ms ($J = 215$ Hz in chloroform), during which coupled spin evolution occurs. This is a well known refocusing pulse sequence which performs the identity operation (section 4.3.1). f_2 is $\tau/2 X_2^2 \tau/2$, similar to f_1 but without the final 180° pulse, so that spin 2 is inverted. f_3 is $Y_2 \tau \bar{Y}_2 X_2 \bar{Y}_1 \bar{X}_1 Y_1$, which implements a CNOT operation, in which 2 is inverted if and only if 1 is in the $|1\rangle$ state. Finally, f_4 is implemented as $Y_2 \tau \bar{Y}_2 \bar{X}_2 \bar{Y}_1 \bar{X}_1 Y_1$, which is similar to f_3 but leaves spin 2 inverted.

(E3) The inverse of (E1) is done by applying the RF pulses $\bar{Y}_1 Y_2$ to take both spins back to $\pm \hat{z}$. Spin 1, which was $|0\rangle$ at the input, is thus transformed into $|0\rangle$ or $|1\rangle$ for constant or balanced functions respectively.

(E4) The result is read out by applying a read-out pulse X_1 to bring spin 1 back into the $\hat{x} - \hat{y}$ plane.

5.3.3 Experimental results

The prediction is that the spectral line of spin 1 will be up for constant f and down for balanced f . The experimentally measured spectra obtained with an effective pure input state immediately reveal whether $f(x)$ is constant or balanced (Fig. 5.8). For the thermal input state [inset], the left line is from molecules with the proper ($|0\rangle$) input state for spin 2 and gives the answer to Deutsch's problem. The right line is from molecules which started off with spin 2 in $|1\rangle$, and with that input state the algorithm fails in distinguishing constant from balanced f , as predicted.

We also characterized the entire deviation density matrix $\rho_\Delta \equiv \rho - \text{Tr}(\rho) I/4$ describing the final 2-qubit state (Fig. 5.9). The deviation density matrix was obtained from the integrals of the proton and carbon spectral lines, acquired for a series of nine experiments with different

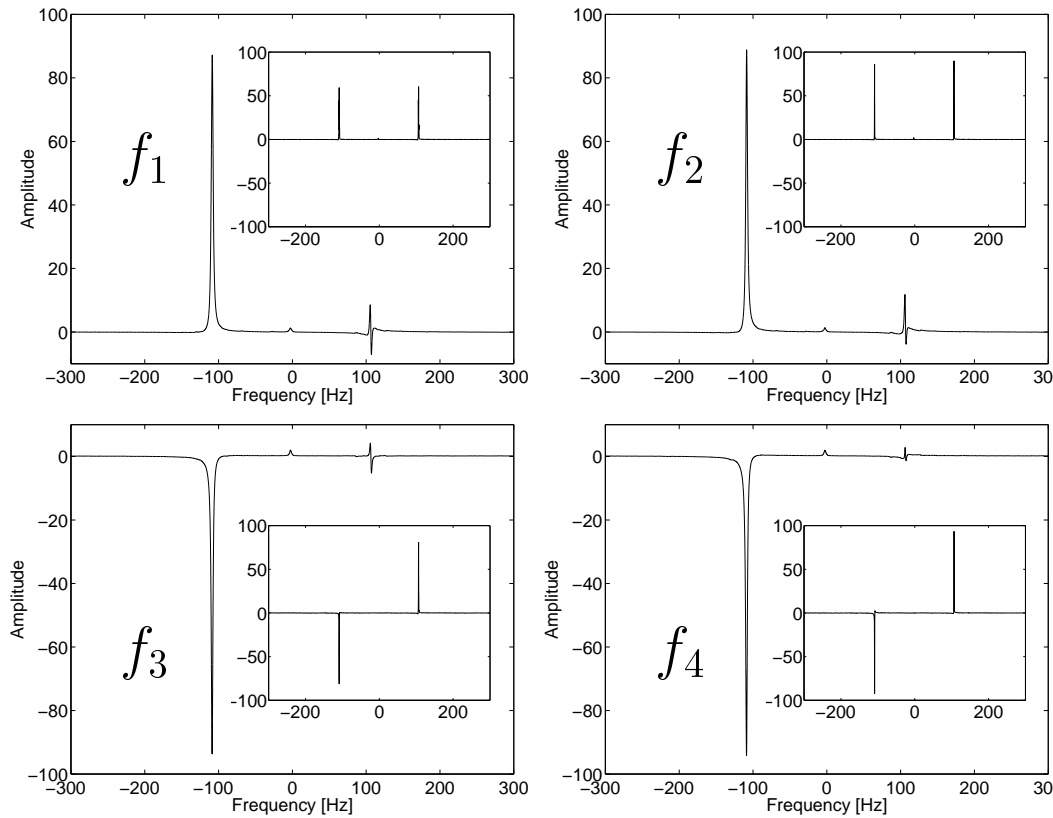


Figure 5.8: Proton spectrum after completion of the Deutsch-Jozsa algorithm and a single read-out pulse X_1 , with an effective pure input state $|00\rangle$ and with a thermal input state [Inset]. The low (high) frequency lines correspond to the transitions $|00\rangle \leftrightarrow |10\rangle$ ($|01\rangle \leftrightarrow |11\rangle$). The frequency is relative to $\omega_0^1/2\pi$ (the Larmor frequency of spin 1), and the amplitude has arbitrary units. The phase is set such that a spectral line is real and positive (negative) when spin 1 is $|0\rangle$ ($|1\rangle$) right before the read-out pulse.

read-out pulses for each spin (quantum state tomography, see section 4.5).

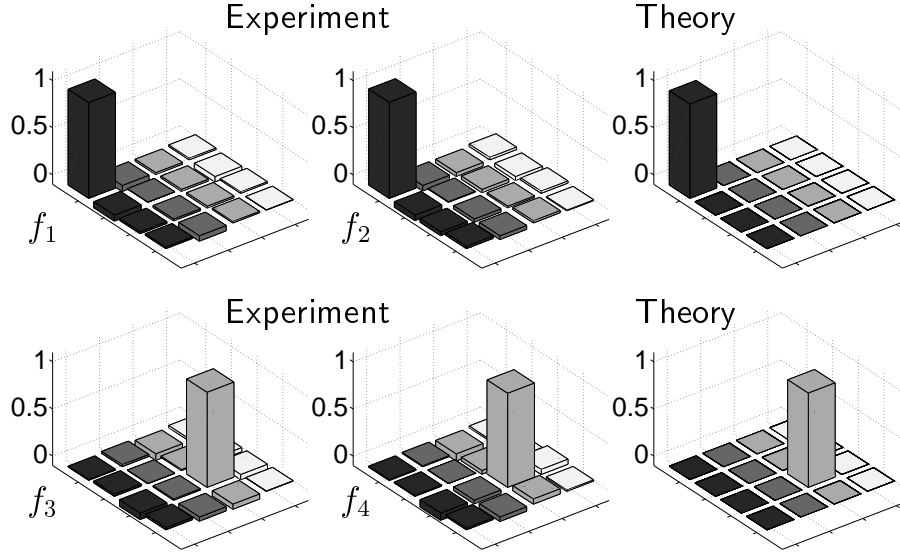


Figure 5.9: Experimentally measured and theoretically expected deviation density matrices after completion of the Deutsch-Jozsa algorithm. The diagonal elements represent the normalized populations of the states $|00\rangle$, $|01\rangle$, $|10\rangle$ and $|11\rangle$ (from left to right). The off-diagonal elements represent coherences between different states. The magnitudes are shown with the sign of the real component; all imaginary components were small.

5.3.4 Discussion

The experimental results unambiguously demonstrate the complete proper functioning of the quantum algorithm and provide data for the following error analysis. In the experiments, the normalized pure-state population measured from the deviation density matrix (ideally equal to 1), varied from 0.998 to 1.019. The other deviation density matrix elements (ideally 0), were smaller than 0.075 in magnitude. The relative error on the experimental pure-state output density matrix ρ_{exp} , defined as

$$\| \rho_{exp} - \rho_{theory} \|_2 / \| \rho_{theory} \|_2, \quad (5.1)$$

where $\| \cdot \|_2$ is the 2-norm matrix distance⁴, varied between 8 and 12%.

Quantum computation requires that a coherent superposition be preserved for the duration of the computation. The relaxation time constants for proton and carbon were $T_1 \approx 19$ and 25 s,

⁴The 2-norm gives the absolute value of the largest eigenvalue. It is a pessimistic measure, compared to the traditional $1 - \text{Tr}(\sqrt{\rho_1}\rho_2\sqrt{\rho_1})$ (the latter is defined only for non-negative matrices, though).

and $T_2 \approx 7$ and 0.3 s respectively; these were much longer than required for our experiment, which finished in about 7 ms, so relaxation introduced negligible errors.

The single most important source of errors in the experiments was the RF field inhomogeneity and pulse length calibration imperfections. A direct measure of this inhomogeneity is the $\approx 200 \mu\text{s}$ time constant of the exponentially decaying envelope observed from applying a single pulse, as a function of pulse width. Including the population permutation sequence, about 7 pulses are applied to each nucleus, with a cumulative duration of $\approx 70 - 100 \mu\text{s}$.

The second most important contribution to errors is the low carbon signal-to-noise ratio: the carbon signal peak height/RMS noise was about 35, versus ≈ 4300 for the proton. The carbon signal was much weaker because the carbon gyromagnetic ratio is 4 times smaller, and the carbon receiver coil is mounted farther away from the sample. Smaller contributions to errors came from incomplete thermalization between subsequent experiments, carrier frequency offsets, and numerical errors in the data analysis.

In summary, the quantum computation succeeded, and the quantum computer solved a problem in fewer steps than is possible classically. Furthermore, for this small-scale quantum computer, imperfections were dominated by technology, rather than by fundamental issues.

5.4 Quantum error detection (2 spins)

5.4.1 Problem description

The goal of this experiment [LVZ⁺99]⁵ was to study the effectiveness of quantum error correction in a real experimental system, focusing on effects arising from imperfections of the logic gates. We did this by testing the two-qubit error detection code of section 2.4.1 on a two-spin molecule.

We designed the experiment such that potential artificial origins of (favorable) bias were eliminated in the following ways. First, we compared the preservation of arbitrary states stored with and without coding (the latter is unprotected but not affected by coding operations). Second, by ensuring that all qubits used in the code decohere at nearly the same rate, we eliminated apparent improvements brought about by having an ancilla with a lifetime much longer than the original unencoded qubit. Third, our experiment utilized only naturally occurring error processes.

⁵This experiment was proposed by Debbie Leung and Ike Chuang. They also worked out the theory. Samples were selected and prepared by Mark Sherwood and Nino Yannoni. I performed the actual experiment. The data analysis and numerical simulations were mostly the work of Debbie, Ike and Xinlan Zhou.

5.4.2 Experimental procedure

The molecule selected for this experiment was ^{13}C -labeled sodium formate (CHOO^-Na^+) at 15°C . The sample was a 0.6 ml, 1.26 molar solution (8:1 molar ratio with anhydrous calcium chloride) in deuterated water. The proton and carbon were used as input (qubit 1) and ancilla (qubit 2) respectively, and have relaxation time constants of $T_1^H = 9$ s, $T_1^C = 13.5$ s, $T_2^H = 0.65$ s and $T_2^C = 0.75$ s. The fact that $T_2 \ll T_1$ ensures that the effect of amplitude damping was small compared to that of phase damping. Furthermore, $T_2^H \approx T_2^C$, as desired.⁶

For the preparation of arbitrary input states, we took advantage of the axisymmetry of phase damping, by which it is sufficient to prepare a set of states in one half of a vertical cross section through the center of the Bloch sphere. The input state was therefore prepared by a $Y_1(\theta)$ pulse, where θ was arrayed from 0° to 180° in steps of 18° .

The state of the ancilla must be effective pure in order for the code to work. The desired state ($|0\rangle$) was obtained by temporal averaging, via a summation of two experiments: one experiment started off with ρ_{eq} and in the other experiment the populations of $|01\rangle$ and $|11\rangle$ were interchanged at the start, via a CNOT_{21} ($Y_1\tau X_1$, from left to right, with $\tau = 1/2J$).

In the coding experiment, we performed the encoding ($Y_2\bar{X}_1\bar{Y}_1\tau Y_1$) and decoding ($Y_1\tau\bar{Y}_1 X_1\bar{Y}_2$) operations before and after phase damping, whereas in the control experiment, these operations were omitted (see Fig. 5.10). The output state of the stored qubit was read out on spin 1 via a X_1 pulse.

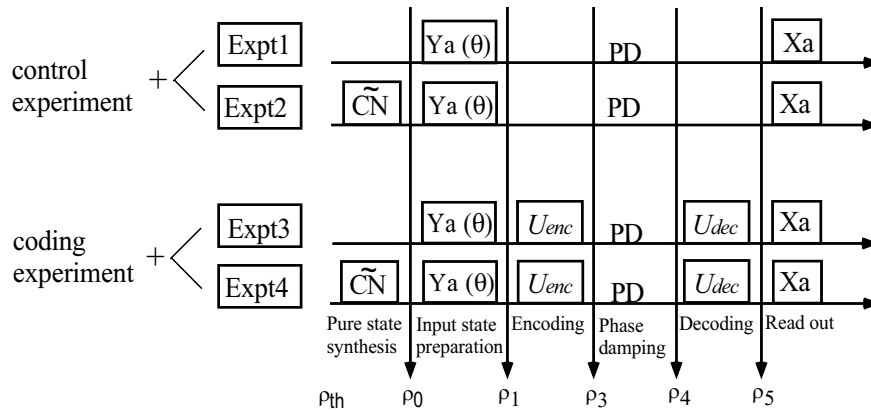


Figure 5.10: Schematic diagram for the two-bit code experiment.

If the ancilla spin is in the effective pure state $|0\rangle$, only the low-frequency line in the doublet of spin 1 is present. However, if a phase error occurs on the encoded state, the ancilla will

⁶We performed a second set of experiments with $^{13}\text{CHCl}_3$, for which $T_2^H \gg T_2^C$. Those were also published in [LVZ⁺99] but we shall not present them here.

be $|1\rangle$ after decoding. Thus, after decoding, the low-frequency line of the doublet of spin 1 corresponds to “accepted” states and the high-frequency line corresponds to “rejected” states.

5.4.3 Experimental results

The predicted accepted output states with and without coding are shown in Fig. 5.11. These plots are the result of numerical simulations which include the phase damping model of Eq. 3.26 in section 3.1.5. The main feature is that the Bloch sphere becomes ellipsoidal without encoding but remains largely spherical (i.e. the state is better preserved) with encoding. We note that the amplitude of the accepted states is shrunk with respect to the original state; this is because the two-bit code can only detect, not correct errors.

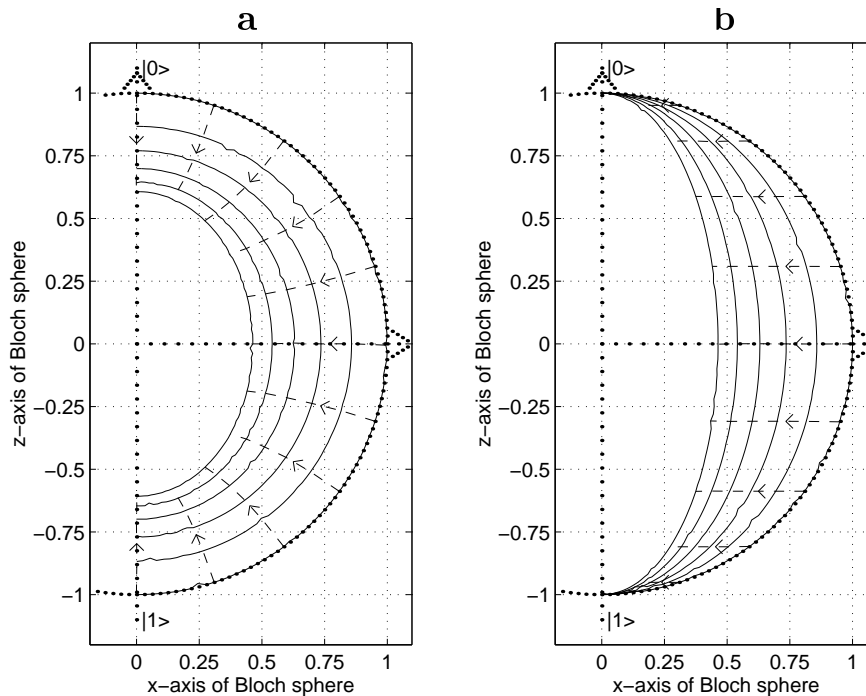


Figure 5.11: Predicted Bloch spheres (a) with and (b) without encoding, for a set of equally spaced storage times ($k \times 61.5$ ms for $k = 0, 1 \dots, 5$), corresponding to a probability of phase error (without encoding) of $p = 0, 0.071, 0.133, 0.185, 0.230$ and 0.269 .

Figure 5.12 shows the experimentally measured accepted output states, again with and without coding. The agreement of the main features between Figs. 5.11 and 5.12 is striking.

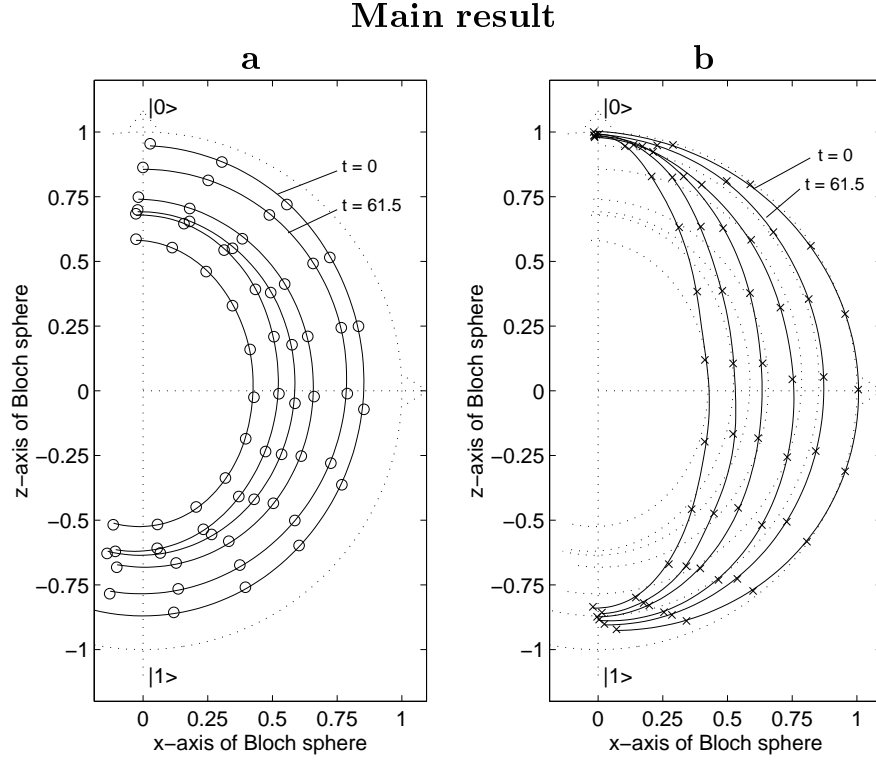


Figure 5.12: Experimentally measured Bloch spheres (a) with and (b) without encoding, for the same storage times as in Fig. 5.11. The circles are experimental data points and the solid lines are least square fitted ellipses.

5.4.4 Discussion

We quantified how well a quantum state is preserved experimentally via the ellipticity of the Bloch sphere, which we define as

$$\sqrt{\frac{I(\theta = 0)}{I(\theta = \frac{\pi}{2})}} \quad (5.2)$$

where the intensity I as a function of θ is ideally of the form

$$I_{ideal}(\theta) = A + B \sin^2 \theta. \quad (5.3)$$

In order to include signal strength attenuation with increasing θ and constant offsets in the angular positions, we actually fitted (non-linear least-squares fit) the experimental data points to the expression

$$I_{exp}(\theta) = (A + B \sin^2(\theta + D))(1 - C(\theta + D)) \quad (5.4)$$

instead.

The data of Fig. 5.13 demonstrate that coding removes the first order term in the growth of

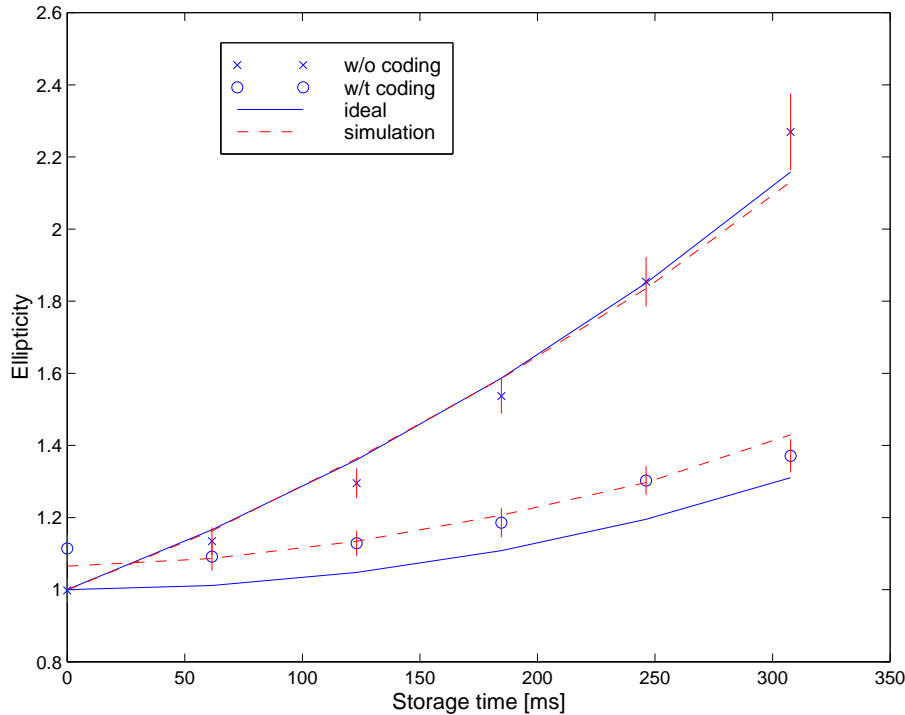


Figure 5.13: Ellipticity as a function of storage time. The experimental datapoints are given for the case with and without coding, along with ideal predictions as well as simulations which take the effect of RF inhomogeneities into account.

the Bloch sphere ellipticity as a function of storage time, which corresponds to the first order improvement in the conditional fidelity expected from the theory (section 2.4.1). However, imperfections in the logic gates caused the ellipticity to increase by 10% for the case of zero storage time (i.e. the zeroth order term). This number represents the cost of “noisy” gates.

While the data of Fig. 5.12 exhibit a clear correction effect, there are notable deviations from the ideal case of Fig. 5.11. First, the ellipses with coding are smaller than their counterparts without coding (this reduces the absolute fidelity but not the conditional fidelity). This is most obvious when the storage time is zero, in which case the coding and the control experiments should produce equal outputs. Second, the signal strength is attenuated with increasing θ relative to ideal ellipses. Third, although the data points are well fitted by ellipses, their angular positions are not exactly as expected (“ θ -offsets”). Finally, the spacings between the ellipses deviate from expectation.

A major cause of experimental errors was RF field inhomogeneity, which causes gate imperfections. This was determined by a series of simulations of RF inhomogeneity effects, which reproduced the reduced amplitude in the coding experiments. The asymmetry in the experimental Bloch spheres is well explained by amplitude damping. We do not have a convincing explanation for the other two discrepancies.

In summary, we have demonstrated experimentally that using a two bit phase damping detection code, the coherence time of qubits in bulk NMR systems can be conditionally lengthened. These experimental results also provide quantitative measures of the major imperfections in the system. The principle source of errors, RF field inhomogeneity, was studied and a numerical simulation was developed to model our data. Despite the imperfections, a net amount of error reduction was observed, when comparing cases with and without coding, including gate errors in both cases.

5.5 Logical labeling (3 spins)

5.5.1 Problem description

The goal of this experiment [VYSC99]⁷ was threefold: (1) to take a step in complexity from two spins to three spins, (2) to explore the use of homonuclear spin systems and (3) to test the concept of logical labeling for the first time. These three goals come together naturally as at least three spins are required for a meaningful demonstration of logical labeling, and all three spins must be homonuclear (section 4.4.3).

The operations needed for logical labeling follow from comparison of Eq. 4.32 with Eq. 4.33: the populations of the states $|001\rangle \leftrightarrow |101\rangle$ and $|010\rangle \leftrightarrow |110\rangle$ must be interchanged, while the remaining four populations must be unaffected. This requires a $CNOT_{21}$ and a $CNOT_{31}$.

As a test of logical labeling and subsequent control over the dynamical behavior of the logically labeled spins, we chose to implement Grover's algorithm on the effective pure two-qubit subspace within the three-spin molecule. With the two-qubit version of this algorithm, one can find the unique but unknown x_0 among $N = 4$ possible values of x which satisfies $f(x_0) = 1$ in just one query, compared to on average 2.25 queries classically.

A fourth, additional, goal was to study the preservation of the effective pure state after many operations. Grover's algorithm lends itself perfectly to such studies in the form of many repeated Grover iterations (section 2.3.2).

5.5.2 Experimental procedure

We selected bromotrifluoroethylene (Fig. 4.3 c) dissolved in deuterated acetone (10 mol%) as the central molecule in our experiments, because the spin-1/2 ^{19}F nuclei have large J -couplings

⁷This experiment was proposed by myself. I also worked out the theory, wrote the framework for dealing with homonuclear spins, invented the "uncoupling frame", wrote the pulse sequences, carried out the experiment and did the data analysis, under the guidance of Ike Chuang. Nino Yannoni and Mark Sherwood came up with the molecule, prepared the sample and gave advice on NMR techniques.

and chemical shifts, as well as long coherence times, which make it suitable for quantum computation. The ^{12}C nuclei are non-magnetic and the interaction of the spin-3/2 Br nucleus with the fluorine spins is averaged out due to fast Br relaxation (chapter 4).

The ^{19}F Larmor frequencies are ≈ 470 MHz (at 11.7 T) and the spectrum is first order, consisting of three well-separated quadruplets, with $\omega_1 - \omega_2/2\pi \approx 13.2$ kHz and $\omega_3 - \omega_1/2\pi \approx 9.5$ kHz. The coupling constants are measured to be $J_{12} = -122.1$ Hz, $J_{13} = 75.0$ Hz and $J_{23} = 53.8$ Hz (see also [EM62]). In order to simultaneously address the four lines in one quadruplet without affecting the other two quadruplets, the envelope of the RF pulses was Gaussian shaped and the RF power was adjusted to obtain pulses of $\approx 300\mu\text{s}$.

The two CNOT gates of the logical labeling step commute and can thus be executed simultaneously. This was done via the pulse sequence of Fig. 5.14. This sequence implements the CNOT gates only up to single-spin Z rotations, which suffices for a diagonal initial state as used here. Furthermore, the I_z^2 , I_z^3 and $I_z^2 I_z^3$ terms in the Hamiltonian have no effect, since spins 2 and 3 remain along $\pm\hat{z}$. I_z^1 can be ignored because the pulses were applied in a reference frame in resonance with each spin.

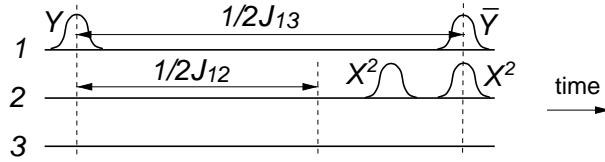


Figure 5.14: The logical labeling pulse sequence. The CNOT_{21} and CNOT_{31} are merged.

After logical labeling, the state must remain effective pure throughout the subsequent computation. This requires that while a computation is carried out using spins 2 and 3, spin 1 must “do nothing”, which is non-trivial in a system of coupled spins [LBCF99]: the effect of J_{12} and J_{13} must be removed. This could be done by using two refocusing X_1^2 pulses during every logical operation between 2 and 3, but we have devised a different method, which exploits the fact that it suffices to remove the effect of J_{12} and J_{13} *within the* $|0\rangle_1$ *subspace*. This uncoupling frame method requires no pulses at all and is described in Fig. 5.15.⁸

Mathematically, the transformation of the state of spins 2 and 3 to a reference frame offset by $\Delta\omega_2 = -\pi J_{12}$ and $\Delta\omega_3 = -\pi J_{13}$ with respect to ω_2 and ω_3 respectively, gives

$$\mathcal{H}' = 2\pi \left[(I_I^1 + I_z^1) J_{23} I_z^2 I_z^3 + (I_I^1 - I_z^1) (J_{23} I_z^2 I_z^3 - J_{12} I_z^2 - J_{13} I_z^3) \right], \quad (5.5)$$

where $I_I = \sigma_I/2$ (one half times the identity matrix). The first (second) term in the expression of \mathcal{H}' acts exclusively on the $|0\rangle_1$ ($|1\rangle_1$) subspace. Any state within the $|0\rangle_1$ subspace evolves

⁸We note that the uncoupling frame is somewhat related to selective decoupling [ME61], a technique to determine the relative sign of J -couplings by moving the reference frame of one nucleus (not several, as here) to the center of a submanifold.

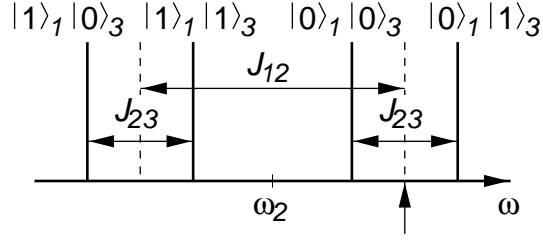


Figure 5.15: Spectrum of the transitions of spin 2, with the states of the other two spins as indicated. With respect to a reference frame rotating at $\omega_2/2\pi - J_{12}/2$ (indicated by an arrow), spins 2 which see a spin 1 in $|0\rangle$, evolve under J_{23} only and are thus *uncoupled* from 1. J_{12} does affect 2's evolution in the $|1\rangle_1$ subspace, but the signal of this subspace does not interfere with that of the $|0\rangle_1$ subspace. Similarly, spin 3's rotating frame must be moved to $\omega_3/2\pi - J_{13}/2$. A separate channel was used for spins 2 and 3.

only under $J_{23}I_z^2I_z^3$ and will remain within the $|0\rangle_1$ subspace. Within the $|0\rangle_1$ subspace and using the uncoupling reference frame, spins 2 and 3 are thus uncoupled from 1.

For the implementation of the Grover algorithm on the logically labeled spins in the uncoupling frame, we used a pulse sequence similar to the one described in [CGK98]. First, Y_2Y_3 rotates both spins from $|00\rangle$ into $(|00\rangle + |01\rangle + |10\rangle + |11\rangle)/2$, an equal superposition of the four possible inputs. The amplitude of the $|x_0\rangle$ term is then amplified in two steps (see section 2.3.2). First, one of four functions $f_{x_0}(x)$ is evaluated, flipping the sign of the $|x_0\rangle$ term. This is done by one of four conditional phase flips $Y_2Y_4 \Phi_2\Theta_3 \bar{Y}_2\bar{Y}_3 1/2J_{23}$, where $\Phi = X$ for f_{00} and f_{10} and $\Phi = \bar{X}$ for f_{01} and f_{11} . $\Theta = X$ for f_{00} and f_{01} and $\Theta = \bar{X}$ for f_{10} and f_{11} . Second, inversion about the average is implemented by a Hadamard gate on both spins, followed by the conditional phase flip corresponding to f_{00} , and another Hadamard gate. The pulse sequence for this inversion step can be reduced to $X_2X_3 Y_2Y_3 1/2J_{23} \bar{Y}_2\bar{Y}_3$.

The entire sequence for Grover's algorithm takes approximately 20 ms and the labeling step takes about 7 ms. The coherence time for the three ^{19}F spins, expressed as the measured transverse relaxation time constant $T_2 \approx 4\text{-}8$ s, is sufficiently long for coherence to be maintained throughout the labeling and computation operations.

5.5.3 Experimental results

Fig. 5.16 shows the measured populations of the eight basis states, before and after the sequence of Fig. 5.14. The results agree with the theoretical predictions of Eqs. 4.32 and 4.33.

We experimentally confirmed that spins 2 and 3 are uncoupled from spin 1 by reconstructing the deviation density matrix of the three-spin system after creating the state $(|00\rangle + |11\rangle)/\sqrt{2}$ in the $|0\rangle_1$ subspace. For this three spin system, quantum state tomography involved a series of 27 consecutive experiments with different sets of read-out pulses. Fig. 5.17 shows the $|0\rangle_1$ subsystem in the predicted effective pure state and uncoupled from the $|1\rangle_1$ subspace. The

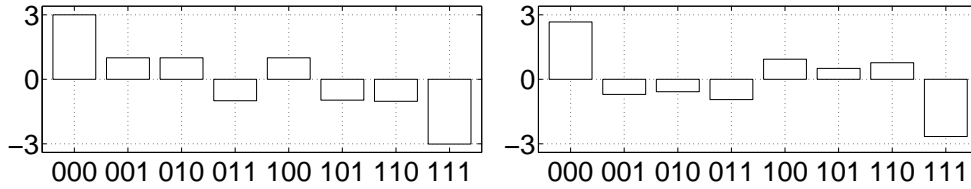


Figure 5.16: Experimentally determined populations (in arbitrary units, and relative to the average) of the states $|000\rangle, \dots, |111\rangle$ (Left) in thermal equilibrium and (Right) after logical labeling. The populations were determined by partial state tomography [CGKL98].

relative error in the state is $\|\rho_{\text{exp}} - \rho_{\text{th}}\|_2 / \|\rho_{\text{th}}\|_2 = 19\%$.

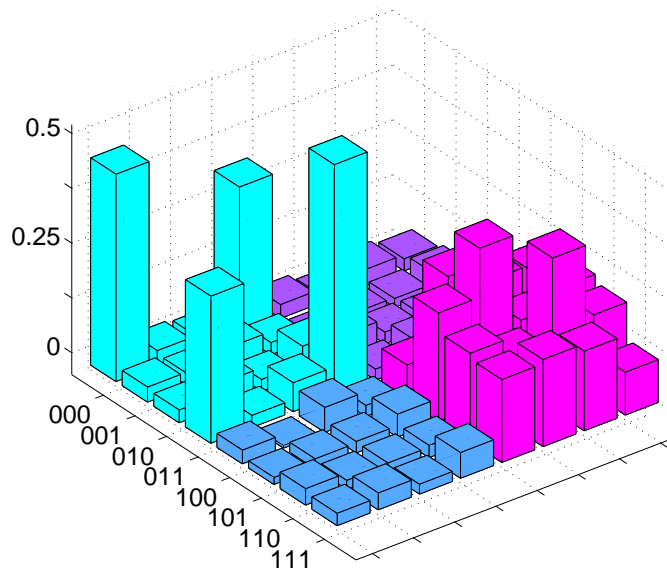


Figure 5.17: Normalized experimental deviation density matrix (with the diagonal shifted to obtain unit trace for the effective pure state), shown in absolute value. The entries in the second quadrant are very small, which means that the $|0\rangle_1$ and $|1\rangle_1$ subspaces are uncoupled. The four density matrix elements which stick out (in the first quadrant) are, in the logically labeled subspace, the $|00\rangle\langle 00|$ and $|11\rangle\langle 11|$ entries (which represent populations) and the $|00\rangle\langle 11|$ and $|11\rangle\langle 00|$ entries (which represent double quantum coherences).

The theoretical prediction for the Grover algorithm is that the output state of qubits 2 and 3 is the (effective pure) state $|x_0\rangle$. This can be determined by a measurement of spins 2 and 3 after a read-out pulse on each spin. The experimental spectra (Fig. 5.18, Left) as well as the deviation density matrices of the logically labeled subspace before, during and after the computation, confirm that the state remains an effective pure state throughout the computation and that the final state is $|x_0\rangle$.

An interesting question is how many logical operations can be executed while preserving the

effective pure character of the spins, and further, how quickly errors accumulate during longer pulse sequences. We study this by iterating the conditional flip and inversion steps in Grover's algorithm, which ideally gives rise to a periodic pattern: for $N = 4$, the amplitude of the x_0 term is expected to be 1 after 1 iteration, and again after 4, 7, \dots iterations [Gro97]. Fig. 5.18 demonstrates the expected periodic behavior in the output state in experiments with up to 37 iterations, which requires 448 pulses and takes about 700 ms.

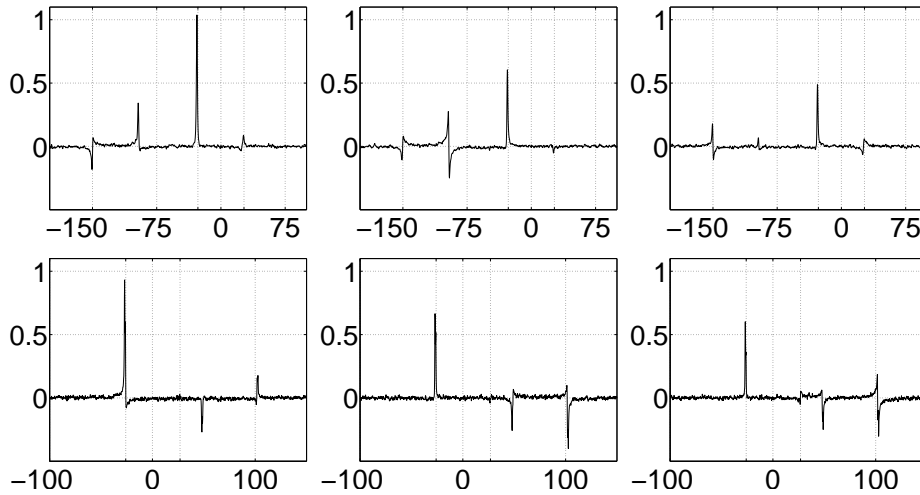


Figure 5.18: Real part of experimental spectra (frequencies in the uncoupling reference frame) for spin 2 (Top) and 3 (Bottom), after executing Grover's algorithm 1 (Left), 19 (Center) and 37 (Right) times, with $|x_0\rangle = |00\rangle$. The $|0\rangle_1$ subspace corresponds to the spectral lines at $\pm J_{23}/2 = \pm 26.9$ Hz. Ideally, the line at -26.9 Hz is positive and absorptive, with unit amplitude, while the line at $+26.9$ Hz is zero. Even after 37 iterations, x_0 can be unambiguously determined.

5.5.4 Discussion

The experiment met all four goals we set. It demonstrated that a k -qubit room temperature system can behave as if it were very cold, up to an exponential decrease in signal strength, when it is properly embedded in an n -spin system. Furthermore, we demonstrated coherent control over a homonuclear three-spin system.

The effective pure states were preserved for an unexpectedly long time and a surprisingly large number of pulses. We attribute this in part to the use of the uncoupling frame, which provides an elegant and simple alternative to refocusing schemes involving 180° pulses. Multiple couplings with ancilla spins can be neutralized simply by moving the carrier frequencies of the computation spins by the appropriate $\sum \pm J/2$. In contrast, refocusing pulses would have to be applied during every single evolution interval and their complexity rapidly increases as more

J -couplings are to be refocused [LBCF99]. This technique may find application in future experiments using logical labeling, as well as in quantum error detection experiments [LVZ⁺99], where the computation must only proceed within the subspace labeled error-free by the ancillae. However, refocusing pulses are still required whenever a coupling must be removed over an entire system rather than in a subspace only.

In addition to decoherence, errors mainly arise from imperfections in the pulses and coupled evolution during the 300 μ s pulses (reduction of τ_1 and τ_2 partially compensated for this effect). Spectra of the quality of Fig. 5.18 were obtained by choosing a particular implementation of the composite \hat{z} rotation in the phase flip step, such that the errors it introduces partially cancel with the errors of the inversion step. For example, while $YXY\bar{Y}$, $\bar{Y}\bar{X}Y$, $X\bar{Y}\bar{X}$ and $\bar{X}YX$ are all mathematically equivalent, the errors may in practice add up or cancel out with the errors from previous or subsequent pulse sequence segments. Clearly, a general optimization procedure will be very helpful for designing effective pulse sequences in future experiments involving more qubits.

5.6 Liquid crystal solutions (2 spins)

5.6.1 Problem description

The goal of this experiment [YSV⁺99]⁹ was to explore the use of liquid crystal solvents for quantum computing. In principle, liquid crystals offer several advantages over liquids as solvents for molecules used for NMR quantum computing. A liquid crystal solvent partly orients the solute molecules (Fig. 5.19) and as a result, the dipolar coupling between nuclear spins in molecules is not averaged out anymore as it is in isotropic solution. Liquid crystal solvents therefore permit a significant increase in clock frequency, while short spin-lattice relaxation times permit fast succession of experiments. Even more importantly, the clock frequency may increase by more than the relaxation rates, so more operations may be completed within the coherence time.

The coupling Hamiltonian for n spins in a molecule dissolved in a liquid crystal solvent is

$$\mathcal{H}^{\text{lc}}/\hbar = - \sum_i^n \omega_0^i I_z^i + \sum_{i<j}^n J_{ij} (I_x^i I_x^j + I_y^i I_y^j + I_z^i I_z^j) + \sum_{i<j}^n D_{ij} \left[2I_z^i I_z^j - \frac{1}{2}(I_x^i I_x^j + I_y^i I_y^j) \right]. \quad (5.6)$$

A dipolar term, which was absent from the coupling Hamiltonian in liquid solution (Eq. 4.5) now appears because the molecules are partially oriented. Also the resonance frequency ω_0^i

⁹Nino Yannoni proposed to use liquid crystal solvents instead of liquid solvents. He also selected a suitable liquid crystal solvent and prepared the sample. Mark Kubinec (at UC Berkeley) and I (at IBM) did experiments. The published data were taken at IBM. Mark Sherwood and Dolores Miller simulated the spectra and verified first-orderiness. This work was done under the guidance of Ike Chuang.

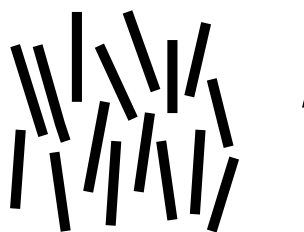


Figure 5.19: Liquid crystals are a phase of matter whose order is intermediate between that of a liquid and that of a crystal. The molecules are typically rod-shaped organic moieties about 25 Angstroms in length and their ordering is a function of temperature. The liquid crystal shown here is in the nematic phase. The degree of orientational order of the constituent molecules decreases with decreasing temperature.

includes the effects of molecular orientation and chemical shift anisotropy [EL75]. The dipolar coupling strength D , which also depends on the orientation, is typically 100 Hz to 10 kHz.

Unfortunately, the pulse sequences used for NMR quantum computing in isotropic liquids can not be applied if the Hamiltonian takes the form of Eq. 5.6. However, for an n -spin system with *first order* spectra, Eq. 5.6 becomes [SEP67]

$$H^{\text{lc}} = - \sum_{i=1}^n \hbar \omega_0^i I_z^i + \hbar \sum_{i < j}^n 2\pi (J_{ij} + 2D_{ij}) I_z^i I_z^j. \quad (5.7)$$

This Hamiltonian has the same form as the Hamiltonian of Eq. 4.5, so the pulse sequences that have been used successfully for NMR quantum computing in isotropic solution can now be applied directly to liquid crystal solutions, permitting computations with $f_{\text{clock}} = 2|(J + 2D)|$ Hz, a frequency that can be much higher than $2|J|$.

5.6.2 Experimental approach and results

We chose ^{13}C -labeled chloroform (CHCl_3) as the quantum computer molecule. This is the molecule we had used successfully in the first quantum computing experiments. The liquid crystal we selected was ZLI-167 (EMI Industries, Hawthorne, NY).

Table 5.1 shows the ^{13}C - ^1H coupling strength, the spin-lattice relaxation time (T_1) and the spin-spin relaxation time (T_2) for ^{13}C and ^1H in chloroform ($^{13}\text{CHCl}_3$) in liquid crystal solution and for comparison also in isotropic solution, both at ambient temperature.

In order to show that quantum computations can be done successfully using liquid-crystal solution NMR, we have implemented the Grover search algorithm for two qubits using $^{13}\text{CHCl}_3$ dissolved in ZLI-1167. The carbon and proton spins were first prepared in an effective pure state created by temporal labeling (via cyclic permutations, see section 4.4.4) followed by the Grover protocol used in the logical labeling experiment of section 5.5.

solvent	J	$J + 2D$	T_1 (^{13}C)	T_1 (^1H)	T_2 (^{13}C)	T_2 (^1H)
acetone- d_6	215	—	25	19	0.3	7
ZLI-1167	—	1706	2	1.4	0.2	0.7

Table 5.1: ^{13}C - ^1H spin couplings [Hz] and relaxation times [s] for $^{13}\text{C}^1\text{HCl}_3$ in isotropic (deuterated acetone) and liquid crystal (ZLI-1167) solution.

The prediction is that the algorithm will put the spins in the state $|x_0\rangle$. The ^{13}C and ^1H readout spectra for the four possible x_0 are shown in Fig. 5.20. As predicted for two spins in an effective pure state, the value of x_0 is clearly indicated by the amplitude and phase of the two resonance lines in the ^{13}C and ^1H spectra. Measurement of the deviation density matrix using quantum state tomography confirms that the output states are as theoretically predicted, as illustrated in Fig. 5.21 for $x_0 = 11$.

5.6.3 Discussion

The ^{13}C - ^1H coupling in the liquid crystal (ZLI-1167) is eight times larger than the scalar coupling in acetone- d_6 , corresponding to a computer with a clock that is eight times faster. The product of the shortest coherence time and the clock frequency $T_2 f_{\text{clock}} = 2T_2 J$, which approximates the number of gates that can be executed while maintaining coherence, is about five times higher in ZLI-1167 than in deuterated acetone, meaning that more complex algorithms could be implemented using the liquid crystal solvent.

Furthermore, the chloroform ^{13}C and ^1H spin-lattice relaxation times are about 12 times shorter in ZLI-1167 than in acetone- d_6 . Since all experiments (including most calibration experiments) require an equilibration time of $5T_1$, an order of magnitude savings in time can be significant, and will become more so as the number of qubits increases. This advantage will be especially important for experiments requiring temporal averaging (or also just signal averaging), or in quantum state tomography experiments.

Another advantage of using liquid crystal solvents is that they permit a different choice of spin-bearing molecules that may be suitable for quantum computing. Dipolar coupling, which is manifest in the NMR spectra of oriented molecules, requires only proximity between the spins of interest. As a result, two spins that are separated by several bonds and which have no scalar coupling may, if spatially proximate, have dipolar coupling sufficiently large for quantum computation. The ability to control the degree of orientation of the solute molecule by varying the solvent temperature and solute concentration [EL75] provides the experimentalist with means of tailoring the NMR spectrum to meet the requirements for quantum computing. In addition, magic-angle spinning and multiple pulse methods can be used to preferentially scale the dipolar splitting in the spectrum of a liquid-crystal-oriented molecule to convert it to first order [OOC⁺91].

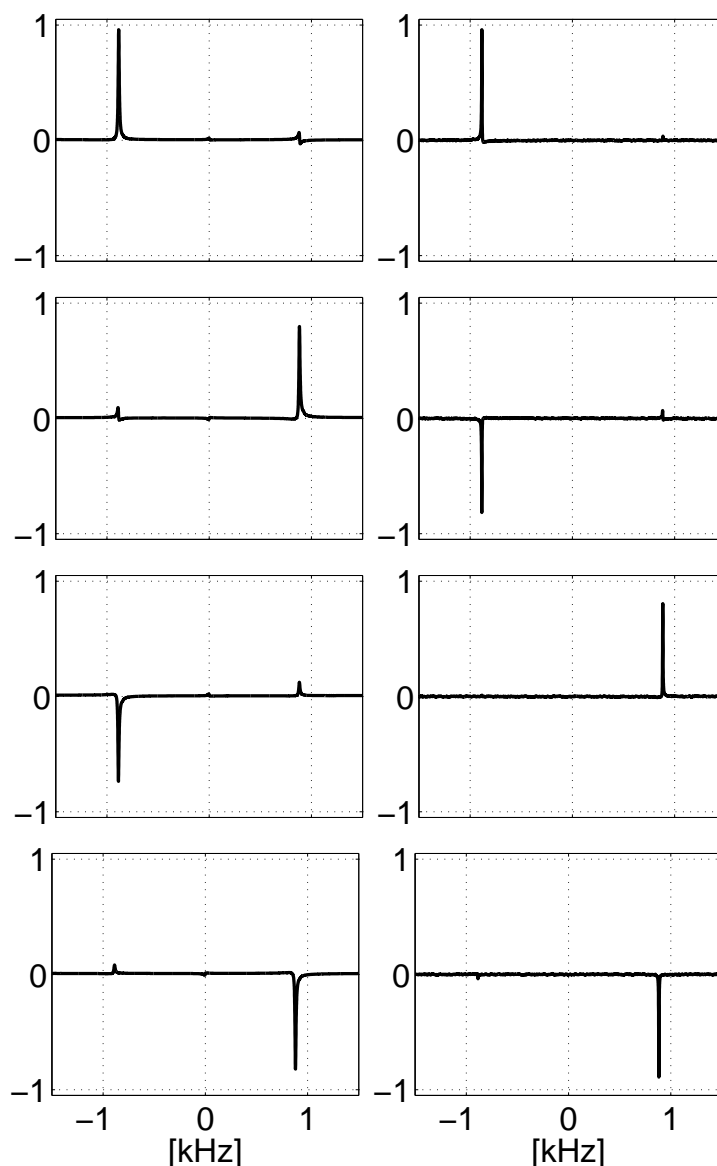


Figure 5.20: Spectral readout of the results of the 2-qubit Grover search using $^{13}\text{C}^1\text{HCl}_3$ in a liquid crystal solvent showing absorption and emission peaks which clearly indicate the value of x_0 (00, 01, 10, and 11, from top to bottom). The real part of the ^1H (left) and ^{13}C (right) spectra are shown, with frequencies relative to $\omega_0^H/2\pi$ and $\omega_0^C/2\pi$. The vertical scale is arbitrary.

Complications do arise with the use of liquid crystal solvents: (1) the NMR lines of small molecules dissolved in liquid crystal solvents are susceptible to a broadening mechanism not found in isotropic solution, most likely due to variations in the degree of orientation caused by thermal gradients in the sample. Nonetheless, resonance line widths < 2 Hz (^{13}C) and < 3 Hz (^1H) were obtained for $^{13}\text{C}^1\text{HCl}_3$ in ZLI-1167; (2) the large dipolar couplings may cause unwanted evolution of the spins during the RF pulses, especially in homonuclear spin systems.

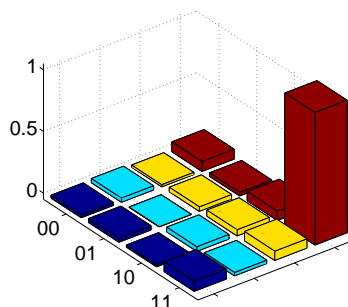


Figure 5.21: Experimentally measured deviation density matrix elements for the $x_0 = 11$ case.

We have not used liquid crystal solvents in any of the later experiments. However, due to their many advantages and only moderate disadvantages, we believe it is worth revisiting this possibility in the context of larger spin systems.

5.7 Cancellation and prevention of systematic errors (3 spins)

5.7.1 Problem description

In this experiment [VSS⁺00]¹⁰ we studied the effect of systematic errors in the one-qubit gates. Aside from the well-understood scaling limitations due to the use of a high-temperature (almost random) system instead of a low-temperature (low entropy) polarized spin system (section 4.4), such errors represent an important limitation in using nuclear spins in molecules to implement larger quantum algorithms.

Single-qubit gates are implemented by applying RF pulses of precise duration and phase, but which in practice greatly vary in strength over the sample volume, causing the gate fidelity [SN96] to be less than 95% (section 5.1). Producing a homogeneous RF field is difficult because of the sample geometry and the necessity of keeping the B_1 field transverse to the B_0 field. If such systematic errors simply accumulated, these observations would imply that for a success rate of only 1%, fewer than 90 gates ($0.95^{90} \approx 0.01$) applied to any one spin could ever be cascaded in these systems.

One technique which has been proposed for controlling errors in quantum gates is quantum error correction (section 2.4), but this is associated with a large overhead. The principle attribute of quantum error correction techniques is their ability to correct completely random errors which originate from fundamentally irreversible *decoherence* phenomena; in principle,

¹⁰I worked out the theory and many of the pulse sequence simplification ideas, along with Matthias Steffen and Ike Chuang. The simplified temporal averaging scheme is due to Ike. The experiment and data analysis was done by myself and Matthias. The molecule was synthesized by Greg Breyta, and proposed by Nino Yannoni and Mark Sherwood, who also gave advice on NMR techniques.

systematic errors, which are inherently *reversible* — at least on an appropriate time scale — should be much easier to control, given knowledge about their origin.

We tested the extent to which systematic errors can (1) be avoided by simplifying the pulse sequences and (2) be made to cancel out in practice. The concrete experiment for this test consisted of repeated executions of the two main steps in Grover’s algorithm (the oracle call and the inversion about the average described in section 2.3.2) for three spins.

The three-qubit Grover algorithm can find a “marked” element x_0 among $N = 8$ possible values of x in only two oracle queries (evaluations of $f(x)$), whereas a classical search needs 4.375 attempts on average to find x_0 . The oracle call requires one TOFFOLI gate plus several one-qubit gates, and so does the inversion about the average. The amplitude of $|x_0\rangle$ is predicted to reach a first maximum after two iterations, and oscillates as the number of iterations increases.

5.7.2 Experimental approach

The first method we developed to reduce the number of one- and two-spin gates needed to implement arbitrary unitary operations was the general pulse simplification methodology of section 4.8. As a result, the pulse sequence for each Toffoli gate used in the algorithm was reduced from 70.5 90° pulses and 8 evolutions of $1/2J$ (if only CNOT’s and 1-qubit gates would have been used to implement the controlled- V ’s, as in the standard methods of [BBC⁺95]) to 19 pulses, 2 evolutions of $1/2J$ and 3 of $1/4J$.

The second method to reduce the complexity concerns the initialization of the qubits to an effective ground state. We generalized the temporal averaging procedure from a scheme based on cyclic permutations to a scheme based on arbitrary linearly independent experiments (section 4.4). Whereas cyclic permutations would require seven experiments with very complex state preparation sequences, all the data shown here were obtained using just three experiments with much simpler preparation sequences. The expected variance of the $2^n - 1$ populations obtained with this state preparation procedure amounts to only 7% of their average value.

The actual pulse sequences used in the experiment are collected in Appendix B.

5.7.3 Experimental Results

We selected ^{13}C -labeled CHFBr_2 ¹¹ for our experiments. The ^1H , ^{19}F and ^{13}C spins served as the quantum bits. The coupling constants in this heteronuclear spin system are $J_{\text{HC}} = 224$ Hz, $J_{\text{HF}} = 50$ Hz and $J_{\text{FC}} = -311$ Hz. As always, the scalar interaction with the Br nuclei is averaged out and only contributes to decoherence.

¹¹Synthesized by heating a mixture of $^{13}\text{CHBr}_3$ (2.25 g, CIL) and HgF_2 (2.8 g, Aldrich) in increments (5°C for 15 min) from 70°C to 85°C in a Kugelrohr apparatus and condensing the product into a cooled bulb. This material was re-distilled bulb-to-bulb at 65°C to give 750 mg (99 % purity) of $^{13}\text{CHFBr}_2$, which was dissolved in d_6 -acetone.

In order to read out the final state of the three spins, we used the extra information given by the multiple lines in the spectrum of each spin. Given that all three spins are in an effective pure energy eigenstate and that they are all mutually coupled, each spectrum contains only a single line, the frequency of which, combined with the knowledge of the J_{ij} , reveals the state of the remaining spins. The inset of Fig. 5.22 (a) gives the experimentally measured ^{13}C output spectrum after two Grover iterations. Fig. 5.22 (a) also gives the complete output *deviation* density matrix.

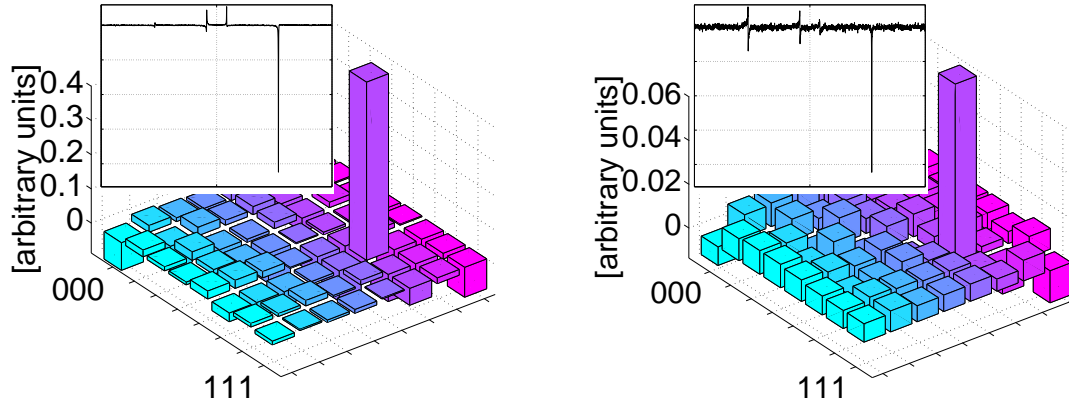


Figure 5.22: (Top) Experimental deviation density matrices ρ_{exp} for $|x_0\rangle = |1\rangle|0\rangle|1\rangle$, shown in magnitude with the sign of the real part (all imaginary components were small), after (a) 2 and (b) 28 Grover iterations. (Bottom) The corresponding ^{13}C spectra (^{13}C was the least significant qubit). The receiver phase and read-out pulse are set such that the spectrum be absorptive and positive for a spin in $|0\rangle$.

The agreement between experimental results and theoretical predictions is good, considering that about 100 pulses were used and that the systematic error rate exceeds 5% per RF pulse (the measured signal loss due to RF field inhomogeneity after applying X_i). This suggests that the systematic errors cancel each other out to some degree. We examined this in more detail in a series of experiments with increasingly longer pulse sequences executing up to 28 Grover iterations (Fig. 5.23).

5.7.4 Discussion

Fig. 5.23 (a) shows that the diagonal entry d_{x_0} of ρ_{exp} oscillates as predicted but the oscillation is damped as a result of errors, with a time constant T_d of 12.8 iterations. However, T_d would have been smaller than 1.5 if the errors due to just the RF field inhomogeneity were cumulative (Fig. 5.23 (a), solid line). Remarkably, after a considerable initial loss, d_{x_0} decays at a rate close to the ^{13}C T_2 decay rate (dashed line), which can be regarded as a lower bound on the overall error rate.

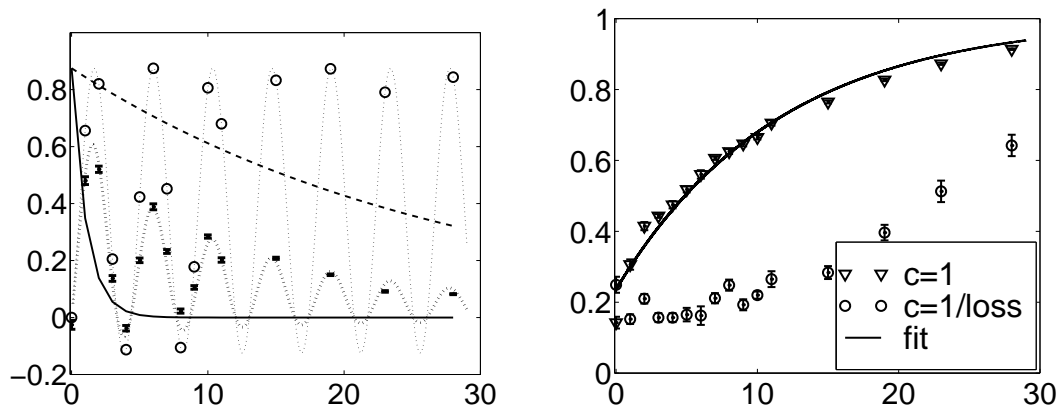


Figure 5.23: (a) Experimental (error bars) and ideal (circles) amplitude of d_{x_0} , with fits (dotted) to guide the eye. Dashed line: the signal decay for ^{13}C due to intrinsic phase randomization or decoherence (for ^{13}C , $T_2 \approx 0.65$ s). Solid line: the signal strength retained after applying a continuous RF pulse of the same cumulative duration per Grover iteration as the pulses in the Grover sequence (averaged over the three spins; measured up to 4 iterations and then extrapolated). (b) The relative error ϵ_r .

A more complete measure to quantify the error and benchmark results is the relative error $\epsilon_r = \|c\rho_{exp} - \rho_{th}\|_2 / \|\rho_{th}\|_2$, where ρ_{exp} and ρ_{th} are the experimental and theoretical (traceless) deviation density matrices. Comparison of ϵ_r with $c = 1$ and c equal to the inverse of the signal loss (Fig. 5.23 (b)) reveals that signal loss dominates over other types of error. Furthermore, the small values of ϵ_r with $c > 1$ suggest that $|x_0\rangle$ can be unambiguously identified, even after almost 1350 pulses. This is confirmed by the density matrix measured after 28 iterations, which has a surprisingly good signature (Fig. 5.22 (b)). Given the error of $> 5\%$ per single 90° rotation, all these observations demonstrate that substantial cancellation of errors took place in our experiments.

The error cancellation achieved was partly due to a judicious choice of the phases of the refocusing pulses, but a detailed mathematical description in terms of error operators is needed to fully exploit this effect in arbitrary pulse sequences. This difficult undertaking is made worthwhile by our observations. This conclusion is strengthened by a similar observation in the experiment of section 5.5. Also, we believe that error cancellation behavior is *not* just a property of the Grover iterations, because we found experimentally that the choice of implementation of the building blocks dramatically affects the cancellation effectiveness.

In summary, more than 280 two-qubit quantum gates involving 1350 RF pulses were successfully cascaded, which far exceeds not only the number of gates used in all previous NMR quantum computing experiments but also the limitation of 90 pulses, imposed by cumulative systematic errors. Whereas the cancellation of systematic errors makes it possible to perform such a surprisingly large number of operations, the methods for simplifying pulse sequences reduce the number of operations needed to implement a given quantum circuit. This combination

permitted the observation of 28 full cycles of the Grover algorithm with 3 spins, and suggests that many other interesting quantum computing experiments may be within reach.

5.8 Efficient cooling (3 spins)

5.8.1 Problem description

The goal of this experiment [CVS01]¹² was to cool down the spin temperature of one out of three spins using the Schulman-Vazirani scheme for efficient cooling [SV99]. A secondary goal was to draw the attention of the quantum computing community to the Schulman-Vazirani algorithm.

The ideas underlying Schulman-Vazirani cooling have been introduced in section 3.1.3. The quantum circuit which summarizes the steps in the Schulman-Vazirani boosting procedure, was described in section 4.4.6, Fig. 5.24. We include it here again for convenience.

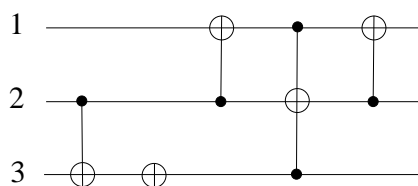


Figure 5.24: A quantum circuit that implements the Schulman-Vazirani boosting procedure for cooling one out of three qubits.

While it is common in NMR to enhance the polarization of a low- γ nucleus by polarization transfer from a high- γ nucleus [EBW87, Fre97], in this experiment the goal was to enhance the polarization of one out of three *equally* polarized spins. Any polarization gain is thus exclusively the result of bootstrapping using the Schulman-Vazirani cooling scheme. In this case, the theoretical maximum achievable polarization enhancement is by a factor of 3/2; this is equivalent to lowering the spin temperature of that spin by the same factor.

5.8.2 Experimental procedure

A 2 mol % solution of C_2F_3Br in deuterated acetone provided three spins with equal polarizations. We chose this particular molecule for its remarkable spectral properties (we had successfully used it in the logical labeling experiment of section 5.5): strong chemical shifts (0, 28.2, and 48.1 ppm, arbitrarily referenced) and large scalar couplings ($J_{ab} = -122.1$ Hz, $J_{ac} = 75.0$

¹²I devised this experiment. Darrick Chang, a summer student, worked out the pulse sequences and took the data under my guidance, and with the help of Matthias Steffen.

Hz, and $J_{bc} = 53.8$ Hz) combined with long relaxation times (T_2 's ≈ 4 -8 s). The experiments were conducted at 30.0°C .

The quantum circuit of Fig. 5.24 results in the unitary operation (with qubit 1 the most significant qubit)

$$U = \begin{pmatrix} 0 & 1 & 0 & 0 & 0 & 0 & 0 & 0 \\ 1 & 0 & 0 & 0 & 0 & 0 & 0 & 0 \\ 0 & 0 & 1 & 0 & 0 & 0 & 0 & 0 \\ 0 & 0 & 0 & 0 & 1 & 0 & 0 & 0 \\ 0 & 0 & 0 & 0 & 0 & 1 & 0 & 0 \\ 0 & 0 & 0 & 1 & 0 & 0 & 0 & 0 \\ 0 & 0 & 0 & 0 & 0 & 0 & 1 & 0 \\ 0 & 0 & 0 & 0 & 0 & 0 & 0 & 1 \end{pmatrix}, \quad (5.8)$$

which transforms the thermal density matrix as

$$I_z^1 + I_z^b + I_z^3 \rightarrow \frac{3}{2} I_z^1 + \frac{1}{2} I_z^2 - I_z^1 I_z^3 - I_z^2 I_z^3. \quad (5.9)$$

The propagator U thus redistributes the populations in such a way that the highest populations are moved to states where qubit 1 is in $|0\rangle$. This can be clearly seen by expressing the resulting density matrix in explicit matrix form:

$$\rho_f = \frac{1}{2} \begin{pmatrix} 1 & 0 & 0 & 0 & 0 & 0 & 0 & 0 \\ 0 & 3 & 0 & 0 & 0 & 0 & 0 & 0 \\ 0 & 0 & 1 & 0 & 0 & 0 & 0 & 0 \\ 0 & 0 & 0 & 1 & 0 & 0 & 0 & 0 \\ 0 & 0 & 0 & 0 & -1 & 0 & 0 & 0 \\ 0 & 0 & 0 & 0 & 0 & -1 & 0 & 0 \\ 0 & 0 & 0 & 0 & 0 & 0 & -1 & 0 \\ 0 & 0 & 0 & 0 & 0 & 0 & 0 & -3 \end{pmatrix}. \quad (5.10)$$

Because the density matrix remains in a diagonal state after application of each quantum gate in Fig. 5.24, the boosting procedure can actually be implemented using a simplified quantum circuit: replacing each gate with a gate whose unitary matrix is correct up to phases preserves the transformation given by Eq.5.8. Consequently, the Toffoli gate, for which the fastest known implementation takes on the order of $7/4J$ seconds (taking all J_{ij} to be $\approx J$), can be substituted with a Toffoli gate correct up to phases — consisting of a $90^\circ \hat{y}$ rotation of qubit 2 when qubit 3 is in $|1\rangle$, followed by a $180^\circ \hat{z}$ rotation of 2 when 1 is in $|1\rangle$ and a $-90^\circ \hat{y}$ rotation of 2 when 3 is in $|1\rangle$ — which takes only $1/J$ seconds. The actual pulse sequence used in the experiment is given in Fig. 5.25. This sequence was designed by standard pulse sequence simplification

techniques supplemented by Bloch-sphere intuition. The resulting unitary operator is

$$\tilde{U} = \begin{pmatrix} 0 & 1 & 0 & 0 & 0 & 0 & 0 & 0 \\ 1 & 0 & 0 & 0 & 0 & 0 & 0 & 0 \\ 0 & 0 & -1 & 0 & 0 & 0 & 0 & 0 \\ 0 & 0 & 0 & 0 & -1 & 0 & 0 & 0 \\ 0 & 0 & 0 & 0 & 0 & 1 & 0 & 0 \\ 0 & 0 & 0 & -1 & 0 & 0 & 0 & 0 \\ 0 & 0 & 0 & 0 & 0 & 0 & 1 & 0 \\ 0 & 0 & 0 & 0 & 0 & 0 & 0 & 1 \end{pmatrix}. \quad (5.11)$$

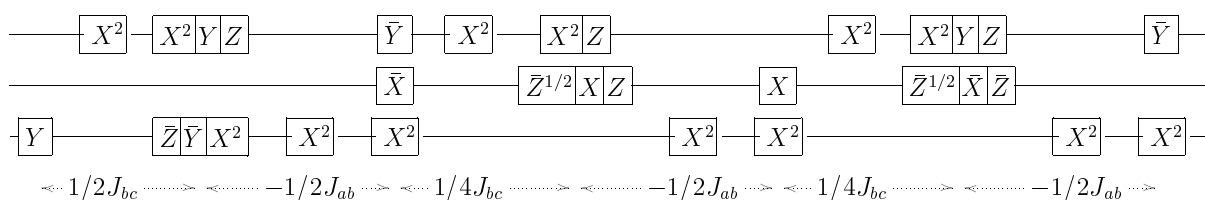


Figure 5.25: Pulse sequence used to implement the boosting procedure. This pulse sequence is designed for molecules with $J_{ab} < 0$ and $J_{ac}, J_{bc} > 0$.

All pulses were spin-selective, and varied in duration from 1 to 3 ms. Hermite 180 and av90 shaped pulses were employed for 180° and 90° rotations respectively, in order to minimize the effect of the J couplings between the selected and non-selected spins during the pulses. Couplings between the unselected spins are irrelevant whenever those spins are along $\pm \hat{z}$, as is the case here.

Bloch-Siegert shifts (sections 4.2.4 and 4.2.5) were accounted for in the pulse sequence out of necessity: they resulted in an extra phase acquired by the non-selected spins in their respective on-resonance reference frames, in some cases by more than 90° per pulse, while even phase shifts on the order of 5° are unacceptable. Bloch-Siegert corrections and other \hat{z} rotations were implicitly performed by changing the phase of subsequent RF pulses. The duration of the pulse sequence of Fig. 5.25 is about 70 ms.

5.8.3 Experimental results

The theoretical predictions for the spectrum of each spin after the boosting procedure can be derived most easily from Eq. 5.10, taking into account the sign and magnitude of the J -couplings. After a readout pulse on spin 1, the four spectral lines in the spectrum of 1 should ideally have normalized amplitudes $1 : 2 : 1 : 2$, compared to $1 : 1 : 1 : 1$ for the thermal equilibrium spectrum (for spins 2 and 3, the boosting procedure ideally results in normalized amplitudes of

$0 : 1 : 0 : 1$ and $-1 : 0 : 0 : 1$, respectively). So the prediction is that the boosting procedure increases the signal of spin 1 averaged over the four spectral lines by a factor of $3/2$, equal to the bound for polarization enhancement established in section 4.4.6. The experimentally measured spectra before and after the boosting procedure are shown in Fig. 5.26. The operation of the boosting procedure was further validated by measuring the full three-spin deviation density matrix, shown in Fig. 5.27.

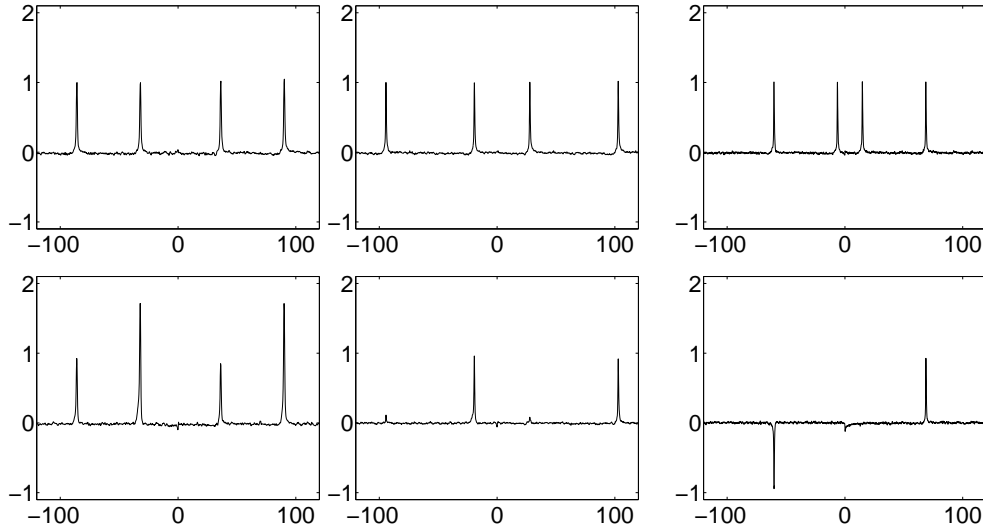


Figure 5.26: Experimentally measured spectra of spin 1 (Left), spin 2 (Center) and spin 3 (Right), after a readout pulse on the corresponding spin, for the spin system in thermal equilibrium (Top) and after applying the boosting procedure (Bottom). The real part of the spectra is shown, and the spectra were rescaled in order to obtain unit amplitude for the thermal equilibrium spectra. Frequencies are in Hz with respect to the Larmor frequency of the respective spins.

5.8.4 Discussion

Clearly, the signal of spin 1 has increased on average as a result of the boosting procedure, and the relative amplitudes of the four lines are in excellent agreement with the theoretical predictions. The measured areas under the four peaks combined before and after polarization transfer have a ratio of 1.255 ± 0.002 . The spectra of spins 2 and 3 after the boosting procedure are also in excellent agreement with the theoretical predictions, up to a small overall reduction in the signal strength.

The experimentally measured density matrix demonstrates not only that the boosting procedure exchanges the populations as intended, but also that it doesn't significantly excite any coherences. The experimentally measured $\text{Tr}(\rho_f I_z^1) / \text{Tr}(\rho_i I_z^1)$ gives a polarization enhancement factor of 1.235 ± 0.016 , consistent with the enhancement obtained just from the peak integrals of

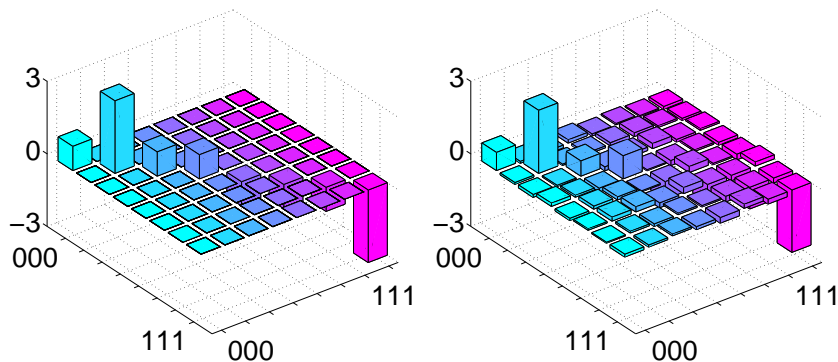


Figure 5.27: Pictorial representation of the theoretical (left) and experimentally measured (right) density matrices, shown in magnitude with the sign of the real part (all imaginary components were very small).

spin 1. The experimental implementation of the boosting procedure thus successfully increased the polarization of spin 1.

Despite the excellent qualitative agreement between the measured and predicted data, the quantitative polarization enhancement of spin 1 is lower than ideally achievable. Given the absence of substantial coherences (Fig. 5.27), we attribute this suboptimal enhancement primarily to signal attenuation due to RF field inhomogeneity and, to a lesser extent, to transverse relaxation. The minor excitation of coherences is attributed mostly to incomplete removal of undesired coupled evolution during the RF pulses.

In summary, we have experimentally demonstrated the building block for the hyperpolarization procedure outlined by Schulman and Vazirani on a homonuclear three-spin system. However, the repeated boosting required in a much larger spin system would be counteracted by relaxation and other causes of signal decay, such as RF field inhomogeneity. Also, when starting from thermal equilibrium at room temperature, the overhead in the number of nuclear spins required for the complete Schulman-Vazirani scheme is impractically large, despite its linear scaling (see section 4.4.6). Nevertheless, for higher initial polarizations, Schulman-Vazirani cooling may be a very valuable tool.

5.9 Order-finding (5 spins)

5.9.1 Problem description

At the time, the quest for the experimental realization of quantum computers had resulted in the creation of specific entangled quantum states with four qubits using trapped ions [SKK⁺00],

and in the creation of a seven-spin coherence using nuclear spins [KLMT00]. Also using nuclear spins, Grover's search algorithm [CGK98, JMH98, VSS⁺00] and the Deutsch-Jozsa algorithm [CVZ⁺98, JM98, MFM⁺00] on two, three and five qubit systems had been demonstrated.

However, a key step which remained yet to be demonstrated was a computation with the structure of Shor's factoring algorithm, which appears to be common to all quantum algorithms that achieve an exponential speedup [CEMM98]. Implementing the two main components of this structure, exponentiated unitary transformations and the quantum Fourier transform (section 2.3.3), is challenging because they require not just the creation of *static* entangled states, but also precise *dynamic* quantum control over the evolution of multiple entangled qubits, over the course of tens to hundreds of quantum gates for the smallest meaningful instances of this class of algorithms. The evolution of the states is precisely where NMR quantum computers appear to have an exponential advantage over classical computers [SC99].

The goal of this experiment [VSB⁺00]¹³ was to experimentally implement a quantum algorithm for finding the order of a permutation (section 2.3.3); its structure is the same as for Shor's factoring algorithm and it scales exponentially faster than any classical algorithm for the problem.

Specifically, we set out to implement the smallest instance of order-finding for which quantum computers outperform classical computers: the case of permutations π on four elements ($M = 4$), using a total of five qubits ($m = 2$ and $n = 3$).

It can be proven that in this case the best classical algorithm needs two queries of the oracle to determine r with certainty, and that using only one query of the oracle, the probability of finding r using a classical algorithm can be no more than $1/2$. One optimal classical strategy is to first ask the oracle for the value of $\pi^3(y)$: when the result is y , r must be 1 or 3; otherwise r must be 2 or 4. In either case, the actual order can be guessed only with probability $1/2$.

In contrast, the probability of success is ~ 0.55 after only one oracle-query using the quantum circuit of Fig. 2.13 on a single quantum computer: depending on the measurement outcome after running the algorithm, we can make a probabilistic guess r' as shown in Fig. 5.28. The probability of success $\Pr[r' = r]$ is independent of the distribution of r or π .

Note that since an ensemble of $\sim 10^{18}$ quantum computers contribute to the signal in our experiment, the order will follow from the output data with virtual certainty.

¹³I was planning a five qubit experiment to demonstrate period finding for some test functions when Richard Cleve proposed to do order-finding, which greatly enhanced the meaningfulness of the experiment. I worked out the theory and invented the much improved temporal labeling scheme. Matthias Steffen and I did the actual experiment together. Matthias wrote most of the pulse sequence framework. The five-spin molecule was discovered by Nino Yannoni and synthesized by Greg Breyta. Dolores Miller and Mark Sherwood did spectral simulations of the molecule. All this work was done under the guidance of Ike Chuang.

m	$r=1$	$r=2$	$r=3$	$r=4$	r'	$m=0$	$m=\text{odd}$	$m=2,6$	$m=4$
0	1	0.5	0.34375	0.25	1	0.5505	0	0	0
1,7	0	0	0.01451	0	2	0.1009	0	0	1
2,6	0	0	0.0625	0.25	3	0.1468	1	0	0
3,5	0	0	0.23549	0	4	0.2018	0	1	0
4	0	0.5	0.03125	0.25					

Figure 5.28: (Left) The probabilities that the measurement result m is 0, 1, ..., or 7, given r (for an ideal single quantum computer). (Right) The optimal probabilities with which to make a guess r' for r , given m .

5.9.2 Experimental approach

We custom synthesized a molecule [GMS68] containing five fluorine nuclear spins which served as the qubits. The molecule as well as the chemical shifts and J -coupling constants are shown in Fig. 5.29. The linewidths of the NMR transitions were ~ 1 Hz, so the T_2^* dephasing times of the spins were ≈ 0.3 s (the T_2 are longer). The T_1 time constants were measured to be between 3 and 12 s.

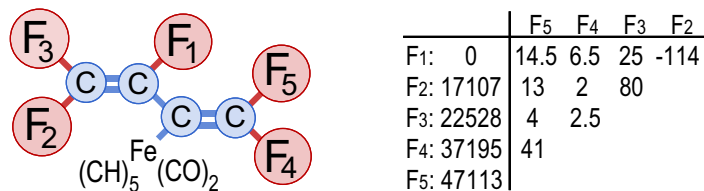


Figure 5.29: Structure of the pentafluorobutadienyl cyclopentadienyl dicarbonyl iron complex, with a table of the relative chemical shifts of the ^{19}F spins at 11.7 T [Hz], and the J -couplings [Hz]. A total of 76 out of the 80 lines in the 5 spectra are resolved.

All five spins were prepared in an effective pure state via the product operator approach to temporal averaging (section 4.4). We used 9 experiments (the theoretical minimum is $\lceil 2^n - 1/n \rceil = 7$), giving a total of 45 product operator terms. The $45 - (2^n - 1) = 14$ extra terms were canceled out pairwise, using NOT operations, which flip the sign of selected terms. The nine state preparation sequences were

$$\begin{aligned}
 &\text{CNOT}_{51} \text{CNOT}_{45} \text{CNOT}_{24} \text{NOT}_3, && \text{CNOT}_{21} \text{CNOT}_{52} \text{CNOT}_{45} \text{CNOT}_{34}, \\
 &\text{CNOT}_{14} \text{CNOT}_{31} \text{CNOT}_{53} \text{NOT}_2, && \text{CNOT}_{12} \text{CNOT}_{15} \text{CNOT}_{13} \text{CNOT}_{41}, \\
 &\text{CNOT}_{32} \text{CNOT}_{13} \text{CNOT}_{25} \text{NOT}_4, && \text{CNOT}_{31} \text{CNOT}_{43} \text{CNOT}_{23} \text{NOT}_5, \\
 &\text{CNOT}_{53} \text{CNOT}_{25} \text{CNOT}_{12} \text{NOT}_4, && \text{CNOT}_{54} \text{CNOT}_{51} \text{NOT}_2, \\
 &\text{CNOT}_{35} \text{CNOT}_{23} \text{NOT}_1.
 \end{aligned}$$

The actual computation was realized via a sequence of ~ 50 to ~ 200 radio-frequency (RF) pulses, separated by time intervals of free evolution under the Hamiltonian, for a total duration

of ~ 50 to ~ 500 ms, depending on π . The pulse sequences for the order-finding algorithm were designed by translating the quantum circuits of Fig. 2.13 into one- and two-qubit operations, employing the simplification methods of section 4.8. The transformation $|x\rangle|y\rangle \mapsto |x\rangle|\pi^x(y)\rangle$ (Eq. 2.84) is realized by one of the following sequences, which form a representative subset of all possible permutations:

- $r = 1$: $\text{cZ}_{54} \text{CNOT}_{35} \text{cZ}_{54}^\dagger \text{CNOT}_{35} \text{cZ}_{34}$ (cZ_{ij} rotates spin j by 90° about \hat{z} if and only if spin i is $|1\rangle$).
- $r = 2$: CNOT_{35} .
- $r = 3$: $\text{CNOT}_{32} \text{CNOT}_{25} \text{CNOT}_{32} \text{CNOT}_{21} \text{cZ}_{14} \text{CNOT}_{51} \text{cZ}_{14}^\dagger \text{CNOT}_{51} \text{cZ}_{54} \text{CNOT}_{21} \text{cZ}_{15} \text{CNOT}_{41} \text{cZ}_{15}^\dagger \text{CNOT}_{41} \text{cZ}_{45}$. (this sequence does the transformation $\pi^x(y)$ for $y = 2$ only; sequences for $r = 3$ that would work for any y are prohibitively long).
- $r = 4$: $\text{CNOT}_{24} \text{cZ}_{34} \text{cZ}_{54} \text{CNOT}_{35} \text{cZ}_{54}$.

Each transformation was tested independently to confirm its proper operation. All pulse sequences were implemented on the four-channel spectrometer described in section 5.1, and using the methods of section 4.2 to serve two qubits with one channel. The frequency of one channel was set at $(\omega_2 + \omega_3)/2$, and the other three channels were set on the resonance of spins 1, 4 and 5. The chemical shift evolutions of spins 2 and 3 were calculated with the help of a time-counter, which kept track of the time elapsed from the start of the pulse sequence. On-resonance excitation of spins 2 and 3 was achieved using phase-ramping techniques. All pulses were spin-selective and Hermite shaped. Rotations about the \hat{z} -axis were implemented by adjusting the phases of the subsequent pulses. Unintended phase shifts of spins i during a pulse on spin $j \neq i$ were calculated and accounted for by adjusting the phase of subsequent pulses. During simultaneous pulses, the effect of these phase shifts was largely removed by shifting the frequency of the pulses via phase-ramping, in such a way that they track the shifting spin frequencies and thereby greatly improve the accuracy of the simultaneous rotations of two or more spins.

Upon completion of the pulse sequence, the states of the three spins in the first register were measured and the order r was determined from the read-out. Since an ensemble of quantum computers rather than a single quantum computer was used, the measurement gives the bitwise average values of m_i ($i = 1, 2, 3$), instead of a sample of $m = m_1 m_2 m_3$ with probabilities given in Fig. 5.28¹⁴. Formally, measurement of spin i returns $O_i = 1 - 2\langle m_i \rangle = 2\text{Tr}(\rho I_{zi})$, where ρ is the final density operator of the system. The O_i are obtained experimentally from integrating the peak areas in the spectrum of the magnetic signal of spin i after a 90° read-out pulse on spin i , phased such that positive spectral lines correspond to positive O_i . The

¹⁴It is not clear that the bitwise average outputs of the QFT suffice to determine r for permutations on arbitrary n . Instead, the continued fraction expansion can be ran on the quantum computer to compute r .

theoretically predicted values of O_i ($i = 1, 2, 3$) for each value of r follow directly from the probabilities for m in Fig. 5.28. For reference, we also include the values of O_4 and O_5 (for $y = 0$; if $y \neq 0$, O_4 and O_5 can be negative): for the case $r = 1$ the O_i are 1, 1, 1, 1, 1; for $r = 2$ they are 1, 1, 0, 1, 0; and for $r = 4$ they are 1, 0, 0, 0, 0. For $r = 3$, the O_i ($i = 1, 2, 3$) are 0, $1/4$, $5/16$, and O_4 and O_5 can be 0, $\pm 1/4$ or $\pm 1/2$, depending on y . The value of r can thus be unambiguously determined from the spectra of the three spins in the first register. This was confirmed experimentally by taking spectra for these three spins, which were in good agreement with the theoretical expectations.

In fact, the complete spectrum of any one of the first three spins uniquely characterizes r by virtue of extra information contained in the splitting of the lines. For the spectrum of spin 1 the values of O_i given above indicate that for $r = 1$, only the 0000 line (see Fig. 5.30) will be visible since spins 2 – 5 are all in $|0\rangle$. Furthermore, this line should be absorptive and positive since spin 1 is also in $|0\rangle$. Similarly, for $r = 2$ the 0000, 0001, 0100 and 0101 lines are expected to be positive, and for $r = 4$ all 16 lines should be positive. Finally, for $r = 3$, the *net* area under the lines of spin 1 should be zero since $O_1 = 0$, although most individual lines are expected to be non-zero and partly dispersive.

5.9.3 Experimental results

The experimentally measured thermal equilibrium spectrum for spin 1 is shown in Fig. 5.30a. After the state preparation, only the 0000 line should remain visible in the spectrum of each spin, reflecting that only molecules with all other spins in the ground state contribute to the signal. The resulting data are remarkably clean, as illustrated for spin 1 in Fig. 5.30b.

Figure 5.31 shows the spectrum of spin 1 after running the order-finding algorithm with an effective pure input state, for the pulse sequences given in section 5.9.2. In all cases, the spectrum is in good agreement with the predictions, both in terms of the number of lines, and their position, sign and amplitude. Slight deviations from the ideally expected spectra are attributed mostly to incomplete refocusing of undesired coupled evolutions and to decoherence.

5.9.4 Discussion

The success of the order-finding experiment required the synthesis of a molecule with unusual NMR properties and the development of several new methods to meet the increasing demands for control over the spin dynamics. The major difficulty was to address and control the qubits sufficiently well to remove undesired couplings while leaving select couplings active — much of the more advanced techniques for single-qubit rotations presented in section 4.2 were developed for this experiment. Furthermore, the pulse sequence had to be executed within the coherence time. Clearly, the same challenges will be faced in moving beyond liquid state NMR, and

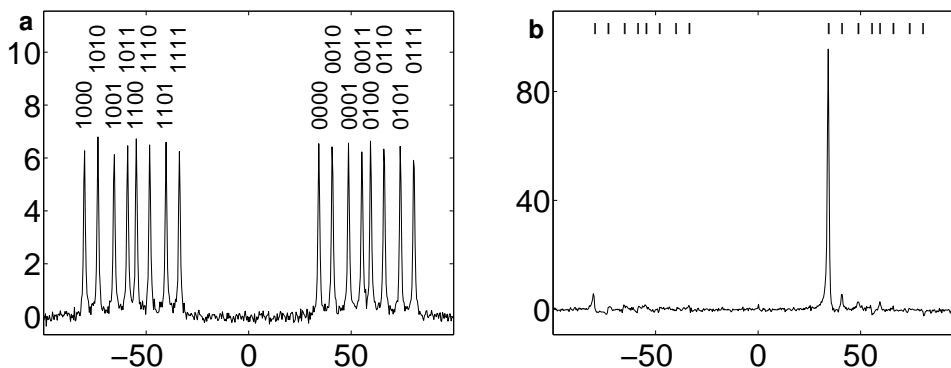


Figure 5.30: (a) The spectrum of spin 1 in thermal equilibrium. Taking into account the sign and magnitude of the $J_{1,j}$, the 16 lines in the spectrum of spin 1 can be labeled as shown. (b) The same spectrum when the spins are in an effective pure state. Only the line labeled 0000 is present. All spectra shown here and in Fig. 5.31 display the real part of the spectrum in the same arbitrary units, and were obtained without phase cycling or signal-averaging (except for Fig. 5.31 c, where 16 identical scans were averaged). A 0.1 Hz filter was applied. Frequencies are in units of Hz with respect to $\omega_1/2\pi$.

we anticipate that solutions such as those reported here will be useful in future quantum computer implementations, in particular in those involving spins, such as solid state NMR [Kan98], electron spins in quantum dots [LD98] and ion traps [SKK⁺00].

5.10 Shor's factoring algorithm (7 spins)

5.10.1 Problem description

Prime factorization of a composite number using a quantum computer has been the “Holy Grail” of the early exploration of small scale quantum computers. The fundamental interest in quantum factoring combined with the unprecedented complexity of the experiment make the experimental demonstration of quantum factoring a landmark achievement. Our goal has been to accomplish this feat [VSB⁺01].¹⁵

The smallest number L for which Shor's algorithm can be meaningfully implemented is $L = 15$, given that the algorithm fails for L even or a prime power ($L = p^\alpha$, with p prime). For $L = 15$, the size of the second register must be at least $m = \lceil \log_2 15 \rceil = 4$ and the first register

¹⁵Ike Chuang encouraged me to think about what it would take to do a quantum factoring experiment, and to lead the work. I worked out the theory and requirements under Ike's guidance. Xinlan Zhou suggested the method for multiplication by four modulo fifteen. Nino Yannoni found the molecule based on my input regarding molecule requirements and Greg Breyta synthesized the molecule. Mark Sherwood helped with the molecule work and with liquid NMR techniques. The software framework for the experiment was written by Matthias Steffen, with my input. He and I did the experiment together and came up with several new techniques for coherent control of multiple coupled spins. I wrote the decoherence model for seven spins.

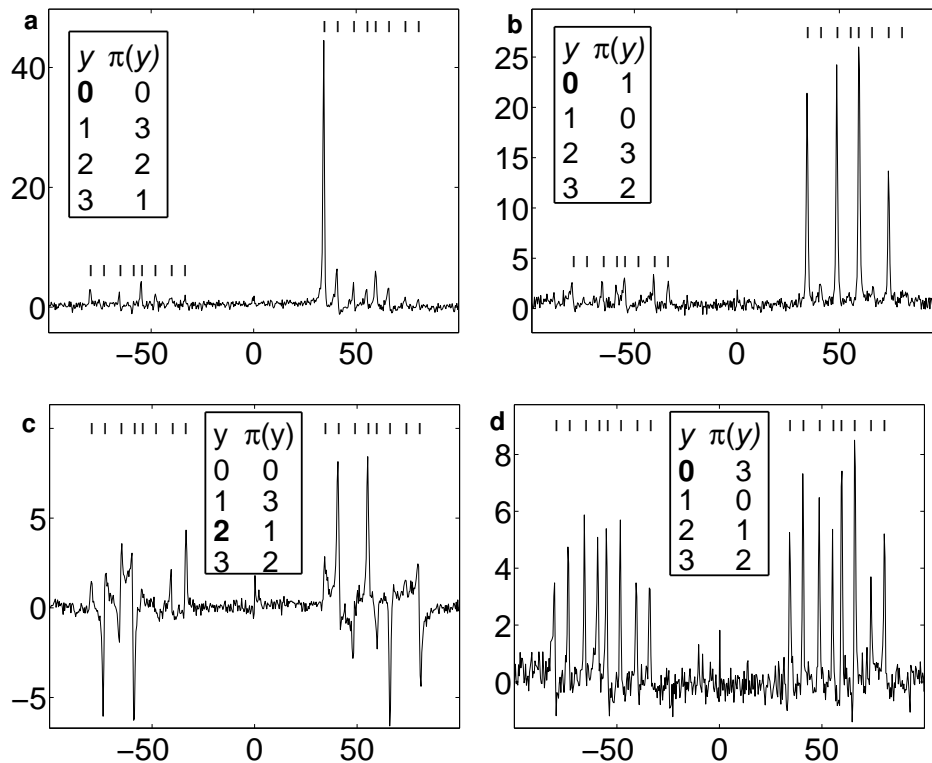


Figure 5.31: Spectra of spin 1 acquired after executing the order-finding algorithm. The respective permutations are shown in inset, with the input element highlighted. The 16 marks on top of each spectrum indicate the position of the 16 lines in the thermal equilibrium spectrum.

must in principle be of size at least $n = 2m = 8$ (section 2.3.3). The quantum circuit is shown in Fig. 5.32, where we used Eq. 2.93 to decompose the modular exponentiation into a sequence of multiplications controlled by one qubit each [BCDP96].

Repeated squaring of a on a classical computer efficiently gives the numbers a, a^2 through $a^{2^{n-1}}$. These numbers are summarized in Table 5.2 for all $a < 15$ and coprime with 15 (in a practical application, it suffices to do this for just one value of a). The table also gives a^x for values of x which are not a power of two, so we can see in advance what the period r of $f(x) = a^x \bmod 15$ is, although this is not needed for Shor's algorithm.

From repeated squaring, we see that $a^4 \bmod 15 = 1$ for all valid a (Table 5.2). This means for the quantum circuit of Fig. 5.32 that the multiplications by a^4, a^8, \dots, a^{128} are trivial: if $|x_k\rangle = |1\rangle$ ($k \geq 2$), we multiply by $a^{2^k} = 1$, i.e. we do nothing, and if $|x_k\rangle = |0\rangle$ we also do nothing. Therefore, all the controlled multiplications except the ones by a and a^2 can be left out. For $a = 4, 11$ or 14 , we even have $a^2 \bmod 15 = 1$, so in this case we only need to keep the controlled multiplication by a . We thus see that at most two qubits of the first register act non-trivially during the modular exponentiation, and we might as well leave out the other

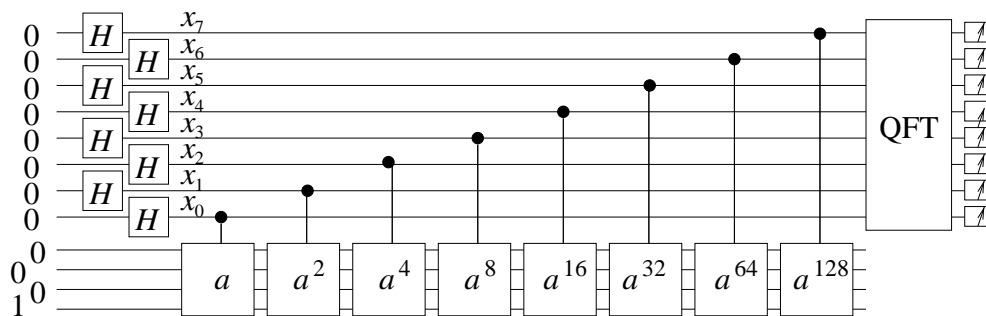


Figure 5.32: Outline of the quantum circuit for quantum factorization of the number fifteen. The first register of $n = 8$ qubits is initialized to $|0\rangle$ and then put into the equal superposition $\sum_{x=0}^{2^n-1} |x\rangle$ using n Hadamard operations. The second register is initialized to $|y\rangle = |1\rangle$. Then we multiply the second register by $a^x \bmod 15$ via n controlled multiplications by a^{2^k} modulo 15. Next the quantum Fourier transform is applied to the first register and the qubits of the first register are measured.

	x								r	$a^{r/2} \pm 1$	gcd with 15
	0	1	2	3	4	5	6	7			
	2	1	2	4	8	1	2	...	4	$2^{4/2} \pm 1 = 3, 5$	3, 5
	4	1	4	1	4	...			2	$4^{2/2} \pm 1 = 3, 5$	3, 5
	7	1	7	4	13	1	7	...	4	$7^{4/2} \pm 1 = 48, 50$	3, 5
a	8	1	8	4	2	1	8	...	4	$8^{4/2} \pm 1 = 63, 65$	3, 5
	11	1	11	1	11	...			2	$11^{2/2} \pm 1 = 10, 15$	5, 3
	13	1	13	4	7	1	13	...	4	$13^{4/2} \pm 1 = 168, 170$	3, 5
	14	1	14	1	14	...			2	$14^{2/2} \pm 1 = 13, 15$	-, 5

Table 5.2: The table gives $f(x) = a^x \bmod 15$ for all $a < 15$ coprime with 15 and for successive values of x . For each value of a , the period r emerges from the sequence of output values $f(x)$. Calculation of the greatest common denominator of $a^{r/2} \pm 1$ and 15 then gives at least one prime factor of 15.

qubits altogether.¹⁶ Since the essence of Shor's algorithm lies in the interplay between modular exponentiation and the QFT, we chose to retain $n = 3$ qubits to represent x .

In total, we shall thus use seven qubits ($n = 3$ and $m = 4$), as in Fig. 5.33. The possible choices of a break down into two groups. The first group ($a = 4, 11$ and 14) is "easy" as only multiplication by a is needed; we will refer to the second group ($a = 2, 7, 8$ and 13) as the "difficult" case. We will implement the algorithm both for the easy and the difficult case, using $a = 11$ and $a = 7$ respectively.

¹⁶In reality, if in the process of repeated squaring we find that $a^{2^k} \bmod 15 = 1$ for some k , while $a^{2^{k-1}} \neq 1$, we know that the period r must be $r = 2^k$. There is then really no need anymore to run the quantum algorithm. This is the case for $L = 15$ for any choice of a . Nevertheless, the non-trivial operation of Shor's algorithm can still be demonstrated [BCDP96].

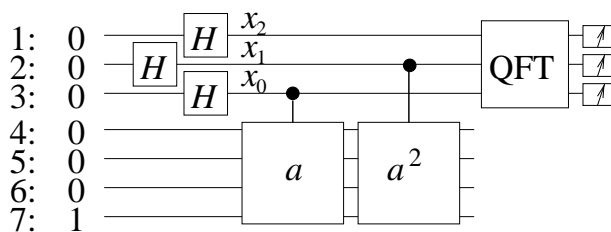


Figure 5.33: Simplified quantum circuit for quantum factorization of the number fifteen.

The controlled multiplications are done as follows. Multiplication of $y = 1$ by a is equivalent to adding $a - 1$ to $y = 1$. The controlled multiplication by a can thus be implemented via a few CNOTs of qubit 3 onto select qubits in the second register, as shown in Fig. 5.34. Multiplication of y by 4 shifts the bits of y over two places:

$$\begin{array}{r}
 y_3 \ y_2 \ y_1 \ y_0 \\
 \times \qquad \qquad \qquad 4 \\
 \hline
 y_3 \ y_2 \ y_1 \ y_0 \ 0 \ 0
 \end{array}$$

In order to take the remainder of $y_3y_2y_1y_000$ divided by 15, we note that the weight of bit y_2 is now 16 and the weight of y_3 is now 32; furthermore, we note that $16 \bmod 15 = 1$ and that $32 \bmod 15 = 2$. In other words, $y_3y_2y_1y_000 \bmod 15 = y_1y_0y_3y_2$. In effect, multiplication of y by 4 modulo 15 comes down to swapping bit y_3 with y_1 and y_2 with y_0 . Controlled multiplication by four can thus be accomplished via two controlled-SWAP or FREDKIN gates, which can be decomposed into CNOT's and TOFFOLI's using the construction of Fig. 2.8. The resulting quantum circuit is shown in Fig. 5.34.

The resulting quantum circuits for the modular exponentiation are shown in Fig. 5.34, both for the easy and the difficult case. The Hadamard gates don't need to be broken up further and we have already discussed the quantum Fourier transform on three qubits in section 2.3.3 as well as in section 5.10.

5.10.2 Experimental approach

Molecule

We chose to use the same molecule which worked so well in the five-qubit experiment (Fig. 5.29), but with the two inner carbon atoms 99% ^{13}C enriched, in order to obtain two extra qubits (from measurements on the 1% natural abundance ^{13}C compound, we had established that those two carbons would be the best choice for isotopic labeling). We dissolved this molecule in deuterated ether. The molecular structure, as well as the coupling constants and chemical shifts, are shown in Fig. 5.35. The assignment of qubits to spins (shown via the labels next to the spin-1/2 nuclei) is the result of a trade-off between sensitivity (for which qubits 1, 2 and 3 should be ^{19}F)

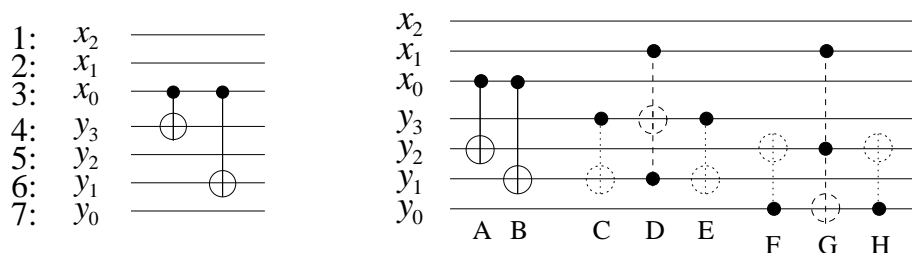


Figure 5.34: Quantum circuit for the modular exponentiation. (Left) for $a = 11$; controlled multiplication of $y = 1$ by 11 is replaced by controlled addition of 10 to $y = 1$. (Right) for $a = 7$; gates A and B correspond to addition of 6 to $y = 1$ controlled by x_0 , and gates C through H multiply the result by 7 controlled by x_1 . As we will see in section 5.10.2, the gates shown in dotted lines can be left out and the gates shown in dashed lines can be replaced by similar but simpler gates.

and the demands on the coupling network. The same assignment was used in all experiments. The ^1H spins in the iron complex broaden the lines of the nearest ^{13}C spin, and were therefore decoupled during the pulse sequence.

i	ω_i	$T_{1,i}$	$T_{2,i}$	J_{7i}	J_{6i}	J_{5i}	J_{4i}	J_{3i}	J_{2i}
1	-22052.0	5.0	1.3	-221.0	37.7	6.6	-114.3	14.5	25.16
2	489.5	13.7	1.8	18.6	-3.9	2.5	79.9	3.9	
3	25088.3	3.0	2.5	1.0	-13.5	41.6	12.9		
4	-4918.7	10.0	1.7	54.1	-5.7	2.1			
5	15186.6	2.8	1.8	19.4	59.5				
6	-4519.1	45.4	2.0	68.9					
7	4244.3	31.6	2.0						

Figure 5.35: The seven spin molecule, along with the measured J -coupling constants [Hz], chemical shifts at 11.7 T [Hz] and relaxation time constants [s].

The synthesis of this unusual molecule was quite complex, and is summarized in Fig. 5.36. Ethyl (2- ^{13}C)bromoacetate (Cambridge Isotopes) was converted to ethyl 2-fluoroacetate by heating with AgF followed by hydrolysis to sodium fluoroacetate using NaOH in MeOH . The resulting salt was converted to 1,1,1,2-tetrafluoroethane using MoF_6 [dP79] and was subsequently treated with two equivalents of BuLi followed by I_2 to provide trifluoroiodoethene [BCHP96]. Half of the ethene was converted to the zinc salt which was recombined with the remaining ethene and coupled using $\text{Pd}(\text{Ph}_3\text{P})_4$ to give (2,3- ^{13}C)-hexafluorobutadiene [JKB⁺87]. The end product was obtained by reacting this butadiene with the anion obtained from treating $[(p\text{-C}_5\text{H}_5)\text{Fe}(\text{CO})_2]_2$ with sodium amalgam [GMS68].

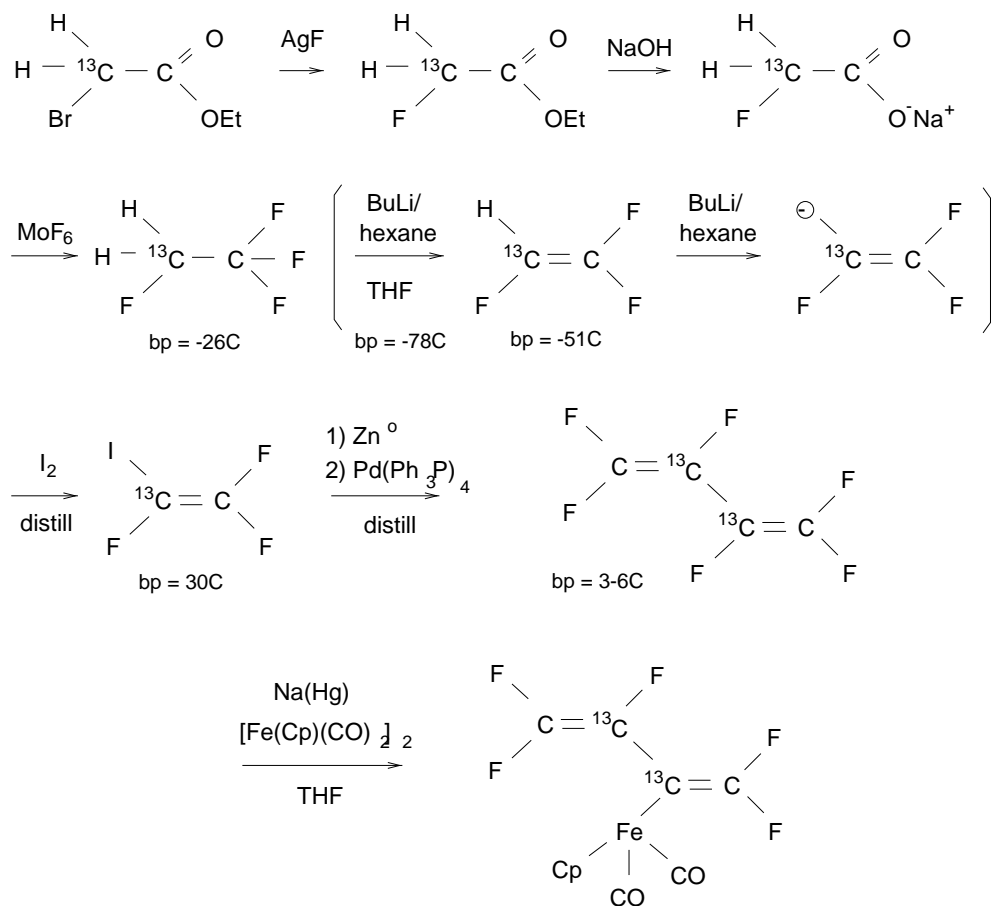


Figure 5.36: Schematic diagram of the synthesis of the seven-spin molecule.

Input state preparation

For the creation of an effective pure state of all seven spins, we used a two-stage extension of the scheme used in the five-spin experiment. In the first stage, the five fluorine spins are made effective pure via summation of the nine experiments of Table 5.3, where the first five qubits are fluorine spins and the last two are carbons.

These state preparation sequences were designed to be as short as possible by making optimal use of the available coupling network. The nine experiments are repeated four times, each time with different additional operations. In this process, all except four of the $IIIIIZI$ and $IIIIIZ$ terms are averaged away (these terms have about one fourth the weight of the other terms, because the carbon gyromagnetic ratio is four times smaller than the fluorine gyromagnetic ratio) by applying a 180° pulse on each carbon spin in almost half of the cases. In the first set of nine experiments, no extra CNOTs are performed. In the second set, additional CNOTs turn the first carbon (spin 6) from I into Z ; in the third set, the second carbon (spin 7) is converted from I into Z and in the fourth set both carbons are converted into Z . The term $IIIIIZZ$ is

Equilibrium	<i>ZIIIII</i>	<i>IZIIIII</i>	<i>IIZIIII</i>	<i>IIIZIII</i>	<i>IIIZII</i>
1. $C_{24}C_{12}C_{31}C_{51}$	<i>ZIIZZII</i>	<i>ZZZZZII</i>	<i>ZIZZZII</i>	$-IIZIIII$	<i>IIIZII</i>
2. $C_{35}C_{43}C_{14}N_2$	<i>ZIIIIII</i>	<i>ZZIIIII</i>	$-IIZIIII$	<i>ZZIIZZII</i>	<i>ZZIIZII</i>
3. $C_{43}C_{14}C_{21}C_{31}N_5$	<i>ZIZIZII</i>	<i>ZZZIZII</i>	<i>IIZIIII</i>	$-IIIIZIII$	<i>ZZZIIII</i>
4. $C_{42}C_{14}C_{51}C_{21}N_1N_5$	<i>ZIZZIII</i>	<i>ZZIZIII</i>	<i>ZZZZIZZ</i>	$-IIIIZIII$	<i>IIIZII</i>
5. $C_{35}C_{43}C_{24}C_{35}$	<i>ZIIIIII</i>	<i>IZZIIII</i>	<i>IIZIIII</i>	<i>IZZZIII</i>	<i>IZZIZII</i>
6. $C_{13}C_{15}C_{21}C_{12}$	<i>ZIZIIII</i>	<i>IZIIIII</i>	<i>IIZIIII</i>	<i>IIZZIII</i>	<i>IIZIZII</i>
7. $C_{42}C_{34}C_{53}C_{31}$	<i>ZIIIZII</i>	<i>IZIZZII</i>	<i>IZZZZII</i>	<i>IIIZIII</i>	<i>IIIZZII</i>
8. $C_{42}C_{34}C_{53}C_{42}C_{34}N_1$	$-ZIIIIII$	<i>IZIZIII</i>	<i>IIZZZII</i>	<i>IIIZIII</i>	<i>IIIZZII</i>
9. $C_{35}C_{34}C_{51}N_4N_2N_3$	<i>ZIIZIII</i>	<i>IZIIZII</i>	$-IIZIIII$	$-IIIZZII$	$-IIIZII$

Table 5.3: First stage of the temporal averaging procedure to prepare an effective pure state of five nuclei of the same species and two other nuclei of another species. The table shows how the terms in the thermal equilibrium density matrix are transformed by each temporal averaging sequence (the *IIIIIZI* and *IIIIIZ* terms are not shown as they are left unaffected in this first stage). C_{ij} stands for CNOT_{ij} and N_i stands for NOT_i .

also created. Summation of the $4 \times 9 = 36$ experiments creates the desired seven-spin effective pure state.

The pulse sequence for each CNOT_{ij} in the temporal averaging sequences was

$$\text{for } J_{ij} > 0 : \quad X_j \frac{1}{4} J_{ij} X_i^2 X_j^2 \frac{1}{4} J_{ij} X_i^2 X_j^2 \bar{Y}_2, \quad (5.12)$$

$$\text{for } J_{ij} < 0 : \quad X_j \frac{1}{4} |J_{ij}| X_i^2 X_j^2 \frac{1}{4} |J_{ij}| X_i^2 X_j^2 Y_2, \quad (5.13)$$

which takes advantage of the fact that the input state is diagonal.

Quantum circuit and pulse sequence simplification

The pulse sequences for the actual Shor algorithm were designed using the guidelines of section 4.8. At the level of quantum circuits, we used the rules of Fig. 4.16 in the following ways:

- Gate C of Fig. 5.34 is a CNOT controlled by a qubit which is in $|0\rangle$ and can thus be left out.
- Gate F of Fig. 5.34 is a CNOT controlled by a qubit which is in $|1\rangle$ and can thus be replaced by a NOT gate.

Furthermore, the evolution of the second register does not matter anymore during the QFT on the first register (see section 2.3.3), as the second register is traced out upon read-out. Therefore,

- We can leave out gate H of Fig. 5.34, since it comes at the end of the modular exponentiation and does not involve any qubits in the first register.

- We can also take out gate E ; it commutes with gates F and G , so we can move it down to the end of the modular exponentiation, where it becomes inconsequential.

Furthermore, we took advantage of the fact that the target of the two TOFFOLI's (gates D and G in Fig. 5.34) are in a computational basis state, not in a superposition state. Therefore, the phases of only half the non-zero entries in the TOFFOLI unitary matrices need to be the same, and we can use a simplified set of gates to implement them.

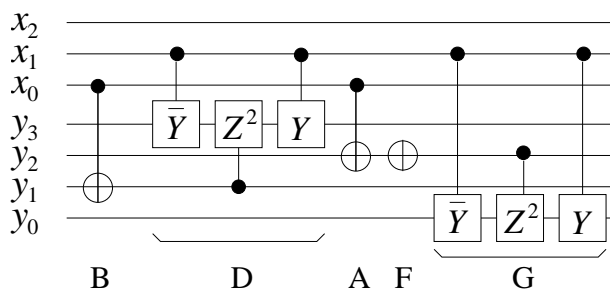


Figure 5.37: Simplified quantum circuit for the modular exponentiation for the “difficult” case ($a = 7$).

In addition, we simplified the refocusing schemes in two ways. Early on in the pulse sequence, certain spins in the second register are still in $|0\rangle$ or $|1\rangle$, and the couplings between any two such spins need not be refocused. In order to maximally take advantage of this simplification, gate A was performed after gate D . This is allowed since A commutes with B and D . During the QFT, the evolution of the second register does not matter anymore, so the couplings between the spins in the second register need not be refocused during the QFT (couplings between the first and second register qubits must still be refocused). We did refocus inhomogeneous dephasing for all spins in the transverse plane at all times.

The quantum circuit resulting from these various simplifications is shown in Fig. 5.37.

Spectrometer

The four-channel spectrometer was converted into a seven-channel spectrometer using the same approach as for the five-qubit experiment of section 5.9: additional rotating reference frames were created using a software time counter, and phase ramping techniques enabled excitation of spins away from the signal source frequency. The frequency source of channel 1 was placed at ω_1 , on resonance with spin 1, source 2 was set at $(\omega_2 + \omega_4)/2$, source 3 at $(\omega_3 + \omega_5)/2$ and source 4 at $(\omega_6 + \omega_7)/2$. In addition, we installed an extra frequency source, power amplifier and power combiner for proton decoupling.

We selected Hermite 180 and Gaussian 90 pulse shapes based on our previous experience, collected in Table 4.2, and on the spectral properties of the molecule and the demands of the algorithm. Generalized Bloch-Siegert effects were precomputed and compensated for, both for

single (section 4.2.4) and simultaneous (section 4.2.5) pulses. Simultaneous pulses on strongly coupled spins were avoided. Furthermore, coupled evolution during the pulses was unwound using symmetrically placed negative delay times, following the guidelines of Table 4.3 for single pulses and Table 4.4 for simultaneous pulses.

The complete pulse sequence for the difficult case contains about 300 180° pulses and about 30 90° pulses. The duration of the temporal averaging part is on the order of 200 ms, the modular exponentiation takes about 400 ms, and the QFT sequence lasts about 120 ms.

Read-out

Upon completion of the pulse sequence, the reduced density matrix of the three qubits in the first register is predicted to be

$$\rho = \sum_l w_l |lN/r\rangle\langle lN/r| = \sum_l w_l |l\frac{8}{r}\rangle\langle l\frac{8}{r}| \quad (5.14)$$

We shall attempt to deduce r from the output spectra of the first three qubits, after a readout pulse, which represent bitwise ensemble averaged values. Once r is known, we can find the prime factors of $L = 15$ as (recall Eq. 2.91)

$$\gcd(a^{r/2} \pm 1, 15). \quad (5.15)$$

5.10.3 Experimental results

Fig. 5.38 shows the thermal equilibrium fluorine spectrum of the sample. Fig. 5.39 zooms in on five of the lines in this spectrum, corresponding to the five fluorine spins of the quantum computer molecule of Fig. 5.35. Fig. 5.40 shows the spectra of the two carbon spins.

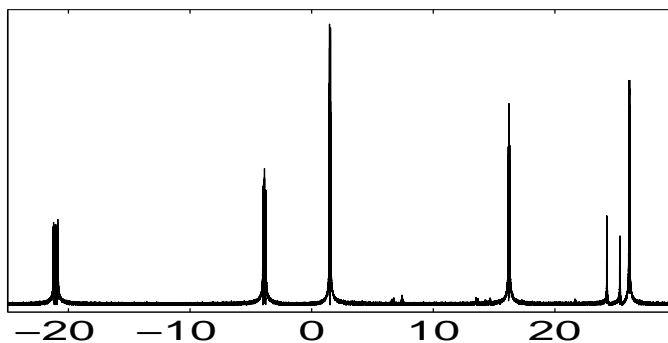


Figure 5.38: Fluorine spectrum of the seven-spin molecule of Fig. 5.35. The five major lines correspond (from left to right) to qubits 1, 4, 2, 5, 3. In addition, two smaller lines from impurities are visible around 25 kHz. The spectrum is shown in absolute value. Frequencies are given in kHz, with respect to an arbitrary reference frequency near 470 MHz.

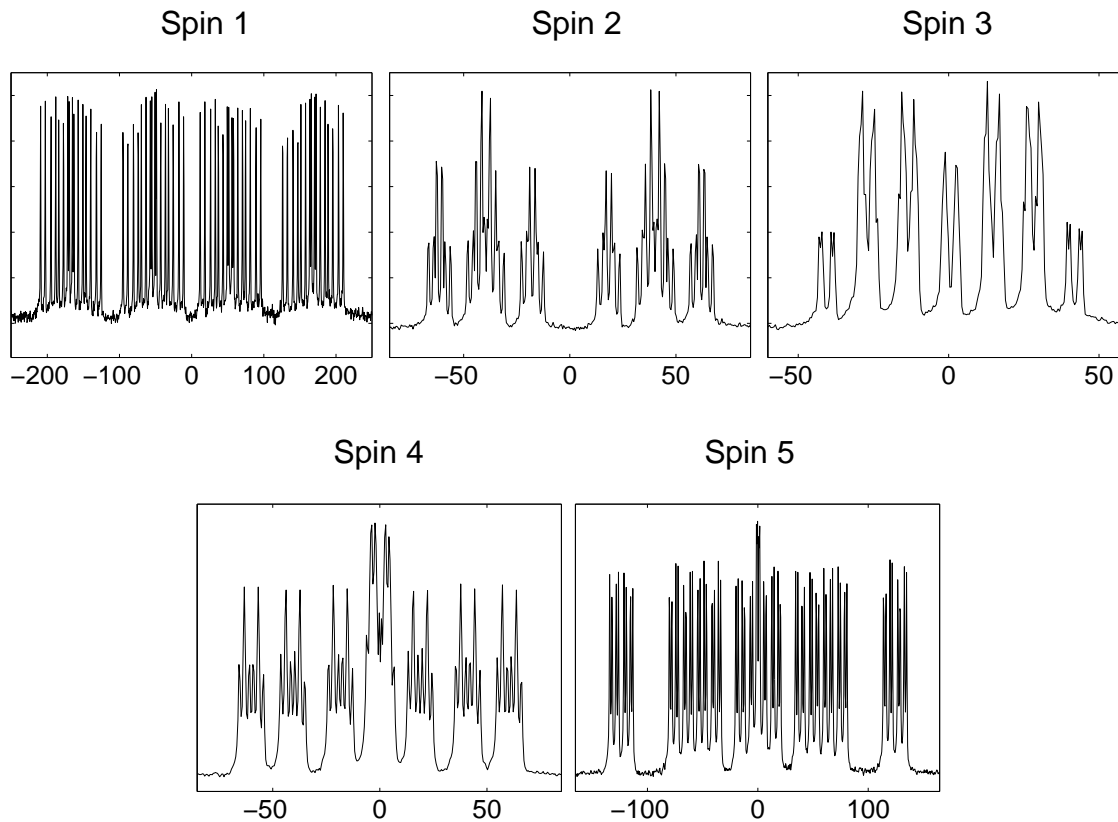


Figure 5.39: Experimentally measured spectra for the five fluorine spins in thermal equilibrium. The real part is displayed, in arbitrary units. Frequencies are with respect to $\omega_i/2\pi$, in Hz.

Each multiplet contains up to $2^6 = 64$ lines, because each spin is coupled to six other spins. For spin 1, all 64 lines are beautifully resolved. For the other spins, some of the lines fall on top of each other, but this does not pose a problem since at the end of Shor’s algorithm we only need to know the overall signature: lines up, lines down, or partly up / partly down.

The spectra of spins 1, 2 and 3 after preparing a seven-spin effective pure ground state are shown in Fig. 5.41. These spectra are the summation of 36 spectra, each obtained after a different input state preparation pulse sequence. As expected, only one line is retained in each multiplet, which indicates that we have distilled a suitable initial state for Shor’s algorithm.

The experimentally measured spectra upon completion of the “easy” case of Shor’s algorithm are shown in Fig. 5.42. Clearly, the lines of spins 1 and 2 are up, so qubits 1 and 2 are in $|0\rangle$; qubit 3 is in a mixture of $|0\rangle$ and $|1\rangle$ as it has positive and negative lines. With qubit 3 the most significant qubit after the QFT [Cop94], the first register is thus in a mixture of $|000\rangle$ and $|100\rangle$, or $|0\rangle$ and $|4\rangle$ in decimal notation. The periodicity in the amplitude of $|x\rangle$ is thus 4, and therefore $r = 8/4 = 2$. If we plug this in in Eq. 5.15, we obtain $\gcd(11^{2/2} \pm 1, 15) = 3, 5$. The

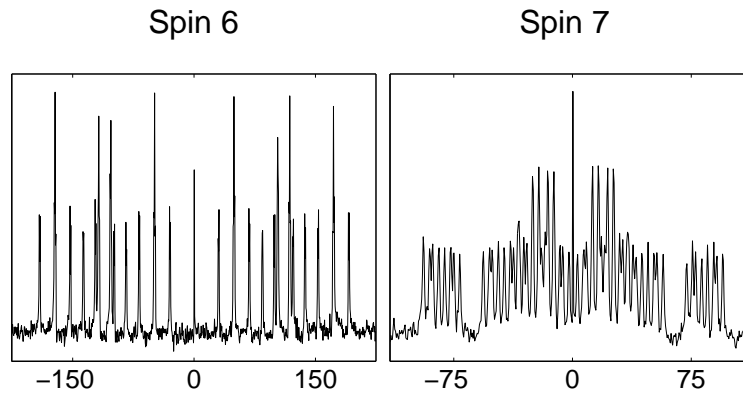


Figure 5.40: Experimentally measured spectra for the two carbon spins in thermal equilibrium. The real part is displayed, in arbitrary units. Frequencies are with respect to $\omega_i/2\pi$, in Hz.

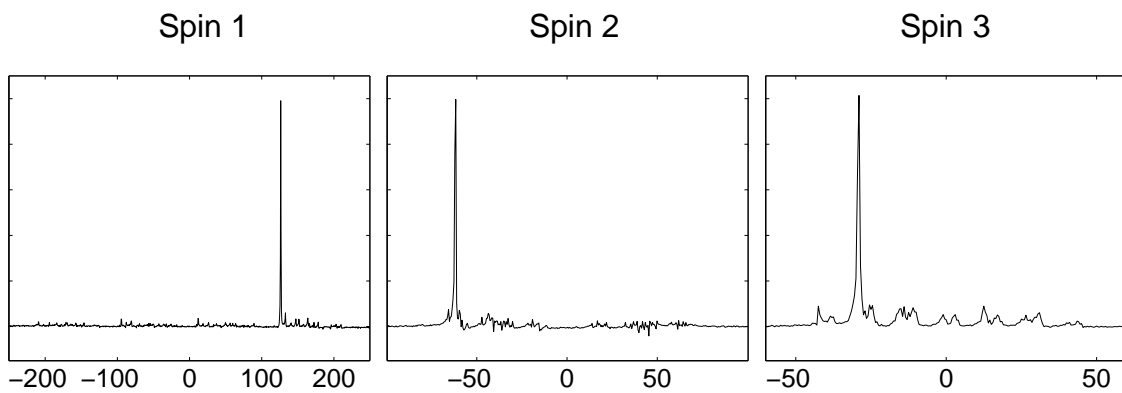


Figure 5.41: Experimentally measured spectra, similar to Fig. 5.39, after preparing all seven spins in the effective pure ground state.

prime factors of 15 have thus been unambiguously derived from the output spectra.

Similar spectra for the “difficult” case are shown in Fig. 5.43. From the spectra, we conclude that qubit 1 is in $|0\rangle$, and qubits 2 and 3 are in a mixture of $|0\rangle$ and $|1\rangle$. The register is thus in a mixture of $|000\rangle$, $|010\rangle$, $|100\rangle$ and $|110\rangle$, which in decimal is $|0\rangle$, $|2\rangle$, $|4\rangle$ and $|6\rangle$. The periodicity in the amplitude of the first register is thus 2, and therefore $r = 8/2 = 4$. Plugging this in in Eq. 5.15 gives $\gcd(7^{4/2} \pm 1, 15) = 3, 5$. Even after the very long pulse sequence of the “difficult” case, the prime factors of 15 have thus successfully been found using Shor’s algorithm and a quantum computer.

There clearly are substantial discrepancies between the measured spectra and the ideally expected spectra, however, most notably for the difficult case. The effective pure state spectra also exhibit small non-idealities. We have worked long and hard trying to improve the quality of the data, learned a lot in the process and made substantial progress since the initial experiments. However, it seemed that something fundamental was preventing us from getting cleaner data than those of Figs. 5.42 and 5.43.

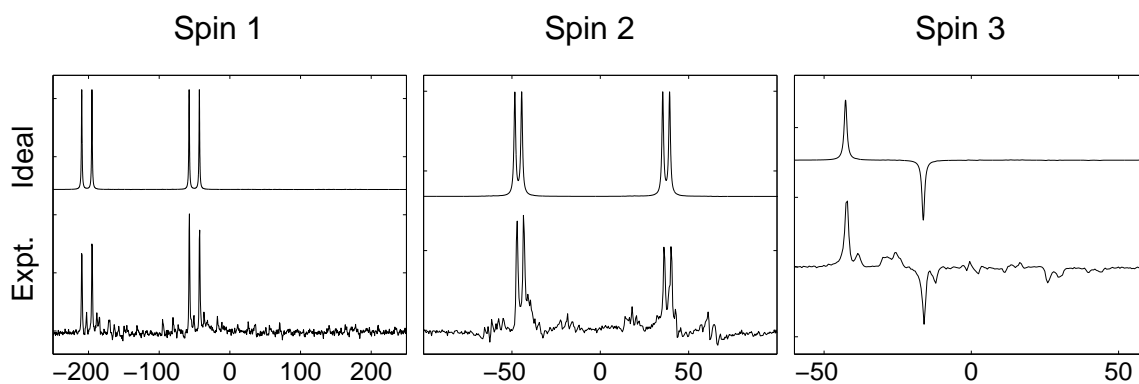


Figure 5.42: (Bottom) Experimentally measured and (Top) ideally expected spectra of spins 1, 2 and 3 after completion of the “easy” case of Shor’s algorithm ($a = 11$). Positive and negative lines indicate that the state of the spin is $|0\rangle$ and $|1\rangle$ respectively.

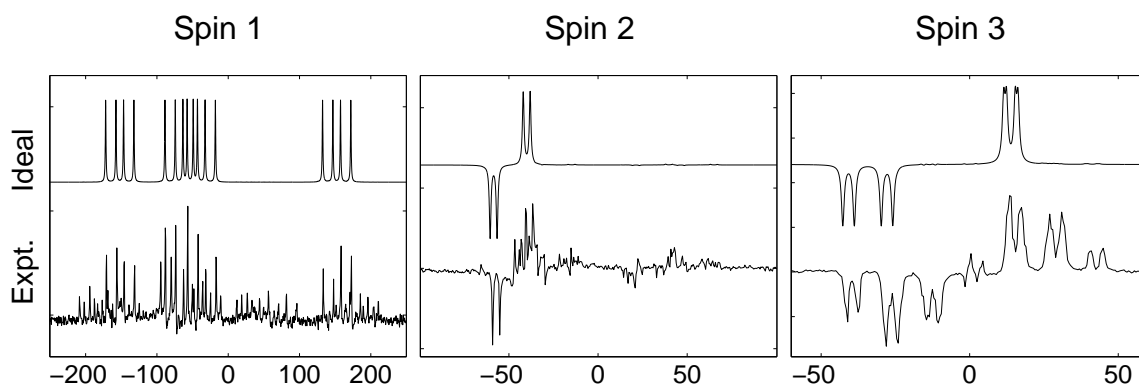


Figure 5.43: Similar to Fig. 5.42 but for the “difficult” case ($a = 7$).

We decided to attempt to model the effect of decoherence, even though it isn’t obvious from the spectra that decoherence would explain the data. We simply wanted to understand what the effect of decoherence is throughout the pulse sequences for Shor’s algorithm.

5.10.4 Decoherence model

The NMR literature gives very detailed descriptions of decoherence in coupled spin systems, going back to the ideas of Redfield [Red57, Red65] and worked out later by many others [VV78, Jee82, EBW87]. This so-called superoperator formalism is very general and allows one to simulate decoherence in nuclear spin systems starting from knowledge of internuclear distances, chemical shift anisotropy tensors, and so forth, and of correlations of these mechanism in time and space, which are governed by molecular tumbling and diffusion rates. While such calculations are in principle amenable to computer simulations, detailed knowledge about the correlation functions and the other parameters is not always available. Furthermore, a full superoperator description of relaxation is exceedingly complex for the case of seven coupled

spins: the superoperator matrix would be of size $4^7 \times 4^7$, and thus have 268435456 degrees of freedom. This is more than most current computers can store in memory, and simulation of decoherence in the course of a sequence of 300 RF pulses appears out of the question with this approach.

We therefore set out to construct a numerical model for decoherence that is simple and workable, while still predictive. The resulting simplified decoherence model is in essence an extension of the Bloch equations [Blo46], an early phenomenological description of nuclear spin relaxation in terms of just T_2 and T_1 . Such a simplified description is justified only if each spin in a molecule experiences a local magnetic field which randomly fluctuates in time and there are negligible correlations between the local field experienced by different nuclei. It is not clear a priori that this is the case in our system, but a simple model can at least serve to give a first idea of the impact of decoherence during the execution of Shor's algorithm. Comparison of the simulation results with the experimental data will reveal the usefulness of this simplified model.

In order to make the model easily compatible with our matrix formalism for unitary operations (section 2.2), we chose to describe decoherence in the operator sum representation or Kraus representation [Kra83]. The operator sum representation of both generalized amplitude damping (T_1) and phase damping (related to T_2) has been described in the quantum computing literature [NC00] (see also section 3.1.5), although only for single spins, and for both processes separately.

We have devised and implemented an integrated model of phase damping and generalized amplitude damping acting on seven coupled spins in the course of arbitrary pulse sequences. We have been able to keep the model workable by assuming that each spin decoheres independently and by making the following observations:

1. Amplitude damping error operators acting on different spins commute.
2. Phase damping error operators acting on different spins commute.
3. Amplitude damping and phase damping commute with each other. This follows from the fact that the error operators E_i for amplitude damping (Eq. 3.20) commute with the E_i for phase damping (Eq. 3.26) when applied to $\sigma_x, \sigma_y, \sigma_z$ and σ_I and thus also when they act on arbitrary ρ .
4. Phase damping commutes with the ideal unitary evolution under \mathcal{H} , as both processes are described by diagonal matrices.

As a result, there is no need to simulate all these processes simultaneously; they can be simulated one after the other, in any order. This prevents an explosion of terms in the operator sum representation, which would have been the case if cross-products of all the E_i had been required. However,

1. Amplitude damping does *not* commute with the ideal unitary evolution under \mathcal{H} .
2. Phase and amplitude damping do *not* commute with the ideal unitary evolution during RF pulses.

In order to still maintain a workable model, we have nevertheless treated these processes as if they did commute. This is not necessarily a good approximation, but it does allow us to get a first estimate of the effect of decoherence.

Concretely, we modeled a delay time of duration t via $e^{-i\mathcal{H}t/\hbar}$ followed by amplitude damping acting on spin 1 for a duration t , then amplitude damping acting on spin 2 and so forth, followed by phase damping acting for the same duration on each spin one after the other. Similarly, a shaped pulse of duration pw was modeled via an ideal shaped pulse, preceded by amplitude damping and phase damping, acting on each spin separately for a duration pw . Thanks to these approximations, the simulation of the complete Shor pulse sequence, including 36 temporal averaging sequences, takes only a few minutes to run on four IBM POWER3-II processors. We measured the characteristic amplitude and phase damping time constants for each spin and plugged those values into the model (excerpts from the simulation code are given in Appendix A). The model thus has no free parameters.

The output spectra obtained from the simulation are shown in Figs. 5.44 and 5.45 for the easy and difficult case respectively, along with the experimental output spectra. In both cases, the model reproduced the main unexpected observed non-idealities in the data in a remarkably convincing manner.

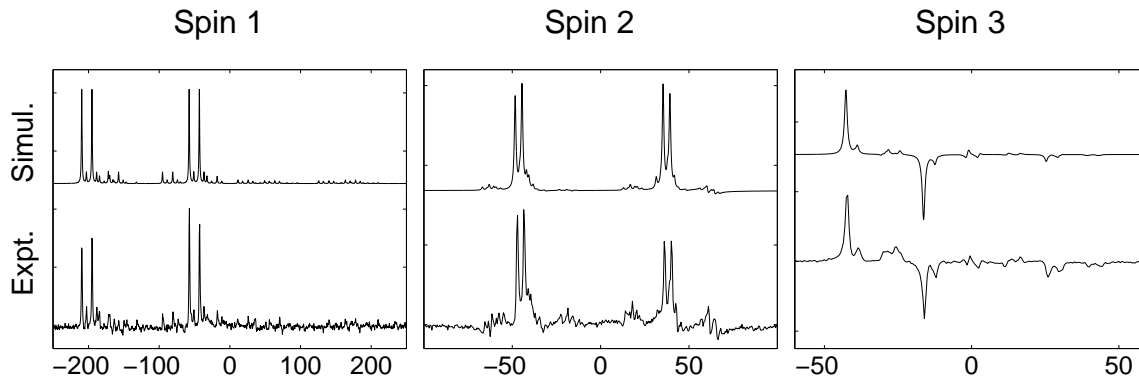


Figure 5.44: Comparison between (bottom) the experimentally measured spectra, which are the same as in Fig. 5.42, and (top) simulated spectra based on the decoherence model, for the “easy” case ($a = 11$).

The good agreement between the spectra predicted by the relaxation model and the experimental spectra suggests that the assumptions underlying the model are valid, at least to a reasonable degree. We attribute the remaining discrepancies between the data and the simulations to the approximations made in the model as well as to experimental imperfections such

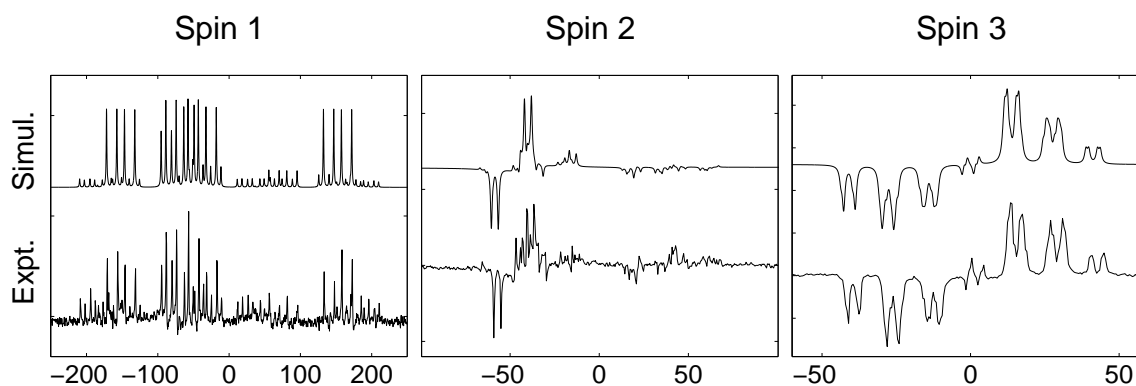


Figure 5.45: Similar to Fig. 5.44 but for the “hard” case ($a = 7$).

as RF inhomogeneity, imperfect calibrations and incomplete unwinding of coupled evolution during the pulses.

5.10.5 Discussion

The prime factors of fifteen can be deduced from the output spectra, both for the easy and the difficult case, demonstrating the proper operation of the factoring algorithm. This is in itself really remarkable.

The unexpected non-idealities in the data are well reproduced by a simple numeric model that incorporates the effect of decoherence. This is the first NMR quantum computing experiment in which decoherence was the dominant source of errors; the demands of Shor’s algorithm are clearly pushing the limits of the current molecule, despite its exceptionally good properties. Certainly, the predictive but workable decoherence model for multiple coupled spins is a valuable tool to assess the feasibility of future NMR quantum computing experiments.

Finally, the good agreement between the measured and simulated spectra suggests that the degree of unitary control in the experiment was very high, which bodes well for related proposed implementations of quantum computers [Kan98, LD98].

5.11 Summary

The sequence of successful experiments presented in this chapter clearly demonstrates that nuclear spins in liquid solution represent a beautiful playground in which to explore quantum computing experimentally. The main results of these experiments are

- experimental proof of principle of quantum computing — the solution of mathematical problems in fewer steps than is possible with any classical machine,

- experimental proof of principle of quantum error detection — coding gives a first order improvement in the conditional fidelity,
- an explicit demonstration of zero temperature dynamics with room temperature nuclear spins,
- the observation of a surprisingly large degree of cancellation of systematic errors — the concatenation of a record 280 two-qubit gates on three spins,
- a demonstration that liquid crystal solvents can be used for NMR quantum computing — such solvents may allow more gates within the coherence time,
- the demonstration of coherent control over up to seven coupled nuclear spins over the course of tens of two-qubit gates,
- the demonstration of a workable yet predictive model of decoherence for seven coupled nuclear spins.

The main experimental challenges we had to address in the course of these experiments include

- the identification and synthesis of suitable molecules,
- the exponential overhead in the creation of effective pure states,
- the limitations of a four-channel spectrometer,
- "turning off" undesired terms in the Hamiltonian, which is especially tricky if they don't commute with the desired terms,
- developing predictive numerical models of unitary and non-unitary spin dynamics.

Despite the successful resolution of these challenges in our experiments, liquid NMR quantum computers are difficult to scale, in particular because of the exponential overhead in the input state preparation. It also appears unlikely that the accuracy threshold for fault-tolerant quantum computation can be reached, except perhaps for very small molecules.

Nevertheless, full quantum algorithms with 10-15 spins may be possible, and interesting demonstrations of coherent control over several dozens of spins may be possible using thermal input states. Certainly, nuclear spins in liquid solution will continue to provide an exciting and accessible avenue to study quantum computation experimentally.

Chapter 6

Conclusions

Quantum computation has now entered the realm of experimental reality: simple quantum computers based on nuclear spins in molecules have been used to solve problems in fewer steps than is possible with any classical device. We have continuously been pushing the state of the art in NMR quantum computing by implementing meaningful quantum algorithms on two, then three, later five and finally seven qubits. In these experiments, we have not been content with just the simplest quantum protocols requiring only nearest neighbour couplings, but instead chose realistic experiments which really put the quantum computers to test.

In order to make this possible, special molecules were synthesized and a large number of experimental techniques have been developed for state initialization, coherent control and read-out. These include more efficient and effective temporal averaging schemes for state preparation, methods to reduce cross-talk during spin-selective shaped pulses, methods to reduce cross-talk between shaped pulses on different spins, the uncoupling frame for automatic refocusing within a subspace, pulse sequence simplification procedures at various levels, software rotating reference frames, refocusing schemes to remove undesired terms in the Hamiltonian, ways to interpret ensemble averaged measurements, and readout schemes based on the multiplet fine structure.

We have gained a good understanding of the main sources of imperfections in the experiments by developing a set of practical and predictive simulation tools which allow us to model both unitary and decoherence processes for molecules with multiple coupled nuclear spins. In the early heteronuclear experiments, RF field inhomogeneity was the dominant source of errors. In the later homonuclear experiments, which require longer pulses, coupled evolution during the RF pulses became the most significant source of errors. Other sources of errors included imperfect calibrations, incomplete frequency drift compensation and limited signal-to-noise. All these imperfections arise from technological rather than from fundamental issues, and we have demonstrated that such systematic errors can be cancelled out to a great extent. Even though

intrinsic decoherence played a role in all the experiments, only in the last experiment did decoherence become the dominant source of errors.

There exist well-understood scaling limitations for nuclear spin quantum computers starting off in thermal equilibrium at room temperature. Most importantly, the probability that all spins in a quantum computer with n spins start off in the desired ground state decreases as $n/2^n$. While a subset of the spins can be efficiently cooled down algorithmically, the overhead for this procedure is impractically large unless substantial hyperpolarization of the nuclear spins can be achieved by other means. An additional problem is that the coherence time of nuclear spins in molecules tends to shorten as the number of spins increases.

Nevertheless, I am convinced that solution NMR quantum computing will continue to help address many open problems and unanswered questions (and raise many more). Those questions include very fundamental ones, such as “where does the power of quantum computing come from?”. But as quantum computation has become an experimental reality, many important open problems are *practical* ones. (1) How can we remove the effect of undesired terms in the Hamiltonian via an approach that is both general and practical? (2) How do we arrange the sequence of operations in a systematic way, so as to maximize the cancellation of systematic errors? (3) How do we create and validate practical and predictive decoherence models?

The work presented in this thesis work constitutes a first step towards answering these important questions, but it represents by no means an endpoint. The significance of the practical open problems will only increase as other, perhaps more scalable implementations of quantum computers reach the stage of realizing actual quantum computations. Similarly, I hope that the significance of the techniques and concepts we developed for NMR quantum computing will grow, as they find useful application in other realizations of quantum computers.

Both the questions and the answers which stemmed from the work on NMR quantum computers have tremendously increased our understanding of what it takes to build a quantum computer. Still, the big question we asked in the beginning remains open: *can* we build a practical quantum computer?

This question can only be answered by measuring the coherence time and testing techniques for initialization, control and read-out of the qubit states in a variety of potential embodiments of quantum computers. The fundamental requirement for any implementation is that the accuracy threshold for fault-tolerant quantum computation be reached¹. Specifically, the probability of error per elementary logic gate should be less than about 0.01 %, in the most optimistic estimates at present. It is clear that reaching the accuracy threshold represents a formidable challenge; it requires not only coherence times long compared to the gate times, but also extremely accurate unitary control over the qubits. Nevertheless, 0.01 % doesn't seem a priori impossible, and in the spirit of Feynman, we say:

¹In order to perform meaningful quantum computations without using quantum error correction, the probability of error should be even lower, so the accuracy threshold is a reasonable upper bound for the error rate.

We know of no laws of physics that prohibit practical quantum computers — we just haven't gotten around to building one . . .

Therefore, while I don't believe that horses can be made to fly, I do think that practical quantum computers may one day be built. It is my hope and expectation that this thesis work has contributed to the realization of this wonderful challenge, which holds such a great promise.

Appendix A

Numerical model

The MATLAB model for simulation of the unitary and non-unitary processes in the course of a pulse sequence contains four primitives:

1. `d.m`: free evolution under the Hamiltonian
2. `X.m`, `Y.m` and `Z.m`: ideal single-spin rotations
3. `gad7.m`: generalized amplitude damping (GAD)
4. `pd7.m`: phase damping (PD)

The last two programs, which model non-unitary processes, act directly on a density matrix. The programs for unitary processes act on density matrices via the program `rho.m`. The simulation programs require that the number of qubits `nq` be declared in advance, and that the Hamiltonian and the Pauli matrices be set up by calling `def.m`.

In the next subsections, we shall give excerpts from the MATLAB code of `def.m`, `rho.m`, `d.m`, `X.m`, `gad7.m` and `pd7.m` and two helper programs. Finally, we will give an excerpt from a pulse sequence which calls these primitives.

A.1 Set up the Hamiltonian and Pauli matrices

```
% File:    def.m
% Date:    1997
% Author:  Lieven Vandersypen <lieven@snow.stanford.edu>
% Declares variables used in simulation programs
% Use: declare nq (number of qubits), then type def

global nqubits Si Sx Sy Sz H
nqubits=nq; % number of qubits
```

```

% Pauli matrices
Si=eye(2); Sx=[0 1 ; 1 0]; Sy=[0 -i; i 0]; Sz=[1 0 ;0 -1];

switch nqubits
...
case 7

% Pauli matrices
Sziiiiiz=mkron(Sz, Si, Si, Si, Si, Si, Si, Si);
...
Siiiiiz=mkron(Si, Si, Si, Si, Si, Si, Si, Sz);

% J-coupling strengths
% the labeling 1 through 7 is in order of frequency

J12=-114; J23=80;      J34=2.5;   J45=41.6;   J56=1;      J67=69;
J13=25;   J24=2;      J35=3.9;   J46=19.4;   J57=-13.5;
J14=6.6;   J25=13;    J36=18.5;  J47=60;
J15=14.5; J26=54;     J37=-3.8;
J16=-221; J27=-5.7;
J17=38;

% Hamiltonian (in the multiply rotating frame)

H=2*pi*J12*Sziiiiiz/2*Siziiii/2 + 2*pi*J13*Sziiiiiz/2*Siiziiii/2 + ...
2*pi*J14*Sziiiiiz/2*Siiiiiz/2 + 2*pi*J15*Sziiiiiz/2*Siiiiiz/2 + ...
2*pi*J16*Sziiiiiz/2*Siiiiiz/2 + 2*pi*J17*Sziiiiiz/2*Siiiiiz/2 + ...
2*pi*J23*Siziiii/2*Siiziiii/2 + 2*pi*J24*Siziiii/2*Siiziiii/2 + ...
2*pi*J25*Siziiii/2*Siiiiiz/2 + 2*pi*J26*Siziiii/2*Siiiiiz/2 + ...
2*pi*J27*Siziiii/2*Siiiiiz/2 + 2*pi*J34*Siiziiii/2*Siiiiiz/2 + ...
2*pi*J35*Siiziiii/2*Siiiiiz/2 + 2*pi*J36*Siiziiii/2*Siiiiiz/2 + ...
2*pi*J37*Siiziiii/2*Siiiiiz/2 + 2*pi*J45*Siiiiiz/2*Siiiiiz/2 + ...
2*pi*J46*Siiiiiz/2*Siiiiiz/2 + 2*pi*J47*Siiiiiz/2*Siiiiiz/2 + ...
2*pi*J56*Siiiiiz/2*Siiiiiz/2 + 2*pi*J57*Siiiiiz/2*Siiiiiz/2 + ...
2*pi*J67*Siiiiiz/2*Siiiiiz/2;

end

```

A.2 Action unitary operator on density matrix

```

% rho.m
% Lieven Vandersypen <lieven@snow.stanford.edu>
%
% calculates the final density matrix rf for an initial density

```

```
% matrix ri and a unitary operation U acting on ri

function rf = rf(ri,U)
global nqubits
rf=U*ri*U';
```

A.3 Time evolution under the Hamiltonian

```
% File: d.m
% Author: Lieven Vandersypen <lieven@snow.stanford.edu>
%
% d(t) simulates a free evolution period of t seconds

function R=d(t)
global H
R=expm(-i*H*t);
end
```

A.4 Single-spin rotations

Ideal rotations about \hat{x} , \hat{y} and \hat{z} are simulated by the programs X.m, Y.m and Z.m. We give here the code for X.m only, as the other programs are analogous.

```
% File: X.m
% Date: 04-Oct-99
% Author: Lieven Vandersypen <lieven@snow.stanford.edu>
%
% Usage: X(spinname, angle)
% Rotation of spin 'spinname' about X over angle*pi/2
% (right hand rule)
% example: X(2,3) rotates spin 2 about X over 270 degrees

function X=X(spinname,angle)

global nqubits

if nargin == 1
    if nqubits == 1
        angle=spinname;    spinname=1;
    else
        error('X.m requires two arguments if nqubits > 1 !')
    end
end
end
```

```
operator=expm(-i*angle*pi/2*[0 1;1 0]/2); % calculate 1-spin operator
X=gop(spinname,operator); % turns 1-spin operator into n-spin operator
```

A.5 Generalized amplitude damping

```
% file: gad7.m
% April 2001
% Lieven Vandersypen <lieven@snow.stanford.edu>
%
% simulate generalized amplitude damping (GAD), 7 spins
% model assumes no correlation of GAD on different spins
%
% Usage rout=gad(rin,p,t,ratio)
%
% rin    initial density matrix
% p      equilibrium polarization
% t      duration for which GAD acts
% ratio  set this to 1 to simulate GAD, set this to say 1e9 to
%         simulate the same sequence without GAD
% rout   final density matrix

function rout=gad(rin,p,t,ratio)

T1_1=ratio(1)*5.0;    % the labeling is in order of frequency
T1_2=ratio(1)*10.0;
T1_3=ratio(1)*13.7;
T1_4=ratio(1)*2.8;
T1_5=ratio(1)*3.0;
T1_6=ratio(1)*31.6;
T1_7=ratio(1)*45.4;

p1=p;                % fluorine polarization
p2=0.5+(p-0.5)*1.25/4.7; % carbon polarization

% T1 effects on spin 1
g=1-exp(-t/T1_1);
E{1}=sqrt(p1)*[1 0; 0 sqrt(1-g)];    E{2}=sqrt(p1)*[0 sqrt(g);0 0];
E{3}=sqrt(1-p1)*[sqrt(1-g) 0;0 1];  E{4}=sqrt(1-p1)*[0 0 ;sqrt(g) 0];
r1=0;
for k=1:4
r1 = r1 + mykron(E{k},eye(2),eye(2),eye(2),eye(2),eye(2),eye(2))*...
rin*mykron(E{k},eye(2),eye(2),eye(2),eye(2),eye(2),eye(2))';
end
```


...

```
% T1 effects on spin 7
g=1-exp(-t/T1_7);
E{1}=sqrt(p2)*[1 0; 0 sqrt(1-g)]; E{2}=sqrt(p2)*[0 sqrt(g);0 0];
E{3}=sqrt(1-p2)*[sqrt(1-g) 0;0 1]; E{4}=sqrt(1-p2)*[0 0 ;sqrt(g) 0];
r7=0;
for k=1:4
r7 = r7 + mykron(eye(2),eye(2),eye(2),eye(2),eye(2),eye(2),E{k})*...
r6*mykron(eye(2),eye(2),eye(2),eye(2),eye(2),eye(2),E{k})';
end

rout=r7;
```

A.6 Phase damping

```
% file: pd7.m
% April 2001
% Lieven Vandersypen <lieven@snow.stanford.edu>
%
% simulates phase damping (PD), 7 spins
% model assumes no correlation of PD on different spins
%
% Usage rout=pd(rin,t,ratio)
%
% rin    initial density matrix
% t      duration for which PD acts
% ratio  set this to 1 to simulate PD, set this to say 1e9 to
%        simulate the same sequence without PD
% rout   final density matrix

function rout=pd(rin,t,ratio)

T2_1=ratio(2)*1.3; % the labeling is in order of frequency
T2_2=ratio(2)*1.7;
T2_3=ratio(2)*1.8;
T2_4=ratio(2)*1.6;
T2_5=ratio(2)*1.5;
T2_6=ratio(2)*2.0;
T2_7=ratio(2)*2.0;

% T2 effects on spin 1
g=(1+exp(-t/T2_1))/2;
E{1}=sqrt(g)*[1 0; 0 1]; E{2}=sqrt(1-g)*[1 0;0 -1];
r1=0;
```

```

for k=1:2
r1 = r1 + mykron(E{k}, eye(2), eye(2), eye(2), eye(2), eye(2), eye(2)) * ...
rin*mykron(E{k}, eye(2), eye(2), eye(2), eye(2), eye(2), eye(2))';

end

...

% T2 effects on spin 7
g=(1+exp(-t/T2_7))/2;
E{1}=sqrt(g)*[1 0; 0 1];    E{2}=sqrt(1-g)*[1 0; 0 -1];
r7=0;
for k=1:2
r7 = r7 + mykron(eye(2), eye(2), eye(2), eye(2), eye(2), eye(2), E{k}) * ...
r6*mykron(eye(2), eye(2), eye(2), eye(2), eye(2), eye(2), E{k})';

end

rout=r7;

```

A.7 Helper programs

```

% File: gop.m    (generalized operator)
% Date: 08-Oct-99
% Author: Lieven Vandersypen <lieven@snow.stanford.edu>
%
% Usage: gop(s,U)
% In:    single-qubit unitary operator U, qubit name s
% Out:   n-spin unitary operator which acts on qubit s with U and
%        trivially on the remaining qubits

function gop=gop(s,U)

global nqubits

goplocal=U;

for position=1:(s-1)
    goplocal=kron(eye(2), goplocal);
end
for position=s+1:nqubits
    goplocal=kron(goplocal, eye(2));
end
gop=goplocal;

```

```

% File:   mykron.m
% Date:   17-Aug-98
% Author: I. Chuang <ike@isl.stanford.edu>
%
% kronecker product function which accepts multiple arguments.

function out = mykron(ma,mb,varargin)

if (length(varargin) == 0)
    out = kron(ma,mb);
    return;
else
    out = mykron(kron(ma,mb),varargin{:});
    return;
end

```

A.8 Pulse sequence code in MATLAB

The following could be an executable in MATLAB which simulates a pulse sequence, taking into account the effect of decoherence.

```

nq=7;
def;

ratio=1; % model GAD and PD (if ratio was set to a larger number,
        % say 1e9, the simulation would use near infinite T1 and T2.

% set up thermal density matrix
p1=(0.5000)+5e-4; p2=p1/4.7*1.25;
rt1=(1-p1)*eye(2) + (2*p1-1)*[1 0 ;0 0]; % fluorine spins
rt2=(1-p2)*eye(2) + (2*p2-1)*[1 0 ;0 0]; % carbon spins
rit=mykron(rt1,rt1,rt1,rt1,rt1,rt2,rt2); % 7-spin molecule

... % [here would go some code which produces R starting from rit]

% the remainder does a cnot_52, with partial refocusing of J couplings

time=abs(1/8/J25)

R=rho(R,X(2,1)*Z(2,-1));

R=rho(R,d(time));
R=gad7(R,p1,time,ratio); R=pd7(R,time,ratio);
R=rho(R,X(1,2)*X(3,2));

```

```
R=rho(R,d(time));  
R=gad7(R,p1,time, ratio); R=pd7(R,time, ratio);  
R=rho(R,X(1,2)*X(2,2)*X(5,2));
```

```
R=rho(R,d(time));  
R=gad7(R,p1,time, ratio); R=pd7(R,time, ratio);  
R=rho(R,X(1,2)*X(3,2));
```

```
R=rho(R,d(time));  
R=gad7(R,p1,time, ratio); R=pd7(R,time, ratio);  
R=rho(R,X(1,2)*X(2,2)*X(5,2));
```

```
R=rho(R,Y(2,-1)*X(7,1)*Z(7,1)*Z(5,1));
```

Appendix B

Pulse sequence three-spin Grover search

We here give the final pulse sequences used in the experiment of Section 5.7. They are taken from the C code submitted to the spectrometer, with additional comments for clarity.

```
=====
NOTATION
=====
```

Yb(1) represents a $1 \cdot \pi/2 = \pi/2$ pulse on spin b about the Y axis
mXc(0.5) represents a $0.5 \cdot \pi/2 = \pi/4$ pulse on spin c about the
-X axis, etcetera

AB(), AC() and BC() represent simultaneous pulses on two spins. The first two arguments are the tip angle in units of $\pi/2$, and the last two arguments are the phase of each pulse.

Example: AC(0.5,2,PHX,PHmY) performs a $\pi/4$ pulse on spin a about the X axis, and a π pulse on spin c about the -Y axis

ABC() represents a simultaneous pulse on all three spins. The first three arguments are the tip angle in units of $\pi/2$, and the last three arguments are the phase of each pulse.

```
=====
OUTLINE
=====
```

```
delay(d1); /* THERMALIZATION */
```

```
tom3htemplab1(); /* TEMPORAL LABELING */
```

```
ABC(1,1,1,PHY,PHY,PHY); /* Hadamard on each spin */
```

```
/* the parameter ctype determines which will be the marked element x0
```

```

    that will be "found" during the execution of the algorithm */

pfa=2; pfb=2; pfc=2;          /* default values */

if (ctype){                  /* if ctype=0, skip search */

    if (((ctype-1)/4)%2) pfa=0;
    if (((ctype-1)/2)%2) pfb=0;
    if (((ctype-1)/1)%2) pfc=0;

loop(v9,v10);                /* start loop Grover iterations */
/* function evaluation */
    ABC(pfa,pfb,pfc,PHX,PHX,PHX); /* depends on ctype */
    tom3hphaseflip4();           /* flip sign 111 term */
    ABC(pfa,pfb,pfc,PHmX,PHmX,PHmX); /* depends on ctype */
/* inversion about the average */
    ABC(1,1,1,PHY,PHY,PHY);     /* pi/2 Y pulse on each spin */
    tom3hphaseflip4();           /* flip sign 111 term */
    ABC(1,1,1,PHmY,PHmY,PHmY); /* pi/2 -Y pulse on each spin */
endloop(v10);

} /* close if (ctype) */

tomoPULSE;                   /* TOMOGRAPHY PULSES */

=====
tom3hphaseflip4() - this function implements a diagonal unitary
operator with the elements [1 1 1 1 1 1 1 -1] on the diagonal
=====

Yb(2); delay(1/8/Jbc); Xa(1); Ya(0.5); Xa(1); delay(1/8/Jbc);
Yb(1); Xb(0.5); delay(1/4/Jab); mYc(2); delay(1/4/Jab); Yb(1); mXb(1);
delay(1/8/Jbc); Ya(2); delay(1/8/Jbc);
mXb(1); Yb(0.5); delay(1/4/Jab); Yc(1); Xc(0.5); Yc(1); delay(1/4/Jab);
Yb(1); delay(1/8/Jac); mYb(2); delay(1/8/Jac);

=====
tom3htemplabl() - this function implements one of several sequences,
each of which transforms the initial (thermal equilibrium) density
matrix into one of the terms of the temporal labeling summation
=====

switch (ptype){
case 0: break;                /* I */
case 1:{                      /* cnotab */
    Yb(1); delay(1/4/Jab); Xc(2); delay(1/4/Jab); BC(1,2,PHX,PHX);
    break; }
case 2:{                      /* cnotac */

```

```

    Yc(1); delay(1/4/Jac); Xb(2); delay(1/4/Jac); BC(2,1,PHX,PHX);
    break; }
case 3:{
    /* cnotbc, Jbc<0 */
    mYc(1); delay(1/4/Jbc); Xa(2); delay(1/4/Jbc); AC(2,1,PHX,PHX);
    break; }
case 4:{
    /* cnotba */
    Ya(1); delay(1/4/Jab); Xc(2); delay(1/4/Jab); AC(1,2,PHX,PHX);
    break; }
case 5:{
    /* cnotca */
    Ya(1); delay(1/4/Jac); Xb(2); delay(1/4/Jac); AB(1,2,PHX,PHX);
    break; }
case 6:{
    /* cnotcb, Jbc<0 */
    mYb(1); delay(1/4/Jbc); Xa(2); delay(1/4/Jbc); AB(2,1,PHX,PHX);
    break; }
case 7:{
    /* cnotab.cnotca (time -->) */
    Yb(1); delay(1/4/Jab); Xc(2); delay(1/4/Jab); BC(1,2,PHX,PHX);
    Ya(1); delay(1/4/Jac); Xb(2); delay(1/4/Jac); AB(1,2,PHX,PHX);
    break; }
}

```


Bibliography

- [ABO97] D. Aharonov and M. Ben-Or. Fault tolerant computation with constant error. In *Proceedings of the Twenty-Ninth Annual ACM Symposium on the Theory of Computing*, pp. 176–188, 1997.
- [Abr61] A. Abragam. *Principles of Nuclear Magnetism*. Clarendon Press, Oxford, 1961.
- [AGH⁺55] A.G. Anderson, R.L. Garwin, E.L. Hahn, J.W. Horton, G.L. Tucker, and R.M. Walker. *J. Appl. Physics*, **26**, 1324, 1955.
- [AGR81] A. Aspect, P. Grangier, and G. Roger. Experimental tests of realistic local theories via Bell’s theorem. *Phys. Rev. Lett.*, **47**(7), 460–463, 1981.
- [AL97] D. S. Abrams and S. Lloyd. Simulation of many-body Fermi systems on a quantum computer. *Phys. Rev. Lett.*, **79**(13), 2586–2589, 1997.
- [AL99] D.S. Abrams and S. Lloyd. Quantum algorithm for providing exponential speed increase for finding eigenvalues and eigenvectors. *Phys. Rev. Lett.*, **83**(24), 5162–5165, 1999.
- [AV93] D. Abramovich and S. Vega. Derivation of broadband and narrowband excitation pulses using the Floquet formalism. *J. Magn. Reson. A*, **105**(18), 30–48, 1993.
- [Ave00] D.V. Averin. Quantum computing and quantum measurement with mesoscopic Josephson junctions. *Fortschr. Phys.*, **48**(9–11), 1055–1074, 2000.
- [BB84] C. H. Bennett and G. Brassard. Quantum cryptography: Public key distribution and coin tossing. In *Proceedings of IEEE International Conference on Computers, Systems and Signal Processing*, pp. 175–179, IEEE, New York, 1984. Bangalore, India, December 1984.
- [BBBV97] C. H. Bennett, E. Bernstein, G. Brassard, and U. Vazirani. Strengths and weaknesses of quantum computing. *SIAM J. Comput.*, **26**(5), 1510–1523, 1997.
- [BBC⁺93] C. H. Bennett, G. Brassard, C. Crépeau, R. Jozsa, A. Peres, and W. Wootters. Teleporting an unknown quantum state via dual classical and EPR channels. *Phys. Rev. Lett.*, **70**, 1895, 1993.
- [BBC⁺95] A. Barenco, C. H. Bennett, R. Cleve, D. P. DiVincenzo, N. Margolus, P. Shor, T. Sleator, J. Smolin, and H. Weinfurter. Elementary gates for quantum computation. *Phys. Rev. A*, **52**, 3457–3467, 1995.
- [BBHT98] M. Boyer, G. Brassard, P. Høyer, and A. Tapp. Tight bounds on quantum searching. *Fortsch. Phys. – Prog. Phys.*, **46**(4–5), 493–505, 1998.

- [BBM⁺98] D. Boschi, S. Branca, F. De Martini, L. Hardy, and S. Popescu. Experimental realization of teleporting an unknown pure quantum state via dual classical and Einstein-Podolski-Rosen channels. *Phys. Rev. Lett.*, **80**, 1121, 1998.
- [BCDP96] D. Beckman, A. N. Chari, S. Devabhaktuni, and J. Preskill. Efficient networks for quantum factoring. *Phys. Rev. A*, **54**(2), 1034, 1996.
- [BCHP96] J. Burdon, P.L. Coe, I.B. Haslock, and R.L. Powell. The hydrofluorocarbon 1,1,1,2-tetrafluoroethane (hfc-134a) as a ready source of trifluorovinyl lithium. *J. Chem. Soc. Chem Commun.*, pp. 49–50, 1996.
- [BCJ⁺99] S. L. Braunstein, C. M. Caves, R. Jozsa, N. Linden, S. Popescu, and R. Schack. Separability of very noisy mixed states and implications for NMR quantum computing. *Phys. Rev. Lett.*, **83**(5), 1054–1057, 1999.
- [BCJD99] G. K. Brennen, C. M. Caves, P. S. Jessen, and I. H. Deutsch. Quantum logic gates in optical lattices. *Physical Review Letters*, **82**, 1060–1063, 1999.
- [BD00] C. H. Bennett and D. P. DiVincenzo. Quantum information and computation. *Nature*, **404**, 247–55, 2000.
- [Bel64] J. S. Bell. On the Einstein-Podolsky-Rosen paradox. *Physics*, **1**, 195–200, 1964.
- [Ben73] C. H. Bennett. Logical reversibility of computation. *IBM J. Res. Dev.*, **17**(6), 525–32, 1973.
- [Ben80] P. Benioff. The computer as a physical system: A microscopic quantum mechanical Hamiltonian model of computers as represented by Turing machines. *J. Stat. Phys.*, **22**(5), 563–591, 1980.
- [Ben92] C. H. Bennett. Quantum cryptography using any two nonorthogonal states. *Phys. Rev. Lett.*, **68**(21), 3121–3124, 1992.
- [Ber84] M.V. Berry. *Proc. R. Soc. London A*, **392**, 45, 1984.
- [BFF⁺84] C.J. Bauer, R. Freeman, T. Frenkiel, J. Keeler, and A.J. Shaka. Gaussian pulses. *J. Magn. Reson.*, **58**, 442–457, 1984.
- [BHIW86] J. C. Bergquist, R. G. Hulet, W. M. Itano, and D. J. Wineland. Observation of quantum jumps in a single atom. *Phys. Rev. Lett.*, **57**(14), 1699–1702, 1986.
- [BHL⁺00] W. T. Buttler, R. J. Hughes, S. K. Lamoreaux, G. L. Morgan, J. E. Nordholt, and C. G. Peterson. Daylight quantum key distribution over 1.6 km. *Phys. Rev. Lett.*, **84**(24), 5652–5655, 2000.
- [BHT98] G. Brassard, P. Høyer, and A. Tapp. Quantum counting. In *Automata, Languages and Programming, 25th Int. Colloquium, Aalborg, Denmark*, pp. 13–17, Springer-Verlag, Berlin, 1998. arXiv e-print quant-ph/9805082.
- [BK98] S.L. Braunstein and H. J. Kimble. Teleportation of continuous quantum variables. *Phys. Rev. Lett.*, **80**, 869–872, 1998.

- [BL00] S. Braunstein and H.-K. Lo, editors. *Scalable Quantum Computers - paving the way to realization*. Wiley, Berlin, Germany, 2000. Reprint of *Fortschr. Phys.*, vol. 48(9-11), 2000. Special issue on the implementation of quantum computers.
- [Blo46] F. Bloch. Nuclear induction. *Phys. Rev.*, **70**(7-8), 460–474, 1946.
- [Blo49] N. Bloembergen. *Physica*, **15**, 386, 1949.
- [BMG⁺87] R. Brüschweiler, J.C. Madsen, C. Griesinger, O.W. Sørensen, and R.R. Ernst. *J. Magn. Reson.*, **73**, 380, 1987.
- [BPM⁺97] D. Bouwmeester, J. W. Pan, K. Mattle, M. Eibl, H. Weinfurter, and A. Zeilinger. Experimental quantum teleportation. *Nature*, **390**(6660), 575–579, 1997.
- [BS40] F. Bloch and A. Siegert. Magnetic resonance for nonrotating fields. *Phys. Rev.*, **57**, 522–527, 1940.
- [BSKM⁺96] M. Brune, F. Schmidt-Kaler, A. Maali, J. Dreyer, E. Hagley, J.-M. Raimond, and S. Haroche. Quantum rabi oscillation: a direct test of field quantization in a cavity. *Phys. Rev. Lett.*, **76**, 1800–1803, 1996.
- [BW92] C. H. Bennett and S. J. Wiesner. Communication via one- and two-particle operators on Einstein-Podolsky-Rosen states. *Phys. Rev. Lett.*, **69**, 2881–2884, 1992.
- [CEMM98] R. Cleve, A. Ekert, C. Macchiavello, and M. Mosca. Quantum algorithms revisited. *Proc. R. Soc. London A*, **454**(1969), 339–354, 1998.
- [CFH97] D. G. Cory, A. F. Fahmy, and T. F. Havel. Ensemble quantum computing by NMR spectroscopy. *Proc. Nat. Acad. Sci. USA*, **94**, 1634–1639, 1997.
- [CGK98] I. L. Chuang, N. Gershenfeld, and M. Kubinec. Experimental implementation of fast quantum searching. *Phys. Rev. Lett.*, **18**(15), 3408–3411, 1998.
- [CGKL98] I. L. Chuang, N. Gershenfeld, M. G. Kubinec, and D. W. Leung. Bulk quantum computation with nuclear-magnetic-resonance: theory and experiment. *Proc. R. Soc. London A*, **454**(1969), 447–467, 1998.
- [Chu36] A. Church. An unsolvable problem of elementary number theory. *Am. J. Math.*, **58**, 345, 1936.
- [CKH⁺00] D. Collins, K.W. Kim, W.C. Holton, H. Sierzputowska-Gracz, and E.O. Stejskal. NMR quantum computation with indirectly coupled gates. *Phys. Rev. A*, **62**, 022304, 2000.
- [CL95] I. L. Chuang and R. Laflamme. Quantum error correction by coding. *arXiv e-print quant-ph/9511003*, Oct 1995.
- [Cle00] R. Cleve. The query complexity of order-finding. In *Proceedings of the 15th Annual IEEE Conference on Computational Complexity, Firenze, Italy*, pp. 54–59, IEEE Computer Society Press, Los Alamitos, CA, 2000. arXiv e-print quant-ph/9911124.
- [CLK⁺00] D.G. Cory, R. Laflamme, E. Knill, L. Viola, T.F. Havel, N. Boulant, G. Boutis, E. Fortunato, S. Lloyd, R. Martinez, C. Negrevergne, M. Pravia, Y. Sharf, G. Teklemariam, Y.S. Weinstein, and W.H. Zurek. NMR based quantum information processing: achievements and prospects. *Fortschr. Phys.*, **48**(9–11), 875–907, 2000.

- [CMP⁺98] D. G. Cory, W. Mass, M. Price, E. Knill, R. Laflamme, W. H. Zurek, T. F. Havel, and S. S. Somaroo. Experimental quantum error correction. *Phys. Rev. Lett.*, **81**(10), 2152–2155, 1998.
- [Cop94] D. Coppersmith. An approximate Fourier transform useful in quantum factoring. *IBM Research Report RC 19642*, 1994.
- [CPH98] D. G. Cory, M. D. Price, and T. F. Havel. Nuclear magnetic resonance spectroscopy: An experimentally accessible paradigm for quantum computing. *Physica D*, **120**, 82–101, 1998.
- [CT91] T. M. Cover and J. A. Thomas. *Elements of Information Theory*. John Wiley and Sons, New York, 1991.
- [CTDL77] C. Cohen-Tannoudji, B. Diu, and F. Laloë. *Quantum Mechanics (2 volumes)*. John Wiley and Sons, New York, 1977.
- [CVS01] D.E. Chang, L.M.K. Vandersypen, and M. Steffen. NMR implementation of a building block for scalable quantum computation. *Chem. Phys. Lett.*, **338**, 337–344, 2001.
- [CVZ⁺98] I. L. Chuang, L. M. K. Vandersypen, X. L. Zhou, D. W. Leung, and S. Lloyd. Experimental realization of a quantum algorithm. *Nature*, **393**(6681), 143–146, 1998.
- [CWK⁺01] B.E. Cole, J.B. Williams, B.T. King, M.S. Sherwin, and C.R. Stanley. Coherent manipulation of semiconductor quantum bits with terahertz radiation. *Nature*, **410**, 60–63, 2001.
- [CZ95] J. I. Cirac and P. Zoller. Quantum computations with cold trapped ions. *Phys. Rev. Lett.*, **74**, 4091, 1995.
- [CZ00] J. I. Cirac and P. Zoller. A scalable quantum computer with ions in an array of microtraps. *Nature*, **404**, 579–581, 2000.
- [DAK00] K. Dorai, Arvind, and A. Kumar. Implementing quantum-logic operations, pseudopure states, and the Deutsch-Jozsa algorithm using non-commuting selective pulses in NMR. *Phys. Rev. A*, **61**, 042306(7), 2000.
- [Dav65] M. D. Davis. *The Undecidable*. Raven Press, Hewlett, New York, 1965.
- [DB00] I.H. Deutsch and G.K. Brennen. Quantum computing with neutral atoms in an optical lattice. *Fortschr. Phys.*, **48**(9-11), 925–943, 2000.
- [DBE95] D. Deutsch, A. Barenco, and A. Ekert. Universality in quantum computation. *Proc. R. Soc. London A*, **449**(1937), 669–677, 1995.
- [DBIW89] F. Diedrich, J.C. Bergquist, W.M. Itano, and D.J. Wineland. Laser cooling to the zero-point energy of motion. *Phys. Rev. Lett.*, **62**, 430, 1989.
- [DBLW00] D.P. DiVincenzo, D.P. Bacon, D.A. Lidar, and K.B. Whaley. Universal quantum computation with the exchange interaction. *Nature*, **408**, 339, 2000.
- [Deu85] D. Deutsch. Quantum theory, the Church-Turing Principle and the universal quantum computer. *Proc. R. Soc. Lond. A*, **400**, 97–117, 1985.
- [Deu89] D. Deutsch. Quantum computational networks. *Proc. R. Soc. London A*, **425**, 73, 1989.

- [Die82] D. Dieks. Communication by EPR devices. *Phys. Lett. A*, **92**(6), 271–272, 1982.
- [DiV95a] D. P. DiVincenzo. Quantum computation. *Science*, **270**, 255, 1995.
- [DiV95b] D. P. DiVincenzo. Two-bit gates are universal for quantum computation. *Phys. Rev. A*, **51**(2), 1015–1022, 1995.
- [DiV98] D. P. DiVincenzo. Quantum gates and circuits. *Proc. R. Soc. London A*, **454**, 261–276, 1998.
- [DiV00] D. P. DiVincenzo. The physical implementation of quantum computers. *Fortschr. Physik*, **48**(9-11), 771–783, 2000.
- [DJ92] D. Deutsch and R. Jozsa. Rapid solution of problems by quantum computation. *Proc. R. Soc. London A*, **439**, 553, 1992.
- [DL99] D.P. DiVincenzo and D. Loss. Quantum computers and quantum coherence. *J. Magnetism and Magnetic Mats.*, **200**, 202, 1999.
- [dP79] M. Van der Puy. The reaction of molybdenum hexafluoride with carboxylic acids. *J. Fluor. Chem.*, **13**, 375–378, 1979.
- [EB90] L. Emsley and G. Bodenhausen. Phase shifts induced by transient bloch-siegert effects in NMR. *Chem. Phys. Lett.*, **168**(3,4), 297–303, 1990.
- [EBW87] R. R. Ernst, G. Bodenhausen, and A. Wokaun. *Principles of Nuclear Magnetic Resonance in One and Two Dimensions*. Oxford University Press, Oxford, 1987.
- [EJ96] A. Ekert and R. Jozsa. Quantum computation and Shor’s factoring algorithm. *Rev. Mod. Phys.*, **68**, 1, 1996.
- [EL75] J.W. Emsley and J.C. Lindon. *NMR Spectroscopy using liquid crystal solvents*. Pergamon Press, Oxford, 1975.
- [EM62] D.D. Elleman and S.L. Manatt. *J. Chem. Phys.*, **36**, 1945–1947, 1962.
- [EM96] A. Ekert and C. Macchiavello. Error correction in quantum communication. *Phys. Rev. Lett.*, **77**, 2585, 1996.
- [EPR35] A. Einstein, B. Podolsky, and N. Rosen. Can quantum-mechanical description of physical reality be considered complete? *Phys. Rev.*, **47**, 777–780, 1935.
- [Fey60] R.P. Feynman. There’s plenty of room at the bottom. In *Engineering and Science*, Caltech, Pasadena, CA, February 1960. Available at <http://www.zyvex.com/nanotech/feynman.html>.
- [Fey82] R. P. Feynman. Simulating physics with computers. *Int. J. Theor. Phys.*, **21**, 467, 1982.
- [Fey85] R. P. Feynman. Quantum mechanical computers. *Optics News*, p. 11, February 1985.
- [Fey96] R. P. Feynman. *Feynman Lectures on Computation*. Addison-Wesley, New York, 1996.
- [FG59] G. Feher and E.A. Gere. Electron spin resonance experiments on donors in silicon. ii. electron spin relaxation effects. *Phys. Rev.*, **114**, 1245–1256, 1959.

- [FKR⁺99] R. Fiederling, M. Keim, G. Reuscher, W. Ossau, G. Schmidt, A. Waag, and L.W. Molenkamp. Injection and detection of a spin-polarized current in a light emitting diode. *Nature*, **402**, 787–790, 1999.
- [FLS65] R. P. Feynman, R. B. Leighton, and M. Sands. Volume III of *The Feynman Lectures on Physics*. Addison-Wesley, Reading, Mass., 1965.
- [FPC⁺00] J.R. Friedman, V. Patel, W. Chen, S.K. Tolpygo, and J.E. Lukens. Quantum superposition of distinct macroscopic states. *Nature*, **406**, 43–46, 2000.
- [Fre97] R. Freeman. *Spin Choreography*. Spektrum, Oxford, 1997.
- [Fre98] R. Freeman. Shaped radiofrequency pulses in high resolution NMR. *Progr. in NMR Spectr.*, **32**, 59–106, 1998.
- [FSH98] R.J. Fitzgerald, K.L. Sauer, and W. Happer. *Chem. Phys. Lett.*, **284**, 87, 1998.
- [FT82] E. Fredkin and T. Toffoli. Conservative logic. *Int. J. Theor. Phys.*, **21**(3/4), 219–253, 1982.
- [FZF⁺00] X. Fang, X. Zhu, M. Feng, X. Mao, and F. Du. Experimental implementation of dense coding using nuclear magnetic resonance. *Phys. Rev. A*, **61**, 022307(5), 2000.
- [GC97] N. Gershenfeld and I. L. Chuang. Bulk spin resonance quantum computation. *Science*, **275**, 350–356, 1997.
- [GC98] N. Gershenfeld and I.L. Chuang. Quantum computing with molecules. *Scientific American*, June 1998.
- [GC99] D. Gottesman and I. L. Chuang. Quantum teleportation is a universal computational primitive. *Nature*, **402**, 390–392, 1999.
- [GF91] H. Geen and R. Freeman. Band-selective radiofrequency pulses. *J. Magn. Reson.*, **93**, 93–141, 1991.
- [GG99] J.-M. Gerard and B. Gayral. In H. Benisty, J.-M. Gerard, and C. Weisbuch, editors, *QED phenomena and applications of microcavities and photonic crystals*, Springer-Verlag, Berlin, 1999.
- [GMS68] M. Green, N. Mayne, and F.G.A. Stone. *J. Chem. Soc. (A)*, p. 902, 1968.
- [Got98] D. Gottesman. Theory of fault-tolerant quantum computation. *Phys. Rev. A*, **57**(1), 127–137, 1998.
- [Gro96] L. K. Grover. A fast quantum mechanical algorithm for database search. In *28th ACM Symposium on Theory of Computation*, p. 212, Association for Computing Machinery, New York, 1996.
- [Gro97] L. K. Grover. Quantum mechanics helps in searching for a needle in a haystack. *Phys. Rev. Lett.*, **79**(2), 325, 1997.
- [GRTZ01] N. Gisin, G. Ribordy, W. Tittel, and H. Zbinden. Quantum cryptography. *arXiv e-print quant-ph/0101098*, 2001.
- [GS01] B. Georgeot and D.L. Shepelyanky. Exponential gain in quantum computing of quantum chaos and localization. *Phys. Rev. Lett.*, **86**(13), 2890–2893, 2001.

- [HBG00] P. Hübler, J. Bargon, and S.J. Glaser. Nuclear magnetic resonance quantum computing exploiting the pure spin state of *para* hydrogen. *J. Chem. Phys.*, **113**(6), 2056–2059, 2000.
- [HHK⁺98] S. E. Hamann, D. L. Haycock, G. Klose, P. H. Pax, I. H. Deutsch, and P. S. Jessen. Resolved-sideband raman cooling to the ground state of an optical lattice. *Phys. Rev. Lett.*, **80**, 4149–4152, 1998.
- [HMM90] X. Hao, J.S. Moodera, and R. Meservey. Spin-filter effect of ferromagnetic europium sulfide tunnel barriers. *Phys. Rev. B*, **42**(13), 8235–8243, 1990.
- [HR76] D.I. Hoult and R.E. Richards. The signal-to-noise ratio of the nuclear magnetic resonance experiment. *J. Magn. Reson.*, **24**, 71–85, 1976.
- [HU79] J.E. Hopcroft and J.D. Ullman. *Introduction to automata theory, languages, and computation*. Addison-Wesley, Reading, MA, 1979.
- [HW60] G. H. Hardy and E. M. Wright. *An Introduction to the Theory of Numbers, Fourth Edition*. Oxford University Press, London, 1960.
- [IAB⁺99] A. Imamoglu, D. D. Awschalom, G. Burkard, D. P. DiVincenzo, D. Loss, M. Sherwin, and A. Small. Quantum information processing using quantum dot spins and cavity QED. *Phys. Rev. Lett.*, **83**(20), 4204, 1999.
- [Jee82] J. Jeener. Superoperators in magnetic resonance. *Adv. Magn. Res.*, **10**, 1–51, 1982.
- [Jef63] C.D. Jeffries. *Dynamic nuclear orientation*. Wiley, New York, 1963.
- [JK99] J. A. Jones and E. Knill. Efficient refocussing of one spin and two spin interactions for NMR quantum computation. *J. Magn. Reson.*, **141**, 322, 1999.
- [JKB⁺87] W.R. Dolbier Jr., H. Karoniak, D.J. Burton, P.L. Heinze, A.R. Bailey, G.S. Shaw, and S.W. Hansen. Kinetic and thermodynamic studies of the thermal electrocyclic interconversions of perfluorinated dienes and cyclobutenes. *J. Am. Chem. Soc.*, **109**, 219–225, 1987.
- [JM98] J. A. Jones and M. Mosca. Implementation of a quantum algorithm to solve Deutsch’s problem on a nuclear magnetic resonance quantum computer. *J. Chem. Phys.*, **109**, 1648, 1998.
- [JM99] J.A. Jones and M. Mosca. Approximate quantum counting on an NMR ensemble quantum computer. *Phys. Rev. Lett.*, **83**, 1050, 1999.
- [JMH98] J. A. Jones, M. Mosca, and R. H. Hansen. Implementation of a quantum search algorithm on a nuclear magnetic resonance quantum computer. *Nature*, **393**(6683), 344, 1998.
- [Jon01] J.A. Jones. NMR quantum computation. *Progr. NMR Spectr.*, **38**, 325–360, 2001.
- [KA98] J.M. Kikkawa and D.D. Awschalom. *Phys. Rev. Lett.*, **80**, 4313, 1998.
- [Kan98] B. Kane. A silicon-based nuclear spin quantum computer. *Nature*, **393**, 133–137, 1998.
- [KCL98] E. Knill, I. Chuang, and R. Laflamme. Effective pure states for bulk quantum computation. *Phys. Rev. A*, **57**(5), 3348–3363, 1998.
- [KF95] Ě. Kupče and R. Freeman. Close encounters between soft pulses. *J. Magn. Reson. A*, **112**, 261–264, 1995.

- [Kit95] A. Yu. Kitaev. Quantum measurements and the Abelian stabilizer problem. *arXiv e-print quant-ph/9511026*, 1995.
- [Kit97] A. Y. Kitaev. Quantum computations: algorithms and error correction. *Russ. Math. Surv.*, **52**(6), 1191–1249, 1997.
- [KL96] E. Knill and R. Laflamme. A theory of quantum error correcting codes. *Phys. Rev. A*, **55**(2), 900–911, 1996.
- [KL98] E. Knill and R. Laflamme. On the power of one bit of quantum information. *Phys. Rev. Lett.*, **81**, 5672–5675, 1998.
- [KLL00] H. Kim, J.-S. Lee, and S. Lee. Implementation of the refined Deutsch-Jozsa algorithm on a three-bit NMR quantum computer. *Phys. Rev. A*, **62**, 022312, 2000.
- [KLM01] E. Knill, R. Laflamme, and G. J. Milburn. A scheme for efficient quantum computation with linear optics. *Nature*, **409**, 46–52, 2001.
- [KLMN01] E. Knill, R. Laflamme, R. Martinez, and C. Negrevergne. Implementation of the five-qubit error correction benchmark. *arXiv:quant-ph/0101034*, 2001.
- [KLMT00] E. Knill, R. Laflamme, R. Martinez, and C.-H. Tseng. An algorithmic benchmark for quantum information processing. *Nature*, **404**, 368–370, 2000.
- [KLZ98] E. Knill, R. Laflamme, and W. H. Zurek. Resilient quantum computation. *Science*, **279**(5349), 342–345, 1998.
- [Knu98] D. E. Knuth. *Seminumerical Algorithms 3rd Edition*, Volume 2 of *The Art of Computer Programming*. Addison-Wesley, Reading, Massachusetts, 1998.
- [Kob94] N. Koblitz. *A Course in Number Theory and Cryptography*. Springer-Verlag, New York, 1994.
- [Kra83] K. Kraus. *States, Effects, and Operations: Fundamental Notions of Quantum Theory*. Lecture Notes in Physics, Vol. 190. Springer-Verlag, Berlin, 1983.
- [KSF01] A. Khitrin, H. Sun, and B.M. Fung. Method of multifrequency excitation for creating pseudopure states for NMR quantum computing. *Phys. Rev. A*, **63**, 020301(4), 2001.
- [KWM⁺98] B. E. King, C. S. Wood, C. J. Myatt, Q. A. Turchette, D. Leibfried, W. M. Itano, C. Monroe, and D. J. Wineland. Cooling the collective motion of trapped ions to initialize a quantum register. *Phys. Rev. Lett.*, **81**, 1525–1529, 1998.
- [Lan61] R. Landauer. Irreversibility and heat generation in the computing process. *IBM J. Res. Dev.*, **5**, 183, 1961.
- [LB99] S. Lloyd and S. Braunstein. Quantum computation over continuous variables. *Phys. Rev. Lett.*, **82**, 1784–1787, 1999.
- [LBCF99] N. Linden, H. Barjat, R.J. Carbajo, and R. Freeman. Pulse sequences for NMR quantum computers: how to manipulate nuclear spins while freezing the motion of coupled neighbours. *Chem. Phys. Lett.*, **305**, 28–34, 1999.

- [LBF98] N. Linden, H. Barjat, and R. Freeman. An implementation of the Deutsch-Jozsa algorithm on a three-qubit NMR quantum computer. *Chem. Phys. Lett.*, **296**, 61–67, 1998.
- [LCW⁺96] C. Livermore, C.H. Crouch, R.M. Westervelt, K.L. Campman, and A.C. Gossard. The Coulomb blockade in coupled quantum dots. *Science*, **274**, 1332–1335, 1996.
- [LCYY00] D. W. Leung, I. L. Chuang, F. Yamaguchi, and Y. Yamamoto. Efficient implementation of coupled logic gates for quantum computation. *Phys. Rev. A*, **61**, 042310(7), 2000.
- [LD98] Daniel Loss and David P. DiVincenzo. Quantum computation with quantum dots. *Phys. Rev. A*, **57**, 120–126, 1998.
- [Lec63] Y. Lecerf. Machines de Turing réversibles. *Comptes Rendus*, **257**, 2597–2600, 1963.
- [Lev01] J. Levy. Universal quantum computation with spin-1/2 pairs and Heisenberg exchange. *arXiv e-print quant-ph/0101057*, 2001.
- [LFF82] M.H. Levitt, R. Freeman, and T. Frenkiel. *J. Magn. Reson.*, **47**, 328, 1982.
- [LGD⁺00] T.D. Ladd, J.R. Goldman, A. Dana, F. Yamaguchi, and Y. Yamamoto. Quantum computation in a one-dimensional crystal lattice with NMR force microscopy. *arXiv e-print quant-ph/0009122*, 2000.
- [LK97] C.K. Law and H.J. Kimble. Deterministic generation of a bit-stream of single-photon pulses. *J. Mod. Optics*, **44**, 2067, 1997.
- [LKF99] N. Linden, Ě. Kupče, and R. Freeman. NMR quantum logic gates for homonuclear spin systems. *Chem. Phys. Lett.*, **311**, 321–327, 1999.
- [LKZ⁺98] R. Laflamme, E. Knill, W. H. Zurek, P. Catasti, and S. V. S. Mariappan. NMR GHZ. *Phil. Trans. Roy. Soc. Lond. A*, **356**, 1941–1948, 1998.
- [Llo93] S. Lloyd. A potentially realizable quantum computer. *Science*, **261**, 1569, 1993.
- [Llo95a] S. Lloyd. Almost any quantum logic gate is universal. *Phys. Rev. Lett.*, **75**(2), 346–349, 1995.
- [Llo95b] Seth Lloyd. Quantum-mechanical computers. *Scientific American*, **273**(4), 44, October 1995.
- [Llo96] S. Lloyd. Universal quantum simulators. *Science*, **273**, 1073, 1996.
- [LMPZ96] R. Laflamme, C. Miquel, J.-P. Paz, and W. H. Zurek. Perfect quantum error correction code. *Phys. Rev. Lett.*, **77**, 198, 1996.
- [LVZ⁺99] D. Leung, L. Vandersypen, X. Zhou, M. Sherwood, C. Yannoni, and I. Chuang. Experimental realization of a two-bit phase damping quantum code. *Phys. Rev. A*, **60**(3), 1924–1943, 1999.
- [MCK00] M. Marjanska, I.L. Chuang, and M.G. Kubinec. *J. Chem. Phys.*, **112**, 5095, 2000.
- [ME61] J.F. Maher and D.F. Evans. *Proc. Chem. Soc.*, pp. 208–209, June 1961.
- [Meh83] M. Mehring. *High resolution NMR in solids*. Springer-Verlag, Berlin, 1983.

- [Mer85] N. D. Mermin. Is the moon there when nobody looks? Reality and the quantum theory. *Physics Today*, p. 45, April 1985.
- [MFM⁺00] R. Marx, A.F. Fahmy, J.M. Myers, W. Bermel, and S.J. Glaser. Approaching five-bit NMR quantum computing. *Phys. Rev. A*, **62**, 123310–8, 2000.
- [MHN⁺97] X. Maître, E. Hagle, G. Nogues, C. Wunderlich, P. Goy, M. Brune, J.-M. Raimond, and S. Haroche. Quantum memory with a single photon in a cavity. *Phys. Rev. Lett.*, **79**, 769–772, 1997.
- [Mil89] G. J. Milburn. Quantum optical Fredkin gate. *Phys. Rev. Lett.*, **62**(18), 2124–2127, 1989.
- [MKA⁺00] I. Malajovich, J. M. Kikkawa, D. D. Awschalom, J. J. Berry, and N. Samarth. Coherent transfer of spin through a semiconductor heterointerface. *Phys. Rev. Lett.*, **84**(5), 2000.
- [MMK⁺95] C. Monroe, D. M. Meekhof, B. E. King, W. M. Itano, and D. J. Wineland. Demonstration of a fundamental quantum logic gate. *Phys. Rev. Lett.*, **75**, 4714, 1995.
- [MOL⁺99] J. E. Mooij, T. P. Orlando, L. Levitov, L. Tian, C. H. van der Waal, and Lloyd S. Josephson persistent-current qubit. *Science*, **285**, 1036–1039, 1999.
- [MPZ00] C. Macchiavello, G.M. Palma, and A. Zeilinger, editors. *Quantum computation and quantum information theory*. World Scientific, Singapore, 2000.
- [MS99] K. Mølmer and A. Sørensen. Multiparticle entanglement of hot trapped ions. *Phys. Rev. Lett.*, **82**, 1835–1838, 1999.
- [MSS99] Y. Maklin, G. Schön, and A. Shnirman. Josephson-junction qubits with controlled couplings. *Nature*, **398**, 305–307, 1999.
- [MTCK96] H. Mabuchi, Q.A. Turchette, M.S. Chapman, and H.J. Kimble. Real-time detection of individual atoms falling through a high finesse optical cavity. *Opt. Lett.*, **21**, 1393–1395, 1996.
- [MZG96] A. Muller, H. Zbinden, and N. Gisin. Quantum cryptography over 23 km in installed under-lake telecom fibre. *Europhys. Lett.*, **33**, 334–339, 1996.
- [NC00] M.A. Nielsen and I.L. Chuang. *Quantum computation and quantum information*. Cambridge University Press, Cambridge, England, 2000.
- [NCL00] R.J. Nelson, D.G. Cory, and S. Lloyd. Experimental demonstration of Greenberger-Horne-Zeilinger correlations using nuclear magnetic resonance. *Phys. Rev. A*, **61**, 022106(5), 2000.
- [NCT97] Y. Nakamura, C.D. Chen, and J.S. Tsai. Spectroscopy of energy-level splitting between two macroscopic quantum states of charge coherently superposed by Josephson coupling. *Phys. Rev. Lett.*, **79**, 2328–2331, 1997.
- [NKL98] M. A. Nielsen, E. Knill, and R. Laflamme. Complete quantum teleportation using nuclear magnetic resonance. *Nature*, **396**(6706), 52–55, 1998.
- [NPT99] Y. Nakamura, Yu. A. Pashkin, and J. S. Tsai. Coherent control of macroscopic quantum states in a single-cooper-pair box. *Nature*, **398**, 786–788, 1999.

- [NRO⁺99] G. Nogues, A. Rauschenbeutel, S. Osnaghi, M. Brune, J. M. Raimond, and S. Haroche. Seeing a single photon without destroying it. *Nature*, **400**, 239–242, 1999.
- [NSD86] W. Nagourney, J. Sandberg, and H. Dehmelt. Shelved optical electron amplifier: observation of quantum jumps. *Phys. Rev. Lett.*, **56**(26), 2797–2799, 1986.
- [OOC⁺91] J.-M. Ouvrard, B. N. Ouvrard, J. Courtieu, C. L. Mayne, and D. M. Grant. *J. Magn. Reson.*, **93**, 225, 1991.
- [OSS⁺01] J.L. O’Brien, S.R. Schofield, M.Y. Simmons, R.G. Clark, A.S. Dzurak, N.J. Curson, B.E. Kane, N. S. McAlpine, M.E. Hawley, and G.W. Brown. Towards the fabrication of phosphorous qubits for a silicon quantum computer. *To appear in Phys. Rev. B*, 2001.
- [OYB⁺99] Y. Ohno, D.K. Young, B. Beschoten, F. Masukura, H. Ohno, and D.D. Awschalom. Electrical spin injection in a ferromagnetic semiconductor heterostructure. *Nature*, **402**, 790–792, 1999.
- [Pap94] C. M. Papadimitriou. *Computational Complexity*. Addison-Wesley, Reading, Massachusetts, 1994.
- [Pat91] S.L. Patt. Single- and multiple-frequency-shifted laminar pulses. *J. Magn. Reson.*, **96**, 94–102, 1991.
- [PD99] P. M. Platzman and M. I. Dykman. Quantum computing with electrons floating on liquid helium. *Science*, **284**, 1967, 1999.
- [Per93] A. Peres. *Quantum Theory: Concepts and Methods*. Kluwer Academic, Dordrecht, 1993.
- [PRN91] J. Pauly, P. Le Roux, and D. Nishimura. Parameter relations for the Shinnar-Le Roux selective excitation pulse design algorithm. *IEEE Transactions on medical imaging*, **10**(1), 53–65, 1991.
- [PRS00] P. Grangier, G. Reymond, and N. Schlosser. Implementations of quantum computing using cavity quantum electrodynamics schemes. *Fortschr. Phys.*, **48**(9-11), 859–874, 2000.
- [Red57] A.G. Redfield. *IBM J. Res. Dev.*, **1**, 19, 1957.
- [Red65] A.G. Redfield. *Adv. Magn. Res.*, **1**, 1–32, 1965.
- [RGR⁺01] H. Rohde, S. T. Gulde, C. F. Roos, P. A. Barton, D. Leibfried, J. Eschner, F. Schmidt-Kaler, and R. Blatt. Sympathetic ground state cooling and coherent manipulation with two-ion-crystals. *J. Opt. B*, **3**, S34, 2001.
- [RLM⁺00] C. F. Roos, D. Leibfried, A. Mundt, F. Schmidt-Kaler, J. Eschner, and R. Blatt. Experimental demonstration of ground state laser cooling with electromagnetically induced transparency. *Phys. Rev. Lett.*, **85**(26), 5547–5550, 2000.
- [RNO⁺00] A. Rauschenbeutel, G. Nogues, S. Osnaghi, P. Bertet, M. Brune, J.-M. Raimond, and S. Haroche. Step-by-step engineered multiparticle entanglement. *Science*, **288**, 2024–2028, 2000.
- [RSA78] R. L. Rivest, A. Shamir, and L. M. Adleman. A method of obtaining digital signatures and public-key cryptosystems. *Comm. ACM*, **21**(2), 120–126, 1978.

- [RYS92] D. Rugar, C.S. Yannoni, and J.A. Sidles. Mechanical detection of magnetic resonance. *Nature*, **360**, 563, 1992.
- [Sak95] J. J. Sakurai. *Modern Quantum Mechanics*. Addison-Wesley, Reading, Mass., 1995.
- [SC99] R. Schack and C. M. Caves. Classical model for bulk-ensemble NMR quantum computation. *Phys. Rev. A*, **60**(6), 4354–4362, 1999.
- [Sch35] E. Schrödinger. Die gegenwärtige Situation in der Quantenmechanik. *Die Naturwissenschaften*, **48**, 807–812, 1935.
- [SCS⁺00] Y. Sharf, D.G. Cory, S.S. Somaroo, T.F. Havel, E. Knill, and R. Laflamme. A study of quantum error correction by geometric algebra and liquid-state NMR spectroscopy. *Molec. Phys.*, **98**(17), 1347–1363, 2000.
- [SEP67] A. Saupe, G. Englert, and A. Povh. *ACS Adv. in Chem. Ser.*, **63**, 51, 1967.
- [SHC00] Y. Sharf, T.F. Havel, and D.G. Cory. Spatially encoded pseudopure states for NMR quantum-information processing. *Phys. Rev. A*, **62**, 052314(8), 2000.
- [Sho94] P. W. Shor. Algorithms for quantum computation: discrete logarithms and factoring. In *Proceedings, 35th Annual Symposium on Foundations of Computer Science*, pp. 124–134, IEEE Press, Los Alamitos, CA, 1994.
- [Sho95] P. W. Shor. Scheme for reducing decoherence in quantum memory. *Phys. Rev. A*, **52**, 2493, 1995.
- [Sho97] P. W. Shor. Polynomial-time algorithms for prime factorization and discrete logarithms on a quantum computer. *SIAM J. Comp.*, **26**(5), 1484–1509, 1997.
- [Sim94] D. Simon. On the power of quantum computation. In *Proceedings, 35th Annual Symposium on Foundations of Computer Science*, pp. 116–123, IEEE Press, Los Alamitos, CA, 1994.
- [Sim97] D. R. Simon. On the power of quantum computation. *SIAM J. Comput.*, **26**(5), 1474–1483, 1997.
- [SKK⁺00] C.A. Sackett, D. Kielpinsky, B.E. King, C. Langer, V. Meyer, C.J. Myatt, M. Rowe, Q.A. Turchette, W.M. Itano, D.J. Wineland, and C. Monroe. Experimental entanglement of four particles. *Nature*, **404**, 256–258, 2000.
- [Sli96] C. P. Slichter. *Principles of Magnetic Resonance*. Springer, Berlin, 1996.
- [SMY⁺01] B.C. Stipe, H.J. Mamin, C.S. Yannoni, T.D. Stowe, T.W. Kenny, and D. Rugar. Electron spin relaxation induced by a micron-sized ferromagnet. *in preparation for submission to Science*, 2001.
- [SN96] B. W. Schumacher and M. A. Nielsen. Quantum data processing and error correction. *Phys. Rev. A*, **54**(4), 2629, 1996.
- [SOF94] U. Sakaguchi, H. Ozawa, and T. Fukumi. Method for effective pure states with any number of spins. *Phys. Rev. A*, **61**, 042313(5), 1994.

- [SPM86] D. Suter, A. Pines, and M. Mehring. Indirect phase detection of NMR spinor transitions. *Phys. Rev. Lett.*, **57**, 242–244, 1986.
- [Ste96] A. M. Steane. Error correcting codes in quantum theory. *Phys. Rev. Lett.*, **77**, 793, 1996.
- [Ste98] A. Steane. Quantum computing. *Rep. Prog. Phys.*, **61**(2), 117–173, 1998.
- [STH⁺99] S. Somaroo, C. H. Tseng, T. F. Havel, R. Laflamme, and D. G. Cory. Quantum simulations on a quantum computer. *Phys. Rev. Lett.*, **82**, 5381–5384, 1999.
- [SV99] L. J. Schulman and U. Vazirani. Molecular scale heat engines and scalable quantum computation. *Proc. 31st Ann. ACM Symp. on Theory of Computing (STOC '99)*, pp. 322–329, 1999.
- [SVC00] M. Steffen, L.M.K. Vandersypen, and I.L. Chuang. Simultaneous soft pulses applied at nearby frequencies. *J. Magn. Reson.*, **146**, 369–374, 2000.
- [SVC01] M. Steffen, L.M.K. Vandersypen, and I.L. Chuang. Toward quantum computation: a five-qubit quantum processor. *IEEE Micro*, **21**(2), 24–34, March 2001.
- [TAH⁺96] S. Tarucha, D.G. Austing, T. Honda, R.J. van der Hage, and L. P. Kouwenhoven. *Phys. Rev. Lett.*, **77**, 3613, 1996.
- [Tap98] A. Tapp. *unpublished*, 1998.
- [THL⁺95] Q. A. Turchette, C. J. Hood, W. Lange, H. Mabuchi, and H. J. Kimble. Measurement of conditional phase shifts for quantum logic. *Phys. Rev. Lett.*, **75**, 4710, 1995.
- [TM73] P.M. Tedrow and R. Meservey. Spin polarization of electrons tunneling from films of Fe, Co, Ni and Ga. *Phys. Rev. B*, **7**(1), 318–326, 1973.
- [Tof80] T. Toffoli. Reversible computing. In W. de Bakker and J. van Leeuwen, editors, *Automata, Languages, and Programming*, pp. 632–644. Springer, New York, 1980.
- [TSS⁺99] D.H. Tseng, S. Somaroo, Y. Sharf, E. Knill, R. Laflamme, T.F. Havel, and D.G. Cory. Quantum simulation of a three-body-interaction hamiltonian on an NMR quantum computer. *Phys. Rev. A*, **61**, 012302(6), 1999.
- [Tur36] A. M. Turing. On computable numbers, with an application to the Entscheidungsproblem. *Proc. Lond. Math. Soc. 2 (reprinted in [Dav65])*, **42**, 230, 1936.
- [TWK⁺98] Q.A. Turchette, C.S. Wood, B.E. King, C.J. Myatt, D. Leibfried, W.M. Itano, C. Monroe, and D.J. Wineland. Deterministic entanglement of two trapped ions. *Phys. Rev. Lett.*, **81**, 3631–3634, 1998.
- [Unr95] W. G. Unruh. Maintaining coherence in quantum computers. *Phys. Rev. A*, **51**(2), 992–997, 1995.
- [VLV⁺01] A.S. Verhulst, O. Liivak, H.M. Vieth, C.S. Yannoni, and I.L. Chuang. Non-thermal nuclear magnetic resonance quantum computing using hyperpolarized xenon. *submitted to Appl. Phys. Lett.*, 2001.
- [VSB⁺00] L.M.K. Vandersypen, M. Steffen, G. Breyta, C.S. Yannoni, R. Cleve, and I. L. Chuang. Experimental realization of an order-finding algorithm with an NMR quantum computer. *Phys. Rev. Lett.*, **85**(25), 5452–5455, 2000.

- [VSB⁺01] L.M.K. Vandersypen, M. Steffen, G. Breyta, C.S. Yannoni, R. Cleve, and I. L. Chuang. Experimental realization of Shor's quantum factoring algorithm. *in preparation*, 2001.
- [VSS⁺00] L.M.K. Vandersypen, M. Steffen, M. H. Sherwood, C.S. Yannoni, G. Breyta, and I. L. Chuang. Implementation of a three-quantum-bit search algorithm. *Appl. Phys. Lett.*, **76**(5), 646–648, 2000.
- [vtW⁺00] C.H. van der Wal, A.C.J. ter Haar, F.K. Wilhelm, R.N. Schouten, C.J.P.M. Harmans, T.P. Orlando, S. Lloyd, and J.E. Mooij. Quantum superposition of macroscopic persistent-current states. *Science*, **290**, 773–777, 2000.
- [VV78] R.L. Vold and R.R. Vold. Nuclear magnetic relaxation in coupled spin systems. *Progr. in NMR Spectr.*, **12**, 79–133, 1978.
- [VYC01] L.M.K. Vandersypen, C.S. Yannoni, and I.L. Chuang. Liquid state NMR quantum computing. In D.M. Grant and R.K. Harris, editors, *to appear in The encyclopedia of NMR (supplement)*. John Wiley and Sons, West Sussex, England, 2001.
- [VYSC99] L. M. K. Vandersypen, C. S. Yannoni, M. H. Sherwood, and I. L. Chuang. Realization of effective pure states for bulk quantum computation. *Phys. Rev. Lett.*, **83**, 3085–3088, 1999.
- [VYW⁺99] R. Vrijen, E. Yablonovitch, K. Wang, H. W. Jiang, A. Balandin, V. Roychowdhury, T. Mor, and D. DiVincenzo. Electron spin resonance transistors for quantum computing in silicon-germanium heterostructures. *arXiv e-print quant-ph/9905096*, 1999.
- [War84] W. Warren. Effects of arbitrary laser or NMR pulse shapes on population inversion and coherence. *J. Chem. Phys.*, **81**(12), 5437–5448, 1984.
- [WMI⁺98] D. J. Wineland, C. Monroe, W. M. Itano, D. Leibfried, B. E. King, and D. M. Meekhof. Experimental issues in coherent quantum-state manipulation of trapped atomic ions. *J. Res. Natl. Inst. Stand. Tech.*, **103**, 259, 1998.
- [WPF⁺01] Y.S. Weinstein, M.A. Pravia, E.M. Fortunato, S. Lloyd, and D.G. Cory. Implementation of the quantum Fourier transform. *Phys. Rev. Lett.*, **86**(9), 1889–1891, 2001.
- [WZ82] W. K. Wootters and W. H. Zurek. A single quantum cannot be cloned. *Nature*, **299**, 802–803, 1982.
- [Yao93] A. C. Yao. Quantum circuit complexity. *Proc. of the 34th Ann. IEEE Symp. on Foundations of Computer Science*, pp. 352–361, 1993.
- [YSV⁺99] C.S. Yannoni, M.H. Sherwood, L.M.K. Vandersypen, M.G. Kubinec, D.C. Miller, and I.L. Chuang. Nuclear magnetic resonance quantum computing using liquid crystal solvents. *Appl. Phys. Lett.*, **75**(22), 3563–3565, 1999.
- [YY99] F. Yamaguchi and Y. Yamamoto. Crystal lattice quantum computer. *Appl. Phys. A*, **68**, 1–8, 1999.
- [Zur82] W. H. Zurek. Environment-induced super-selection rules. *Phys. Rev. D*, **26**(8), 1862–1880, 1982.
- [Zur91] W. H. Zurek. Decoherence and the transition from quantum to classical. *Phys. Today*, **44**(10), 36–44, 1991.